UNIVERSITY OF CALIFORNIA SAN DIEGO

Hybrid Terahertz Metamaterials: From Perfect Absorption to Superconducting Plasmonics

A dissertation submitted in partial satisfaction of the
requirements for the degree
Doctor of Philosophy

in

Physics

by

Jacob Schalch

Committee in charge:

Professor Richard Averitt, Chair
Professor Julio Barreiro
Professor Shaya Fainman
Professor Misha Fogler
Professor Boubacar Kante

2018

The dissertation of Jacob Schalch is approved, and it is acceptable in quality and form for publication on microfilm and electronically:

_____

_____

_____

_____

_____

Chair

University of California San Diego

2018

DEDICATION

To my parents who pushed me to ask questions without answers and believe in something bigger than myself.

EPIGRAPH

An expert is a person who has made all the mistakes that can be made in a very narrow field.

—Niels Bohr

TABLE OF CONTENTS

LIST OF FIGURES

LIST OF TABLES

ACKNOWLEDGEMENTS

There seems to be an unspoken understanding among many graduate students and professors that suffering is an integral part of earning a PhD. I'd certainly like to think that I've paid my dues in the currency of late nights, setbacks, and frustrations. But I can't say I've suffered. Conversely, the many years of my PhD have been some of the best of my life and its not just the weather, beaches, and IPAs (though it's not not that). I owe my educational success and personal happiness to the coworkers, collaborators, friends, and family who have supported me every step of the way.

First, I'd like to thank Professor Richard Averitt. I was one of his first students at UCSD, and since I began he granted me more autonomy and responsibility than I probably had any business having. But along with this responsibility he gave me the respect of a peer and collaborator and helped me grow into this mantle. Rarely have I met a physicist as brilliant and successful yet also approachable, patient, and kind. I consider myself incredibly lucky to have spent my PhD in his group.

Equally important to my career here has been the greater Averitt group. Dylan, Kevin, Peter, Gufeng, Jingdi, and Verner have all contributed in some way to the work presented in this dissertation. Their camaraderie and skills have kept me sane and productive respectively, lending expertise in everything from intricacies of ultrafast experiments to secret surf spots. I'm proud to call them all my colleagues but also my friends.

My most vital collaboration has been with the group of professor Xin Zhang in the Boston University Mechanical Engineering Department. Over the course of my time in the Averitt group, Xin's group has done nearly 100% of the sample micro fabrication I have required for my various research endeavors, and I have done nearly 100% of the measurements for their projects. Though several thousand miles away, I worked more closely with them than with anyone else and developed the rapport to match. In particular, I would like to thank Xiaoguang Zhao and Guangwu Duan who skillfully fabricated most of the samples I will present here, but who's knowledge and

expertise were also crucial for the development of my own skills, intuition, and knowledge in the field of metamaterials. I will repeatedly sing their praises throughout this dissertation, but no amount will do justice to the degree of their contributions to my PhD.

I would also like to thank Rick's former student and my spiritual predecessor George Keiser. As the only "metamaterials guy" in the lab I have largely had to find my own way, but intensive training with George early on accelerated this process immensely. Through zealous readings and re-readings of his papers and thesis, long email chains, and two weeks working with him in person, George has played an outsized role in the development of the the skills necessary for my PhD.

Outside of the lab, I must thank my family first and foremost. Though I know it pains them that I am so far away, their support for me has been unwavering. My parents' fierce intellect and idealism has driven me towards a scientific career since I was in diapers, but it is only through their sacrifices and love that all of this has been possible. My siblings Liza, Peter, and Calvin have been a source of constancy and council. I'm proud of them all.

Finally I thank my larger family here in San Diego. The UCSD physics staff who have always been willing to help out. My graduate cohort who, through the trials of first year and the qualifying exam became some of my closest friends. The greater graduate community at UCSD, and the Graduate Student Association with their endless free beer. My (many) house mates who have been integral to my social life and also my financial survival. My climbing, biking, surfing, and skiing buddies, who have kept me active and alive (so far). And of course to my lovely girlfriend Valerie, who has stuck with me through the long hours away at the lab, the impenetrable physics conversations at parties, and the vague threat of some day having to live near a national laboratory.

It is hard to overstate how important the people who have surrounded me have been to my time in grad school. It is through them and toghether with them that I have thrived here. I will be thrilled if future chapters of my life contain even half as many wonderful people as I have come

to know here.

Chapter 4, in part is a reprint of the material as it appears in Applied Physics Letters 2018. Jacob Schalch, Guangwu Duan, Xiaoguang Zhao, Xin Zhang, and Richard D. Averitt, American Institute of Physics, 2018. The dissertation author was the primary investigator and author of this paper.

We acknowledge support from the National Science Foundation (NSF) (ECCS-1309835) and Army Research Office (ARO) (W911NF-16-1-0361). We thank Boston University Photonics Center for technical support.

Chapter 5, in part is currently being prepared for submission for publication of the material. Jacob Schalch, Yahua Tang, Hao Zhang, Xiaoguang Zhao, Xin Zhang, Qiye Wen, Richard D. Averitt. The dissertation author was the primary investigator and author of this material.

This work is supported by Natural Science Foundation of China under Grants 51572042, Science Challenge Project under Grant No. TZ2018003 and International Science and Technology Cooperation Program of China under Grant No. 2015DFR50870. We acknowledge support from the Department of Energy Basic Energy Sciences(DOE-BES) (DE-SC0018218). We thank Boston University Photonics Center for technical support.

Chapter 6, in part is currently being prepared for submission for publication of the material. Jacob Schalch, Kirk Post, Guangwu Duan, Xiaoguang, Zhao, Young-Duck Kim, James Hone, Michael Fogler, Xin Zhang, Dimitri Basov, and Richard D. Averitt. The dissertation author was the primary investigator and author of this material.

We acknowledge support from the Department of Energy Basic Energy Sciences(DOE-BES) (DE-SC0018218) for work performed at UC San Diego and Columbia University. We thank Boston University Photonics Center for technical support.

VITA

2011	B. A. in Physics, Oberlin College
2011-2012	Research Assistant, Paul Scherrer Institut
2014	M. S. in Physics, University of California San Diego
2012-2015	Graduate Teaching Assistant, University of California San Diego
2018	Ph. D. in Physics, University of California San Diego

PUBLICATIONS

Jacob Schalch, Guangwu Duan, Xiaoguang Zhao, Xin Zhang, and Richard D. Averitt, *Terahertz Metamaterial Perfect Absorber With Continuously Tunable Air Spacer Layer*, Applied Physics Letters **113**, 061113 (2018). https://doi.org/10.1063/1.5041282.

Jacob Schalch, Kirk Post, Guangwu Duan, Xiaoguang, Zhao, Young-Duck Kim, James Hone, Xin Zhang, Dimitri Basov, and Richard D. Averitt. *Metamaterial coupling to the superconducting Josephson Plasma Resonance in* $La_{2-x}Sr_xCuO_4$, (in preparation)

Jacob Schalch, Yahua Tang, Hao Zhang, Xiaoguang Zhao, Xin Zhang, Qiye Wen, Richard D. Averitt. *Broadband electrically tunable terahertz optical switch with suppressed reflection*, (in preparation)

Guangwu Duan, **Jacob Schalch**, Xiaoguang Zhao, Jingdi Zhang, Richard D. Averitt, and Xin Zhang, *An Air-Spaced Terahertz Metamaterial Perfect Absorber*, Sensors and Actuators A: Physical **280**, 303-308 (2018). https://doi.org/10.1016/j.sna.2018.07.052

Guangwu Duan, **Jacob Schalch**, Xiaoguang Zhao, Jingdi Zhang, Richard D. Averitt, and Xin Zhang, *Analysis of the Thickness Depednence of Metamaterial Absorbers at Terahertz Frequencies*, Optics Express **26**(3), 2242-2251 (2018). https://doi.org/10.1364/OE.26.002242

Guangwu Duan, **Jacob Schalch**, Xiaoguang Zhao, Jingdi Zhang, Richard D. Averitt, and Xin Zhang, *Identifying the Perfect Absorption of Metamaterial Absorbers*, Physical Review B **97**(3), 035128 (2018). https://doi.org/10.1103/PhysRevB.97.035128

Xiaoguang Zhao, **Jacob Schalch**, Jingdi Zhang, Huseyin Rahmi Seren, Guangwu Duan, Richard D. Averitt, and Xin Zhang, *Electromechanically Tunable Metasurface Transmission Waveplate at Terahertz Frequencies*, Optica **5**(3), 303-310 (2018). https://doi.org/10.1364/OPTICA.5.000303

Meng Wu, Xiaoguang Zhao, Jingdi Zhang, **Jacob Schalch**, Guangwu Duan, Kevin Cremin, Richard D. Averitt, and Xin Zhang, *A Three-Dimensional All-Metal Terahertz Metamaterial Perfect Absorber*, Applied Physics Letters **111**(5), 051101 (2017). https://doi.org/10.1063/1.4996897

ABSTRACT OF THE DISSERTATION

Hybrid Terahertz Metamaterials: From Perfect Absorption to Superconducting Plasmonics

by

Jacob Schalch

Doctor of Philosophy in Physics

University of California San Diego, 2018

Professor Richard Averitt, Chair

Metamaterials operating at terahertz (THz) region of the electromagnetic spectrum have remained have remained a promising area of study not only for realizing technologies in a historically underdeveloped spectral regime, but also as a scientific tool for exploring and controlling fundamental physical phenomena at meV energy scales in a variety of condensed matter systems. In this thesis, I will present several projects in which metamaterials and more traditional condensed matter systems are integrated into hybrid metamaterial systems. We leverage these systems to realize new practical THz devices, as well as to couple to and control quantum phenomena in condensed matter systems. I will begin with an introduction to the conceptual,

numerical, and experimental techniques in the THz metamaterial toolbox. The first research endeavor I will discuss is a metamaterial system that incorporates perhaps the simplest material; air. This metamaterial perfect absorber with a continuously tunable air dielectric layer allows for comprehensive exploration of metamaterial absorber systems, and demonstrates some unique phenomena owing to its lossless dielectric layer. Next I will introduce an applications oriented device; an electrically actuated broadband terahertz switch which transitions from a non-reflective, transmissive state to a fully absorptive state. It employs an all dielectric metamaterial layer to suppress reflections and trap light, and an electrically actuated phase change material, VO_2 to transition between states. The final section of this dissertation will explore strong coupling effects between a metamaterial and the superconducting c-axis Josephson plasmon in the layered cuprate, $La_{2-x}Sr_xCuO_4$. Preliminary measurements are first presented then followed by high field THz measurements in which complex nonlinear behavior is observed.

Chapter 1

Introduction

Condensed matter physics has advanced at a dizzying pace in recent decades, thanks in large part to parallel progress in computational power, material fabrication crystal growth, and optical experimental techniques among others. Nowhere is this confluence of progress more apparent than in the relatively young field of terahertz metamaterials. Advances in computational power and simulation algorithms have permitted increasingly rapid and accurate modelling and simulations, allowing scientists and engineers to conceive, design, and optimize a metamaterial and its response before it ever leaves the drawing board. Progress in nano-scale fabrication techniques have enabled the high fidelity construction of increasingly complex and tiny structures, while progress in the fabrication of complex solid state systems have allowed designers to integrate a broad array of complex constituent materials into metamaterial devices. Finally, the development of new optical techniques have allowed the study of metamaterials in an ever-broadening regimes of time scales, fluence, and frequency, in particular in the terahertz regime. This dissertation will discuss several projects in which all of these techniques are applied in order to create novel metamaterial devices, each of which incorporate more traditional condensed matter systems in order to realize both scientific and practical functionalists.

Metmaterials are artificial materials with repetitive structure on a small scale. In an

ordinary crystal, the different atoms and the geometric lattice they reside in work in concert to imbue the crystal with its macroscopic properties that are different from that of its elemental constituents. Likewise, the choices of constituent materials and the shapes in which they are patterned allow a metamaterial to act as an effectively homogeneous medium. Whereas the former is constrained by the inconveniences of physical chemistry, the latter is limited only by human creativity and the development of the previously mentioned fields. The combination of strong interaction with electromagnetic fields and freedom of design has made it possible to create innumerable custom tailored responses, including some not seen in nature. Some early and well known examples of this at radio-frequencies include negative index of refraction [2] [3], perfect lensing [4], and electromagnetic cloaking [5] [6] [7]; phenomena which until recently were considered to be the realm of science fiction. Since then the field has blossomed. Applications of metamaterials range from basic scientific exploration to commercial consumer technology. The electromagnetic spectral ranges in which they operate span from radio waves to visible light, and the types of designs and functionalities which have been produced are innumerable.

The metamaterials and techniques presented in this dissertation pertain to the terahertz (THz) regime of the electromagnetic spectrum. The THz regime lies between microwaves and infrared radiation on the electromagnetic spectrum, corresponding to a frequencies between between $0.3 - 3 \times 10^{12}$ oscillations per second (or equivalently 1mm to 0.1mm in free space wavelength). This spectral regime is of great interest both from a scientific and applications perspective. In condensed matter systems for instance, 2D electron gas plasmons [8], coherent phonons [9], spin phenomena, gap phenomena [10], and superconducting energy gaps often lie within this energy range [11]. Meanwhile, in the broader community, THz technology has shown promise for imaging [12], communications [13], security applications [14], and chemical and biological sensing [15] among others. But historically, the THz regime has been one in which little technology exists; one in which it is difficult both to produce and to detect light, giving rise to the term ”the THz gap”. It has only been in the past few decades that interest in THz science

and technology swelled, thanks to the development of new THz techniques and parallel advances in ultrafast laser technology [16]. In particular, THz time domain spectroscopy has allowed for broadband spectroscopy across the THz band [17] and new laser sources and techniques have enabled the generation of large amplitude THz pulses to drive nonlinear THz phenomena [18] [19] [20]. Thus recent and rapid developments of the THz metamaterials on which this dissertation is focused have only been made possible by the synchronous growth of metamaterials and THz techniques.

These advances in THz technologies have also also enabled further study of more traditional condensed matter systems and the phenomena which occur in them at THz energy scale. Though the bandgap energies of typical semiconductors are often far greater than that of THz light, the intraband carrier dynamics that govern nonlinear optical effects occur at THz frequencies and can shed light on the many body physics therein [10]. Similarly, in lower dimensional systems such as semiconductor nanostructures, quantum dots, and the like, modifications of the bulk electronic bands result in phenomena which occur at THz frequencies [8]. Likewise, a plethora of interesting physical phenomena occur at THz frequencies in correlated electron systems, and namely in superconductors [11]. Of particular interest in this dissertation is the emergence of collective oscillations of tunneling superconducting charge carriers in the family of layered Cuprates LSCO [21] [22]. The existence of these phenomena at THz frequencies further present the possibility of interaction and interplay between THz metamaterials and these THz phenomena.

Though the several research efforts presented in this dissertation are all concerned with the THz regime, their themes, techniques, and purposes will be broad. Each involves the a THz metamaterial which integrate both simple constituent materials and complex condensed matter systems. The types of metamaterials presented will be diverse, as will be the experimental methods employed to study them. The purposes of the metamaterial devices presented will range from practical and applications oriented devices, to complex systems designed to explore and

exploit the interactions between light and complex electronic phases of matter. Each will demonstrate the vital interplay between the computational simulation, device fabrication, and ultrafast optical techniques which which are necessary to realize and characterize a THz metamaterial device. Ultimately I hope that the topics surveyed in this dissertation will provide an idea of the flexibility of THz metamaterials for scientific and device applications as well as offer insights and outlooks into yet unexplored metamaterial functionalities for ultrafast optical condensed matter experiments.

1.1 Scope of the Thesis

Due to the disparate concepts, techniques, and purposes of the original research presented in this dissertation, it will be necessary to introduce a broad suite of concepts, numerical and experimental techniques, and condensed matter systems.

Our discussion will begin with an introduction to the fundamentals of metamaterials, followed by an extended look at one of the most canonical types; the split ring resonator (SRR). Using the SRR as an example, I will discuss the mechanism which imbues metamaterials with their unique properties, and the various ways in which those properties are understood. Starting from a microscopic scale, we will see that the SRR can be understood as a tiny RLC circuit, and how this results in resonant behavior accompanied by strong localization and enhancement of electromagnetic fields. Next we will zoom out, and see how these microscopic properties lead to an effective medium response, whereby tailored optical properties, including some not present elsewhere in nature, can be realized and characterized via the effective medium theory. Following that I will briefly discuss the plethora of other types and classes of of metamaterials and the contexts in which they can be useful. I will pay particular attention to THz metamaterials and a class of metamaterial on which much of my work was focused; the metamaterial perfect absorber (MPA). Finally I will survey approaches to achieving nonlinearity, tuning, and coupling effects in

metamaterials. .

Following this it is necessary to introduce the metamaterial tool box; the means by which metamaterials can be designed, fabricated, and measured. It is worth repeating that metamaterials have developed as a truly interdisciplinary field, built upon simultaneous and dramatic advances in computational power and algorithms, micro-fabrication techniques, and optical experimental techniques. In this section we will follow the work flow of a metamaterial project and see how these techniques and technologies fit together. First I will discuss numerical simulation techniques, covering the conceptual underpinnings and practical approach towards both time domain and frequency domain solvers. Next, I will discuss common fabrication techniques which are employed for THz metamaterials as well as for condensed matter crystals in general. Finally, I will cover the experimental techniques employed in an ultrafast THz laboratory. First I will discuss a workhorse system for high sensitivity linear time domain spectroscopy; the photoconductive terahertz time domain spectrometer, going into depth on one such instrument which I constructed for the measurement of both complex transmission and reflection between 200 GHz and 3 THz. Then I will discuss some of the other experimental techniques employed, in particular the generation of large THz fields necessary to generate a nonlinear response.

Following this extended introduction I will present the several projects undertaken during this dissertation, all of which combine metamaterials with more traditional complex condensed matter systems to realize unique behaviors and functionalities. The first of these three integrates a material which has debatable complexity, but which is certainly not condensed; air. This metamaterial perfect absorber has a dielectric spacer layer comprised entirely of air, which can be tuned to an arbtrary thickness for a unique and tunable response. I will begin with a discussion of the analytical inspiration for this project, the interference theory of metamaterial perfect absorbers; a powerful but simple analytical tool which can be used to understand the evolution of the absorption bands of an MPA as a function of the spacer layer thickness. Then the variable air spacer metamaterial perfect absorber result will be presented, which comprehensively validates

the interference theory in addition to showing some unique properties not seen in other MPAs.

The next project is one which aims to utilize an extensively studied but still controversial phase change material, VO_2, integrated into metamaterial device to realize an electrically actuated broadband THz switch. This device combines some of the concepts of metamaterial perfect absorbers as well as more traditional optical modulator designs. But whereas a typical modulator integrating phase change materials goes from a partially reflective, partially transmissive mode in its insulating state, to a mostly reflective state in its metallic state, this device utilizes a metamaterial layer to strongly suppress reflections in both states. Instead it transitions from a transmissive state with minimal reflection, to an almost entirely absorbing state, with almost no light transmitted nor reflected. I will first introduce VO_2, and then explore the performance of the device and speculate on various ways in which the design can be improved for certain applications.

The final portion of this dissertation addresses strong coupling between a metamaterial and a resonant superconducting quantum tunneling phenomenon known as the Josephson plasma resonance. It will first be necessary to introduce strong coupling effects in general and in the context of metamaterial systems. Then the electrodynamics of superconductivity and more specifically on the c-axis of the layered cuprate LSCO will be introduced in some depth. Then a preliminary experimental effort will be presented, demonstrating evidence of strong coupling effects between the metamaterial and the LSCO. Finally, the results of a high-field THz study will show still more unique nonlinear interactions between the two subsystems.

The conclusion will summarize results as well as provide some speculation on future research directions. The appendix will provide detailed application notes related the operation and construction of a dual mode photoconductive THz time domain spectrometer, and its constituent equipment.

Chapter 2

Metamaterial Fundamentals

Metamaterials are artificial materials which consist of inhomogeneous (having variations in material type and geometry) repetitive structures on a small length scale, but act as a homogeneous medium with properties entirely different from its constituent materials on a large length scale. An ordinary crystal consists of one or more types of atoms arranged into a simple geometrical pattern (called a unit cell). This pattern is repeated ad infinitum in all directions to form a 3D crystal lattice. On a macroscopic scale (a scale much larger than the unit cell), the properties of this crystal, be they mechanical, acoustic, or electromagnetic, are determined by the identity of those atoms and their geometry in this unit cell. Similarly, a metamaterial unit cell consists of multiple types of materials, structured into some simple geometry, and repeated into a large lattice. Though those materials themselves are made of many atoms and the length scales are consequently far larger than an atomic crystal, the concept is the same. Their properties depend both on the constituent materials and how the constituent materials are arranged. Zooming out to a much larger length scale, a metamaterial acts as a homogeneous medium, with properties that are entirely different than that of its constituent materials, controlled instead by the geometry of the unit cell structure. Whereas the atomic structure of a crystal's unit cell and thus its properties are constrained by the limits of physical chemistry (i.e. what atoms are available and will go together

in what structure and under what conditions), this limitation is largely absent for metamaterials. The geometry of a metamaterial unit cell and constituent materials is limited only by fabrication technology, giving researchers an almost limitless parameter space in which metamaterials can be designed, optimized, and controlled in order to realize the desired macroscopic properties. This imbues metamaterials with an extraordinary flexibility, and the ability to manifest properties not observed in nature.

It is first useful to review the basic electrodynamics of common materials. When an electric or magnetic field is applied to a material, that material will respond by becoming electrically and magnetically polarized respectively. The constants that determines the degree of these polarizations are the electric permittivity ε and the magnetic permeability μ such that:

$$P = E(\varepsilon_r - 1)\varepsilon_0$$

$$M = H(\mu_r - 1)\mu_0$$

where P is the polarization, E is the electric field, ε_r is the relative permittivity, and ε_0 is the free space permittivity. Likewise M, H, μ_r, and μ_0 is the magnetization, magnetic field, relative permeability, and free space permeability respectively. For the sake of simplicity, in the remainder of this dissertation, we will let ε_0=$\mu_0 = 1$ such that $\mu_r = \mu$ and $\varepsilon_r = \varepsilon$. Depending on the signs of μ and ε, a variety of responses are possible. Figure 2.1 shows μ and ε as independent axes. When both are positive (top right quadrant), we have a common dielectric material in which electromagnetic waves can propagate. When $\mu\varepsilon < 0$ (top left and bottom right quadrants) waves are evenescant and will quickly dissipate, as with metals, plasmas, etc.. But practically speaking, most materials are not strongly magnetic, and thus lie along $\mu = 1$ (red dotted line); a very limited parameter space. No known natural materials exist in the bottom left quadrant, where both μ and ε are negative.

The harbinger of the modern metamaterial emerged in 1967 with the speculative work

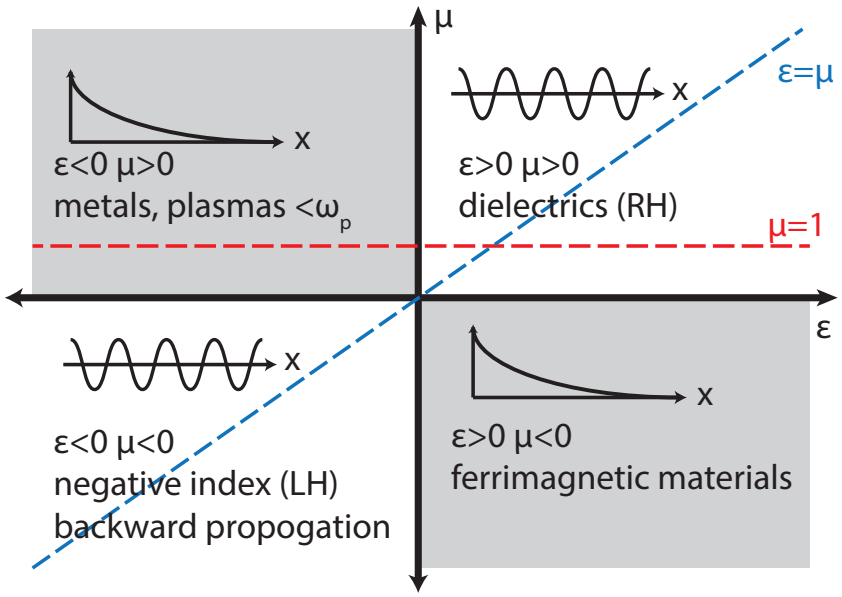

Figure 2.1: The plane of relative permittivity ε and permeability μ. Most materials are only weakly magnetic and thus lie close to $\varepsilon = 1$ (red dotted line). No natural materials are known which exist in the bottom left quadrant. In this reigon, the index of refraction is negative resulting in so called "left-handed" (LH) materials. To match the impedance of free space ($Z = 1$) the material must be engineered such that $\varepsilon = \mu$ (blue dotted line).

of Viktor Veselago [2]. He imagined such a material with simultaneously negaive μ and ε and mathematically explored how it would behave. He found that under these conditions, waves would propagate as in a normal material, but the wave crests would move in the opposite direction, i.e. the phase velocity of the light would be opposite to the group velocity. This phenomenon is known as negative index of refraction, or alternatively left handed media. He went on to predict a number of other phenomena, including the reversal of snell's law, the reversal of the doppler effect, perfect lensing, and the reversal of chrenkov radiation among others before finally lamenting the absence of any such materials in reality.

It was not until 33 years later that such a material emerged. John Pendry proposed artificial and effectively homogeneous materials made from ordinary dielectric and metallic components with small scale structure, that when designed correctly would resonate at microwave frequencies in order to produce strong electric and magnetic responses [4]. Inspired by this work, David

Smith and colleagues here at UC San Diego proposed and later realized a material based on this concept which had simletaneously negative permittivity and permeability [3]. These devices were simple, typically consisting of a combination of metallic rods and "C" shapes on a dielectric substrate. The size of these shapes could be several centimeters, as even at that size, the condition of being subwavelength ($\sim \lambda/10$) was easily met. These general design concepts were quickly applied to verify negative index [23], realize a super-lens [24], and create an electromagnetic cloak [5], resulting in an explosion of interest in the scientific community.

In the past past 20 years, metamaterials have grown from the imaginations of a hand full of physicists into a field which spans a variety of disciplines in physics, chemistry, engineering, and even made forays into the private sector. We now have electromagnetic metamaterials operating at frequencies anywhere from visible light to microwaves and across vast swaths of the electromagnetic spectrum. The same principles have even been applied to create acoustic and mechanical metamaterials. They have been developed for purposes as diverse as shielding buildings from the seismic waves of an earthquake [25], steering radiation for communication [26], and realizing analogues of exotic quantum states [27]. But before discussing the more complex applications of metamaterials which will be the focus of this dissertation, it is useful to explore the basic mechanisms that give them their unique characteristics by examining an example in depth. For this, we will go back to one of the earliest and simplest, but arguably most powerful and ubiquitous types of metamaterial designs; the split ring resonator.

2.1 The Split Ring Resonator

The split ring resonator (SRR) is without a doubt the oldest and most canonical metamaterial and it has been the the basis of many of the metamaterials discussed up to this point. As the name would imply, the simplest form of a split ring resonator resembles a ring of an electrically conductive material (often copper or gold) with a small gap in the ring at one point. John Pendry

first proposed the use of what would later be called the SRR in order to achieve a strong magnetic response [28]. SRRs were later employed in early pioneering work in metamaterials including the electromagnetic cloak, and are still the basis of much of modern metamaterials research; their usefulness is seemingly inexhaustible. While it is undoubtedly the richness and complexity of the physics of the SRR that have contributed to their ubiquity, the basic electrodynamics of the SRR are surprisingly simple. An in depth exploration of their operating principles will thus serve as an excellent introduction to concepts that can be applied to virtually any metamaterial.

2.1.1 Simple Models of the SRR

To build an intuitive understanding of the SRR and its resonant properties, I will begin with by invoking two of the most familiar and simple objects in classical mechanics and electromagnetism respectively: the mass on a spring, and the RLC circuit.

A mass on a spring is one of the first examples of harmonic motion that a student encounters in grade school, and thus in my mind serves as the conceptual underpinning of all harmonic oscillations. It consists of a mass sitting on a surface, and attached by a spring to a wall (Figure 2.2a). When displaced from its equilibrium position at $x = 0$, the mass will experience a restoring force $F = -kx$, and from newtons second law, an acceleration given by $a = \ddot{x} = \frac{-kx}{m}$. Adding in a damping force from friction $F_f = -\mu mg\dot{x}$ and writing out the toal equation of motion we get:

$$0 = m\ddot{x} + \mu gm\dot{x} + kx \tag{2.1}$$

This simple second-order differential equation has the general solution:

$$x(t) = A_1 e^{s_1 t} + A_2 e^{s_2 t} \tag{2.2}$$

where by substituting equation 2.2 into equation 2.1, we get the quadratic equation $ms^2 + \mu gms + k = 0$. The solutions of of the equation are given by:

$$s_1, s_2 = \frac{-\mu gs \pm \sqrt{(\mu gs)^2 - 4mk}}{2m} \tag{2.3}$$

And A_1 and A_2 are given by initial conditions. First considering a lossless case ($\mu = 0$), and given an initial position given by $x(0) = A$, the mass will slide back and fourth about its equilibrium position in simple harmonic motion with an angular frequency $\omega_0 = \sqrt{\frac{k}{m}}$ given by equation 2.3. In terms of energy, when the mass is at its maximum displacement A, it is momentarily stationary, and all of the energy of the system is stored in the potential energy of the spring given by $PE = \frac{1}{2}kx(t)^2 = \frac{1}{2}kA^2$ (blue line Figure 2.2b). As it swings back, this spring potential energy is converted into kinetic energy. At the equilibrium position, the spring stores no energy and the kinetic energy given by $KE = \frac{1}{2}m\dot{x}^2$ is at a maximum (red line). But inertia carries the mass along past the equilibrium to the negative extrema at $x = -A$. Thus the energy of the system oscillates between kinetic and potential energy, at angular frequency $\omega_0 = \sqrt{\frac{k}{m}}$. If modest losses are introduced in the form of friction, the resonant frequency will be altered slightly, and the total mechanical energy (kinetic+potential) will exponentially dissipate (black dotted line).

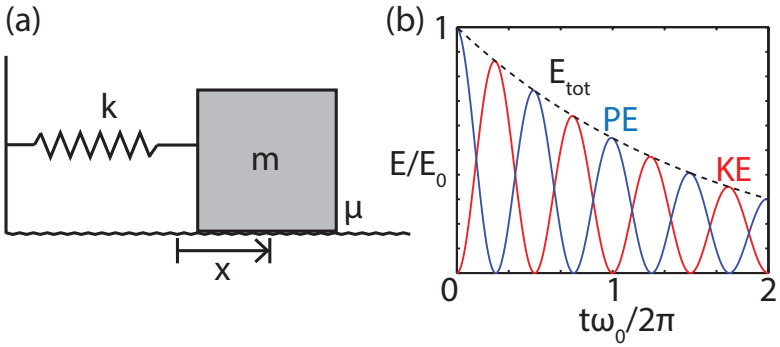

Figure 2.2: (a) A mass (m) on a spring with spring constant k on a surface with a friction coefficient μ and having a displacement x. (b) The total energy of the system $E_{tot} = KE + PE$ (black dotted line), the kenetic energy of the mass $KE = \frac{1}{2}m\dot{x}^2$, and the spring potential energy of the system $PE = \frac{1}{2}kx^2$ as a function of time

In many ways, the RLC circuit is identical. As the name would imply, it consists of a resistor (R) an inductor (L) and a capacitor (C) wired in series in a closed loop (see Figure 2.3a). The capacitor will take the role of storing potential energy previously held by gravity; as charge accumulates on the plates of the capacitor, energy is stored in the resulting electric field in between. The kinetic energy of the mass is replaced with the energy of the inductor; when current flows through though the inductor energy is stored in the resulting magnetic field. This give the current a kind of inertia: when no current flows through the inductor, it is difficult to get it flowing, but once it is flowing, it is equally difficult to get it to stop. The resistor will be the dissapative element, stealing away total energy from the system, when it is in motion, just as friction dissipates energy from objects in motion. For the characteristic equation, it is convenient to invoke Kirchhhoff's law; that the sum of the voltages across the entire loop is zero:

$$LQ''(t) + RQ'(t) + \frac{1}{C}Q(t) = 0 \tag{2.4}$$

where here Q is the charge on the capacitor and resultingly, Q' is the current flowing in the circuit and Q'' is the rate of change of that current. It is easy to see that in the absence of the second term, this equation is effectively identical to Eq. 2.1. If we assume a harmonic solution of the form $Q = Q_0 e^{st}$, plug this into Eq. 2.4 and simplify, we find a quadratic equation for the natural frequency s which we can solve for:

$$s = -\alpha \pm \sqrt{\alpha^2 - \omega_0^2} = 0 \tag{2.5}$$

where $\alpha = R/2L$ is the damping factor which will determine how quickly the oscillating currents dissipate and $\omega_0 = \sqrt{\frac{1}{LC}}$ is the resonant frequency. For obvious reasons it is often also called the "LC" frequency, and will be referred to as such throughout this dissertation. Just as $\omega_0 = \sqrt{\frac{k}{m}}$ was the natural oscillating frequency of the mass on a spring, so too is $\omega_0 = \sqrt{\frac{1}{LC}}$ for the RLC circuit.

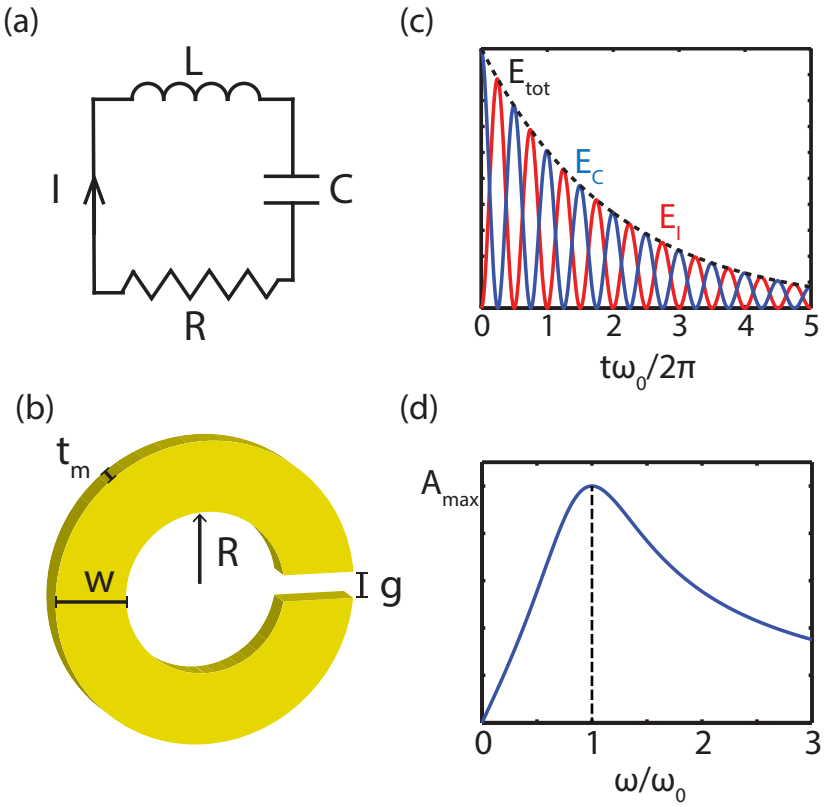

Figure 2.3: (a) A series RLC circuit. (b) The total electromagnetic energy $E_{tot} = E_C + E_L$ the energy stored in the capacitor $E_C = \frac{1}{2}CV^2$, and the energy stored in the inductor $E_L = \frac{1}{2}LI^2$ as a function of time with some damping. (c) A split ring resonator as an RLC circuit. (d) the driving amplitude of an RLC circuit as a function of the driving frequency w.

The phenomenology is the same as well: beginning with some starting charge on the capacitor Q_0 (mass displacement x_0), electrical (spring) potential energy is stored. As currents (the mass) begin to move, the energy accumulates in the magnetic fields of the inductor (the kinetic energy of the mass) until no potential energy is left. At this point the current continues to flow (mass continues to move) under the influence of the magnetic fields (inertia) and the capacitor becomes charged (the mass rises) again. Energy is slowly dissipated from the system by the resistor (friction). When driving this with a harmonic external field $E_0 \cos \omega t$ the amplitude of

the oscillations is given by:

$$A = \frac{\omega E_0}{\sqrt{(L\omega^2 - \frac{1}{C})^2 + R^2\omega^2}} \tag{2.6}$$

Thus the amplitude of the driven currents depends on the driving frequency, with the maximum occurring at ω_0 (see inset Figure 2.4c).

Though not a perfect analogy, the SRR is for our purposes a very small, very simple RLC circuit (See Figure 2.3c). An inductor is generally a coil of wire looped many times such that substantial magnetic fields are generated through the center. The loop of the SRR is just that, albeit with only one winding. A capacitor is two metallic plates held close together such that large electric fields are confined in between when statically charged. The opposite sides of the gap in the SRR fill exactly the same role. A resistor dissipates energy from flowing electrons, and though the conductivity of gold or copper is high, it is not perfect, and thus the entire loop of the SRR acts as a restive element. Of course in this instance there is no active battery or generator which is driving the oscillations of current. Instead, the SRR is driven by the electric and magnetic fields of light. If the electric field goes across the gap for instance, this field will drive charges into the capacitive gap, effectively "charging" it, and allowing the harmonic process to begin. Likewise, if an oscillating magnetic field threads through the loop of the SRR, Faraday's law demands that a current will be driven in the loop in order to produce an opposing magnetic field.

This equivalence allows for the beginnings of a true quantitative look at how the SRRs behavior is determined. The general formula for capacitance is $C = \varepsilon A/d$. Where A is the area of the plates, d is the distance between them, and ε is the permittivity of the material in between them. Examining their analogues in the SRR, we see that:

$$C = \frac{\varepsilon w t_m}{g} \tag{2.7}$$

where w is the width of the metallic loop, t_m is the thickness of the SRR metal, ε is the permittivity of the surrounding region, and g is the size of the capacitive gap region. The self inductance is more complicated to compute rigorously, but for a closed ring, it can be adequately approximated by

$$L \simeq \mu R^2 \tag{2.8}$$

where R is the inner radius of the loop and μ is the permeability of the surrounding material. Together Eq. 2.7 and Eq. 2.8 allow us to approximate the LC frequency of a SRR as:

$$\omega_0 \simeq \frac{1}{Rn}\sqrt{\frac{g}{wt_m}} \tag{2.9}$$

where $n = \sqrt{\varepsilon\mu}$ is the index of refraction of the host material. This approximation along with the $\lambda/10$ size condition for the MM regime provides a useful analytical approximation for the dimensions of an SRR for a given desired resonant frequency. Thus when employing a numerical simulation technique for instance, we can begin with a good expectation of the frequency at which the resonant behavior will occur, as well as its general dependence on the structural parameters of the SRR, greatly accelerating the design and optimization process.

Unfortunately this model is just that, an imperfect approximation. It is possible to improve the predictive power of the RLC model with more careful calculation of the R, L, and C, but difficult to be entirely precise without enlisting the help of a full wave simulation [29]. But perhaps the most fundamental flaw that this method only predicts one mode. This LC mode occurs at the lowest frequency and as a result is the most deeply subwavelength where effective medium approaches are most valid. But SRRs have other normal modes as well.

2.1.2 Resonant Modes of the SRR

As in many other systems in classical and quantum physics, the SRR can be characterized with multiple normal modes. The distributions of surface currents, electric, and magnetic fields are shown for the first three modes of the SRR in Figure 2.4. This can be thought of as a classic boundary condition problem, with the capacitive gap of the SRR providing the first condition; no current flows through it.

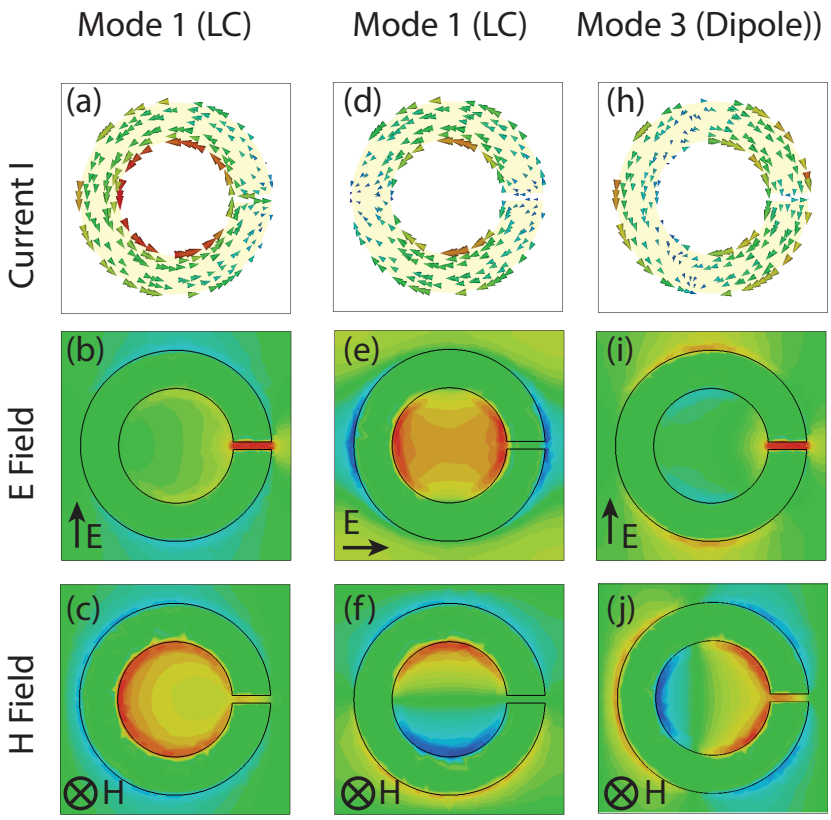

Figure 2.4: The surface current, electric and magnetic fields of resonant modes of the SRR. (a-c) The surface current, electric field, and magnetic field for the lowest energy (LC) mode. (d-f) The surface current, electric field, and magnetic field for the intermediate energy mode. (h-j) The surface current, electric field, and magnetic field for the higher energy (dipole) mode. Note the arrows which indicate the direction of the fields being shown.

As with other types of systems, the lowest energy mode will have the fewest nodes; in this case, there are no other nodes in the current distribution around the ring and the parity of the

mjode is odd. This is the LC resonance, and it's characteristic current distribution electric field, and magnetic field are shown in Figure 2.3 a, b, and c respectively. This large current flowing from one side of the gap, around the SRR to the other produces a large magnetic field into the page when the flow is maximal (Figure 2.3 c). When the current is zero and the charge stored on the capacitive gap of the SRR is maximal, there will be a large electric field across the gap. Just as these electric and magnetic fields can be thought of as being a result of the circulating current, the inverse is also true: this mode can be excited either by an incident electric field polarized across the gap (y-direction) or by a magnetic field perpendicular to the plane of the SRR (z-direction).

The second mode has one node in the current distribution, opposite to the gap (Figure 2.3 d). This mode has the next highest frequency and is a so called even mode, in that it is symmetric about the xz-plane. Among other things, this means that the current around the ring integrates to zero. As a result, this mode will not couple to electric fields along the y-axis nor magnetic fields along the z-axis. In order to excite this mode, an electric field polarized parallel to the x-axis is necessary.

The third mode is another odd mode; note that there are now 3 current nodes (one at the gap and two more on the SRR). This mode couples to magnetic and electric fields in the same way that the LC mode does, but occurs at higher frequencies. In general, it is characterized by currents on both the left and right side of the SRR traveling up and down in phase with each other. This is the dipole mode of the SRR, and will be important for future discussion.

2.1.3 Field Enhancement and Local Fields

As we saw previously, the ways in which the electromagnetic fields are distributed in an SRR play an important role in the ways in which the SRR can be excited and thus interact with incident electromagnetic wave. In this section we will extend this discussion, as well as the previously introduced concepts of resonance to show that together, these characteristics are crucially responsible for the unique properties of the SRR on both a microscopic and macroscopic

scale.

As we saw previously in section 2.1.1, the amplitude of oscillation in any driven simple oscillator depends on the frequency at which it is driven and is maximal at the natural or resonant frequency ω_0 (See Figure 2.3 d). The driving field in the case of the SRR is an incident electromagnetic field. If that field is tuned close to a resonance of the SRR with a polarization which can couple to the resonance, the surface currents will be driven maximally.

Specifically, let us consider an SRR similar to the one presented in the previous sections, and excited by an electromagnetic wave incident into the plane of the SRR with the electric field polarized across the gap (See Figure 2.3). At the LC resonant frequency, the currents shown previously in Figure 2.4a will be strongly driven, resulting in large accumulations of opposite charge on the sides of the capacitive gap. This will result in a strong electric field in that small region pointing in the opposite direction to the incident electric field, but far larger in magnitude. So large in fact that upon averaging over the entire unit cell, the fields in the gap region dominate the overall response.

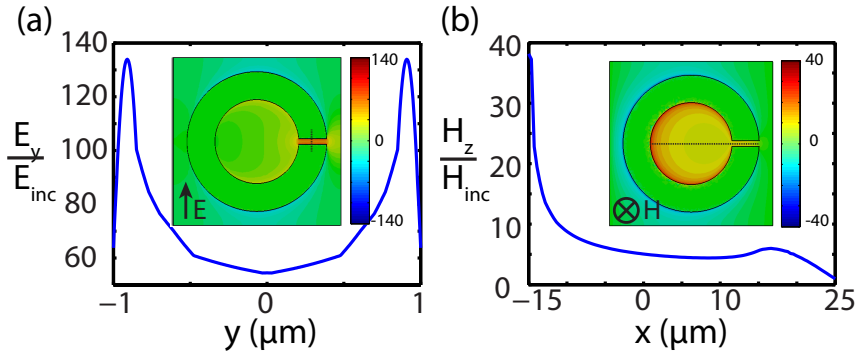

Figure 2.5: (a) the electric field enhancement across the gap of the SRR. (inset) the electric field enhancment distribution across the entire unit cell. The cross section is marked with a dashed line. (b) The out-of-plane magnetic field enhancement relative to the incident magnetic field. (inset) the magnetic field enhancement distribution. The cross section shown is indicated with a dotted line. Note that the displayed magnetic fields are orthogonal to that of the incident wave.

The first consequence of this phenomena is the ability to perform massive electric field enhancement EFE on an an ultra-subwavelength scale. Figure 2.8 a and b show the EFE over the

entire unit cell, and along a cross section through the gap as for several choices of gap size. Near the edges of the gap, and for small gap sizes, the EFE=$\frac{E_y}{|E_{incident}|}$) reaches values as high as 133. For a typical high field THz source with field strengths of 300kV/cm this EFE will result in local fields on the order of 10MV/cm. The magnitudes and distribution of this EFE can be controlled easily by judicious choices of SRR gap width and other geometric parameters. With these massive electric fields, the SRR can be utilized to generate nonlinear responses in underlying condensed matter systems or in the SRR it's self, though special care must be taken. Even at THz frequencies these field amplitudes are sufficiently high to cause irreparable damage to the metamaterial and other materials alike [30]. This effect can even be utilized to create what amounts to a microscopic particle accelerator: large fields can rip electrons off of the SRR, accelerate them through free space and collide them into the other side of the gap with sufficient energy to produce potentially harmful UV-radiation and even x-rays [31].

The second consequence is the influence is that of the effective homogeneous response of the SRR metamaterial. Due to the dominance of the localized field in the average polarization of the metamaterial unit cell, it plays an important role in the determination of the effective homogeneous electric permittivity ε_r of the metamaterial as a whole. This will be discussed in more depth later.

The resonant excitation of this SRR also results in an enhancement of the magnetic fields. Figure 2.4c shows the magnetic field enhancement MFE=$\frac{H_z}{|H_{incident}|}$ across the SRR while the MFE along the dotted cross section is shown in Figure 2.4d. Note that the MFE is highest along the left inner edge of the SRR. As with the electric fields, the strength and distribution of the MFE can be tuned by changing various geometric parameters. Note that crucially, and unlike the EFE, the magnetic field in this case is primarily perpendicular to the plane of the SRR, and thus perpendicular to the magnetic field of the incident EM wave. As in the case of the EFE, the MFE can be utilized both to drive large nonlinear magnetic effects on a deeply subwavelength scale, as well as to influence the effective homogeneous parameters (in this case the magnetic

permeability μ_r of the metamaterial. In this particular case, the orthogonality of the MFE and the incident magnetic field result in a bianisotropic response; one where the electric and magnetic polarization of a material are not necessarily along the same axis as the incident fields [32]. These enhancements of the incident electric and magnetic field and the ability to tune their strength, distribution, and direction, are a crucial part of the utility of metamaterials, both in their local and macroscopic responses to electromagnetic waves. They provide a mechanism to deliver ultrafast, ultra strong, transients magnetic and electric fields to a sample in order to explore nonlinear field driven effects.

2.1.4 Far Field Response

The local or "near field" response of the SRR discussed previously is vital to understanding its utility, it is very difficult to measure these quantities in an experimental setting. Instead, most studies of metamaterials are conducted in the "far field", that is, measurements of electromagnetic waves far away from the metamaterial. Thus it is useful to connect the observations about the characteristics of the SRR that we have made so far to the hallmarks of these properties that we can more readily observe in a laboratory setting.

The simplest type of experiment that we often perform in order to characterize a metamaterial is spectroscopy. In the most general sense spectroscopy consists of illuminating a sample with a light source that emits a broad distribution of different frequencies, and then observing how much light passes through or is reflected back towards the light source. Ordinarily when light is shone on an inhomogeneous surface (like, say a rough ocean) we expect light to be scattered off in all directions as it strikes different regions of the object which are oriented in different directions and comprised of different materials. This diffuse reflection and transmission is a result of the incident wavelength being considerably smaller than the length scale of the inhomogenaities of the material. Consider then such an experiment where the sample is a metamaterial comprised of many SRRs (Figure 2.6a). Though the metamaterial is also inhomogeneous, the length scale

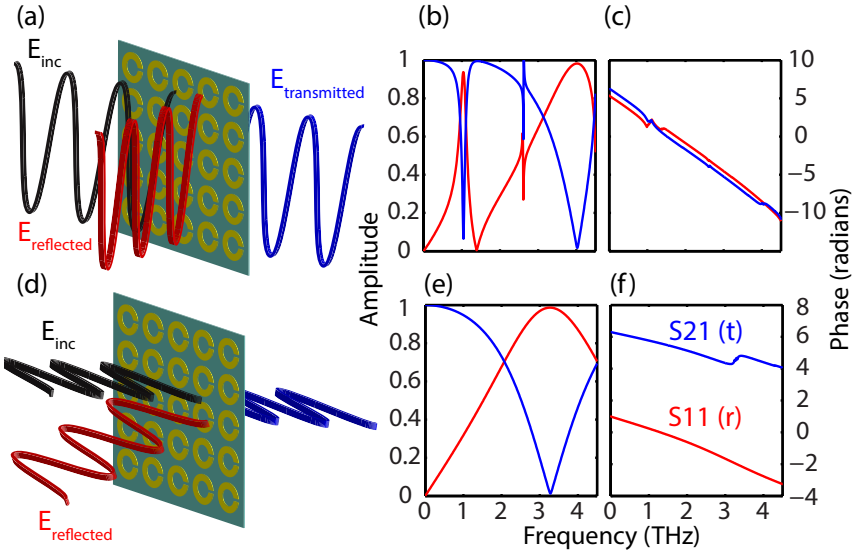

Figure 2.6: Reflection and transmission in the far field of a SRR metamaterial. (a) The experimental schematic showing a vertical electric field polarization. (b) the magnitude, and (c) the phase of the transmitted (blue) and reflected (red) light. (d) The same experiment but with the electric field of the light polarized horizontally. (e) The magnitude, and (f) phase of the reflected and transmitted light for the horizontal polarization.

of that inhomogenaity is far smaller than the wavelength ($\frac{\lambda}{10}$, and thus light is reflected and transmitted specularly (like glassy flat water). In a spectroscopy experiment, we measure this transmitted and reflected light as a function of its frequency to find the reflection and transmission coefficients (often represented instead as scattering parameters S11 and S21 respectively). The transmission and reflection is in general complex, having both a magnitude and phase, and is plotted for this metamaterial in Figure 2.6 b. Generally, a minimum in the transmitted light and/or a maximum in the reflected light indicates that the sample is interacting strongly with the incident light at that frequency. In figure 2.6b, we can see that there are two such frequencies. The first at 1 THz is the LC resonance of the SRR (see Figure 2.4abc). The second at 3THz is the dipole resonance of the SRR (see Figure 2.4hij).

Crucially, the result of a spectroscopy experiment will depend on the polariztaion of the incident light: that is, in what direction the electric and magnetic fields of the light are oriented relative to the sample. The schematic in Figure 2.6c shows the same experiment but with the

electric field of the incident light rotated 90 degrees. In the reflection and transmission, the LC resonance is notably absent, but a mode does appear at 2THz. This is the mode shown in Figure 2.4def, and is distinct from both the LC and dipole mode. It can only be excited when the E field is at least partially polarized in this direction. Conversely, this polarization is incapable of exciting the LC and dipole modes.

These complex reflection and transmission coefficients serve as an effective means of identifying resonance frequencies in a metamaterial sample and in materials in general, but this same information can be taken much further to determine the effective medium properties of a metamaterial as well.

2.2 Effective Medium Theory

One of the key utilities of metamaterials is their ability to act as a an effectively homogeneous medium who's properties are not that of its constituent materials, and indeed in many cases not that of any known homogeneous matter. While the local properties that we have looked at so far give some clues as to how the electrodynamics of the SRR on a small scale contribute to these macroscopic properties, it is not yet clear how they can be rigorously determined. In order to illustrate this process we will once again use the SRR discussed in the previous section. We will consider the situation in which incident light is polarized across the capacitive gap, exciting the LC and dipole resonance modes (Figure 2.6abc).

The first approach comes from realizing that the response of a SRR is similar to that of a generic Lorentzian or plasmnoic oscillator in other condensed matter physics systems (i.e. a Drude metal or a phonon). Like an ordinary Lorentzian oscillator, the resonant excitation of the SRR will result in a large polarization response with a Lorentzian frequency dependency. As a result, the permittivity can be expressed in much the same way, though the exact format of the

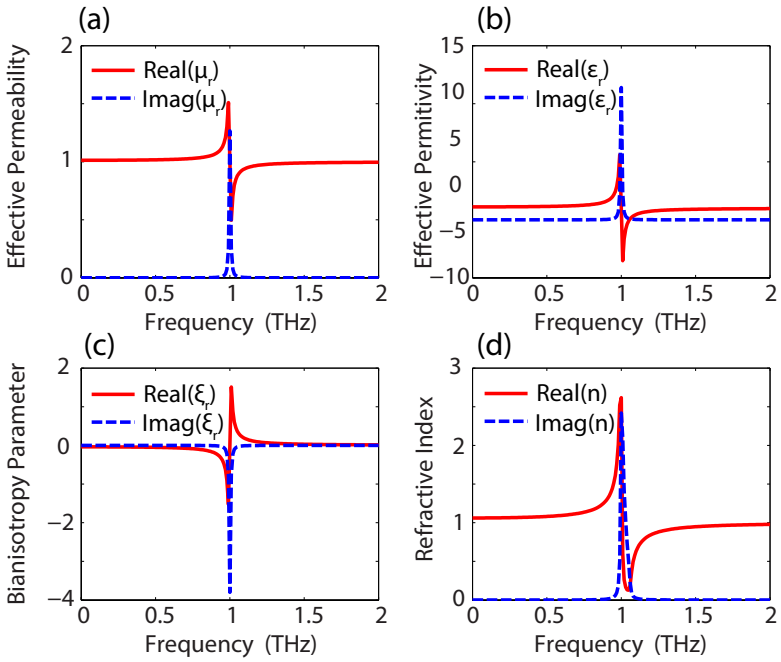

Figure 2.7: The effective medium parameters of a SRR from drude theory. The real (Red) and imaginary (blue) parts of (a) the relative permeability μ, (b) the relative permittivity ε, (c) the bianisotropy parameter ξ, and the (d) the refractive index n.

equation often depends on the source [32]:

$$\varepsilon(\omega) = 1 + \left(\frac{gc_0}{R_o^2}\right)^2 \frac{F}{\omega_{LC}^2 - \omega^2 - i\gamma\omega} \tag{2.10}$$

where g is the SRR gap width, R_o is the SRR outer radius, $F = \frac{R_o^2}{p^2}$ is an area filling fraction, ω_{LC} is the LC resonance frequency, c_0 is the speed of light in vaccuum, and γ is the damping frequency. Below the resonant frequency, the permittivity is positive, and rapidly approaches infiniti as the frequency nears ω_{LC}. Above ω_{LC} the permittivity is large and negative, before rising and eventually going positive again. This expression for the permittivity is mathematically identical to that of a Drude oscillator a simple substitution for the plasma frequency $\omega_p^2 = F\frac{gc_0}{R_o^2}^2$.

The magnetic permiability has a very similar form:

$$\mu(\omega) = 1 + \frac{F}{\omega_{LC}^2 - \omega^2 - i\gamma\omega} \tag{2.11}$$

As this expression is nearly identical to that of ε, it is unsurprising that it has the same qualitative behavior. As has been noted before, in a simple SRR, strong circulating currents will result in a magnetic field perpendicular to the plane of the SRR. Depending on the polarization of the excitation beam this can mean substantial magnetic field is generated perpendicular to that of the incident electromagnetic wave. This gives rise to a bianisotorpy parameter parameter ξ which is given by:

$$\xi(\omega) = -\frac{gc_0}{R_o^2}\frac{F}{\omega_{LC}^2 - \omega^2 - i\gamma\omega} \tag{2.12}$$

This expression, unlike the others gives a value of ξ which approachces zero at low and high frequencies. It is singular at ω_{LC} but the relative sign is opposite. Putting these together in matrix form, we can express the electromagnetic response of the metamaterial parallel to the incident elecric and magnetic fields using the following matrix notation and accounting for the bianisotropy of the material:

$$\begin{bmatrix} \vec{D} \\ \vec{B} \end{bmatrix} = \begin{bmatrix} \bar{\varepsilon} & -i\bar{\bar{\xi}} \\ i\bar{\bar{\xi}} & \bar{\bar{\mu}} \end{bmatrix} \begin{bmatrix} \vec{E} \\ \vec{H} \end{bmatrix} \tag{2.13}$$

We can see from this expression that the electric displacement $\vec{D}$ will have contributions from both the electric field (via ε) but also from the magnetic field (via the bianisotropy parameter μ). A similar phenomenon occurs with the magnetic field $\vec{B}$. This cross coupling term can be significant, as is the case with the LC resonance of a basic SRR in particular, and if it is ignored can generate significant errors in predicting the response of the metamaterial. Given the above

equations, the effective index of refraction can be expressed as:

$$n^2 = \varepsilon\mu - \xi^2 \tag{2.14}$$

and the impedance can be expressed as:

$$Z_{\pm} = \mu(\pm n - i\xi)^{-1} \tag{2.15}$$

In addition to significantly complicating the mathematics of the effective medium theory, bianisotropic effects in MM designs can be both an interesting topic and a headache for metamaterial designers. Among other things, neglecting to account for bianisotropic effects has caused a number of erroneous claims of negative index. Generally this bianisotropy arises from a broken symmetry in the metamateiral unit cell design. Thus by increasing the symmetry, bianisotropic effects can be suppressed. When we explore other types of SRRs and metamaterial resonators later, we will see how these complications can be avoided with clever design.

This formulation of a SRR metamaterial as a Lorentzian oscillator is useful not only due to the simplicity of the model, but also its familiarity; in principle, the myriad of analytical and phenomenological work in condensed matter which characterizes various physical processes in materials with these oscillators can, in principle, be applied to the analysis of metamaterial systems, as the mathematics are effectively identical. But the above analysis is limited. It is only valid for SRR geometries similar to the one presented, it is only an approximation and some numbers will likely need to be fudged to replicate real world data, and most importantly, it only accounts for a single (LC) resonance. Though this analysis can be adapted to other scenarios by adding additional parameters, oscillators, and other tweaks, it is necessary to have a more rigorous and general way to extract effective medium parameters.

2.2.1 Effective Medium Parameter Extraction

In many instances in physics, it is conceptually convenient to average over the local electromagnetic fields and current distributions of an inhomogeneous medium. In an ideal situation, the observed far field interactions of this effective medium would be no different from that of the inhomogeneous medium which it replaces. But as has been mentioned previously, the retrieval of the exact distribution of currents and fields is not easy, particularly in an experimental environment, and so it is more useful to have a technique to be able to retrieve this information from far field data, which is typically more readily available. Fortunately such a method has been by Smith et. al. inspired in large part by the desire to utilize this method for characterizing metamaterials [33]. While the process is too lengthy and complex for a full review here, it is useful to introduce some of its major points.

This method seeks to tie the electric and magnetic fields on either side of a homogeneous slab to its index of refraction and the impedance:

$$\begin{bmatrix} E' \\ i\omega H' \end{bmatrix} = \begin{bmatrix} \cos nkd & -\frac{z}{k}\sin nkd \\ \frac{k}{z}\sin nkd & \cos nkd \end{bmatrix} \begin{bmatrix} E \\ i\omega \end{bmatrix} = T \begin{bmatrix} E \\ i\omega H \end{bmatrix} \tag{2.16}$$

Where $n = \sqrt{\varepsilon\mu}$, $z = \sqrt{\frac{\mu}{\varepsilon}}$, $k = \frac{\omega n}{c}$, and d is the effective thickness of the slab. Here the primed fields indicate the fields on the far side of the slab (i.e. after passing through it), and T denotes the transfer matrix. While these represent the field amplitudes near the slab, they can be directly related to the scattering parameters (reflection and transmission) with the following relations:

$$S_{21} = \frac{2}{T_{11} + T_{22} + (ikT_{12} + \frac{T_{21}}{ik})} \tag{2.17}$$

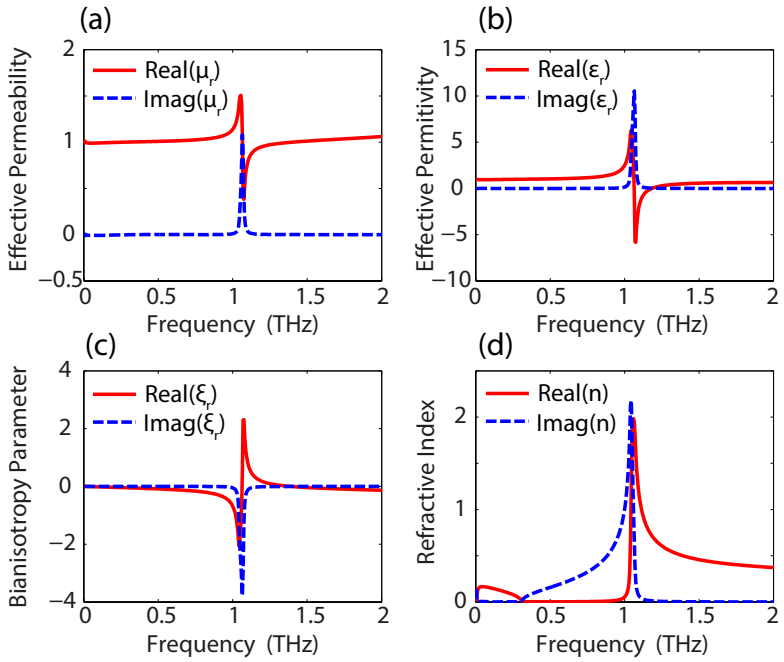

Figure 2.8: The effective medium parameters of a SRR from effective parameter retrieval. The real (Red) and imaginary (blue) parts of (a) the relative permeability μ, (b) the relative permittivity ε, (c) the bianisotropy parameter ξ, and the (d) the refractive index n.

$$S_{11} = \frac{T_{11} - T_{22} + (ikT_{12} - \frac{T_{21}}{ik})}{T_{11} + T_{22} + (ikT_{12} + \frac{T_{21}}{ik})} \tag{2.18}$$

$$S_{22} = \frac{T_{22} - T_{11} + (ikT_{12} - \frac{T_{21}}{ik})}{T_{11} + T_{22} + (ikT_{12} + \frac{T_{21}}{ik})} \tag{2.19}$$

$$S_{11} = \frac{2det(T)}{T_{11} + T_{22} + (ikT_{12} + \frac{T_{21}}{ik})} \tag{2.20}$$

It is notable that for a single slab of a truly homogeneous material, $S_{11} = S_{22}$ and $S_{21} = S_{12}$;

That is, the it does not matter in which direction the beam passes through the slab. In fact, the second condition is true in all circumstances in which the material is not non-reciprocal [34]. Under these conditions, the expressions simplify considerably. At this point the values from equation 2.16 can be plugged in and the expressions can be inverted to yield expressions for the index of refraction and impedance:

$$n = \frac{1}{kd} \arccos \frac{1}{2S_{21}} (1 - S_{11}^2 + S_{21}^2), \tag{2.21}$$

$$z = \sqrt{\frac{(1+S_{11})^2 - S_{21}^2}{(1-S_{11})^2 - S_{21}^2}} \tag{2.22}$$

This provides a complete description for a single slab comprised of a homogeneous material. Unfortunately, the application of these expressions is not always straightforward. In particular the *arccos* function has multiple branches which make unambiguous determination of the index difficult, especially near the resonant frequency. Furthermore, special care must be taken in choosing an appropriate value of d. While the thickness of a metalic split ring for instance may be only a few hundred nanometers, use of this as the effective path length kd will often lead to erroneous results.

In Figure 2.22 an example of this transformation on the scattering parameters shown previously for the simple SRR is shown. Using the scattering parameters shown in Figure 2.6bc, the permittivity ε the permeability μ, the index of refraction n and the impedance z are shown in Figure 2.22 a, b, c, and d respectively. At the LC resonance, the circulating currents in the SRR are driven maximally, as are the resulting electric and magnetic field enhancements. This is evident in the characteristic Lorentzian oscillator response in the permeability, permittivity, and bianisotropy at 1 THz (Figure 2.22abc). This is a common frequency dependent response for oscillators in many fields of physics, from masses on springs and other mechanical oscillators

to the RLC circuit as we have already seen as well as many types of excitations appearing in condensed matter physics.

This concludes this extended introduction into the rich and varied physics of the basic SRR. Though we have stuck with a single example structure for this entire section, many of the general concepts and phenomena extend across a great variety of other metamaterials and systems. In the next section, we will take a look at some of the many different types of metamaterials. We will begin with variations of the classic SRR and then move on to other metamaterials that operate in entirely different ways.

2.3 Other Types of Metamaterial Resonators

Though deeply subwavelength size and regular periodic structure are features common to all metamaterials, the types of metamaterials and the resonators they are based on vary drastically. With more or less arbitrary control over the constituent materials and the geometric characteristics of a metamtaerial unit cell, the accessible parameter space is vast and it can be a challenging to zero in on what general type of metamaterial design is most suitable for a given application, frequency range, etc. In the following I review some of the general categories of metamaterial resonators and their uses, with a special focus THz metamateirals and metamateiral absorbers, both of which are of particular relevance to this dissertation.

Though the SRR we have investigated so far as an introduction to metamaterials maybe the simplest geometrically, it is far from the only type of SRR, and in fact its strong bianisotropy makes it far from the simplest to understand. In the early days of metamaterials, one of the key design considerations was aimed at creating a metamaterial which did not have a strong magnetic response and thus avoided the issues of bianisotropy. The first experimental verification of negative refractive index utilized a metamaterial which incorporated broadside coupled SRRs (BC-SRR) [23]. In this case, the BC-SRR consists of two concentric ordinary SRRs arranged such

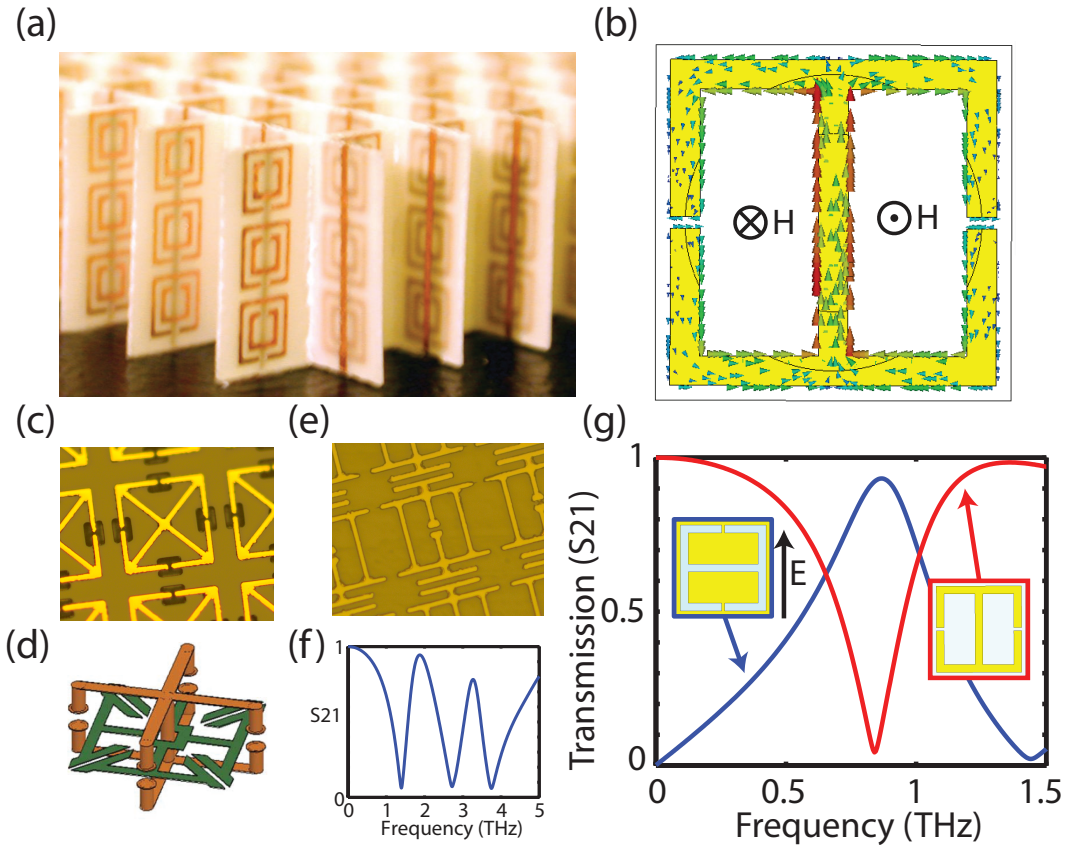

Figure 2.9: Other types of split ring resonators. (a) the metamaterial used in the first observation of negative (from index[23]). The anti-parallel concentric SRRs are used to minimize bianisotropic effects. b) the ELC SRR is two mirrored SRRs put together. Currents generate magnetic fields in opposite directions, minimizing magnetic effects. c) a 2D polarization independent version of the ELC SRR. d) a 3D polarization independent ELC SRR (from [35]). e-f) a 3 band SRR design as well as its transmission (S21) spectra showing 3 distinct resonance bands. g) The transmission (S21) of a ELC SRR and a complimentalry-SRR version of it. The transmission of the two is reversed via Babinet's principle.

that the inner SRR is rotated 180 degrees relative to the outer one such that the capacitive gaps are on opposite sides (Figure 2.9a). When an incident electric field polarizes the capacitive gaps in the same direction, the current which is driven in the two SRRs flows in opposite directions (i.e. opposite handedness) and thus the magnetic field in the center of the SRRs mostly cancels. This in turn minimizes bianisotropic effects and prevents the magnetic field of the SRR from strongly coupling to farfield waves. A similar effect can be accomplished by placing the two SRRs not concentrically but stacked on top of each other with some spacer material in between [36]. This

can also be accomplished with the so called electric LC (ELC) resonator (2.9b). This design is essentially two mirrored SRRs placed edge to edge (gap to gap versions work as well). In a similar fashion, when an incident electric field charges the capacitive gaps, circulating current flows on each side of the ELC-SRR, but with an opposite chirality. This results in magnetic fields threading through each side of the SRR which are equal and opposite, resulting in zero total magnetization.

Another important design consideration is robustness to the angle of incidence and/or polarization of the incident light. An ordinary SRR works well so long as the incident electric field is polarized across the capacitive gap (transverse electric polarization (TE)). If the electric field of the incident is only partially aligned to the gap, performance will suffer, and if it is orthogonal, the LC resonance will not be excited at all (for certain geometries the magnetic field can excite the LC resonance, but we will focus on electric excitation for now). By increasing the symmetry of the unit cell, this limitation can be overcome. Figure 2.9c shows a variation of the ELC-SRR which is 4 fold rotationally symmetric. As a result, its response is completely azimuthally independent, and it can be excited with electric fields polarized along either of its sets of capacitive gaps. Though this azimuthal polarization independence is good enough for many applications and experimental environments, in others it may be beneficial to take this concept even further. Figure 2.9d is a 3D metamaterial unit cell which is designed to have a response which is completely independent of both incidence and polarization angle. It consists of a planar polarization independent ELC-SRR similar to the one that was just discussed, nested inside of two perpendicular stand-up SRRs. Though the SRRs can be thought of as independent, they are each tuned to have a nearly identical response, thus any incident wave is sure to excite at least one of the SRRs in order to create the desired effect.

It may also be desirable to have a metamateiral which operates over a broad frequency range, or at several distinct frequencies. One simple conceptually straightforward approach is to simply combine two or more SRRs into a single metamaterial, either taking a multi-layered

approach, or by creating a superlattice of different metamaterial sublattices. The former often introduces undesirable losses, whereas the latter reduces the effective density of each SRR sublattice, thereby reducing the effective oscillator strength of the SRRs. Never the less, both approaches have been applied effectively for various applications[37][38][39]. Another approach for multi-band functionality is to introduce additional geometric features to an SRR in order to imbue it with additional resonant modes of operation. Figure 2.9e is a microscope image of such a SRR design. Its complex geometry results in three distinct resonant bands over a relatively small frequency window (Figure 2.9f). While ordinary split rings have multiple resonances (as seen in section 2.1.2), making alterations to the SRR geometry in order to change one mode will in general strongly influence others as well. With judicious design, this can be avoided, and the resonant frequencies can be tuned and adjusted independently, as is the case in this example.

Another interesting variation on the split ring resonator that will be of relevance later in this dissertation is the complimentary split ring resonator (C-SRR). The C-SRR is an interesting application of Babinet's principle, which states that the diffraction from an opaque scatterer is identical to that of a hole of the same dimensions. This can be intuitively motivated by the fact that the superposition of scattered light from both an object and its compliment put together must be that of an unobstructed beam. Thus, the C-SRR is the dual of the SRR, and thus its response (i.e. transmission and reflection), is likewise the dual of that of the SRR. The structure of the C-SRR is the inverse of an SRR; where there would ordinarily be exposed substrate there is metal, and vice versa (see insets Figure 2.9g). Similarly, the reflection and transmission spectra are reversed: the transmission of a C-SRR is identical to the reflection of a SRR (Figure 2.9g), and reflection is identical to the transmission of an SRR (though this is only strictly true in the ideal case of zero losses[40]). Fundamentally, thet SRR can be considered to be a resonant magnetic dipole (due to the axial dipole moment), whereas the CSRR behaves an an electric dipole that can be excited by an axial electric field. Thus the regions of the unit cell which would ordinarily host large current densities in an SRR are replaced by areas of large electric field in the C-SRR and vice versa. It is

important to note that while the consideration of out-of-plane magnetic and electric excitations are useful for understanding this phenomenon conceptually, more ordinarily, metamterials are excited with a TEM wave (i.e. an electric field polarized across the SRR capacitive gap). In this more ordinary excitation geometry, the polarization of the incident light must be rotated 90 degrees in order to successfully excite the C-SRR; the magnetic and electric field vectors must be switched. As a practical result, the C-SRR is a convenient way to change the observable features associated with a resonance of the metamaterial from a transmission minimum to a transmission maximum. While this has obvious utility in band pass filters and the like [41], we will see later that this can also be a useful trick for enhancing coupling behavior, or for avoiding complications which arise with various fabrication techniques.

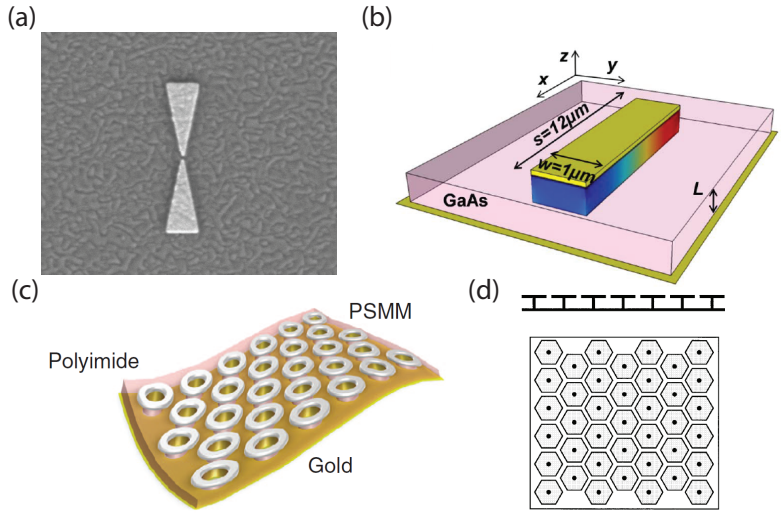

Figure 2.10: Other types of plasmonic metamaterials. a) A $\frac{\lambda}{2}$ split gap dipole with a bowtie shape. The small gap produces massive electric field enhancement. b) a nano-patch/antenna metamaterial designed to produce large out of plane field enhancements via TM10 waveguide modes (From [42]. c) A plasmonic disk resonator metamaterial produces a plasmonic resonance similar to that of dipoles, with the added advantage of azimuthally polarization independent response (From [43]). d) A "Seivenpiper mushroom" metamaterial structure consisting of metallic patches suspended over a ground plane and connected with a small via (From [44])

Though SRRs are popular, compact, and come in many variations, they are far from the only metallic type of metamaterial unit cell. A simple half wavelength dipole ($L \simeq \frac{\lambda}{2}$) is not

nearly as deeply subwavelength as a SRR, but when placed in a periodic lattice can serve as the basis of a metamaterial as well with similarly rich physics. If large in plane field enhancement is desirable, small gaps can be left between dipoles in adjascent unit cells, or a gap can be formed in the middle of the dipole [31]. Figure 2.10a is an infrared wavelength bowtie antenna fabricaated by electron-beam lithography. Due to the tiny size of the central gap, it is capable of producing massive EFE in an extremely small area. Alternatively, the introduction of a ground plane underneath a dipole or patch type antenna structure and seperated by a dielectric spacer layer creates large out-of-plane EFE. Figure 2.10b shows such a design optimized for large oscillator strength; this structure produces a high quality factor resonance in which the energy density of the incident wave is enhanced by 1e4 [42]. As with split ring resonators, robustness to polarization is often desirable as well. By simply creating a cross shaped structure, a dipole metamaterial can be made to operate independently of polarization. More generally, plasmonic structures with high planar symmetry will display polarization insensitivity, as with the plasmonic disks in figure 2.10c. Figure 2.10 is a structure known as the ”Seivenpiper Mushroom”. It consists of patch antennas over a conducting ground plane, but also introduces condingg vias which electrically connect the ground plane to the patches [44]. This introduction reduces the propagation of waves through to the ground plane, and results in an extremely high impedance surface.

Metallic metamaterial devices encompasses a huge swath of designs and applications, but share common features: they rely on resonantly driven currents in order to produce a response. While this in general produces a strong and narrow band response, there are severe limitations. First, due to the strong resonant nature of these designs, the desired properties will in general only exist over a very narrow frequency band. Second, metallic metamaterials are inherently lossy due in large part to the ohmic loss in the metals. These two problems are actually related, and while metallic metamaterials can be made to operate over a broader bandwidth, it is always accompanied by additional loss. Furthermore, the latter issue is crucially frequency dependent. While metals like copper and gold are nearly lossless for practical consideration at microwave

frequencies, this is not so at for higher frequencies. When the incident electromagnetic fields oscillation frequency reaches the plasma frequency (ω_p), electrons in the metal can no longer respond rapidly enough to screen the incident wave (as in an metal). Above this frequency, incident waves will be only partially screened and the material will display dielectric properties. For most metals, the plasma frequency falls into the visible spectrum, and thus for high frequency metamaterial applications, metallic resonators are far less suitable.

Metamaterials with all dielectric components avoid some of these limitations by relying not on coupling to plasmonic or phonoic degrees of freedom, but instead through contrast in refractive index. Dielectric metamaterials in general consist of high index sub-wavelength inclusions which rely on an entirely different phenomenology from the metamaterials discussed so far. Nevertheless, many of the phenomena demonstrated in plasmonic metamaterials have already been reproduced using the dielectric approach including negative refractive index[45], hyperbolicity[46], and optical chirality[47] among others. This approach avoids the issue of losses through Ohmic heat and allows for further miniaturization of metamaterials well into the visible optical regime. It is necessary however to distinguish between photonic crystals and dielectric metamaterials; whereas the former uses wavelength-scale periodicity to create artificial bandgap effects to manipulate light, dielectric materials rely on near field coupling between constituent elements.

Many dielectric metamaterials rely on small high-index inclusions which support highly confined resonant modes. When light interacts with a small dielectric particle of high symmetry, a magnetic dipole (first Mie resonance) and an electric dipole (second Mie resonance) are excited (Figure 2.11a). The magnetic Mie resonance results in a circulating diplacement current, much like the free current in a SRR produces a magnetic dipole [48]. But the displacement current is lossless and not limited by metallic plasma frequencies, though band gap energies of the dielectric material do place an upper limit on the viable frequency range. By introducing an ensemble of these dielectric particle as a metamaterial unit cell, a large degree of freedom over the effective

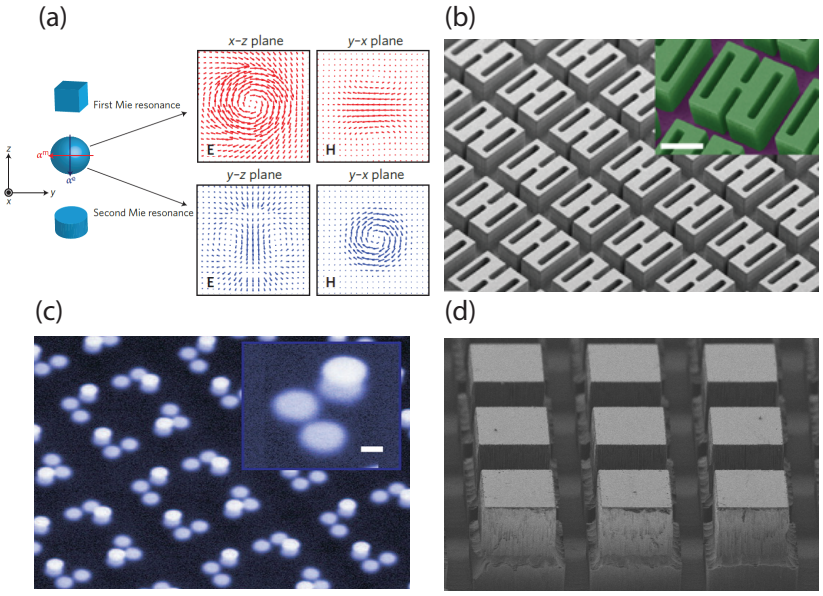

Figure 2.11: Examples of dielectric metamaterials. a) electric and magnetic dipole (Mie) resonances are supported by high-symmetry high-index meta-atoms. The electric and magnetic field distributions of the first adn second Mire resonance are shown (From [48]). b) A chiral dielectric metamaterial for optical frequencies consists of sets of high-index particles in chiral arrangements inspired by chiral organic molecules (from [47]). c) A broadband metamaterial anti-reflection surface composed entirely of high resistivity silicon. d) a broadband dielectric metamaterial absorber formed from deep etching of doped silicon.

medium properties of the metamaterial can be achieved. Figure 2.11b shows an optical frequency metamaterial who's unit cell consists of a set of high index particles in a chiral arrangement; the result being a material which transmits circularly polarized light of only one chirality. Similarly, Figure 2.11c is a broadband metasurface which acts as an anti-reflection surface. Surfaces with high refractive index are poorly impedance matched to free space and create significant surface reflections. But by structuring this all-silicon wafer into a two tiered box pattern, the effective medium impedance of the surface is matchced to free space, and reflections are minimized. Figure 2.11d is a similar design, but by introducing doping to the silicon structures, the loss of the material can also be engineered to create a broadband perfect absorber. This all-dielectric approach to metamaterials offers significant advantages in some many, particularly when loss is undesirable, or when the desired frequency range is too high for the use of metallic inclusions (i.e.

at visible frequencies).

2.3.1 Terahertz Metamaterials

Terahertz waves lie in between the microwave and infrared regions of the electromagnetic spectrum. 1 THz corresponds to 10^{12} oscillations per second or alternatively a wavelength of 0.3mm. Though few outside of specialized scientific fields have even heard of them they are of great interest both for applications in science as well as commercial and military technology. In condensed matter systems, 2D electron gas plasmons, some low frequency phonons, surface plasmons, as well as various gap, spin, and free carrier degrees of freedom can be observed at THz frequencies (Figure 2.12). In biology, soft condensed matter, and chemistry, various physical processes occur at THz energy scales and thus can be probed with THz techniques [49][50]. In astronomy, black body THz is emitted by low temperature interstellar dust and other objects can be used to characterize everything from planetary atmospheres to the astrochemistry of star formation [51]. In both medical and security applications, THz waves can be used to penetrate and probe tissue, clothing, and other materials while avoiding the harmful effects of ionizing radiation like X-rays used for the same purpose[52][14]. Similarly, THz can be used in manufacturing processes to aid in quality control and process monitoring by non-destructivley probing devices and in high speed communication [53][13]. Thus any technologies which generate, manipulate, or detect light at THz frequencies are of great utility for scientific and practical endeavors. The entirety of the work on metamaterials in this dissertation occurs at THz frequencies and thus the motivations and challenges specific to THz materials are worth discussing.

Historically there has been a dearth of technologies operating in this band of the electromagnetic spectrum leading it to be called the ”THz Gap”. Fundamentally this difficulty originates from the fact that the methods employed to produce and detect light at other frequencies are poorly suited to THz waves. At lower frequencies in the radio and microwave bands, light is generally produced by applying an alternating voltage bias to a metallic resonator like an antenna,

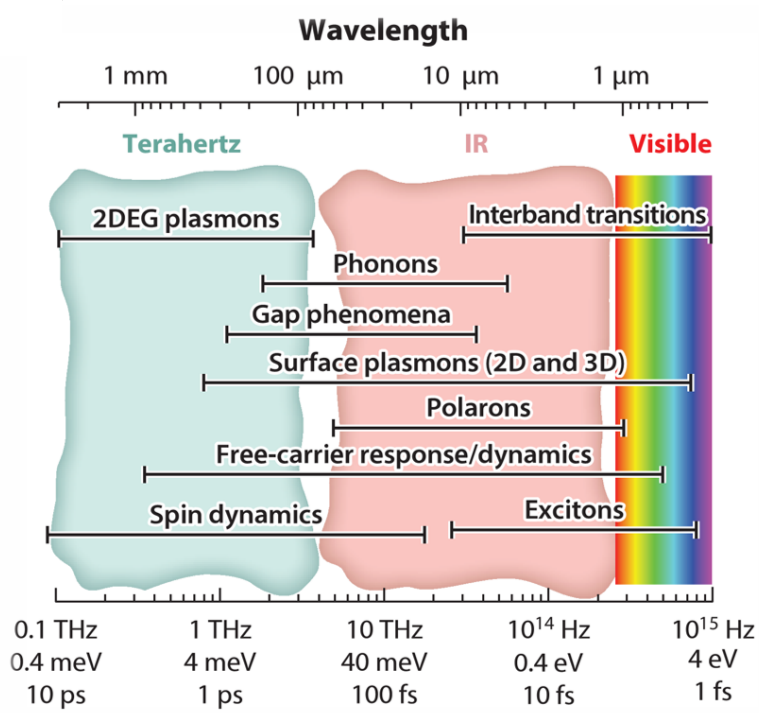

Figure 2.12: The THz spectrum and the approximate ranges over which various physical phenomena in condensed matter systems occur.

thereby creating freespace radiation. But electronics cannot be driven easily above 100GHz and most metals cease to conduct electricity as efficiently. On the other side, infrared and visible and ultraviolet photons have energies around which many atomic, molecular, and solid state electronic transitions occur. Thus semiconductor devices and diffuse gasses provide a convenient means to turn electrical potential into light and vise versa. But the energy associated with THz waves is far smaller than most natural electronic transitions, so these methods are unsuitable as well. Only with the recent advent of practical femptosecond laser sources has the proliferation of THz science and technology become possible. Producing and detecting THz light has not been the only technological hurdle. The absence of practical optical elements such as polarizers, lenses, and gratings that could operate at THz frequencies has also been a challenge

Unsurprisingly metamaterials have played a significant role in filling this gap. The

development of THz metamaterials has borrowed both from the early metamaterial work at radio frequencies, and from concepts more typically applied to optical frequencies. This confluence of technology and ideas has allowed for the rapid development of THz metamterialas for waveplates [54], detectors [55], artificial magnetism [56], phase modulators [57], and near field devices just to name a few. In combination with parallel development of thz sources in particular, metamaterials have contributed significantly to the growth of THz as a field, inspiring new technologies and demand alike.

The free space wavelength of light at 1THz is $300\mu m$. To meet the general guideline for metamaterial resonator size of $\frac{\lambda}{10}$, THz metamaterials typically have unit cells approximately $30\mu m$ in size. This length scale is well suited to many of the microfabrication techniques commonly found in integrated circuit and and semiconductor manufacturing. For instance, a simple single layer metamaterial design such as a metallic split ring on a dielectric substrate can be easily fabricated by photolithography where feature sizes can be on the order of a few microns. More complicated structures can integrate additional layers, various materials, micro electro mechanical systems (MEMS), and other features in order to access much of the same design freedom afforded at other frequencies.

Progress in the development of THz metamaterials, the THz sources that have fueled demand for them, and the microfabrication techniques that have allowed for their construction have interwoven to contribute to the meteoric rise of THz in science and technology in the past twenty years. In the following sections several types of metamaterial functionalities will be discussed, and though in general the same concepts can and have been applied across the electromagnetic spectrum, we will focus on examples in the THz regime.

2.3.2 Metamaterial Perfect Absorbers

An important subclass of metamaterials in general is metamaterial perfect absorbers (MPA). Materials that exhibit near perfect absorption of electromagnetic wave are important for

a wide variety of photonic applications. These include energy harvesting[58], communications, imaging[59], EM detection[60], and the chemical[49][15] and biological sensing[61][50] mentioned earlier. As the name would suggest, MPAs are devices designed to absorb nearly all of the incident light at its design frequency. There are a number of methods to accomplish this feat, but broadly speaking they share the same functionalities: impedance matching of the environment prevents Fresnel reflections when light interacts with the material interface, and some mechanism for the light energy to be dissipated (usually as heat) in the material. Early stealth technology used ferrite nanoparticles which would be magnetically excited by radio waves and convert the energy to heat. Anechoic chambers typically use foam cones impregnated with graphite or ferrite particles, often in a gradient density in order to provide a "soft" index gradient from free space to the absorber. Even a simple Fabry-Perot cavity will generate destructive interference of reflected waves at a frequency determined by its geometry. But all of these approaches are imperfect, and many require a significant thikness of absorbing material (for instance a Fabry Perot's first absorption band occurs at $\frac{\lambda}{4}$. But with their accompanying flexibility in design, MPAs can be engineered to provide unparalleled absorption characteristics with a far superior form factor. The thickness of many MPAs relative to the design wavelength is on the order of $\frac{\lambda}{100}$.

The mechanism by which a metamaterial perfect absorber operates can be understood in a number of different ways, but fundamentally they all have one feature in common: the effective medium impedance of the metamaterial must be matched to that of its environment (usually air) in order to eliminate reflections. In free space, $\varepsilon = \mu = 1$ so $Z = \sqrt{\frac{\mu}{\varepsilon}} = 1$. This means that in order to match the free space impedance, the effective permittivity and permeability must be equal ($\varepsilon = \mu$). While this is a challenge with ordinary nonmagnetic materials, metamaterials allow easy access to a much broader parameter space (see the diagonal line of $\varepsilon = \mu$ in Figure 2.1) and thus this impedance matching can be more readily attained.

The most canonical MPA design (See Figure 2.13a,b) consists of a layer of metamaterial resonators (often SRRs), thin dielectric spacer layer, and a ground plane (a uniform metallic

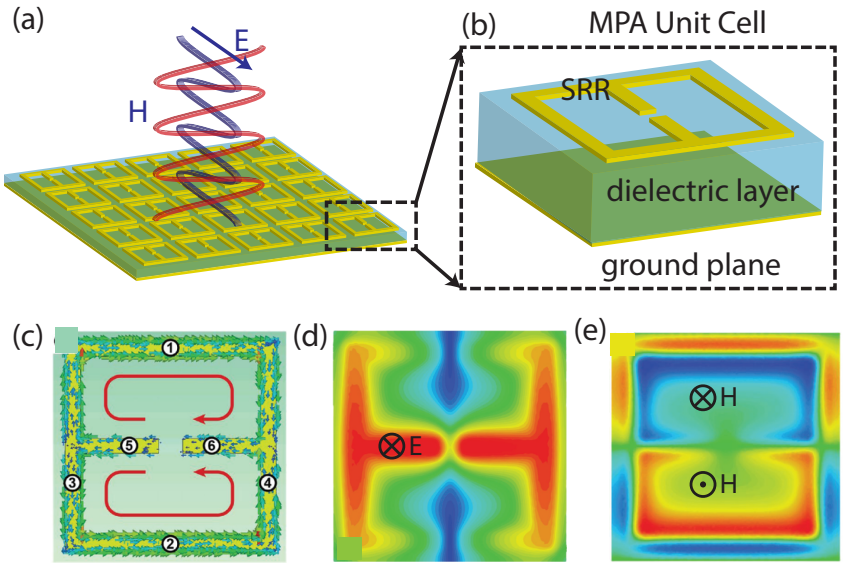

Figure 2.13: The metamaterial-dielectric-ground plane perfect absorber. a) a common MPA design and b) a closeup of its unit cell which consists of a SRR layer, a dielectric spacer layer, and a metallic ground plane. c) The current density on the SRR shows the typical circulating currents associated with a SRR LC resonance. The magnetic b) and electric c) field distributions in the dielectric spacer layer. Though the ELC-SRR in isolation is non-magnetic, the introduction of the ground plane and resulting counterpropogating currents give rise to a strong magnetic fields in the spacer layer, contributing to its effective permeability.

layer). The total absorption can be calculated from the complex reflection and transmission as $A = 1 - |r|^2 - |t|^2$. The ground plane is entriely opaque and thus it can safely be assumed that $t = 0$, and thus $|r|$ must be minimized in order to achieve maximal absorption. In much the same way as we saw in previous chapters, the geometric parameters of the MPA can be tuned in order to optimize the impedance matching with air and minimze reflections. But in this case the effective medium response is influenced by the presence of the ground plane as well. When resonantly excited circulating currents are driven as in a typical ELC-SRR (Figure 2.13c), which in turn generate large electric fields in the capacitive gap and influence the effective electric permittivity (Figure 2.13d). To match ε to μ we must have control over the magnetic permiability as well, but as we saw in Figure 2.9b, the ELC-SRR by it's self produces no magnetic response. However, large currents are also produced on the ground plane, and tend to propagate in the opposite direction of those on the SRR, creating large magnetic fields parallel to the magnetic

field of the incident THz wave 2.13e. Thus the magnetic response can also be engineered to achieve the impedance matching condition, and the energy will ultimately be dissipated through Ohmic heating due to the driven currents in the SRR and ground plane. This explanation is highly qualitative, and in practice optimizing the design of this type of absorber is usually done by trial and error. As we will see later in Chapter 4, there is in fact another way to understand the absorption mechanism of these types of absorbers that is both more intuitive and more analytically tractable.

As with other types of metamaterials, MPAs come in all shapes and sizes and the desired functionality will inform the design approach and working mechanisms that allow them to operate. There are of course variations on the metamaterial-dielectric-ground plane design, as nearly any plasmonic resonator will due for the metamaterial layer. Figure 2.14a shows a microscope image of one such MPA which has three metallic rings of different sizes in each unit cell. Each has a different resonant frequency given by its geometry, and thus each gives rise to a seperate narrow absorption band (Figure 2.14b). Notably, because each absorption band comes from a separate resonator, the absorption bands changing the geometry of one of the rings will shift the associated band, but will not significantly effect the others. Figure 2.14c shows an all dielectric MPA consisting of $30\mu m$ thick resonators on a substrate, both made entirely of doped silicon[62]. The low Q dielectric resoances give rise to a very broad absorption band (Figure 2.14d). The converse, shown in Figure 2.14e is a MPA made entirely of metal[63]. The unit cell is essentially two SRRs standing on end and perpendicular to each other. As a result of this unusual geometry, the SRRs can be excited both magnetically or electrically and from any direction. The metamaterial gives an extremely high Q absorption band which is nearly independent not only of polarization angle, but angle of incidence as well. Many of these design concepts will be revisited later in this dissertation.

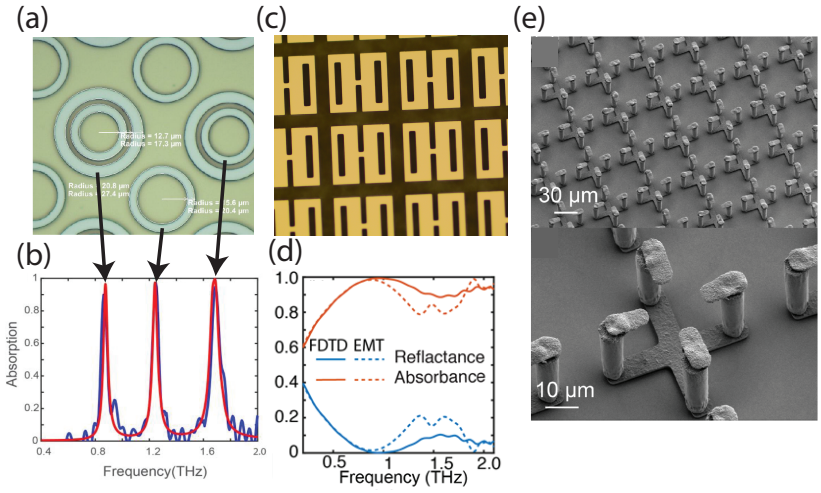

Figure 2.14: Other types of metamaterial absorbers. a) a metamaterial-dielectric-ground plane MPA with three distinct ring resonators of different sizes give rise to three distinct and narrow absorption bands b). c) A all dielectric metamaterial made of heavily doped silicon. Several low Q dielectric resonant modes leads to a broadband absorption while the small conductivity of the silicon allows electromagnetic energy to be dissipated as heat d). e) a freestanding 3D MPA consisting entirely of copper. This design amounts to two SRRs standing up on end and placed orthogonally on top of each other. The result is a very high Q absorber which is extremely robust to both polarization angle and angle of incidence (From [63]).

2.3.3 Nonlinearities and Tuning

So far all of the discussed metamaterials as well as their properties have been static. That is, once the metamaterial has been fabricated, its properties are fixed and cannot be altered by any external stimuli. Clearly this is a major limitation for many applications. So just as the geometries and constituent materials of metamaterials are egnineered in order to imbue it with static properties, so too can metamaterials be engineered to have tuneable properties: ones which change depending on some external stimuli, or nonlinear properties, where the response of the metamaterial depends on the strength of the incident electromagnetic field. Though the mechanisms by which these capabilities can be achieved are inumerable, we will look at a few examples that are representative of some of the general methods employed.

The effective medium response of a metamaterial is highly sensitive to its microscopic geometry as we have seen. Thus one of the most obvious ways to alter that response dynamically

is to achieve dynamic control of that geometry. At THz frequencies where length scales are on the order of microns, this is typically accomplished with micro electro mechanical systems (MEMS). Figure 2.15a shows an example of such an approach in the form of cantilever metamaterials[64]. These can be thought of as a SRR standing on its side, such that it can be excited by the magnetic field of an incident THz wave. The top arm of the SRR is a free-standing cantilever which is held a small distance away from a pad on one end, forming a capacitive gap. When a voltage bias is applied to the cantilever relative to the pad, electrostatic forces which result will pull the cantilever towards the pad, closing the distance and increasing the effective capacitance. This in turn shifts the resonance to lower frequencies. With this convenient means of tuning, this metamaterial device can be used as a tunable waveplate, which can be switched from a state which linearly polarizes transmitted light to one which circularly polarizes it.

Rather than tune the physical geometry of a metamaterial, the other option is to alter the poperties of its constituent materials. The second example is an absorber whos properties are tuned by optical excitation and was actually discussed previously in 2.14c. Recall that this broadband absorber dissipates incident electromagnetic energy through dielectric resonances which are made lossy by a significant electron doping. When an pulse of photons with an energy equal to or greater than the bandgap of silicon ($1.1eV = 1127nm$), this will excite additional electrons into the conduction band and alter the absorption characteristics. Figure 2.15b shows the absorption as a function of 800nm pulse fluence. As the pump fluence increases, so too does the total population of conduction electrons in the regions of the sample that are near an exposed surface. For large pump fluence, these regions of the sample become effectively metallic, and the absorption is significantly reduced at 0.7 THz, while a shifted absorption band appears at higher frequency. Unlike MEMS based tuning, tuning by optical excitation has the potential to be extremely fast, as the timescales are governed only by the pulse duration and the carrier lifetime of the electrons (in this example). For applications in communications devices, optical modulators, and the like, this is a very promising approach.

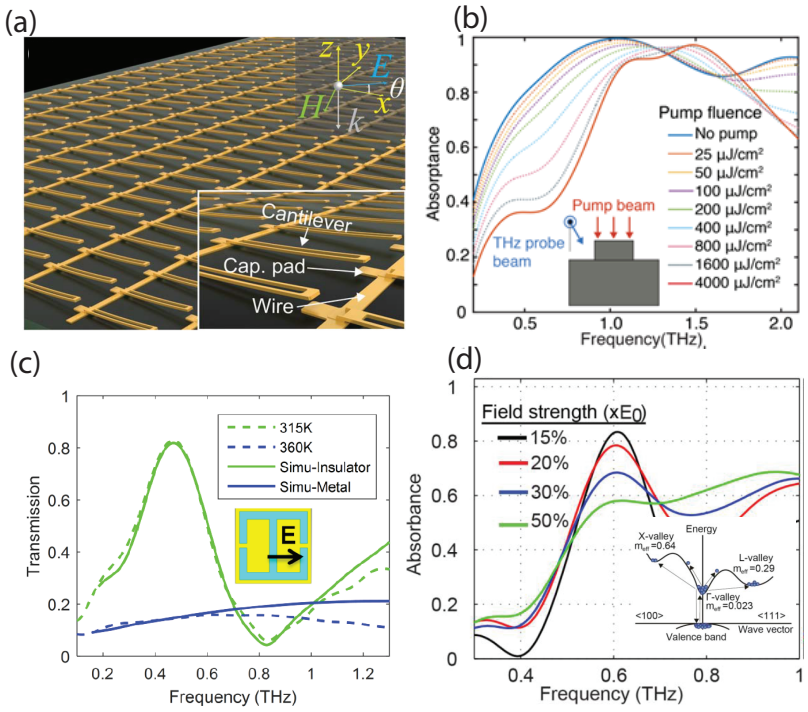

Figure 2.15: Nonlinear and tunable metamaterials. a) a cantilever metamaterial array from[64]. When a voltage bias is applied to the cantilevers and ground plane, electrostatic forces pull on the cantilever and increase the capacitance, in turn reducing the resonant frequency. With the proper choice of incident THz polarization, this tuneability can be used to create a switchable quarter wave plate. b) the absorption of the broadband doped silicon MPA as a function of incident 800nm pump fluence shown in Figure 2.14c. As additional carriers are excited, the dielectric resonance is damped and a new higher frequency band emerges. c) the transmission of a C-SRR on a VO_2 film. At 315K, an ordinary transmission band associated with the resonance of the C-SRR is visible. Above the transition temperature at 360K, the resonance is entirely screened and the sample is mostly opaque. d) The nonlinear response of InAs plasmonic disks from[43]. (Inset) the band struture of InAs shows nearby low mobility valleys into which carriers can be scatterered by large incident THz fields.

But optical excitation isn't the only way to alter the properties of a constituent material in a metamaterial. The example in Figure 2.15c shows a simple complimentary split ring resonator. But rather than an ordinary dielectric substrate, the substrate underneath the C-SRR is VO_2; a well studied phase change material which undergoes a dramatic phase change in which the electrical conductivity increases by several orders of magnitude. At room temperature, the substrate acts as a dielectric, and there is a strong resonant transmission peak at 0.5 THz (green lines). However, upon heating above the transition temperature at 360K, the substrate becomes mostly metallic

and the plasmonic resonance is entirely screened, leaving a low and mostly frequency independent transmission (blue lines). This method produces a dramatic tuning effect, as well as a temperature hysteresis which can be exploited to make devices which have ”memory” of their previous state, but heating a sample is not terribly convenient for most applications. Fortunately, the phase change VO_2 can also be induced with optical excitation[65], large THz fields[30], and as we will see shortly, a sufficiently large DC electric field.

Another important method by which the response of a THz metamaterial can be altered is by interactions with the THz light it's self. Previously (Figure 2.10c) we saw a plasmonic metamaterial made of disks of indium arsenide. Relative to other semiconductors, electrons in the conduction band of InAs have high carrier mobility and low effective mass, making them well suited for plasmonic applications. However, InAs also has lower mobility conduction band valleys, and with a sufficiently large THz field, electrons can be driven into these low mobility states. The result is a metamterial whos response to THz light depends on the intensity of those THz fields. Figure 2.10d shows the absorption of the metamaterial as a function of incident field strength[43]. As the fields are increased, and more carriers are driven into lower mobility regions of the band structure, the plasmonic resonance is strongly damped and the associated absorption feature is weakened. Under a large enough THz excitation, almost any material (including air!) will show a nonlinear response. Engineering metamaterials to take advantage of these nonlinearities and to induce them at more a more practical THz flux remains has become a popular route to dynamic control, especially as high-field THz sources have co-developed.

2.3.4 Metamaterial Coupling

Much of our original discussion of metamaterials focused on examining how various properties both in the near field and in the effective medium approximations arose out of the geometry of a single unit cell. But the reality is more complicated, as metamaterial resonators can couple to eachother, to the lattice that they occupy, or to other resonances and excitations in

nearby states of matter. Coupling is in extremely general term encompassing a huge variety of phenomena. In this section we will only briefly introduce some of the general coupling concepts. Some will be revisited in greater detail in later chapters.

The first illustrative example is that of broadside coupling effects in a metamaterial with a unit cell consisting of two SRR in close proximity to each other (BC-SRR). Coupling of this type and variations of it have been studied extensively[66][67][68] and can be understood more formally through coupled mode theory formalism[69]. The basic concept of a BC-SRR is shown schematically in Figure 2.16a. Two SRRs are stacked vertically with one rotated 180 degrees relative to the other. In isolation the electric (1) and magnetic (2) mode of an SRR are degenerate (they occur at the same frequency). But when brought into close proximity, nearfield interactions between the SRRs modify their mutual capacitence and inductance and lift this degeneracy, resulting in a splitting of the mode. The electrically coupled mode (when the fields in both capacitive gaps face the same way), has anti-symmetric currents, and thus zero total magnetic field threading through the SRRs. If we imagine the two SRRs as anti-parallel magnets, it should be intuitive that this energetically unfavorable state results in a higher energy for this mode (3). Alternatively, when the currents are symmetric and thus the magnetic fields are alligned, the energy of this magnetic mode is lower (4). Further control can be realized by tuning of the structure. Figure 2.16b shows a BC-SRR device with MEMS functionality, allowing the top layer of SRRs to be laterally shiften relative to the bottom layer with an application of a voltage bias to comb drive actuator. This allows for a tuning of the mode frequencies and resulting phase delay of the effective medium.

Even when unit cells consist of only a single resonator, they can couple strongly to the lattice its self and the response of otherwise identical metamaterials can depend strongly on the periodicity of the lattice[70]. Figure 2.16c shows the Q factor of a simple SRR on a dielectric substrate similar to the one considered in 2.1. When the periodicity of the lattice approaches some critical value, radiative losses are strongly suppressed and there is a dramatic enhancement

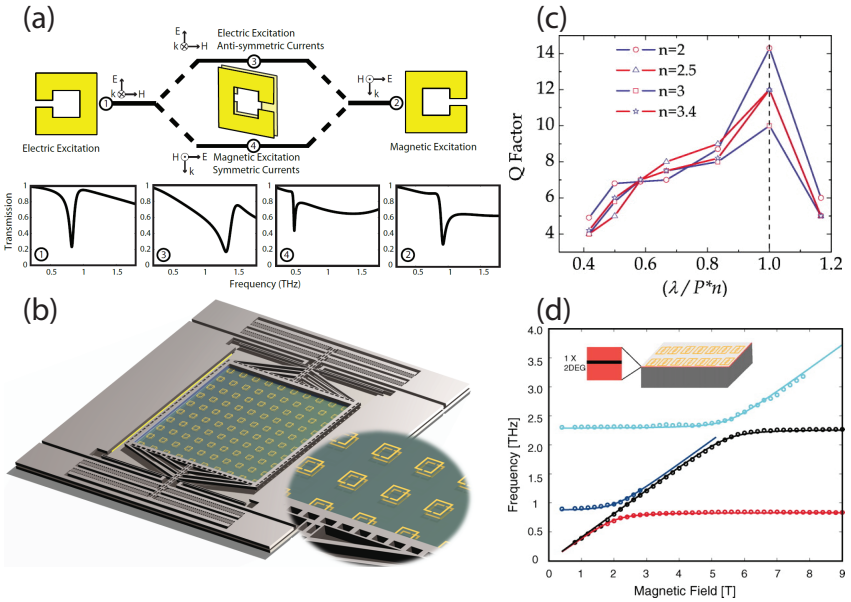

Figure 2.16: Coupling in metamaterials. a) a schematic illustrating the coupling of a broadside coupled resonator. An isolated SRR has a degenerate magnetic and electric mode (the LC resonance), but stacked in close proximity as shown, this degeneracy is lifted resulting in an electric mode with counterpropogating (anti-symmetric) currents at higher energy, and a magnetic mode with propagating (symmetric) currents at lower energy (From [68]). b) An extension of this coupling phenomena using MEMS. An electrically actuated comb drive laterally translates the two layers of SRRs relative to one another, altering the degree and mechanisms of coupling to achieve large tunability. c) The q factor of a simple SRR on a dielectric substrate as a function of the lattice periodicity and for several values of substrate index n. Radiative coupling with the lattice results in a strong dependency; radiative losses are minimized (and thus Q maximized) when the periodicity is equal to the resonant wavelength in the substrate material (From [70]). d) An example of metamateirals used for strong light-matter coupling. A metamaterial layer is placed on top of a stack of quantum wells hosting cyclotron transitions (inset). As the energy of this transition is tuned relative to the fixed resonance of the metamaterial, and avoided crossing occurs which is indicative of strong coupling (From [71]).

of the Q factor. This critical periodicity P matches the SRR resonant wavelength normalized by the refractive index of the substrate n. It is clear from this analysis that a complete understanding of a metamaterial cannot come simply from the analysis of an isolated unit cell; the lattice its self plays an important role in tailoring the response, and likewise offers new avenues for tuning and control.

Another exciting application of coupling effects with metamaterials takes advantage of their capability to amplify and concentrate electromagnetic fields into deeply subwavelength

regions. The ability to enhance and finely tune electromagnetic fields using metamaterials provides an instrument for fundamental studies of cavity quantum electrodynamics (QED) and enables study of metamaterial enhanced light-matter coupling in a variety of systems. In recent years, the so called ultrastrong light-matter coupling regime has attracted significant attention. This regime is reached when the rate of exchange of photons between two subsystems (i.e. a metamaterial enhanced EM wave, and an excitation in a condensed matter system), approaches or exceeds the frequency of that resonance or excitation. Figure 2.16d shows such an experiment in which metamaterials are placed on top of a 2D electron gas which hosts quantized cyclotron transitions[71]. The metamaterial resonance frequency is fixed, but the cyclotron transitions depend linearly on a constant applied magnetic field. As this transition frequency is tuned close to that of the metamaterial, an avoided crossing of the resonances occurs; a hallmark of ultrastrong coupling. This concept of light-matter coupling effects and their profound consequences will be a primary focus of chapter 4, and will be addressed in greater depth there.

This concludes our extended introduction into the world of metamaterials. Hopefully it is clear by this point the depth and breadth of the physics associated with this relatively new field. In the next chapter, we will walk through the various techniques, concepts, and processes that are required to design, create, and test a THz metamaterial.

Chapter 3

Experimental Techniques

In the previous section we reviewed what metamaterials are, how they work, and what they can do with a special focus on techniques and phenomena at THz frequencies. In this section we will walk through the process by which a THz metamaterial goes from the drawing board to reality. Once a desired function has been identified, and the general resonator type and geometry has been chosen (or perhaps more realistically guessed), the first step of a project involving metamaterials is electromagnetic simulations. These can be used to test designs, optimize geometries, and ultimately predict experimental results. Once a design has been satisfactorily identified, the metamaterials must be fabricated using a variety of microfabrication techniques in the case of THz metamaterials. At this point they are ready to be measured experimentally with the hope that agreement between experiments and simulations will validate the entire process. In our lab we utilize a variety of ultrafast optical and THz techniques in order to characterize samples. We will review several of these techniques with a special focus on THz time domain spectroscopy, which allows us to retrieve the complex reflection transmission parameters.

It should be clear from the steps outlined above that THz metamaterials exist in a unique intersection between a number of seemingly disparate fields. The field of THz metamaterials has only been enabled by rapid and concurrent progress in metamaterials, computation, micro-

fabrication, and ultra-fast optics. Without any one of them, this field as we know it would not exist.

3.1 Simulation

In recent decades, electromagnetic simulations have developed rapidly in parallel with advances in computation in general. What in the past would require extensive programming, expertise, and computational resources, is now commercially available in a relatively affordable and user friendly package that can run easily on a modest desktop computer. Popular software suites for modeling metamaterials and other electromagnetic simulations include Ansys HFSS, COMSOL, and CST-Microwave studio, the last of which was used almost exclusively for the simulations presented in this dissertation. There are a number of different approaches for performing computational electromagnetic calculations, but the general strategy is the same: discrete space and time or frequency into finite chunks, and solve discrete versions of maxwells equations iteratively in this discrete space. In the following sections, two such approaches that are of particular relevance for the work presented in this dissertation.

3.1.1 Finite Difference Time Domain

Broadly speaking finite difference time domain (FDTD) simulations operate as follows: a structure is created and assigned with appropriate material properties (ε and μ). Boundary conditions on the edges of this model are defined, as is some electromagnetic excitation. The model is split into discrete hexahedral boxes called a ”mesh”. Then maxwells equations are solved, on the vertecies of that mesh at one point in time, in order to determine the evolution of the fields to the next discrete time step. This process then repeats iteravely to model the time evolution of the electromagnetic fields until some time maximum time is reached. If frequency domain results are required, the time domain signals can simply be fourrier transformed. To

illustrate how FDTD works, I will walk through a simple 1D example that will illustrate the basics of one of the most common approaches to FDTD, though of course this will be far from representing the full complexity nor all of the calculation approaches employed. This story starts (as most good stories do) with Maxwell's equations.

$$\frac{\partial \vec{H}}{\partial t} = -\frac{1}{\mu}\nabla \times \vec{E} - \frac{\sigma_m}{\mu}\vec{H} \tag{3.1}$$

$$\frac{\partial \vec{E}}{\partial t} = \frac{1}{\varepsilon}\nabla \times \vec{H} - \frac{\sigma_e}{\varepsilon}\vec{E} \tag{3.2}$$

$$\nabla \cdot E = \rho_e \tag{3.3}$$

$$\nabla \cdot H = \rho_m \tag{3.4}$$

Where σ_e, ρ_e, σ_m, and ρ_m are the electric and magnetic conductivity and charge density respectively. Note that here we have written Maxwell's equations such that the time differentials are on the time differentials are on the left side. For our example, lets consider the 1D case a TM_y polarized wave traveling in the z direction with no field sources (i.e. $\rho_e = \rho_m 0$). The above equations then become:

$$\frac{\partial H_x}{\partial t} = -\frac{1}{\mu}(\frac{\partial E_y}{\partial z} - \sigma_m H_x) \tag{3.5}$$

$$\frac{\partial E_y}{\partial t} = -\frac{1}{\varepsilon}(\frac{\partial H_x}{\partial z} - \sigma_e E_y) \tag{3.6}$$

This constitutes two coupled first order differential equations. This calculation can also be approached as an uncoupled first order equation. For σ_m=0, we can substitute equation 3.1.1 into equation 3.1.1 in order to yield:

$$\frac{\partial^2 H_x}{\partial t^2} = \frac{1}{\varepsilon\mu}\frac{\partial^2 H_x}{\partial z^2} \tag{3.7}$$

Though for this example we will stick with the coupled first order differential equations. We now discritize equation 3.1.1 and equation 3.1.1. We will now simply invoke the fundamental theorem of calculus with respect to a discrete time step. We can do this by looking at the difference between t and $t+\Delta t$ (forward difference) or $t-\Delta t$ (backward difference), or in our case, $t-\Delta t$ and $t+\Delta t$ (central difference). In this scheme, the time differentials (For instance for H_x) can be expressed as

$$\frac{\partial H(t)}{\partial t} \simeq \frac{H(t+\Delta t) - H(t-\Delta t)}{2\Delta t} \tag{3.8}$$

It can be easily shown by Taylor expanding about t that this approximation is accurate to $\mathcal{O}(\Delta t^2)$, whereas the forward and backward difference approaches are only accurate to $\mathcal{O}(\Delta t)$, which is why we (and many FDTD solvers) will stick with the central difference approach. We now must discretize our first order equations. We will first make a confusing redefinition such that $\Delta\tilde{t} = 2\Delta t$ and $\Delta\tilde{x} = 2\Delta x$ and henceforth $\Delta\tilde{t} = \Delta t$ and $\Delta\tilde{x} = \Delta x$. To add to the confusion, we will split time into two separate spaces coordinate systems, one at half steps of Δt for the electric fields such that $t = n\Delta t + \frac{\Delta t}{2}$ and one in whole steps for the magnetic field such that $t = n\Delta t$. The same will happen with our discretization of space. The electric field will be defined on half steps of Δx such

that $x = i\Delta t + \frac{\Delta x}{2}$ (where i is another integer index and not to be confused with the imaginary unit). The magnetic field is then defined on a complementary half space such that $x = i\Delta x$. This will all make sense soon I promise. To keep track of these coordinates we and functional dependencies will introduce the notation $H^n_{i+\frac{1}{2}} = H(n\Delta\tilde{t}, i\Delta\tilde{x} + \frac{\Delta\tilde{x}}{2})$ and $E_i^{n+\frac{1}{2}} = H(n\Delta\tilde{t} + \frac{\Delta\tilde{t}}{2}, i\Delta\tilde{x})$. Profoundly, this indicates that in order to determine the fields at any given coordinate in spacetime, we only need H at adjascent times, and we only need E at adjacent space. This is illustrated schematically in Figure 3.1. Returning to our 1D TM_y case and considering the lossless case ($\sigma_m = \sigma_e = 0$), the discrete form of equation 3.1.1 and equation 3.1.1 become:

$$H_i^{n+\frac{1}{2}} = H_i^{n-\frac{1}{2}} + \frac{\Delta t}{\Delta x}\frac{1}{\mu}(E^n_{i+\frac{1}{2}} - E^n_{i-\frac{1}{2}}) \tag{3.9}$$

$$E^{n+1}_{i+\frac{1}{2}} = E^n_{i+\frac{1}{2}} + \frac{\Delta t}{\Delta x}\frac{1}{\varepsilon}(H_{i+1}^{n+\frac{1}{2}} - H_i^{n+\frac{1}{2}}) \tag{3.10}$$

These are our update equations called the Yee algorithm, which allow us to find the fields at the next time step given the fields at the previous time step. Figure 3.1 shows schematically how this algorithm works in the 2D spacetime plane. Magnetic field information is marked with a blue dot and Electric field information with a red square. To determine, for instance, the H field at any point in spacetime, the only information needed is the H field at the same spatial coordinate on the previous whole timestep, and the E field on the previous half timestep and at the spatial coordinates both one half step ahead and behind (green arrows). The implications of this algorithm are dramatic. First, we performing calculations using simple arithmetic, something a computer can do very quickly and in a way that scales linearly. Second, we have cut down our computations by a factor of 4 (we are only solving for one of the two fields at only every other spatial step with each iteration). It also means that once E and H has been calculated for a

given adjascent pair of half timesteps, all of the prior information used to determine those fields can simply be thrown out! Thus this method demands relatively little information to be held in memory.

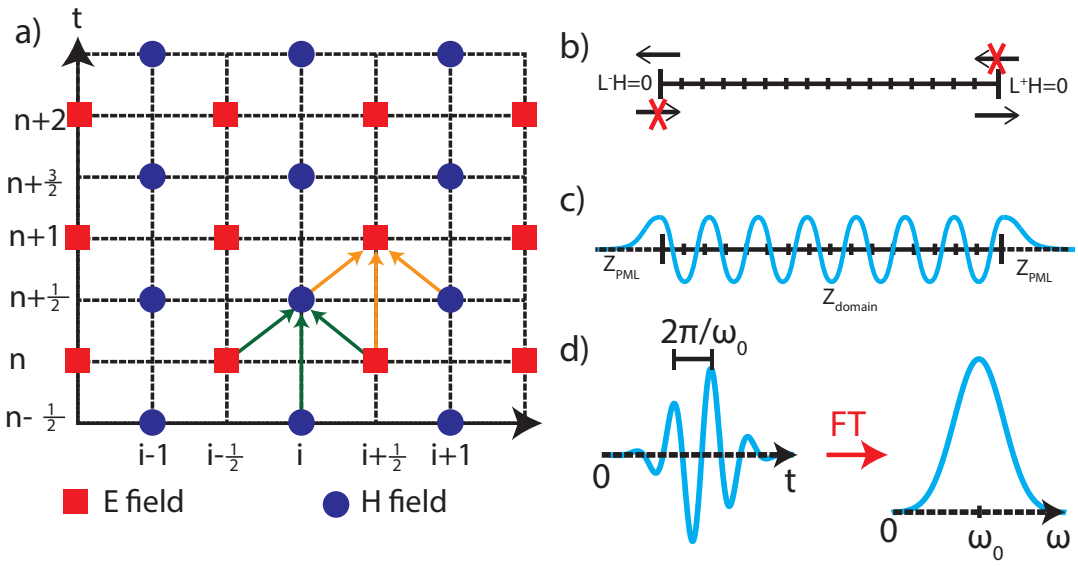

Figure 3.1: A visualization of FDTD simulation algorithms in 1D. (a) A 2 dimensional grid representing one dimensional space and time. Points on the grid for which magnetic and electric fields must be calculated are indicated with blue circles and red squares respectively. The arrows show what information is used in the calculation of fields at future timesteps. b) the Mur absorbing boundary condition. c) the Perfectly Matched Layer absorbing boundary condition. d) A typical gaussian excitation with a constant frequency offset in both the time domain (left) and the frequency domain (right).

But it is worth a reminding ourselves that this example is relatively simple. With our TM_y assumption we reduced our field vectors to scalars. By removing sources and losses ($\rho_{m,e} = \sigma_{m,e}$) we have dramatically simplified the update equations, and perhaps most importantly, we have considered only a 1D case. Furthermore we have said nothing how in practice we choose to discretize our variables (called meshing), boundary conditions or the like. It is worth briefly mentioning some of these considerations. The first is our choice of time and spatial step. Qualitatively, we can not have the phase of our EM wave change too dramatically between steps, lest we get divergences in our update equation. This means that our choice of time step Δt is related to our choice of spatial step Δx. Sparing you the derivation, the general condition for

stability is $\Delta t \leq \frac{\Delta x}{\sqrt{D}c}$ where c is the speed of light in the medium and D is number of spatial dimensions. For good stability Δx should be on the order of $\frac{\lambda}{20}$. Furthermore, FDTD simulations have numerical dispersion; that is, the velocity of light in the simulation has a dependency on its frequency. This unusual dispersion relation is given by:

$$\sin^2\left(\frac{\omega\Delta t}{2}\right) = \left(\frac{c\Delta t}{\Delta x}\right)^2 \sin^2\left(\frac{k\Delta x}{2}\right) \tag{3.11}$$

In practice this nonlinear dispersion results in sinusoidal appearing in front of and behind a pulse, as various frequency components are retarded or accelerated in sinusoidal fashion. This concludes our brief mathematical foray into an example of FDTD simulations. Hopefully it should be clear why FDTD is such a useful approach; it uses simple math rather than difficult matrix inversions, and it requires little memory allowing for large computational domains and complicated structures.

We will now discuss more generally how the simultaneously sophisticated and relatively user-friendly software is used to perform far more complex calculations. One important consideration is boundary conditions, of which there are many types, but a few of particular relevance. One of the simplest types of boundaries is the transverse electric $E_t = 0$ and transverse magnetic boundary conditions $H_t = 0$. From a mathematical perspective this is simple: on the edges of our simulation volume i_{min}, i_{max}, we simply enforce that the component of the field parallel to the boundary be zero, as with an electric or magnetic perfect conductor respectively. This is effectively forms a mirror plane, and can be of great utility for metamaterial simulations. For a TEM wave traveling in the z direction with the electric field polarized in the y direction, we simply place an $E_t = 0$ boundary y_max and y_min, and $H_t = 0$ boundary x_max and x_min edges of our simulation volume. When we simulate just one metamaterial unit cell, these boundaries effectively act as mirrors, creating the effect of an infinite 2D array of unit cells (recall the method of images). The user should however beware; these mirror conditions reverse the direction of

every other unit cell, so with lower symmetry structures (like the simple SRR) this approach is not strictly identical to an infinite periodic lattice. Most of the time the differences are negligible.

Next we must specify boundary conditions on at z_{max} and z_{min} as well. In order for a wave to propogate thorugh these boundaries they must be "open". The electric and magnetic boundary conditions will take care of enforcing the TEM_{00} character of the wave. But open boundaries are mathematically notrivial and there are a number of approaches for them. One approach is called the Mur absorbing boundary condition[72]. In essence, this approach splits the electromagnetic field into a forward propogating part and a backward propagating part. We can see this by splitting the wave equation in two

$$0 = \Big(\frac{\partial^2}{\partial t^2} - c^2\frac{\partial^2}{\partial z^2}\Big)H = \Big(\frac{\partial}{\partial t} - c\frac{\partial}{\partial z}\Big)\Big(\frac{\partial}{\partial t} + ic\frac{\partial}{\partial z}\Big) \tag{3.12}$$

where on the right hand side, the first term becomes an operator L^- corresponding to a wave propagating in the negative direction and L^+ corresponds to a forward propagating wave. At this point we simply enforce that on the negative boundary of the simulation domain, $L^-H = 0$ and on the positive edge of the simulation domain, $L^+H = 0$ (Figure 3.1b). Thus the boundaries will allow waves to freely propagate out of the domain, but not in. Another more common approach is the so called perfectly matched layer (PML). This approach extends the simulation domain by a handful of grid steps, and attempts to match the impedance of the original boundary of the simulation domain to that of this added layer in order prevent reflections from this boundary (Figure 3.1c). But this is not as simple as setting $\varepsilon_{domain} = \varepsilon PML$ and $\mu_{domain} = \mu PML$. The wave must also be dissipated, lest it reflect off of the hard edge of the PML and return to the simulation domain. Thus we must introduce loss through magnetic and electric conductivity such that:

$$Z_{domain} = \sqrt{\frac{\mu_{domain}}{\varepsilon_{domain}}} = Z_{PML} = \sqrt{\frac{\mu_{PML} - j\frac{\sigma_m}{\omega}}{\varepsilon_{PML} - j\frac{\sigma_e}{\omega}}} \tag{3.13}$$

. We must also take care that the losses are not too rapid: the wave must be dissipated over at

least a few grid steps in order to avoid instability. Fortunately, in CST, all of these concerns are taken care automatically; the user must simply select "open boundary condition".

Next we must define some excitation. This is simply some field intensity defined as a function of time and enforced on one of the boundaries. Most often a simple Gaussian pulse is used but special care must be taken; the fourrier transform of a Gaussian pulse is a Gaussian pulse. Practically this means that the frequency content of that pulse will be centered at zero frequency and thus infinite wavelength. Recalling our stability conditions mentioned earlier, this is a problem. Fortunately, the solution is as simple as multiplying our Gaussian pulse by $\sin \omega_0 t$. In the frequency domain, this off pulse is still Gaussian, but centered at ω_0 (Figure 3.1d). It should be noted that naievely defining an excitation as some time varying field on one of the boundaries (i.e. E_0^i), once the pulse has been emitted and $E_0^i = 0$, thsis condition will turn that port into a reflecting boundary! This is generally undesirable, so once the excitation has entirely left the port, it is ideal to remove that enforced condition, allowing the boundary to be open. With electric and magnetic boundary conditions parpendicular to the excitation direction and open boundaries elsewhere, the lowest order propogating mode is the $TEM_0 0$ mode and thus, generally no polarization angle must be defined; the solver will simply use the correct mode. However, this clearly allows only for ecitations at normal incidence with $\vec{E} \parallel y$ and $\vec{H} \parallel x$. While this limitation can be overcome in the time domain, this approach will be discussed more thoroughly in in the frequency domain section.

The last topic that I will cover in our discussion of FDTD simulations is the way in which we break up the simulation domain spatially discrete pieces. This process is called "meshing". In our 1D example, the "meshing" was simply the selection of Δx. In the 3 dimensional analogue, this linear step becomes a hexahedral volume. As in the 1D case, we will solve for the H and E fields independently on two sublattices which are offset relative to each other (Figure 3.2b). As has been mentioned previously, our choice of meshing size can have effects on the stability and numerical dispersion of our simulation. While decreasing the size of our mesh generally

improves the fidelity of our simulation, it of course comes at a cost of computational resources. Explicitly, the computational cost will scale with the number of points on our mesh grid, so for an isotropic cubic domain it will be proportional to $\frac{1}{\Delta x^3}$. In commercial solvers, the mesh grid is drawn automatically, and for FDTD simulations, typically hexahedral meshing is used. That being said, the mesh drawing algorithms do not always do a good job. Consider again the simple SRR from chapter 2. Figure 3.2b shows the initial mesh drawn by the simulation for this structure. It is clear that this mesh does not follow the geometric boundaries of the circular SRR well, and that in order to do so properly, a much finer mesh would be required. In fact in general it should come as no surprise that a hexahedral meshing schema is poorly suited to curved geometries. That being this mesh is remarkably sufficient for accurate retrieval of the S-parameters. Only if high resolution near-field information is desired does it need to be significantly refined (at significant computational cost!).

With the structure, boundaries, excitation, and mesh defined, the simulation is ready to go. The solver will draw a mesh, and solve Maxwell's equations iteratively; leapfrogging from the magnetic to electric field and back. Generally the only information that will be saved for all time steps is the fields at the ports. The simulation will terminate once some condition has been met; either a maximum number of time steps, a certain amount of total energy remaining in the domain, etc. At this point, the fields at the ports (port signals) can be Fourier transformed and normalized to the input pulse to yield scattering parameters and other useful information. In order to obtain meaningful results, these solver conditions may need to be tweaked. The solver time may need to be extended or cut short to allow all more energy to leave solver domain and to avoid multiple internal reflections respectively. Both of these effects produce wiggles in the S-parameters but for different reasons: the former due to the numerical dispersion mentioned earlier, and the latter due to etalon effects. Sometimes getting a FDTD simulation can be more art and trial and error than science, but with experience it becomes easier to avoid the common pitfalls that yield erroneous or inaccurate results.

3.1.2 Finite Element Method Frequency Domain

In the previous section we discussed the general operating principles of the FDTD simulation method for simulating complex electromagnetic interactions. This approach is conceptually straightforward and is advantageous for certain types of simulations, but it is far from the only option. One weakness of the FDTD simulation method is that any frequency dependent information must be extrapolated from time domain information by Fourier transform. The next approach we will discuss find solutions directly in the Frequency domain and is another solver type available in commercial software like CST. Though this section will focus on Finite Element Method Frquency Domain simulations (FEMFD) because that is what is available with CST, I will briefly begin with an aside on Finite Difference Frequency Domain (FDFD) because it is more similar conceptually to the concepts we just discussed, and has many attributes in common with FEMFD as well.

Fundamentally, FDFD solvers operate in much the same way as FDTD, they split the simulation domiain into a mesh grid and solve the wave equation for points on that grid. But in this case, we use the wave equation for the frequency domain:

$$\left(\frac{d^2}{dx^2}+k^2\right)u(x)=f(x) \tag{3.14}$$

. Or in the discrete form:

$$u_{i-1}-(2-(k\Delta x)^2)u_i+u_{i+1}=\Delta x^2 f_i \tag{3.15}$$

. Where similar to, we see that the function f_i is can be determined by knowing u at the same coordinate as well as one coordinate in either direction. This can be written in matrix form as:

$$\bar{\bar{A}}\bar{U}=\bar{F} \tag{3.16}$$

. Where $\bar{U}$ and $\bar{F}$ are vectors describing $f(x)$ and $u(x)$ respectively and $\bar{\bar{A}}$ is a tri-diagonal matrix representing an operator (that is, a matrix where only the diagonal, and and the entries one step above and one step below the diagonal are nonzero). To solve this equation, one needs simply to invert $\bar{\bar{A}}$ and find such that $\bar{U} = \bar{\bar{A}}^{-1}\bar{F}$. While this approach is discrete in space, and discrete in frequency, there is not a simple causal process for sequentially solving the equation at different frequency points. Instead, discrete frequency points are chosen, a solution is attempted and checked in an attempt to minimize $|\bar{\bar{A}}\bar{U} - \bar{F}|$ and the cycle is repeated until a satisfactory solution converges. It should be mentioned that matrix inversion is an extremely computationally intensive process, requiring memory of order $\mathcal{O}(N^2)$ and time $\mathcal{O}(N^3)$ (though both can be improved by one order with the use of sparse matricies) where N is the number of mesh points in the domain.

One of the advantages of this method is relatively easy implementation of more complex boundary conditions. Though there are several notable examples, the one most pertinent to our current discussion of metamaterials is periodic boundary conditions. Rather than the electric and magnetic boundaries considered in FDTD simulations, periodic boundaries simulate a perfect periodic structure simply by enforcing that the fields at on one side of the simulation volume are identical to that on the other. While this avoids the mirror image issue that arises with low symmetry objects mentioned before (See Figure 3.2a), it also affords another useful opportunity: the ability to introduce a phase shift between boundaries in order to simulate non-zero, polarization and incidence angles. This is accomplished enforcing the condition $u(x = L) = u(0)e^{-jkx_0L}$ where L is the length of the simulation domain in a given dimension and x_0 is desired the phase shift for that direction (Figure 3.2d). While these periodic boundary conditions allow for measuring polarization and angle of incidence responses, using them also removes removes the natural port mode for a $TEM_0 0$ mode. As a result, care must be taken to ensure that the field distribution of the mode which the solver chooses to use as an excitation is the one that was intended. It should already be clear that from a conceptual and computational viewpoint, FDFD is considerably more challenging than FDTD. Unfortunately, the leap from FDFD to FEMFD is even worse, so I will

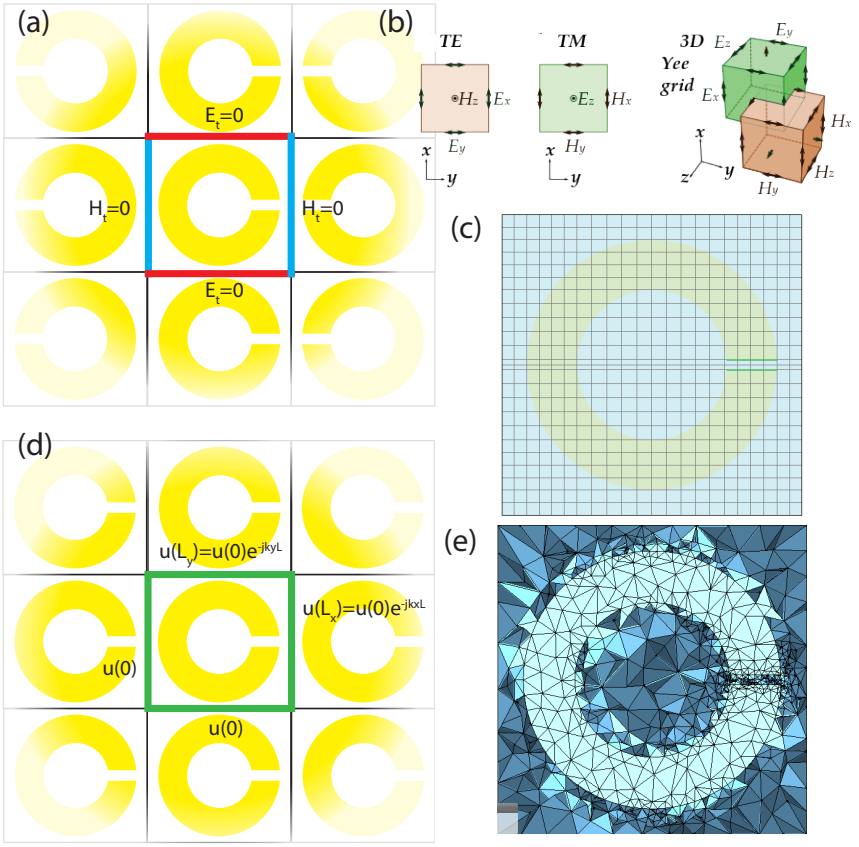

Figure 3.2: (a) A schematic representation of $E_t = 0$ and $H_t = 0$ boundary conditions for MM simulation. Note that neighboring columns are mirrored. b) The 3D generalization of the Yee algorithm shows the hexahedral sublattices on which H and E are solved. c) A hexahedral mesh for FDTD simulations of the structure discussed in chapter 2. d) A schematic representation of periodic boundary conditions. Note that all SRRs face the same way. e) A tetrahedral mesh for FEMFD simulations of the structure discussed in chapter 2. The voxels are significantly smaller in the region surrounding the capcaitive gap of the SRR.

keep the discussion of it as brief, broad, and general as possible, while attempting to cover its most important and relevant characteristics.

The first step in a FEM simulation and the one in which it differs most obviously from finite difference techniques is in the simulation domain discretization. Unlike the hexahedrals typically used for finite difference techniques, FEM methods most often use a tetrahedral mesh (Figure 3.2e). Meshing code separates the simulation domain into tetrahedrons such that each shares edges and points with other tetrahedrons (no point to edge). As with FD methods, these

tetrahedrons should be smaller and denser near complex and small scale geometry. It is clear in Figure 3.2e that in the case of a SRR, this tetrahedral meshing captures the curvature of the SRR far better than a hexahedral mesh. Next, each tetrahedron and each vertex is given an index and an Nx4 matrix is constructed where N is the number of tetrahedrons, and each column catalogues the four vertecies of that tetrahedron. For each of these tetrahedrons, a linear interpolation of the fields between the four nodes is constructed, and thus 4 equations with 4 unknowns. But of course these unknowns are interconnected with the systems of equations associated with all tetrahedrons which share any vertecy. Thus in total we have a much larger system of equations that include contributions from each tetrahedron, which we evaluate using a funcional which optimizes the system of equations. This process can be refined and re-expressed in a matrix formulation which is formulaic for a computer to carry out but tedious to do by hand. Even in an incredibly simple case involving only 2 tetrahedrals which share 3 of their 4 points, ultimately this yeilds a 5x5 matrix which must be inverted. As with FDFD, this calculation must be iterative performed until some threshhold accuracy is met. But this only provides a solution for one frequency point, next the procedure must be repeated for additional frequencies, and the solution between frequencies must be interpolated until some solver condition (usually accuracy) is met at which point the solver terminates. It is fitting then that this vague overview of FEMFD should terminate as well; sufficed to say, the method is powerful but conceptually and computationally demanding, and if nothing else I hope this description emphasizes just how impressive these commercial solvers are.

So which solver should we use and under which circumstances? FDTD simulations are efficient and scale well. With N mesh voxels and N_t time steps will solve in a time proportional to $N_t N$. Because the voxels are hexahedral, in 1D, $N = N_z$, in 2D $N = N_z Ny$, and in 3D $N = N_x N_y Nz$, scaling as one would expect. The memory usage is of order $\mathcal{O}(N)$ because only a full grid worth of information is required to iterate to the next time step. In practice, this means that FDTD simulations are well suited for large and complicated simulation volumes, for instance, if one wishes to model a full array of metamaterials rather than just one. Likewise it means

that for small simple geometries (i.e. a single metamaterial unit cell), calculations will be fast. Furthermore, because frequency information is determined by Fourier transforms of time domain data, information across a broad bandwith can be quickly retrieved. But there are of course drawbacks. Hexahedral voxels are poorly suited for modeling curved structures, especially if precise near-field information is desired. Terminating a simulation too early can result in artifacts in the frequency domain. This is particularly problematic for high-Q resonators (like MPAs), which ”ring” for a long time. Electric and Magnetic boundary conditions are imperfect, and limit the excitation to a $TEM_0 0$ plane wave. An analogue to periodic boundary conditions exist for the FDTD solver, but does not allow for easy retrieval of far field data (scattering parameters).

On the other hand, FEMFD calculations are much more computationally demanding, but offer some undeniable benefits. For N tetrahedral voxels, the computational time cost is $\mathcal{O}(N^3)$ (matrix inversion generally scales this way) and the memory cost is $\mathcal{O}(N^2)$. Using sparse matrices these can both be reduced by one order. Furthermore, dynamic scaling of the tetrahedrons allows for more flexible meshing (larger voxels near complicated geometry and fewer far away). But this computational cost is for a single iteration at a single frequency. In practice multiple iterations will be required at each of multiple frequencies especially of the bandwith is large. But this cost is a fair price for some applications. Hexahedral meshing can easily resolve complex and curved geometries. Periodic boundary conditions allow both for a perfect periodic lattice as well as excitations at arbitrary polarization and angle of incidence while still allowing for easy retrieval of scattering parameters. FEMFD simulations are particularly useful for high-Q structures or simulations over relatively small bandwidths. Just keep the simulation domain as small or else you’ll be waiting for an answer all night! Some additional useful tips can be found in the appendix.

Much of the time of executing a metamaterial project goes into simulations. It is here that ideas can be tested and tweaked, structures can be optimized, hypotheses tested, and mechanisms investigated. All it costs is time, both the users and the computers. Far less time and resources

than that required to fabricate, ship, and measure a sample in a haphazard game of trial and error. But once the design has been settled upon, It is time to actually build the thing.

3.2 Fabrication

Over the course of my education, my toils to bring a metamaterial design into the material word have typically gone as follows: I attach a simulation file and perhaps a description or schematic to an email and send it off. A week or so later, a metamaterial built to those specifications with tolerances best measured in billionths of a meter arrives in my mail. Vouila. In all seriousness, I owe my degree to my collaborators at Boston University. Under the direction of Professor Xin Zhang, her students Guangwu Duan, Xiaoguang Zhao, and others have brought their unparalleled skills and experience to bear in constructing whatever device I could dream up. Though several thousand miles away they were my closest colleagues fore every project presented here. So while I personally have not had any hands on experience in microfabrication, it is as much an integral part of this story as any other.

The projects presented in the later chapters of this dissertation all incorporate metamaterials of various types as well as some complex matter that requires additional fabrication considerations. In this section I will briefly introduce some of the most relevant techinques involved in both the fabrication of metamaterial structures, as well as the general techniques employed in the growth of various condensed matter crystals.

3.2.1 Microfabricatoin Techniques

One of the most ubiquitous and and widespread microfabrication methods is lithography; a process not dissimilar from the method by which a photograph is developed. Specifically, photolithography is one of the most common approaches for fabrication of metamaterials, and thus it will be useful to walk through a slight variation of this process in order to illustrate how

an array of SRRs is fabricated. We begin the fabrication process with a silicon wafer coated with a very thin layer of Silicon Nitride (SiN_x) as our substrate (Figure 3.3a). This provides the mechanical support for the metamaterial. Next a thin, uniform film of gold (typically 200nm) is deposited by electron beam physical vapor deposition (Figure 3.3b). This process operates by accelerating electrons to a high velocity and smashing them into an ingot of metal (in this case gold) which is held above the sample. Atoms of gold sublimate with each impact and fly off of the ingot and onto the substrate where they stick. This process slowly deposits extremely uniform layers such that the thickness can be carefully controlled. Next a photoresist is applied (Figure 3.3c). This is typically accomplished by spin coating: A viscous solution of the photoresist is placed on the wafer, and then the wafer is rapidly spun, flinging off the excess. What is left is a thin, uniform layer typically less than a few microns thick. Next a photomask must be aligned. A photomask typically consists of a wafer of glass with a pattern of Chromium deposited on top that matches the pattern that we wish to make (i.e. the metamaterial array). This pattern is typically etched into the chromium by laser writing; where a laser either scans or rasterizes across the Cr, abblating away the Cr in locations where it is not wanted.

Once the mask is in place close, or even in direct contact with the wafer, intense UV light is used to illuminate the mask, only passing through the areas where the Cr has been removed (Figure 3.3e). The exposure of the photoresist in the illuminated areas undergoes a chemical reaction that ”softens” the photoresist. In the next step, this softened photoresist is washed away with chemical ”developer” similar to in photographic developing processes (Figure 3.3f). The developer is typically delivered in a process similar to spin coating. I’ll note here that this is a depiction of positive photoresist; it is the most common and becomes soluble to the developer when exposed to light. Negative photoresists are also used, where instead the light exposure ”hardens” them.

Next is the etching process (Figure 3.3g). Typically in this context, a wet etch is used. A chemical agent is introduced to the wafer, in order to eat away and remove the gold in the

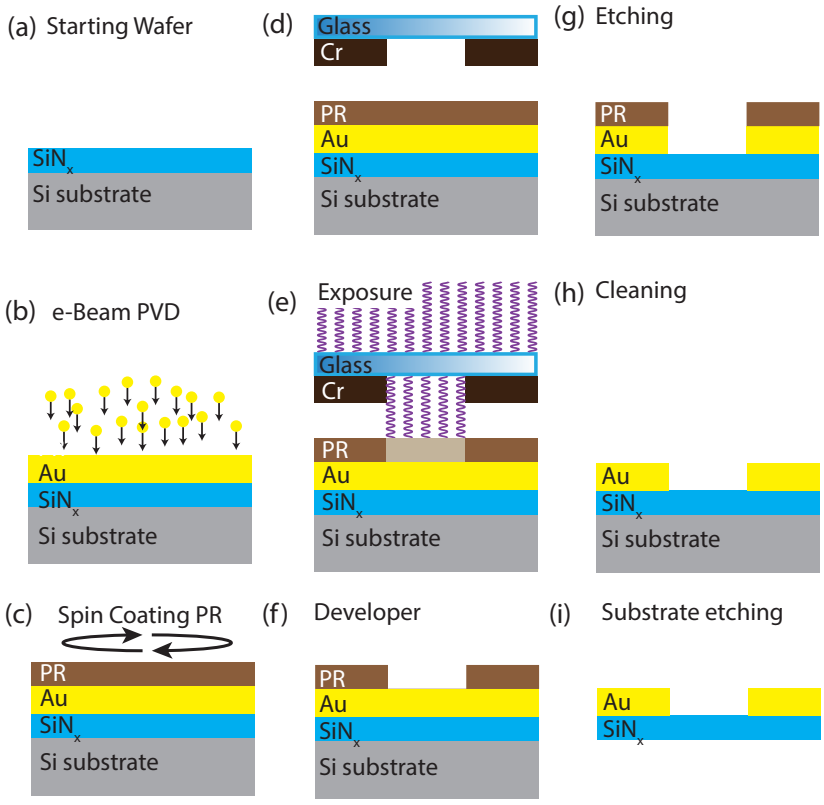

Figure 3.3: The microfabrication process of photolithography. a) The starting material. b) e-beam physical vapor deposition of gold. c) Spin coating of photoresist. d-e) Aligning and exposure using a photomask. f) developing the photoresist. g) Etching the exposed gold. h) Removing the remainging photoresist. i) Etching away the Si substrate.

now exposed areas. This process must be executed carefully: if the etching agent is applied for too long, the liquid will begin to undercut the areas which are protected with photoresist. While generally undesirable, this undercutting is vital, for instance in the micromechanical cantilever metamaterial discussed in section 2.3.3 where the cantilevers had to be ”released” from their initial position by etching away the material underneath. Finally, the remaining photoresist is removed with another chemical agent, a ”resist stripper”, which decoheres the resist from the gold (Figure 3.3h). All that is left is the substrate with the metallic metamateiral on top.

Normally this is where the process would end, but as I alluded to earlier, I’ve added one extra step here that will be relevant later in chapter 4. Though in a more typical situation the

metamaterial would sit directly on a thick substrate (i.e. silicon), with the addition of the thin SiN_x layer, we can actually etch away all of the Silicon in a large window region using another etching process with KOH. All that is left afterwards is a 200nm thick metamaterial on top of a 400nm thick SiN_x film (Figure 3.3i). The substrate is now so thin that effectively the metamaterial is free standing, which can be leveraged to create high-Q, air-spacer absorbers, and other interesting devices [73].

This is not the only variation on lithography. In fact, for every step there is a variety of techniques, chemicals, resists, etc. which may be used depending on the demands of the sample and the materials involved. One major variation on this technique is e-beam lithography. The spatial resolution of photolithography is limited by the diffraction limit of the light used (hence the use of UV light rather than longer wavelengths). For typical photolithography of a metamaterial, the width of gold inclusions must be about $4\mu m$ at a minimum, and gaps (i.e. capacitive gaps of an SRR) should not be smaller than $2\mu m$. On the other hand, electrons can be focused to much smaller beams and as a result can be leveraged to create far smaller features. It is slow (no mask is used) and expensive, but the spatial resolution can be as high as $10nm$, orders of magnitude smaller than for photolithography. Another approach which forgoes the mask (but keeps the photons) is direct laser writing. This process is essentially the same as the one used to create a mask for regular photolithography: rather than dealing with photoresists and etchants and the like, a tightly focused laser simply scans or rasterizes across the sample, ablating away the metal where it is not needed. As with e-beam lithography, without the benefit of a re-usable mask, this process is relatively slow and not suitable for high volume fabrications.

Next I will walk through an entirely different appraoch used more commonly for etching patterns into semiconductors and dielectrics. This process was utilized for some of the dielectric resonators discussed previously in chapter 2.3 and will be relevant again in chapter 5. Reactive ion etching is a type of dry etching (unlike the wet etches with liquid chemicals more common in lithography). As a result, many of the early steps are very similar to the photolithography

discussed earlier. Here, we will consider the etching of a pure silicon wafer that has already had a photoresist deposited, exposed, and developed, (i.e. steps a-f in Figure 3.3) in Figure 3.4a. As with lithography, this masking can be done a number of different ways. The wafer is then placed into vacuum chamber and gasses are introduced (Figure 3.4b). Then a powerful RF microwave emitter is activated, turning the gases into a plasma of ions and electrons (Figure 3.4c). There are a wide variety of plasma species to choose from depending on their chemical interactions with the material being etched. A negative DC bias is then applied to the substrate, which accelerates the ions towards it . The resulting collisions enhance the chemical reaction and quickly remove exposed material (Figure 3.4c). Finally, much as in photolithography, a ”resist stripper” is used to remove the remaining resist, leaving a monolithic silicon wafer with deeply etched metamaterial patterns in it (Figure 3.4d).

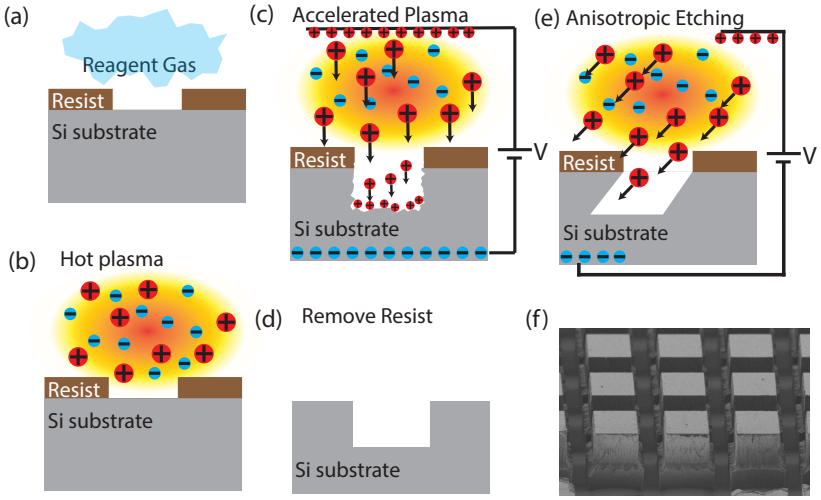

Figure 3.4: Reactive ion etching microfabrication techniques. a) Beginning with a silicon wafer with a patterned and developed photoresist and a gaseous chemical reagent introduced to the sample environment. b) a microwave field ionizes the reagent into a plasma c) a bias voltage accelerates positive ions towards the exposed wafer and accelerates the etch isotropically. d) the remainign photoresist is stripped away. e) anisotropic etching. f) an example of a 2 layer Deep RIE etched structure.

As with other microfabrication techniques, there are a great number of variations and parameters which can be altered in this process to achieve more complex structures. For instance,

the direction of the accelerating bias can be changed such that the ion plasma impacts the wafer at non-normal incidence. This allows for anisotropic etching, for instance creating angular undercut patterns in the wafer (Figure 3.4e). Deep RIE allows for high aspect ratio structures and deep trenches to be etched and often cryogenic temperatures, or chemical reagents which adhere to the side walls of the etch and protect it, preventing lateral etching. This method was employed for the all silicon broadband metamaterial absorber presented in chapter 2.3.2. Another variation of this technique, inductively coupled plasma reactive ion etching (ICP-RIE) uses allows for separate control of the current of reactive ions and their energy which affords a greater degree of control over the etching process. This method will be relevant later in chapter 4.

RIE and photolithography are just two of a great variety of microfabrication techniques and once more, the examples processes we have walked through are the simplest possible variation of each. In practice, many passes of material deposition, lithography, etching, cleaning, etc. are performed in sequence to realize complex structures with multiple layers, additional dimensionality, inclusions of multiple different materials, and whatever other properties or structures are desired. As a metamaterial designer, it is important to have at least a cursory understanding of how these processes work so that you know the limits and demands of what can be realistically fabricated. That being said, skilled and creative fabrication experts are constantly combining existing techniques in new ways and inventing new ones in order to push the envelope on what is possible. So it never hurts to ask.

3.2.2 Crystal Growth

Thus far, this dissertation has almost exclusively focused on concepts and techniques related to inhomogeneous solid matter with sub-wavelength structure (i.e. metamaterials). But ultimately I study condensed matter physics, and the constituent matter incorporated into metamterial structures is just as important to their operation. Moreover, whereas more ordinary metamaterials typically consist of somewhat trivial materials (isotropic and low-dispersion metals and

dielectrics), the focus of my PhD has primarily been in integrating more complex matter into metmaterials. Though this is often done in order to enable new functionalities, tunable, or nonlinear behavior, in my case this integration is done in large part to use metamaterials themselves as a tool to study the constituent complex matter or interactions therein. As such, it is appropriate to briefly review some of the techniques that are used to grow crystalline samples in a more traditional condensed matter laboratory setting. In what is becoming a refrain, I will remind the reader that this is only the most cursory review of two very general concepts, and that fabrication of exotic materials is an entire field in its own right.

The first general technique I will discuss is called traveling solvent folating zone (TSFZ) technique. Large and pure single crystals (where parts of the sample are crystalagraphically co-allgined) are vital for high quality solid state electronics as well as for the study of physical properties of materials. This method has been one of the most powerful and common both in laboratory settings as well as in large scale commercial operations, but the conditions of the crystal growth must be precisely controlled and growth mechanisms well understood in order to produce a high quality crystal.

Beginning with precursor materials, often oxides which contain the desired elements, are mixed in stoichiometric quantities for the desired result (though there will be an excess of oxygen). These powders are thoroughly mixed and annealed at high temperatures, often multiple times, with thorough crushing and mixing of the powder in anneals. If performed correctly, the resulting powder should be a polycrystal of desired material; that is the powder consists of a multitude of small ”grains” of the desired crystal, but the crystallagraphic axes of these grains are not aligned to one another. This powder is compressed to form a solid but brittle polycrystaline rod. Next, the two rods are placed in a heating oven end to end (Figure 3.5a). The two rods rotate in opposite directions, and the heat source is turned on. There are a variety of heating methods: electrical inductance, resistance, laser heating, etc. But commonly, light focused from several halogen lamps onto the sample is used. The near ends of the polycrystal rods melt and

surface tension of the molten material forms a liquid bridge between the two rods. Very slowly (often only a few mm/day, in the case of $CaWO_4$ 0.01mm/day! [74]), the heating zone is moved upwards relative to the rotating and thus the top of the bottom rod cools and solidifies while more of the top rod melts. Though initially totally polycrystaline, as the top of the bottom rod cools and solidifies, one particular crystal grain may act as a "seed"[1]. That is, surrounding cooling material will preferentially solidify onto the seed with it's crystal axes aligned to that of the seed. As the float zone continues to move, the polycrystal will contain ever fewer and larger crystal domains, as one of the seeded domains may become dominant. Eventually only there will be only one domain: a single crystal. The multi-domain and polycrystaline regions can be cut away.

This is of course a vastly simplified picture. In reality, the temperature gradient of the float zone, and temperature must be carefully controlled. Generally the growth occurs in some flow of oxygen and/or inert gasses whos mixture needs to be carefully tuned. The rotation and translation rate of each rod must be independently controlled as well. For a single crystal a few centimeters long and less than a centimeter wide, this process can take days, and generally requires constant monitoring. Once the crystal has been grown, x-ray techniques can be used to determine the orientation of its crystallagraphic axes and wire or diamond saws can be used to cleave it along the desired plane. For optical experiments, this can be a crucial step. Many crystals are anisotropic (their properties are different along different crystal axes), and probing the crystal light polarized in one direction vs another will yeild entirely different results. Indeed this is one of the great advantages of using a large single crystal. Because they are 3 dimensional, they can be arbitrarily cleaved along any direction desired by the experimenter for their experiment. In chapter 6 we will see exciting example of a strongly anisotropic crystal grown by TSFZ and then integrated into a metamaterial system.

But if we do not desire a large bulk single crystal (they are often inconvenient for a variety

[1] in many cases, rather than using a polycrystaline rod on the bottom, an existing single crystal is used instead as a "seed". While this is of course more efficient, it requires that there is single crystal of the type being grown already on hand. This is more common in a commercial setting than in a laboratory where a crystal may be one of a kind.

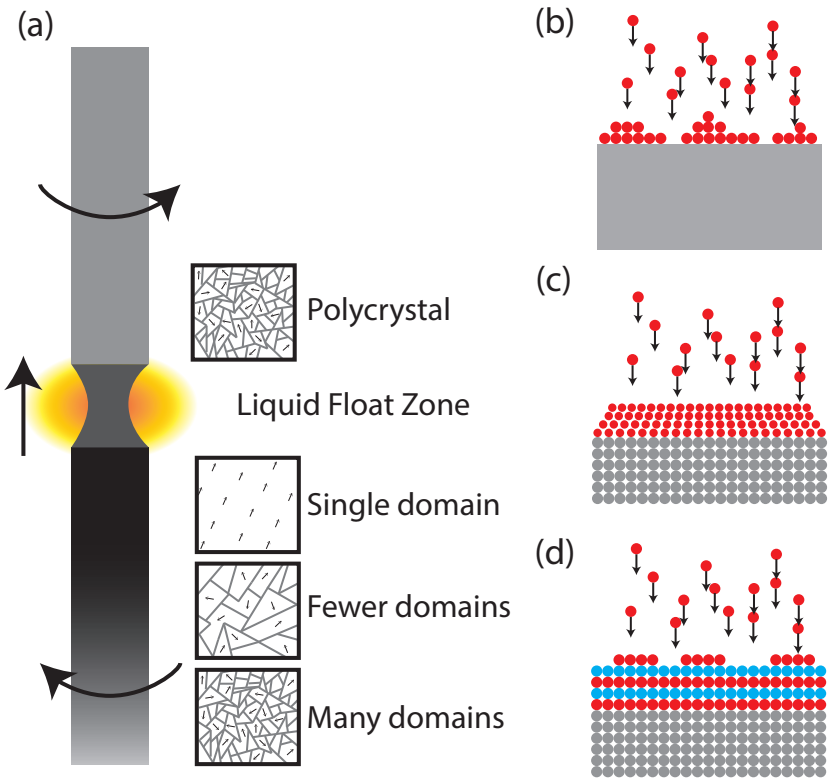

Figure 3.5: Various crystal growth techniques. a) The traveling solvent floating zone technique for single crystal growth. b) generic physical deposition thin film growth. c) Growth of a strained film. Note that the natural periodicity of the substrate is different from the deposited film resulting in a stretched lattice. d) Molecular beam epitaxy allows for growth crystal films one atomic layer at a time.

of reasons), thin films of crystals can also be grown. There are many ways to perform this feat but they generally fall into only a few catagories. In chemical deposition, a fluid or gas undergoes a chemical change upon interacting with a sold surface, leaving a solid layer on that surface. It is primary advantage is that it is not directional: a film will be uniformly deposited on every exposed surface of the material rather than only ones that are facing one direction. Electroplating is perhaps one of the most well known examples of this process and is useful for depositing metals on irregular surfaces. This typically consists of a surface being submurged in liquid precurors, typically a mixture of salts and the metal to be deposited, and then connected to a DC voltage source. The electric current reduces the disolved metal cations, compelling them to stick

to the submerged surface and creating a coating. This is the process by which the copper was deposited on the 3D MPA shown in Figure 2.14e. Chemical vapor deposition is another common and commercially widespread chemical deposition technique used for fabricating high quality films. In this process a wafer under a hgih vaccuum is exposed to volatile precursors which react with the wafer and deposit the desired film, leaving biproducts which are puumped away. This method can be enhanced by exciting the precursor gas into a plasma. Spin coating is another method of chemical vapor deposition which was discussed previously, in which a liquid is poured over a wafer and then the wafer is supn rapidly to remove excess liquid. In our discussion of photolithography, this is how the photoresist was deposited, and we will see this technique many more times in later chapters.

Another catagory of thin film deposition is physical deposition. Generally speaking, these methods involve the desired material to be deposited in a high vacuum environment balistically traveling to a substrate wafer and becoming attached to it. The material that we wish to deposited is placed in an energetic environment so that particles of the material escape its surface. This heating can be accomplished a number of ways. The material can simply be heated by a electric resistive heater. A beam of intense continuous or pulsed laser light can likewise be used. Sputtering relies on a nobel gas plasma to be directed into the material in order to knock material from it. In our earlier discussion of photolithography in section 3.2.1, an electron beam was directed into a gold ingot in order to liberate gold particles (Figure 3.3b). Regardless of the methods employed, once the particles have been liberated from the bulk host, they will travel ballistically across the vacuum chamber until they collide with the much cooler surface of the wafer on which they are to be deposited. Much like frost forming on a cold surface, these particles will adhere and crystasllize into a uniform thin film across the substrate.

One variation on this technique that will be of relevance later is reactive sputtering. In this scenario, rather than a vacuum, the chamber is filled with a mixture of gases which are intended to intaract with particles as they fly towards the wafer. In chapter 5 this technique will be employed

in order to go from a vanadium precursor material to a VO_2 film on the substrate.

Another important category of thin film deposition which can be done in either physical or chemical mode is epitaxy. In this method, the substrate on to which the film will be deposited is it's self a single crystal of that crystal, or a slight variation of it. In homeoepitaxy, both the substrate and film are the same crystal, but the film may be made to have a higher purity, or may be doped differently than the substrate. Alternatively heteroepitaxy makes use of the crystal lattice of the substrate in order to force the growth of a crystal whos lattice must match up with the underlying crystal. This can be utilized in order to grow crystals that would not be able to be fabricated otherwise, or to introduce strain into a film, stretching or compressing its lattice into unnatural dimensions. Molecular-beam epitaxy is a particularly sophisticated version of physical deposition which is extraordinarily precise and slow. It allows for deposition of single crystal layers one atom thick at a time, and can be used to create superlattices, i.e. by alternating between different atomic crystal layers.

Relative to single crystals, it is more difficult to achieve high quality single crystal films, and even in those cases, it is generally impossible to select the crystallagraphic plane which the film grows on. For optical experiments, particularly in transmission, they are almost always a necessity, and they are not only compatible with various microfabrication techniques, but are an integral part of many of them as we have seen. As with the various methods of microfabrication discussed earlier, various single crystal and film growth techniques can be stacked or combined in innumerable ways in order to grant a high degree of control over the final product. But as always in multi-step processes, care must be taken to ensure that various steps are co-compatible, and etchants, reagents, plasmas, and the like used in one step will not cause unwanted damage of materials deposited in another.

3.3 Measurement Techniques

Once a sample has been sucessfully fabricated, it is time to measure its response. One of the most common general techniques for probing a sample with light is spectroscopy. Broadly speaking, in spectroscopy a broadband pulse of light illuminates a sample, and the transmitted and reflected light is measured as a function of frequency. As we have seen earlier, this can allow us to identify interactions between the light and the material it probes, such as resonances of a metamaterial. At visible frequencies, this is a straightforward affair. A simple light bulb produces light which spans the entire visible spectrum and can be used to illuminate the sample while a prism can split the transmitted light into its constituent components forming in order to form a rudimentary spectrometer. Unfortunately, we are interested exclusively in THz metamaterials, and performing spectroscopic measurements at THz frequencies is not nearly as straightforward. There are no THz lightbulbs, and there are no (simple) THz spectrometers. In this section, I will detail how this spectroscopy is done before discussing several other ultra-fast optical techniques which we employ not only to measure linear optical properties of materials, but to alter them on very short timescales.

3.3.1 Photoconductive THz-TDS

Terahertz time domain spectroscopy (THz-TDS) is the primary experimental technique employed to study the metamaterial systems reported in this dissertation. Ordinary spectroscopy at higher frequencies typically relies on a broadband continuous and incoherent light source to illuminate the sample, and a spectrometer to split up the spectral components of the transmitted or reflected light. In this technique, an ultra-short pulse of THz light (generally only one wave cycle) is generated and focused onto a sample. Though brief, this pulse contains Fourier components across a broad THz spectrum (0.2-3THz for our system). The relatively low oscillation frequency of the THz radiation allows for direct measurement of the eclectic field of this pulse (both ampli-

tude and phase) as a function of time, not just the intensity as with ordinary spectroscopy. The transmitted or reflected THz pulse is measured in the time domain, Fourrier Transformed, and then normalized to an appropriate reference pulse in order to yield a frequency domain transmission or reflection coefficients with both amplitude and phase. This phase information is vital for retrieval of effective paramaters for instance (See section 2.2.1) and for a full understanding of the light matter interactions more generally. It is a crucial advantage of time domain spectroscopy. Conversely, in ordinary spectroscopy, phase information must be reconstruction with dubious mathematical operations like the Kramers-Kronig relations. But equally important for metamaterial applications specifically, the complex reflection and transmission (S-parameters) are easily simulated as shown in section 3.1, and thus offer a one to one way to compare experimentally measured data to simulated predictions in order to validate the experimental process. Though most spectrometers (for all frequency ranges) operate only in one mode, either reflection or transmission, I sought to construct and THz-TDS instrument which would be able to perform both more or less concurrently, in order to straightforwardly perform comprehensive measurements of THz metamaterial systems. The remainder of this section introduces this system, its components, and measurement process.

As has been alluded to previously, generation and detection of THz light is not a straightforward task. It requires many steps, the first of which in this case is a powerful, continuous, green laser. Light amplification by stimulated emission of radiation (LASER) is a process whereby a photon interacts with an atom already in its excited state resulting in the relaxation the atom to its ground state and the emission of two photons that are identical in phase, direction, and frequency given by $\nu = (E_2 - E_1)/h$ where E_1 and E_2 are the ground and excited state energies of the atom respectively. This process cascades to produce an intense coherent beam of light, but only if there are a large population of atoms in this excited state waiting to decay, and very few in the lower energy state that they will decay to. Creating these conditions is called population inversion, as ordinarily, the electron population of the lower energy state would be far larger. But driving

electrons into their excited state paradoxically reduces the absorption of that transition and with it the ability to drive additional electrons into it, so practice, multi level systems are used.

In our system, the laser gain medium is Nd^{3+} ions doped in a yttrium vanadate crystalline matrix ($Nd:YVO_4$). The The Nd^{3+} ions act as a four energy level system, which have a strong absorption of light at 810nm. The lasing process in this situation is shown in Figure 3.6a and occurs as follows. A powerful diode laser acts as the "pumping source". They are bright, efficient, monochromatic, compact, and their output is nearly identical to the principle absorption band of the Nd^{3+} ions, making them efficient at driving the Nd^{3+} into its excited state. The (simplified) pumping and lasing sequence goes as follows: Initially the electron population of the Nd^{3+} is predominantly in the $^4I_{9/2}$ ground state. The diode laser pumps the Nd^{3+} at one of its pricniple absorption bands at 810nm, efficiently driving electrons into the "pump bands" 1.53eV above the ground state. These electrons quickly cascade down in energy until they arrive the first metastable state (long lifetime) that they encounter, in this case $^4F_{3/2}$. Due to this long lifetime, electrons accumulate into a large population. The most probable transition from there is down to $^4I_{1/2}$ which is an unstable (short lifetime) state, and thus remains depopulated. It is by this process that population inversion is achieved, and lasing can occur through this $^4F_{3/2}$ to $^4I_{1/2}$ transition, associated with a 1064nm photon.

One we have a powerful beam of 1064nm laser light, this must be frequency doubled through second harmonic generation in a nonlinear crystal. In this laser, a phase-matched, temperature-tuned lithium triobate (LBO) nonlinear crystal is used as a doubling medium (Figure 3.6b). The second harmonic power ($P_{2\omega}$) in a nonlinear system is given by:

$$P_{2\omega} \propto \frac{d_{eff}^2 P_{\omega}^2 l^2 [\phi]}{A} \tag{3.17}$$

Where d_{eff} is the effective nonlinear coefficient, P_w is the fundamental frequency input power,

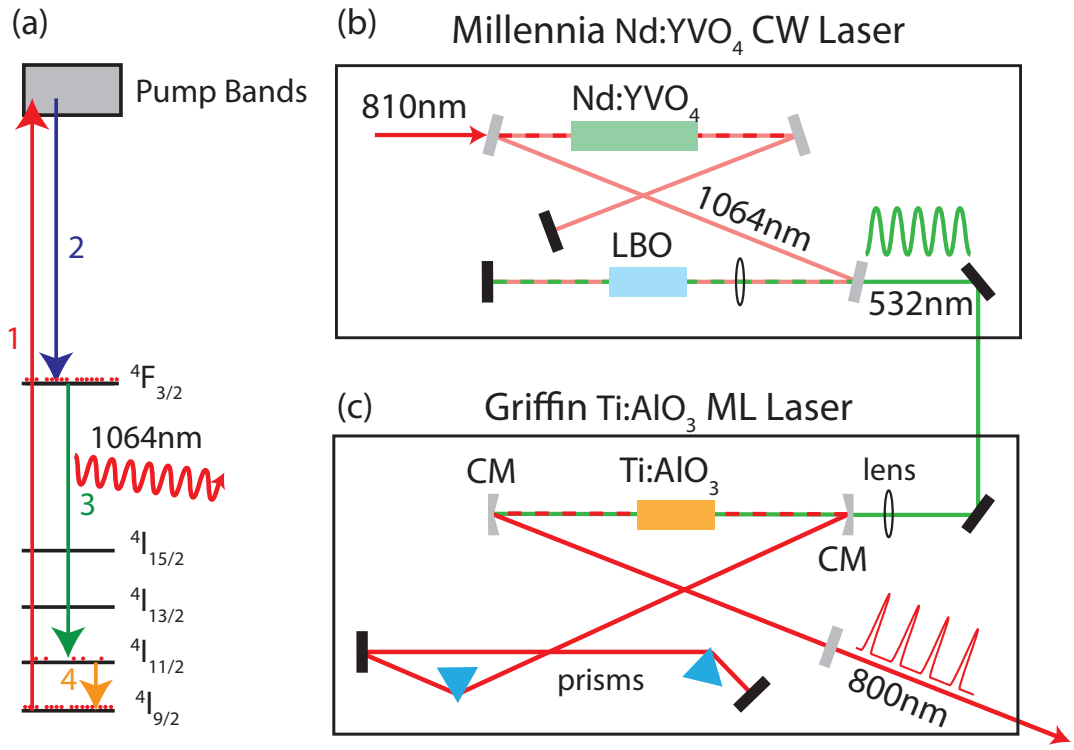

Figure 3.6: a) The mode of operation for the $Nd:YVO_4$ CW 532nm laser. Each step of the lasing process is shown with an associated color. b) An optical schematic of the diode laser pumped $Nd:YVO_4$ laser. c) An optical schematic of the $Ti:AlO_3$ ML 800nm laser. The pulsed 800nm output beam goes on towards the THz optics.

l is the length of the nonlinear crystal, $[\phi]$ is the phase matching factor, and A is the cross-sectional area of the beam. In this laser, LBO crystal actually sits inside the laser cavity (with the $Nd:YVO_4$), converting the intracavity light to the green 532nm wavelength. The LBO is relatively alignment insensitive and is housed inside of a small temperature-regulating oven. This oven actively regulates the LBO crystals temperature and thus its thermal expansion and resultant lattice constant in order to optimize the phase matching (ϕ) condition for second harmonic generation. Finally, a dichroic output coupler allows the 532nm light to exit the laser cavity while reflecting the 1064nm light back into the cavity. The result is a 5W continuous 532nm laser with extremely high stability, 2.3mm beam diameter, and $< 0.5mrad$ divergence. In practice, this entire system is a single commercially available unit, which operates robustly, rarely requiring

tuning or maintenence from the end user. The next step, turning this 532nm continuous laser light into ultrashort pulses of 800nm light, is considerably less user-friendly.

In this case, (and in almost all cases), we employ a Titanium-doped Sapphire ($Ti:AlO_3$ or colloquially Ti:Sapph) laser. This is another solid-state laser, this time using $Ti:AlO_3$ as its gain medium. The key difference between this and the $Nd:YVO_4$ laser discussed previously is the introduction of a time-dependent gain to the laser cavity that allows for a process called mode-locking (ML), in which a fixed phase separation is imposed between all lasing frequencies[75]. The resulting interference between various laser modes produces ultrashort laser pulses between 750-850nm, and as short as 10 fs. The $Ti:AlO_3$ laser is pumped with the CW 532nm output of the $Nd:YVO_4$ laser. The pump light is focused through a lens and onto a point in the center of the $Ti:AlO_3$ crystal (Figure 3.6c). The position of the two curved mirrors (CM1 and CM2) relative to the lens and crystal can be adjusted to maximize the CW output of the oscillator laser. Once this output has been optimized, ML can be initiated. The two intra-cavity prisms compress the resulting laser pulses in time by compensating for the temporal dispersion that occurs as the beam travels through dispersive media like the crystal. Ultimately the 800nm beam is sent out of the cavity through the output coupler, the remaining 532nm light is filtered out, and the beam is sent on to the THz optics.

Mode locking generally refers to a process by which the gain of the gain medium (in this case the $Ti:AlO_3$) can be altered as a function of time. Broadly, there are two categories, passive and active mode locking. In the active case, this can be accomplished, for example, by the addition of an eternally driven amplitude or phase modulator which modifies the gain with a electrically driven signal[76]. In the passive case, spontaneous gain modulation occurs due to the inclusion of a nonlinear optical element, such as a saturable absorber[77][78], or a Kerr-lensing element[79]. This particular laser uses the latter effect. The Kerr effect is a process by which the refractive index of a nonlinear medium is modified by light passing through it by $\Delta n = n_2 I$ where n_2 is the equilibrium refractive index and I is the light intensity. This in turn effecting the

propagation of that light and can result in a phase modulation or Kerr lensing. The latter effect causes an index gradient which is maximal at the center of the beam, and results in a focusing and resulting reduction of the beam size. This leads to a better overlap of the laser and pump beam and thus higher gain at the peak of the pulse.

To illustrate how this generates mode locking, consider a scenario where we start with a single intense pulse of light which is bouncing back and fourth through the cavity and gain medium. Each time that pulse enters the gain medium, the Kerr lensing effect increases the pulses overlap with the pump beam and with it the gain, resulting in an even more intense pulse. In fact, because the leading and trailing edge of the pulse have a lower intensity, this effect will intensify those two parts of the pulse much less than the central peak, resulting in an even shorter pulse. The result is a positive feedback loop; with each pass thorugh the gain medium, the most intense part of the pulse is further amplified, while the weaker edges of the pulse or other pulses that may be circulating are attenuated by losses, resulting in an an intense and extremely short pulse. These pulses make a round trip of the entire cavity in time $t = c/L$ where L is the total effective cavity length. Using an output coupler to allow some of the light out of the cavity, a pulse will be emitted with a frequency of $1/t$. Our laser has a total cavity length of 1m, and thus 80 million pulses per second, a reprate of 80MHz. Though this mode locking process is self reinforcing, the power fluctuations of the CW lasing mode are not generally sufficient to kick off the process and a more significant power fluctuation is needed. For this laser, a small perturbation to one of the prisms (i.e. nudging it with a finger) is sufficient to initiate mode locking.

The process for alligning and tuning the $Ti:AlO_3$ laser can be challenging, as there are many different failure modes and bad lasing-states, as well as multiple diagnostics which must be performed in order to fully assess the quality of the output. Some of these details and other helpful tips can be found in appendix A.3. If the lasers are tuned well and the mode locking is stable, it should be possible to achieve 800mW of 800nm pulses with a FWHM of 60nm at a rep-rate of 80MHz using $< 5W$ of 532nm pump laser power. After another pulse compression

step using a four pass single prism pulse compressor, the beam is ready to be sent to the THz optics.

In this photoconductive system, the 800nm pulses are used both to generate THz pulses through a dramatic down conversion, as well as to detect the THz pulses once they have interacted with a sample. A photoconductive THz "emitter" antenna is shown schematically in Figure 3.7a. It consists two parallel $5\mu m$ wide strips of gold patterned onto a *GaAs* substrate and positioned $80\mu m$ apart, forming a stripline antenna. A DC bias of $100V$ is applied across the antenna, resulting in an electric field from one side to the other. Ordinarily, the GaAs is insulating and no current traverses across the gap, but when a $800nm$ pulse is focused onto the GaAs, electrons are excited into the conduction band. The electric field then accerates these photocarriers across the gap, creating a time varying current density, $J(t)$, which generates far-field THz radiation.

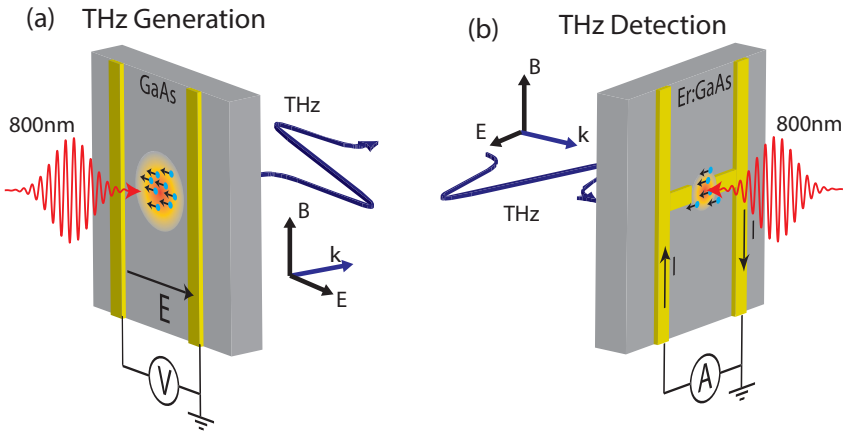

Figure 3.7: a) A schematic of the PC THz emitter with an incident 800nm pulse from the left and an emitted THz pulse to the right. The pulse is the result of the acceleration of charges in the illuminated area between the striplines. b) A schematic of the PC THz detector which operates similar to the emitter. An incident 800nm pulse from the right liberates charges on the GaAs while the electric field of THz pulse incident from the left accelerates them towards the antenna contacts, producing a current which is amplified and read.

The shape of the emitted THz pulse depend on a number of factors including the laser pulse duration, the bias, the the geometry of the stripline antenna, and crucially the properties and dynamics of the *GaAs*[17]. In this case, the 800nm pulse is only $2 \times 10^{-15} s$ in duration, while the

carrier lifetime of excited electrons in the undoped GaAs is closer to $1 \times 10^{-9}s$, far shorter and longer respectively than the desired timescale of $2 \times 10^{-12}s$. Instead, the characteristic timescale of the emitter is primarily determined by the geometry of the antenna. Approximating the antenna as a dipole of antenna, its characteristic frequency is given by:

$$f_{center} = \frac{c}{\lambda} = \frac{c}{2nL} \simeq 0.6THz. \tag{3.18}$$

where c is the speed of light in vaccuum, and λ is the desired wavelength in the GaAs medium, given by $\lambda = 2nL$ where $n = 3.4$ is the refractive index of GaAs, and $L = 80\mu m$ is the distance between the gold strips.

The detection of the THz waves is essentially the inverse of the emission Figure 3.7b. In much the same way, a 800nm pulse transiently excites a region of the GaAs, generating short-lived photocarriers. However, rather than being accelerated by an applied DC bias, the carriers are accelerated by the electric field of the THz pulse it's self. The charges travel to the antenna and generate a current which is measured directly. But there are some crucial differences between the emitter and detector antennas. The amplitude of the current depends on a convolution of the time-dependent photo-conductivity of the GaAs substrate and the THz electric field [38]:

$$J(\tau) \propto \int_{-\infty}^{\infty} E_{THz}(t)\sigma(t-\tau)dt \tag{3.19}$$

But as we have perviously mentioned, the carrier lifetime in undoped GaAs is $>> 1ps$ and thus our current would integrate out to zero! In order to avoid this problem and measure the instantaneous electric field, the detector antenna differs from the emitter antenna in two ways: First, the detector includes two bowtie-like strips which extend into the center of the excited reigon as shown in Figure 3.7b. This reduces the effective resistance of the antenna without significantly altering its impedance[80]. In doing so, the measured current signal is increased while the characteristic frequency of the antenna is unchanged. Second, a substrate with a far

shorter carrier lifetime is used. Though there are a number of ways to achieve ultra-short carrier lifetimes including low temperature grown GaAs[81] and radiation damaged Si[17], our PC system employs GaAs with Er-doped nanoislands[82]. These nanoislands reduce the carrier lifetimes so dramatically taht the time dependent conductivity can be well approximated as a delta function on the timescales relevant to the experiment $\sigma(t) \rightarrow \delta(t)$. With this substitution, equation 3.19 becomes:

$$J(\tau) \propto \int_{-\infty}^{\infty} E_{THz}(t)\delta(t-\tau)dt = E_{THz}(\tau) \tag{3.20}$$

And thus the current provides a direct linear measure of the instantaneous electric field of the THz pulse.

A partial schematic of the dual-mode PC THz-TDS system is shown in Figure 3.8a. Because it is particularly useful in metamaterial studies to be able to measure both reflection and transmission, this instrument was built in order to be capable of measuring both without modification. Switching between the two operating modes requires only the adjustment of a few parameters in the control software.

The femptosecond 800nm laser pulse is emitted by the $Ti:AlO_3$ laser oscillator. This beam is split into two, and one beam is directed to the THz emitter. The THz light generated by the emitter emitter and is aided in its coupling to free spcae by a small hemispherical silicon lens which is placed directly against the back side of the GaAs substrate. The interface between the GaAs emitter and the Si lens is well impednace matched in order to reduce reflections, and the curved hemispherical surface of the Si helps isotropically couple the THz radiation to free space. This THz light is collected by a large off-axis parabolic mirror (OAP) which collimates it, sending it through a large high resistivity silicon beam splitter and then to another OAPM. This OAP focuses the THz light onto a focal spot about 3mm in diameter on the sample. OAPs are used rather than lenses or other optics because they are non-dispersive, and create fewer abberations,

allowing for a smaller focal point. They are however significantly more difficult to align. Once the THz light interacts with the sample, some will be transmitted and some reflected. The Transmitted light propagates on to a symmetric pair of OAPs which focus it into the transmission detector. The reflected light reflected back along its incidence path, but half of it is split off by the Si beam splitter after collumnation, and sent into another OAP to be focused onto the reflection detector.

The other 800nm ”gate” beam acts as an ultrafast switch for the detectors. It is sent to a variable delay stage which translates back and fourth, adjusting the relative distance and with it the delay time between the pulses going to the emitter and the pulses going to the detectors. Next the gate beam is split into two again; one goes to the transmission detector and the other to a reflection detector. Because the detectors are only ”on” when the 800nm pulse illuminates them, a current will only be measured if the THz pulse is hitting the detector from the other side at exaclty the same time and furthermore, will only be sensitive to the instantaneous electric field of that THz pulse. By sequentially altering the delay stage position, and with it the time delay between the arrival of the THz pulse and the 800nm pulse at the detector, the waveform of the entire THz pulse can be mapped out, one time slice at a time.

In practice, there are several things to keep in mind. First, a pulse arrives at both the emitters and detectors 80 million times per second. With such frequent pulses, the current measured in the detectors is effectively a DC current; averaging the signal all of these pulses for a given delay time. Never the less, this current is very small. First, it must be amplified in a current amplifier. This amplified signal is then fed into a lock-in amplifier, which amplifies a signal which is modulated at an arbitrary frequency. In many ultrafast optical experiments, this modulation is performed by a mechanical chopper disk or an acousto optic modulator [citations?]. But in this case, we can simply apply a square wave voltage bias of the THz emitter whith a frequency on the order of 1KHz in order to modulate the emitted THz pulses. The lock-in can then amplify the components of the current signal that have the same modulation frequency, and separate the signal due to the THz pulse from the background, ultimately sending a constant voltage signal to

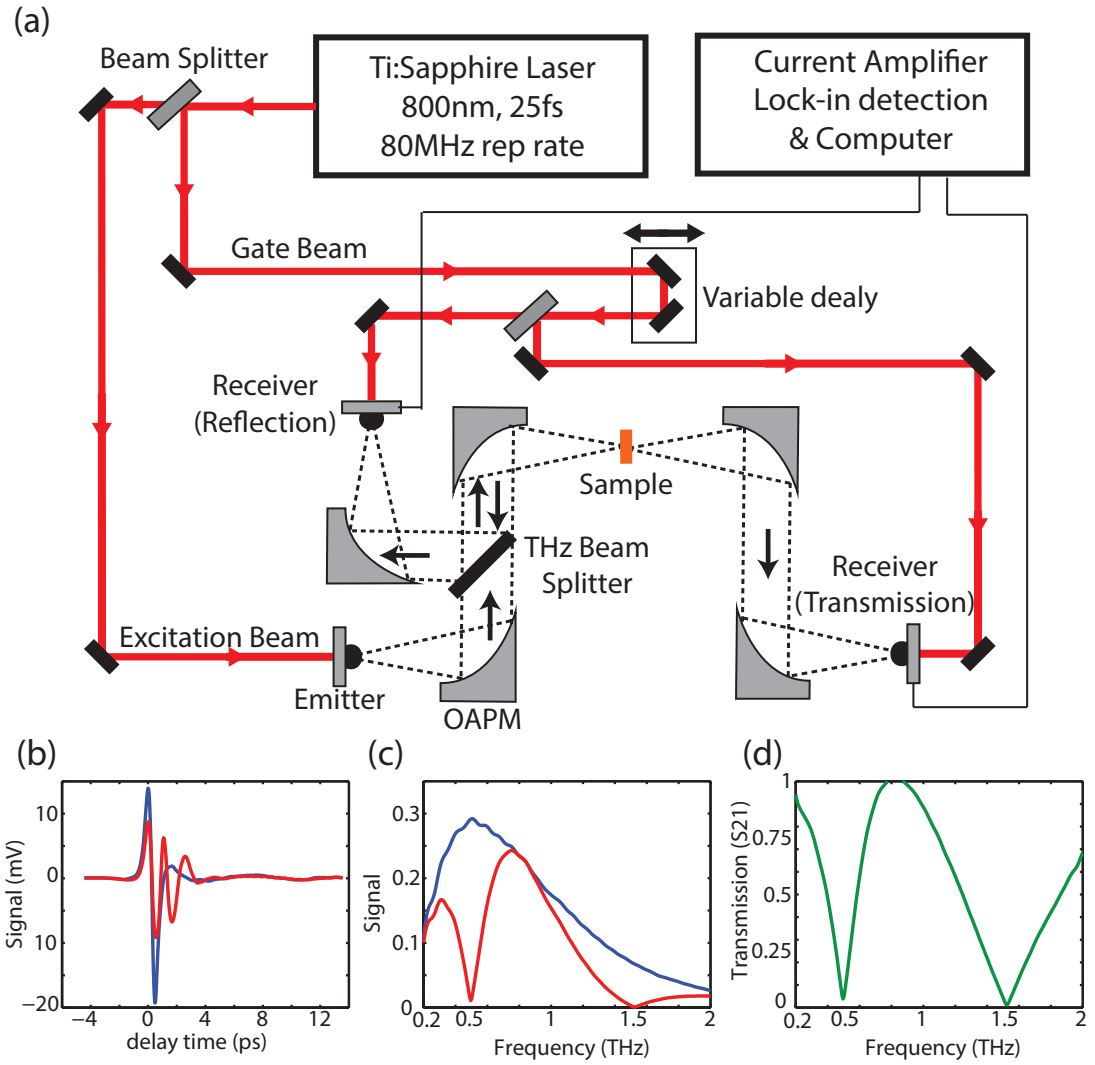

Figure 3.8: a) A schematic of the dual mode THz TDS. Short 800nm pulses from the $Ti:AlO_3$ laser are split into several paths. One goes to the PC THz emitter to generate THz light. The other goes to a delay stage which alter its flight time depending on its translation. These pulses then go to the PC THz detectors in order to excite them. The THz optics consist of 5 large parabolic mirrors which collect the light from the emitter and focus it onto a sample. Some is transmitted through and focused onto one detector, some is reflected back, partially split off by a Si beam splitter, adn focused onto another detector. b) The raw time domain signal as a function of delay time for a reference pulse (blue) and a sample pulse (red). c) The magnitude of the Fourrier transforms of the reference and sample pulses (phase not shown). d) The magnitude of the transmission (S21) calculated by normalizing the FD sample signal by the FD reference signal (phase not shown).

the computer. With a lock-in time constant of 0.3s, the signal is gathered for about 1s before the delay stage moves to a new position, and the signal for a different delay time is measured. More details on the instrument configuration can be found in appendix section A.7.1.

A measurement on the dual-mode PC THz-TDS is executed as follows: Before we can measure the effect of a sample on the THz pulse, we must know what the pulse its self looks like. This process is known as *referencing*. Typically, for a transmission experiment, the reference is nothing; the beam simply passes through the air and to the detector. But if for instance the sample has a substrate, whos effect it is desirable to remove, an identical substrate without the sample can be used as a reference instead. In a reflection experiment, air will not reflect any light back, so a gold mirror is typically used instead, and reflects nearly all of the incident light back towards the reflection detector (assuming the mirror is well aligned). First a time domain scan of the reference is performed (blue line Figure 3.8b). Then the sample is moved into the focus of the THz pulse and a time scan is performed of it as well (red line Figure 3.8b). Both of these time signal pulses are then Fourrier transformed yeilding a complex, frequency dependent signal. The magnitude for both the reference (red) and sample (blue) are shown in Figure 3.8c. Next the sample pulse is divided by the signal pulse in order to yield the complex transmission ($S21(f) = \frac{Signal(f)}{Reference(f)}$) shown in Figure 3.8d (magnitude only). In this manner, influence of the sample on the transmitted THz light can easily be discerned, in this case as evidenced by two strong resonant dips in reflectively at 0.5 and 1.5 THz.

This system is extremely well suited for linear THz-TDS measurements in both reflection and transmission. The extemely high repetition rate of the laser and resultant averaging over many pulses gives excellent dynamic range and low noise. The pulse to pulse consistency and (sometimes) reliability of the laser oscillator excitation source likewise contributes the sensitivity of the experiment while the PC THz generation and detection allow for measurements across a large spectral range. When well optimized, the system can reliably measure from 0.2THz-3THz with a signal to noise ratio of $\simeq 10,000$. Though reflection measurements are trickier, and 3/4ths

of the signal is lost on the two passes through the Si beam splitter, reflection measurements can be made with a similar fidelity. It is a workhorse system. That being said, the low pulse energies of 800nm oscillator pulses and by extension the THz pulses preclude the possibility of observing nonlineaer THz effects. For that, other ultrafast THz techniques are necessary.

3.3.2 High Field THz

Nonlinearities in physical systems are an extremely general concept which are of great interest in the scientific community but also a great utility, especially in ultrafast optics. We have already discussed how nonlinear processes contribute for instance to the frequency doubling in the $Nd:YVO_4$ diode pumped laser earlier in section 3.3.1 as well as to the Zeeman effect which is responsible for the mode locking in the $Ti:AlO_3$ oscillator laser. In an optical material, the electric polarization scales linearly with applied electric field by:

$$\vec{P}(t) = \chi_1 \vec{E}(t) + \chi_2 \vec{E}^2(t) + \chi_3 \vec{E}^3(t) + ... \tag{3.21}$$

Where χ_n are the first, second, third, etc. order electric susceptibility. In most materials, χ_1 is significantly larger than the other terms, and dominates the total response. But for a sufficiently large electric field, the terms which are higher order in E will eventually dominate, resulting in a host of optical phenomena. This includes the production of photons at twice the input frequency (second harmonic generation), or ones with the sum or difference of two incident light fields (sum and difference frequency generation), and optical parametric amplification to name a few [142]. These are interesting phenomena to study in their own right in metamaterials and other condensed matter systems as we will see in chapter 6. But materials with large nonlinear susceptibility can also be used to aid in the generation of the large THz fields that are neccessary to drive nonlinear effects in these samples in the first place.

In the context of high field THz generation, there are a number of methods and materials

including *ZnTe*[83], nonlinear organic crystals[84], and $LiNO_3$. Though our ultrafast lab employs all of these methods and others in various contexts, for our discussion here we will focus on $LiNO_3$ (lithium niobate), a large χ_2 material which is capable of producing extremely large THz fields through difference frequency mixing (DFG)[85]. $LiNO_3$ is a particularly useful material for high field THz generation because it is a common material used in the telecommunications industray and can readily be grown into large crystals. Beyond this, $LiNO_3$ has a large bandgap and a high damage threshold. This reduce two-photon effects and make it suitale for pumping with a high intensity beam.

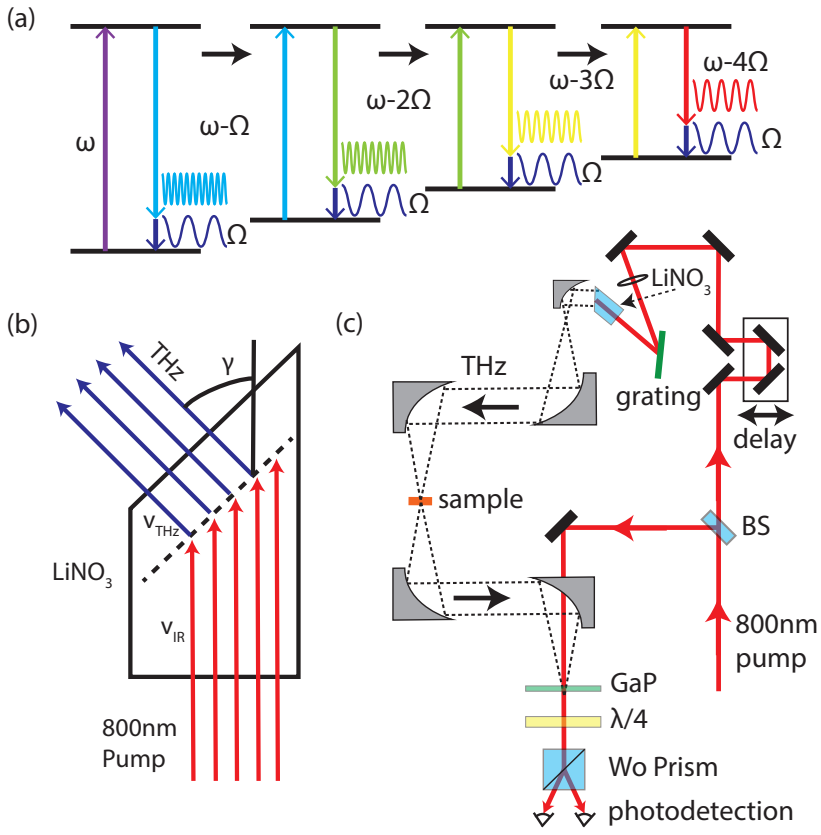

Figure 3.9: A schematic of the design principles of $LbNiO_3$ THz generation and detection. a) A schematic of the cascading multiphoton optical rectification process in $LbNiO_3$ b) The pulse front of the 800nm beam is tilted such that the generatd THz pulse leaves the slanted side of the crystal with a flat pulse front. c) A general chematic of a $LbNiO_3$ system including a delay line on the THz generation and a gate beam for detection.

$LiNO_3$ produces THz light through optical rectification, which can be considered a type

of intrapulse difference frequency generation (DFG) process. That is, rather than two separate pulses being mixed in a nonlinear crystal, two different frequency components of the same broadband pulse interact to produce a significantly lower energy photon. A single infrared photon at frequency ω can be down converted more than once ($\omega \rightarrow \omega - \Omega \rightarrow \omega - 2\Omega \rightarrow ...$) in order to generate multiple THz photons at frequency Ω (Seen schematically in Figure 3.9a). This repeated downconversion is called cascading, and is made possible by the relatively small frequency difference between the IR photons, which allows for phase-matching in each cycle. That being said, the phase velocity of the infrared photons in the $LiNO_3$ is considerably different than that of the generated THz light, and as a result a special technique called tilted pulse front pumping must be employed in order to sove this phase mismatch issue. The phase mismatch of the IR pump and THz light is given by:

$$\Delta k(\Omega) = \frac{\Omega}{c}[n(\Omega) - n_g(\omega_0)] \tag{3.22}$$

Where ω_0 is the center frequency of the IR pulse the refractive index at this frequency is $n_g(\omega_0) = 2.25$ and the THz refractive index is $n(\Omega) = 4.95$. In order to overcome this mismatch, the pulsefront of the IR pump beam is tilted by an optcial grating at an angle relative to its propagation direction given by $\cos\gamma = \frac{n_g(\omega_o)}{n(\Omega)}$. Due to this tilt, the effective propogation distance of the IR pulse is $1/\cos\gamma$ larger than the THz propogation distance, and the phase mismatch is modified and equation 3.22 becomes:

$$\Delta k(\Omega) = \frac{\Omega}{c}\left[n(\Omega) - \frac{n_g(\omega_0)}{\cos\gamma}\right] = 0 \tag{3.23}$$

. As a result, the THz pulse front in the $LiNO_3$ propogates at an angle relative to the incident IR pump pulse as shown in Figure 3.9b, in a manner that is reminiscent of Cherenkov radiation. If the crystal is cut at an the appropriate angle, the THz pulse will arrive at normal incidence at this face of the crystal and efficiently propogate out and into the THz optics. Though the

conversion efficiency of this process is relatively low at around 1%, use of high energy pump pulses can generate the massive THz fields required to facilitate nonlinear THz spectroscopy. A regeneratively amplified $Ti:AlO_3$ laser producing pulse energies of several mJ at a KHz reprate is easily capable of producing peak THz field strengths of 1MV/cm or higher [18][86][87].

Now that we have discussed how these high field THz pulses are generated, it is useful to talk about how they are actually utilized in an experiment. It is convenient to begin by applying them in a way we are already conceptually familiar with: THz-TDS. Just as with the photoconductive THz-TDS system in section 3.3.1, we need to generate THz pulses, focus them onto a sample, and then detect the reflected and/or transmitted light using a detector which is ”switched” by another ultrafast laser pulse on a variable time delay. Functionally, the only differences are the methods of generation and detection, which both warrant some discussion. Figure 3.9c shows a generic schematic for a nonlinear THz-TDS with $LiNO_3$ tilted pulse THz generation and electro optic sampling for detection.

An suitable laser source (such as a regenerative amplifier, noncolinear paratrically amplified or colinear parametrically amplified) generates ultrashort high-energy 800nm pulses. The beam is split, with one going to a varibale delay line and then to the THz generation crystal, while the other is sent to the detection apparatus. On the generation side, the laser is focused onto a diffraction grating. The angle of the grating is adjusted such that the 1st order diffracted pump beam will have the appropriate tilted pulse front. The beam then enters the trapezoidal $LiNO_3$ crystal at normal incidence and generates THz light through optical rectification. The high field THz beam propogates normally out of the angled face of the crystal and is collected by a small OAP, then collimated by a large OAP and focused on the sample by another OAP. Upon passing throught the sample, another OAP pair collimnates and focuses the THz beam onto an electro-optic crystal, in this case Gallium Phosphide (GaP). The gate beam is directed through a hole in the final OAP and onto the GaP detection crystal, colinear with the THz pulse.

The detection is accomplished by application of another nonlinear optical phenomenon.

The Pockels effect is a electro-optic (EO) effect in which the index of refraction of a medium is modified linearly in proportion to an applied electric field. This effect only occurs in non-centro symmetric crystals such as lithium niobate ($LiNbO_3$), lithium tantalate ($LiTaO_3$), potassium di-deuterium phosphate ($KD*P$), zinc telleride ($ZnTe$), β-barium borate (BBO) the same crystal used for second harmonic generation in the $Nd:YVO_4$ laser if you recall), gallium selenide (GaS) and in this case gallium phosphide (GaP) among others. The Pockels effect induced by the electric field of the THz pulse will modify the refractive index of the crystal differently along different axes. As the 800nm pulse passes through this medium, its different polarization components will experience a different path length and phase delay, resulting in a rotation of the polarization state. It should be noted that the choice of sampling crystal is important. Various crystals will perform better in some frequency ranges than others (ZnTe has a large EO coefficient but also a large absorption from a phonon in the around 2 THz). Thin crystals will have a smaller polarization rotation and thus give a smaller signal, and can introduce multiple etalon reflections to the signal, but because the THz pulse envelope varies little over the thickness of the crystal, give a more reliable measure of field strength. Thick crystals will give a larger polarization rotation and thus a larger signal, as well as pushing etalon reflections to longer times, but it will no longer be safe to assume that the THz field is constant across the entire crystal, and over-rotation of the gate pulse can be a problem for crystals with very large EO coefficients.

Once the polarization of the gate pulse has been rotated through its interactions with the THz pulse in the EO crystal, they are elliptically polarized by a quarter wave plate and sent through a Wollostan prism. The prism splits the beam into its two orthogonal polarization components and each goes into a different photodiode. When no THz pulse is present, the signal from both diodes is equal. Balanced photo detection subtracts the two signals, returning 0. But when a THz field is present, there will be a finite difference measured between the two signals which is directly proprotional to the THz field. As with PC THz-TDS, the delay stage scan through a time delay between the THz generation and gate beams to map out the THz pulse,

while a lock-in amplifier and a mechanical chopper are used to lock into the signal. A sequence of time domain spectroscopy measurements can be performed, each with a different THz field strength. When the THz fields become sufficiently high to drive nonlinear effects in the sample, the transmission or reflection spectrum will change accordingly.

3.3.3 Pump Probe

While nonlinear THz TDS can tell us how a sample responds to large THz fields as a function of frequency, it may also be desirable to know how the response of a sample to large light fields evolves over time as it recovers back to its equilibrium. This general class of techniques is called pump-probe, and is conceptually very similar to the techniques that have already been discussed. The basic principle goes as follows: a powerful pulse of light is focused onto the sample, which excites a change to some degree of freedom in the sample. Another much weaker pulse is then focused onto the sample to probe its transmission or reflection. By altering the time delay between these two pulses, the effect of the first powerful pulse can be traced out as a function of time, in much the same way as the gating is performed in TDS measurements. In fact, TDS can in some sense be thought of as a pump-probe measurement performed on the detection crystal.

If this sounds vague and general, that's because it is. If suitable laser sources are available, virtually any intensity, pulse duration, and light frequency of laser pulse can be used for either the pump or the probe. The choice of these parameters will give access to different optically accessible degrees of freedom in the sample, such as lattice, orbital, charge, or spin. In "degenerate" pump probe, the frequency of the pump and probe pulses are identical and generally the excitations being pumped are the same ones being probed. But in complex condensed matter systems, different degrees of freedom are often interconnected. By pumping at one frequency and probing at another, the interactions between these degrees of freedom can be investigated as a function of time (non-degenerate pump probe). Furthermore, a plethora of different measurement techniques

can be applied to the probe including Kerr or Faraday elipticity probe, transient grating, or Raman techniques among many others. It should be obvious that given the enormous array of choices for the pump beam, the probe beam, the measurement geometry, and/or detection scheme, etc. the combinatorics of different possible pump probe measurements are daunting.

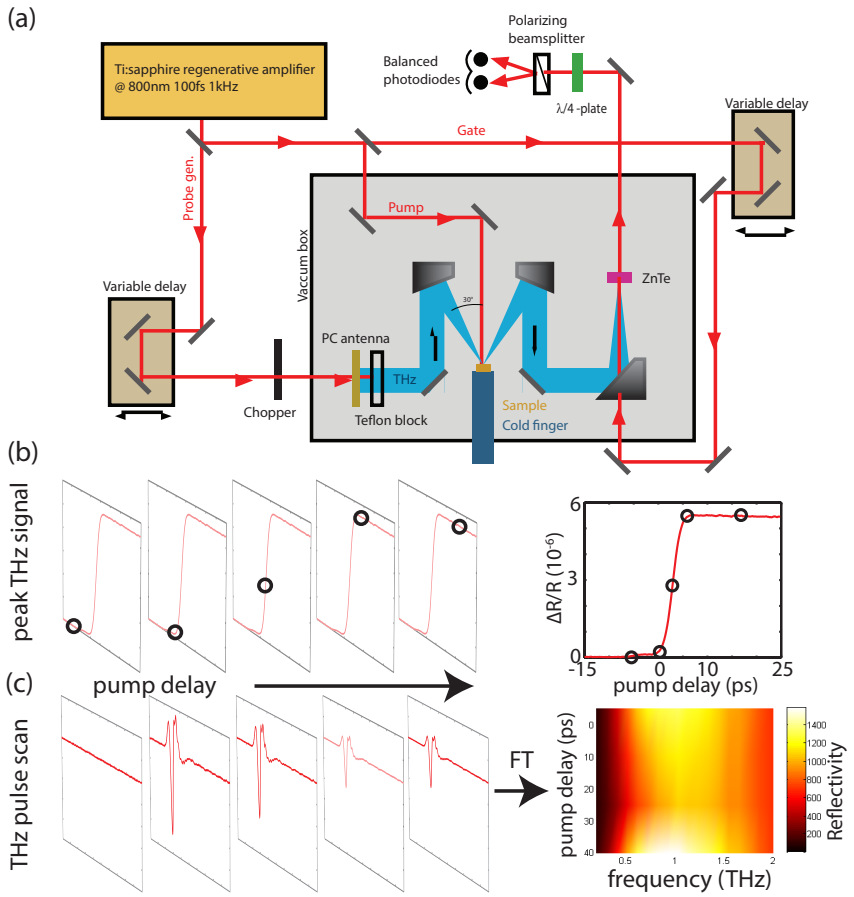

Figure 3.10: a) a schematic of a IR pump THz probe instrument in reflection geometry. Both the detection gate beam and THz generation beamlines have variable delay stages. b) Moving the delay stages in unison and measuring the peak of the THz pulse at various time delays produces a 1D pump probe scan. c) Scanning the gate pulse delay for each choice of pump delay maps out the THz pulse for each delay time, which can then be Fourrier transformed in a 2D pump probe scan.

As pump probe techniques will not factor heavily into this dissertation, we will briefly cover two illustrative examples of pump probe experiments, the first being 1 dimensional (1D) pump probe. Figure 3.10b shows a schematic for a instrument set up for 800nm IR pump and

THz probe. It is in a reflection geometry and uses different crystals for generation and detection of the THz beam, but otherwise is extremely similar in layout to the system discussed in section 3.3.2. The major change is the addition of a third 800nm beam, which hits the sample at normal incidence and has no delay stage. This is the pump beam. Before a 1D measurement, one delay stage is scanned until the peak of the reflected THz pulse is found. At this point, the gate delay and THz generation delay are held fixed relative to one another and the pump beam is introduced. By scanning both delay stages together, the delay between the fixed and the THz probe measurement can be altered in a similar fashion to THz TDS. At each delay time, the intensity of the peak of the THz pulse is measured (Figure 3.10b). Putting these measurements together the time evolution of the peak THz reflectively as a function of pump-probe delay can be mapped out. In these measurements, the ”reference” pulse is often simply the probe pulse measured in the absence of the pump. This has distinct advantages in that there is no possibility for drift or misalignment if the ”sample” and ”reference” are in fact the same surface, simply being measured at different times, enabling high sensativity measurements. The quantity commonly reported in 1D pump probe measurements is $\frac{\Delta R}{R} = \frac{R_{w/pump} - R_{w/opump}}{R_{w/opump}}$; that is the difference between the equilibrium reflectivity and the pumped reflectivity, normalized to the equilibrium reflectivity.

By allowing both delay stages to move freely, we can introduce another degree of freedom to this measurement in so called two dimensional (2D) pump probe. This technique is essentially performing THz TDS as described in section 3.3.1, but with the addition of a pump beam and with it another delay time that can be altered. As with 1D pump probe, a variable delay is introduced between the 800nm pump and THz probe pulses by the delay stage on the left side of Figure 3.10a. But at every step in the pump probe delay, the delay on the gate beam (right side Figure 3.10a) is scanned fully in order to measure the entire THz pulse, rather than just the peak of it. As with THz TDS, this THz wave form can be Fourrier transformed and normalized to a reference. The result is a series of reflectivity spectra, each measured at a different delay time relative to the pump, so that the dynamics of the pump induced changes to the reflectively spectra can be traced

out. The result is a 2D map representing reflectivity, with the pump-probe time delay on one axis, and frequency on the other (Figure 3.10c).

Pump probe is a diverse and powerful tool for measuring the time evolution of light induced perturbations to the electronic degrees of freedom in solid state systems. In addition to the characteristics of the light used for the pump and probe and detection method, additional parameters such as temperature and pump beam intensity (or "fluence") create an infinite parameter space to be explored for any given sample. For metamaterials, pump probe techniques are necessary for the study of samples which can be modified by optical excitation. For instance, the pump probe instrument described above was used for the measurements of the tunable silicon broadband absorber shown in Figure 2.14c and discussed in Section 2.3.2 and 2.3.3. Though the long lived photocarriers in the Si do not yield particularly interesting dynamics, THz TDS for short delay times for a variety of 800nm pump fluences in order to show the pump-induced absorption (Figure 2.15b).

But metamaterials can also be used as a tool for pump probe experiments due in particular to the ability to dramatically enhance and localize incident THz fields. For instance, the dramatic electric field enhancement of a SRR can be used to amplify the electric field of an incident THz pump beam[30][31]. Similarly, the magnetic field enhancement and bianisotropy of a metamaterial can be exploited, not only to enhance the incident magnetic fields, but also to rotate them relative to the incident polarization[88][89]. The far field properties can also be put to use. For instance, a metamaterial layer could be used as a band pass filter for a high field THz pump, allowing only the desired frequency components of the pump beam through to the sample[90][91]. I should emphasize here that though the technologies and concepts exist for metamaterial-enhanced pump probe experiments, this is a largely unexplored field which is ripe with opportunity. In the conclusion, I will discuss some future directions for this type of experiment.

This concludes the review sections of this dissertation. Hopefully by this point the basic

concepts of metamaterials as well as the depth and power of the scientific toolbox they provide is clear. Similarly, following our review of the numerical, fabrication, and measurement techniques which must come together for successful metamaterial study, I hope I have conveyed both the varied and collaborative efforts that are called upon as well as the serendipity of the co-evolution of the technologies which make it possible. In the chapters that follow, the concepts and methods presented earlier will be applied in three original studies of metamaterial systems. Each study will highlight different metamaterial design concepts, interacting condensed matter systems, and philosophies of use for hybrid metamaterial systems.

Chapter 4

Terahertz Metamaterial Perfect Absorber With A Continuously Tunable Air Spacer Layer

In this section we We present a comprehensive investigation of a continuously tunable metamaterial perfect absorber operating at terahertz frequencies. In particular, we investigate a three-layer absorber structure consisting of a layer of split ring resonators and a metallic ground plane, with a central layer consisting of a mechanically tunable air-spaced layer. The absorber was characterized using THz TDS in reflection (at normal incidence) as a function of spacer thickness from 0 to 1000μm. Our experimental measurements reveal the detailed evolution of the absorption bands as a function of spacing, in excellent agreement with analysis using interference theory and simulation. Our Fabry-Pérot-like structure provides an avenue for achieving massive tunability in metamaterial absorber devices and reveals extremely high quality factor absorptions. Before delving into the details of this experiment, it is useful to review some of the analytical theories which are used to describe MPAs, which factored heavily into the inspiration for this project.

4.1 Theories of Metamaterial Absorbers

Materials that exhibit near perfect absorption of electromagnetic (EM) waves are important for a wide variety of photonic applications including energy harvesting, communications, and chemical and biological sensing among others. Metamaterials have played a crucial role in the realization of perfect absorbers owing to their ability to be custom tailored to match the impedance of free space and thus minimize reflections as has been described previously in section 2.3.2. That being said, it is not necessarily obvious how these effective parameters are achieved, nor how the design of a MPA contributes to the realization of perfect absorption. To that end, there are a number of of theoretical tools which have been used to understand the working mechanism of MPAs.

One approach is one that has already been discussed, the effective medium theory (See section 2.2.1. From this perspective, the target effective medium parameters of a MPA are clear: impedance matching to free space (i.e. $\varepsilon = \mu$) in order to minimize reflections at the MPA surface, and high losses in order to dissipate the incident energy such that no light is transmitted. But the entire metamaterial is treated in a lump model with overall transmission and reflection coefficients. This theory dos not allow the contributions of different parts of the MPA to be disentangled, nor does it offer any insight into how a metamaterial must be designed or tweaked in order to achieve perfect absorption. If you have an MPA, this theory can tell you how it achieves perfect absorption in the language of homogeneous materials, but it will be of little help in getting to that MPA in the first place.

Similarly, coupled mode theory describes a system with lump parameters such as mode amplitudes, decay rates, and coupling coefficients[69], and can be used to describe a variety of systems from optical resonators[92], to waveguides[93], and metamaterials[94][95]. This theory reduces the metamaterial response to only three parameters: the resonant frequency ω_0, the radiative quality factor Q_r and the absorptive quality factor Q_a. Coupled mode theory shows that

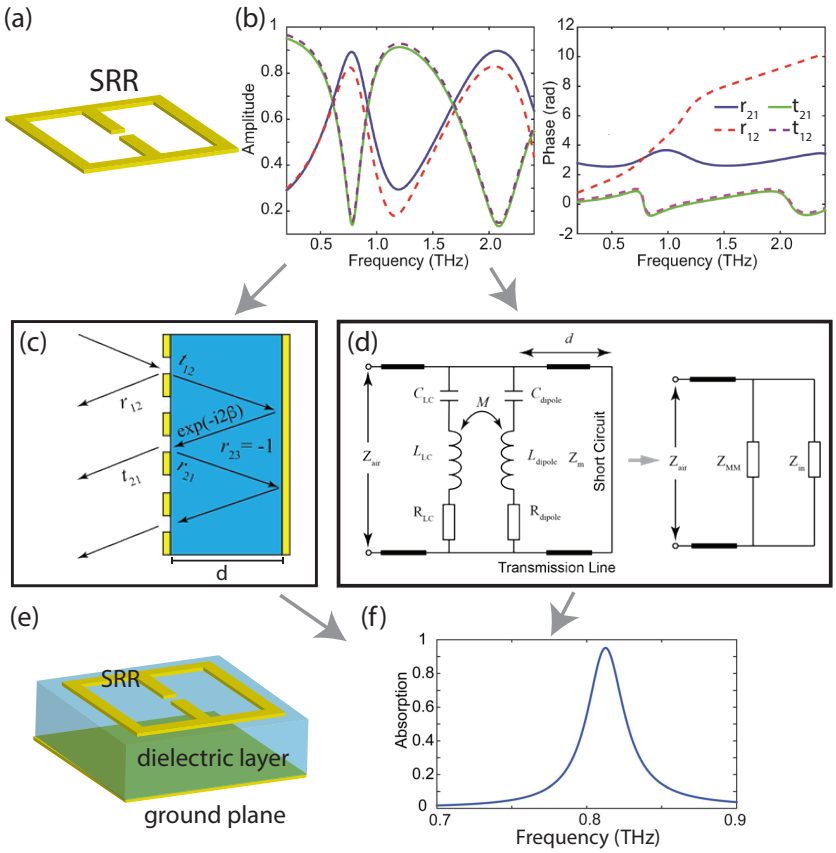

Figure 4.1: a) A unit cell of an isolated metamaterial layer (in this case a generic SRR) and b) its associated complex reflection and transmission coefficients[1]. c) a schematic of the interference theory of metamaterial absorbers where the total reflection is taken as the sum of multiple back reflected waves[MPA theory review]. d) a schematic of the transmission line theory approach to metamaterial absorbers where each resonance of the metamaterial layer is modeled as a serial RLC circuit, the dielectric layer as a transmission line of length d and the ground plane as a short circuit [MPA theory review]. Both the complex reflection and transmission of the metamaterial layer can be applied with either approach in order to predict the behavior once a dielectric layer of thickness d and a metallic ground plane is introduced e). f) the resulting calculated absorption[73].

the condition for perfect absorption is $Q_r = Q_a$, allowing the MPA to be viewed in the language of energy and loss rates. But as with effective medium theory, the parameters are usually retrieved from simulated or tested spectra as lump parameters, and in doing so, the ability to connect characteristics of the metamaterial to the absorption is diminished.

There are other techniques that are of more practical utility for designing MPAs, and are particularly well suited to the common three layer MPA format consisting of a metmaterial

layer, a dielectric spacer, and a metallic ground plane. Transmission line theory exploits the scalability of electromagnetic theory, and seeks to approximate metmaterials in a way which is farmiliar to engineers; the transmission line model [96][97]. In this theory, the each resonance of the metamaterial layer is modeled with a serially connected resistance, capacitance, and inductance. Figure 4.1d shows such an approach for a SRR, including the contributions from both the LC resonance and the Dipole resonance with a coupling term connecting the two. Generally, these parameters are determined by fitting simulated or measured scattering parameters of the metamaterial layer. The impedance of this layer can then be expressed analytically as[98]:

$$Z_{LC,dipole} = R_{LC,dipole} + \frac{2\varepsilon_i}{\omega C_{LC,dipole}(\varepsilon_r+1)^2} + j\omega L_{LC,dipole} + \frac{2}{j\omega C_{LC,dipole}(\varepsilon_r+1)} \tag{4.1}$$

Where $R_{LC,dipole}$, $C_{LC,dipole}$, and $L_{LC,dipole}$ are retrieved from a simulation or measurement of a freestanding metamaterial layer (without the spacer material), and $\varepsilon_d = \varepsilon_r + i\varepsilon_i$ is the complex permittivity of the spacer layer. This consideration of the effects of the spacer layer dielectric properties on the resonances of the metamaterial layer its self are a substantial part of the power of the transmission line theory. The dielectric layer is modeled as a transmission line with length d equal to the thickness of the spacer layer and a characteristic impedance $Z_m = \sqrt{\frac{\mu_d}{\varepsilon_d}}$. Together with the ground plane which is modeled with a short circuit, the impedance of the dielectric layer and ground plane are given by:

$$Z_{in} = jZ_m \tan k_0 d\sqrt{\varepsilon_d \mu_d} \tag{4.2}$$

Where k_0 is the free space wavenumber. The overall impedance of the MPA is then given by

$$Z_{MPA} = \frac{Z_{MM}Z_{in}}{Z_{MM}+Z_{in}} \tag{4.3}$$

The condition for perfect absorption is $Z_{MPA} = Z_{vacuum}$. This approach allows the contribution

of the metamaterial layer to be separated from that of the transmission line and ground plane. Likewise, it shows both intuitively and precisely how the dielectric environment of the spacer layer effects the resonances of the metamaterial due in particular to the shift in the effective capacitance of the metamaterial due to the introduction of a dielectric. However, this theory still does not lend itself to a simple and intuitive mathematical expression of the influence of various parameters on the total absorption characteristics of the MPA.

4.1.1 Interference Theory of Metamaterial Absorbers

Where other analytical theories of metamaterial absorbers fall short, the interference theory of metamaterial absorbers particularly useful for characterizing three layer MPAs and served as the primary inspiration for the variable air spacer metamaterial absorber. In the interference theory of MPAs, the total reflection from a three layer metamaterial can be modeled as a superposition of light which is reflected initially from the metamaterial surface, as well as light internally reflected in the dielectric spacer and later transmitted back through the metamaterial layer[99]. This is shown schematically in Figure 4.1a. Delineating the air as region 1 and the dielectric layer as region 2, the light is initially reflected with an amplitude and phase shift given by $\tilde{r}_{12} = r_{12}e^{i\phi_{12}}$ while the transmitted light has amplitude and phase given by $\tilde{t}_{12} = t_{12}e^{i\theta_{12}}$. The transmitted light travels through the spacer layer accumulating a propagation phase of $\tilde{\beta} = \sqrt{\varepsilon_d}k_0 d$, where as before, ε_d is the spacer complex permittivity, d is the spacer layer thickness, and k_0 is the freespace wavenumber. At the ground plane this light will be totally reflected (i.e. $\tilde{r} = -1$), and the light will again accumulate another phase change of $\tilde{\beta}$ as it propagates back through the spacer layer. Partial reflection and transmission at the air-metamaterial interface occurs again, with complex coefficients $\tilde{r}_{21}$ and $\tilde{t}_{21}$ respectively. These partial internal reflections and transmissions repeat ad infinitum, but in taking the sum of all of the reflected rays, a simple geometric series

emerges:

$$\tilde{r}_{tot} = \tilde{r}_{12} + (-1)\tilde{t}_{12}\tilde{t}_{21}e^{i2\tilde{\beta}} + (-1)^2\tilde{t}_{12}\tilde{t}_{21}\tilde{r}_{21}e^{i4\tilde{\beta}} + ... \tag{4.4}$$

$$= \tilde{r}_{12} - \tilde{t}_{12}\tilde{t}_{21}e^{i2\tilde{\beta}}\sum_{n=0}^{\infty}(-\tilde{r}_{21}e^{i2\tilde{\beta}})^k \tag{4.5}$$

$$= \tilde{r}_{12} - \frac{\tilde{t}_{12}\tilde{t}_{21}e^{i2\tilde{\beta}}}{1+\tilde{r}_{21}e^{i2\tilde{\beta}}} = r \tag{4.6}$$

Thus the total reflection can be easily expressed in terms of the behavior of the isolated metamaterial layer, and the thickness and dielectric properties of the spacer layer using equation 4.6. Given that there is no transmission through the ground plane, the absorption can be easily calculated as $A = 1 - |r|^2$. Two crucial limitations should be noted at this point. First, as with the other MPA theories, the complex reflection and transmission coefficeints for the metamaterial layer ($\tilde{r}_{12}$, $\tilde{r}_{21}$, $\tilde{r}_{12}$, and $\tilde{t}_{21}$) must be retrieved from simulations or measurements. Furthermore, once retrieved the effects of the ground dielectric spacer permittivity on the properties of the metamaterial layer are not accounted for. In order to account for this, the transmission line theory discussed previously in section 4.1 can be employed as follows: the freestanding metamaterial layer properties are simulated and fit to the transmission line model. These values are plugged into equation 4.1, where an arbitrary spacer permittivity ε_d can be applied, and the modified impedance can be used to calculate new values of the complex transmission and reflection of the metamaterial layer. Finally these coefficients can be plugged into equation 4.6 in order to calculate the total reflection for the MPA. Thus, using the two theories in concert, a single set of simulated coefficients can be used to calculate the absorption from an absorber with arbitrary spacer permittivity and thickness.

The conditions which result in a perfect absorption are discussed in detail in [98]. Both the critical spacer thickness and the corresponding frequency of the absorption peak can be identified analytically. This result shows that for a given spacer thickness, the frequency of the perfect absorption will decrease dramatically as the real part of the ε_d is increased. For an increase in the imaginary part of ε_d, the perfect absorption frequency will likewise decrease, though this effect is

far more subtle.

But the interference theory of metamaterial absorbers can be taken further in order to determine the spacer thicknesses which yield a maximum absorption at any given frequency. Though I will avoid performing the lengthy derivation here, it can be found in detail in the appendix of [1]. In short, this derivation seeks to set $\frac{\partial r}{\partial d} = 0$ and in doing so determine the values of spacer thickness d which result in a maximum or minimum in the total MPA reflection. Ultimately, these values of the spacer layer thickness are given by:

$$d_0 = \frac{\arctan\left(\frac{a-\frac{n_r}{n_i}b+exp(2\pi m\frac{n_i}{n_r})}{b+\frac{n_r}{n_i}a}\right)}{2n_r k} + \frac{m\pi}{n_r k} \tag{4.7}$$

where $n_d = n_r + in_i$ is the complex refractive index of the spacer layer, and $\tilde{r}_{21} = a + ib$ is the complex reflectivity of the metamaterial layer. m is an integer starting from zero. This means that for any given frequency, another absorption band will emerge for each time the spacer layer thickness reaches an multiple of $\frac{pi}{n_r k}$. These multiple solutions will of course arise at all frequencies, resulting in a series of "m-curves"; analytically derived curves which track the points of maximum absorption as a function of frequency and spacer thickness (Figure 4.1).

Clearly, the interference theory of metamaterial absorbers is a powerful analytical tool for the analysis and understanding of three layer MPAs and in particular for characterizing the evolution of absorption bands as a function of spacer layer thickness and or permittivity. It will be invaluable in the following sections in which we examine a three layer MPA which has a continuously tunable spacer layer.

4.2 Intoduction

While MPAs are generally used in the limit of thin spacer layers ($d << \lambda$), we have just alluded to the rich development of absorption resonances occurs with the increasing spacer layer

thickness[1], providing a potential route to tune the absorption with high precision. However, MPAs usually operate at distinct dielectric spacer layer thicknesses, limiting the tunability and making a detailed comparison with theory difficult.

We have overcome this limitation by creating a three layer MPA operating at the THz frequencies ranging from $\sim$0.1 to 2.0 THz. Our Fabry-Pèrot-like device has two components: a gold ground plane and a MM layer consisting of split ring resonators (SRRs) on a thin silicon nitride (SiN_x) membrane. The two layers are separated with a central layer of air with a mechanically tunable thickness ranging from 0 to 1000μm. Using the photo-conductive THz-TDS[100], we have performed detailed measurements of the electromagnetic response as a function of spacer layer thickness. The results are compared with interference theory based simulations that, in conjunction with the analytical results, provide a comprehensive description of our tunable MPA.

The variable air spacer MPA (VAS-MPA) consists of three components: a gold-coated wafer as the metallic ground plane, a stepper motor linear translation stage, and a free-standing MM layer (Figure 4.2). The ground plane is a silicon wafer coated with a 200nm thick gold layer, held in a holder at a fixed location. A free standing SRR/SiN_x layer is held parallel to the ground plane and attached to a stepper motor translation stage which translates the MM layer to control the air spacer layer thickness, which can be adjusted to arbitrary thicknesses with a precision of 0.7μm. The free-standing MM layer was fabricated using micromachining techniques as was described in detail previously in our discussion of photolithography in section 3.2.1. As before, we starting with a double-sided silicon wafer coated with 400 nm thick SiN_x thin films. Photolithography and e-beam evaporation were utilized to fabricate the 200 nm thick gold SRRs on top of the substrate. Subsequently, the SiNx thin film on the backside was patterned into a 10×10mm window using photolithography followed by reactive ion etching. Finally, KOH wet etching was employed to completely remove the bulk silicon in the window region, leaving only the top SiNx thin film with patterned SRRs.

We the home-built, dual mode THz-TDS system described previously in section 3.3.1

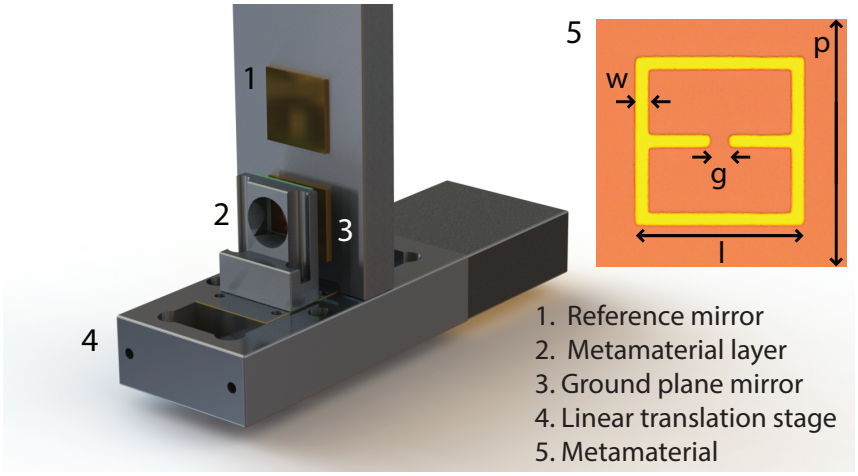

Figure 4.2: Schematic of VAS-MPA. The SRR/SiN_x layer is parallel to the ground plane mirror and can be translated with high precision to create a spacer of arbitrary thickness. (Inset) A microscopy image of a single MM unit cell, where $p = 120\mu m$, $l = 110\mu m$, $w = 5\mu m$, and $g = 8\mu m$.

to measure the complex reflection and transmission coefficients of the isolated SRR/SiN_x and VAS-MPA[101]. A titanium sapphire laser generates 800nm, 20fs pulses at a repetition rate of 80MHz, which is used to generate and detect the THz pulses using photoconductive antennas. The THz pulses impinge on the sample at normal incidence, and both transmission and reflection can be measured. For the transmission measurements of the isolated SRR/SiNx layer, the transmitted pulse is compared with a reference pulse transmitted though air. For the reflection measurements of both the SRR/SiNx layer and the VAS-MPA, the reflected pulse is compared with a reference pulse which is nearly perfectly reflected by a gold-coated silicon substrate. The time domain sample and reference pulses are Fourier transformed to obtain the frequency domain transmission and reflection spectra.

In order to characterize the evolution of the absorption spectrum of the VAS-MPA with the spacer layer thickness, we first measure the electromagnetic response of the isolated SRR/SiNx layer. Figure 4.3 shows the complex reflection ($\tilde{r}_{21} \simeq \tilde{r}_{12} = r_{MM}$) and transmission ($\tilde{t}_{21} = \tilde{t}_{12} = r_{MM}$) coefficients (amplitude and phase) of the SRR/SiN_x layer. Unlike in our previous discussion of the interference theory in section 4.1.1, here there is no need to distinguish between

the direction of the wave propogating through the MM layer. The transmission coefficients will be strictly identical and the reflection coefficients will be effectively identical due to the extremely thin SRR/SiN_x. The two lowest frequency resonant modes of the isolated SRR/SiN_x layer appear as minima in the transmission and maxima in the reflection. The fundamental inductor-capacitor (LC) resonance is at 0.5 THz, and the dipole resonance is at 1.5 THz. These results are verified by replicating the experiment numerically using the finite element method frequency domain (FEMFD) solver CST Microwave Studio 2016 (solid lines). For the simulations, we construct a unit cell geometry of the SRR/SiN_x where gold is modeled as a lossy metal with a conductivity of 4.56×10^7 S/m and SiN_x is modeled as a lossy dielectric with a relative permittivity of $\varepsilon = 7.6(1 + 0.0053i)$[102]. Periodic boundary conditions are employed plane wave pulse at normal incidence in order to retrieve the complex scattering parameters $S_{11} = r_{MM}$ and $S_{21} = S_{12} = t_{MM}$ as described in detail in section 3.1. The simulation results are plotted in Figure 4.3, revealing excellent agreement with the experiment. These results can be used in conjunction with interference theory to model the absorption of the VAS-MPA as a function of the air spacer thickness.

Recall from section 4.1.1 that the overall reflection can be accurately calculated as the superposition of multiple reflections[99]:

$$r = r_{MM} - \frac{t_{MM}^2}{r_{MM} + e^{-i2\beta}} \tag{4.8}$$

Where we have simplified equation 4.6 slightly using the above substitutions. Furthermore, here the spacer layer is air ($n = \varepsilon = 1$) so $\beta = kd$ is the one-way phase delay across the spacer, k is the wave numebr in vacuum, and r_{MM} and t_{MM} are the complex reflection and transmission coefficients of the isolated SRR/SiN_x layer as presented in Figure 4.3. In addition, the air spacer layer does not result in any capacitence shift of the resonant properties of the MM layer, and it is not neccessary to use tranmission line theory to adjust the complex reflection and transmission

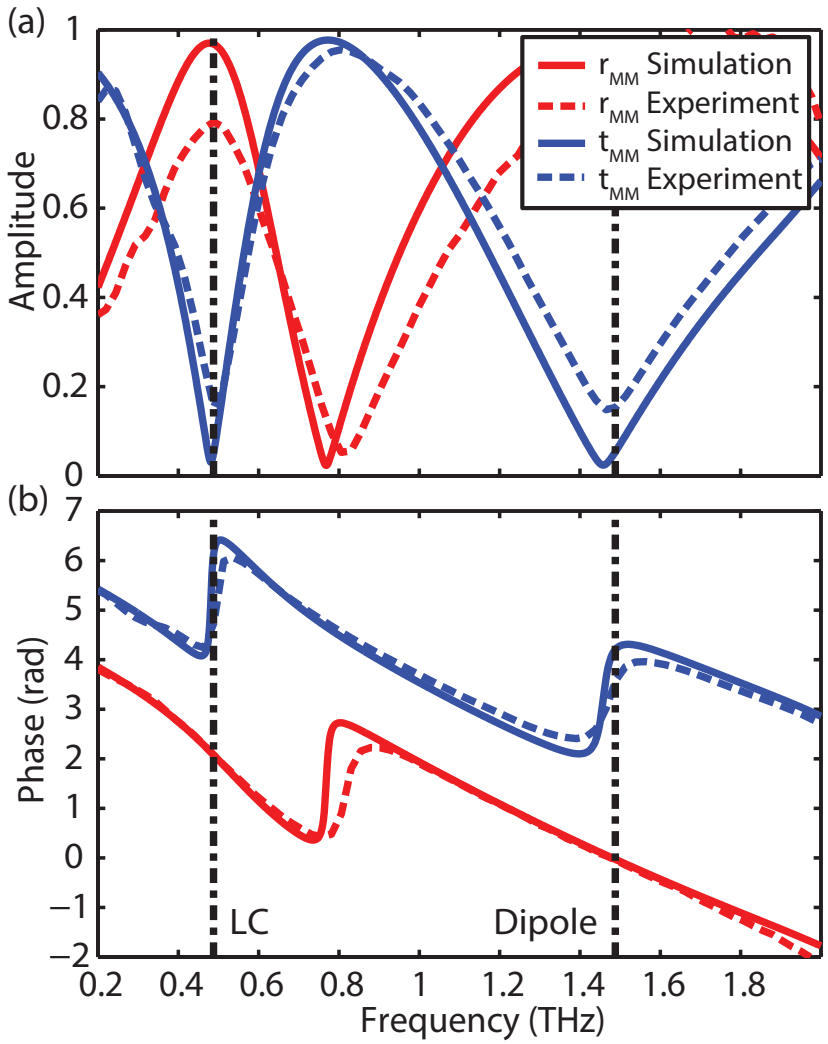

Figure 4.3: The magnitude a) and phase b) of the transmission (blue) and reflection (red) coefficients for the isolated MM layer (i.e., in the absence of a ground plane). The dashed and solid lines correspond to the experimental measurement and numerical simulation results, respectively. The LC resonance (0.5 THz) and dipole resonance (1.5 THz) frequencies are marked with vertical dashed lines, corresponding to minima in transmission and maxima in reflection.

coeffients of the MM layer. Due to the presence of the metallic ground plane, the transmission channel of the absorber is entirely suppressed and the absorption can be calculated as $A = 1 - |r|^2$. As in our previous discussion of the interference theory, this equation can be inverted and optimized in order to derive the spacer thickness that yields the maximum absorption at a given frequency [1]. Thankfully, in this situation, due to the air spacer layer, $n_i = 0$ and $n = 1$ which

leads to a considerable simplifications. Equation 4.7 simplifies to:

$$d_m = d_0 = -\frac{\theta}{2k} + \frac{m\pi}{k} \tag{4.9}$$

Where θ is the phase of r_{MM}. This expression shows that, at a given frequency, multiple absorption maxima arise, associated with phase accumulations within the spacer layer which are integer multiples of 2π as in a traditional Fabry-Pérot cavity. Remarkably, this derivation demonstrates that the value of t_{MM} does not contribute to determining the values of d_m [see Equations (6)(9) in Reference [1]. We emphasize, however, that for determining frequencies and spacer thicknesses which yield perfect absorption, t_{MM} is relevant.

4.3 Results

Figure 4.4a shows a color map of the measured THz-TDS absorption spectra of the VAS-MPA in reflection at normal incidence for different values of air spacer thickness d with a constant background subtracted to account for imperfect referencing. We start with a separation of one millimeter between the SRR/SiN_x layer and the ground plane, measure the absorption spectrum, and then sequentially repeat the measurement, with the SRR/SiN_x layer translated closer to the ground plane with each subsequent measurement, until the two are in direct contact. The decrement of spacer layer thickness d between measurements is $15\mu m$ for $1000\mu m > d > 500\mu m$ and $5\mu m$ for $500\mu m > d > 0\mu m$. To validate this result, Eq. 4.8 is used in conjunction with the simulated reflection and transmission of the SRR/SiN_x layer to calculate the complex absorption of the VAS-MPA as a function of air spacer thickness d between 0 and $1mm$ (Figure 4.4b). In Figure 4.4a and 4.4b, the LC and dipole resonant frequencies of the isolated SRR/SiN_x layer are indicated with vertical dashed lines, around which absorption is suppressed due to the strong reflection and weak transmission at the SRR/SiN_x layer. In the limit of zero spacer thickness, the absorption bands approach the LC and dipole resonance frequencies of the SRR/SiN_x layer.

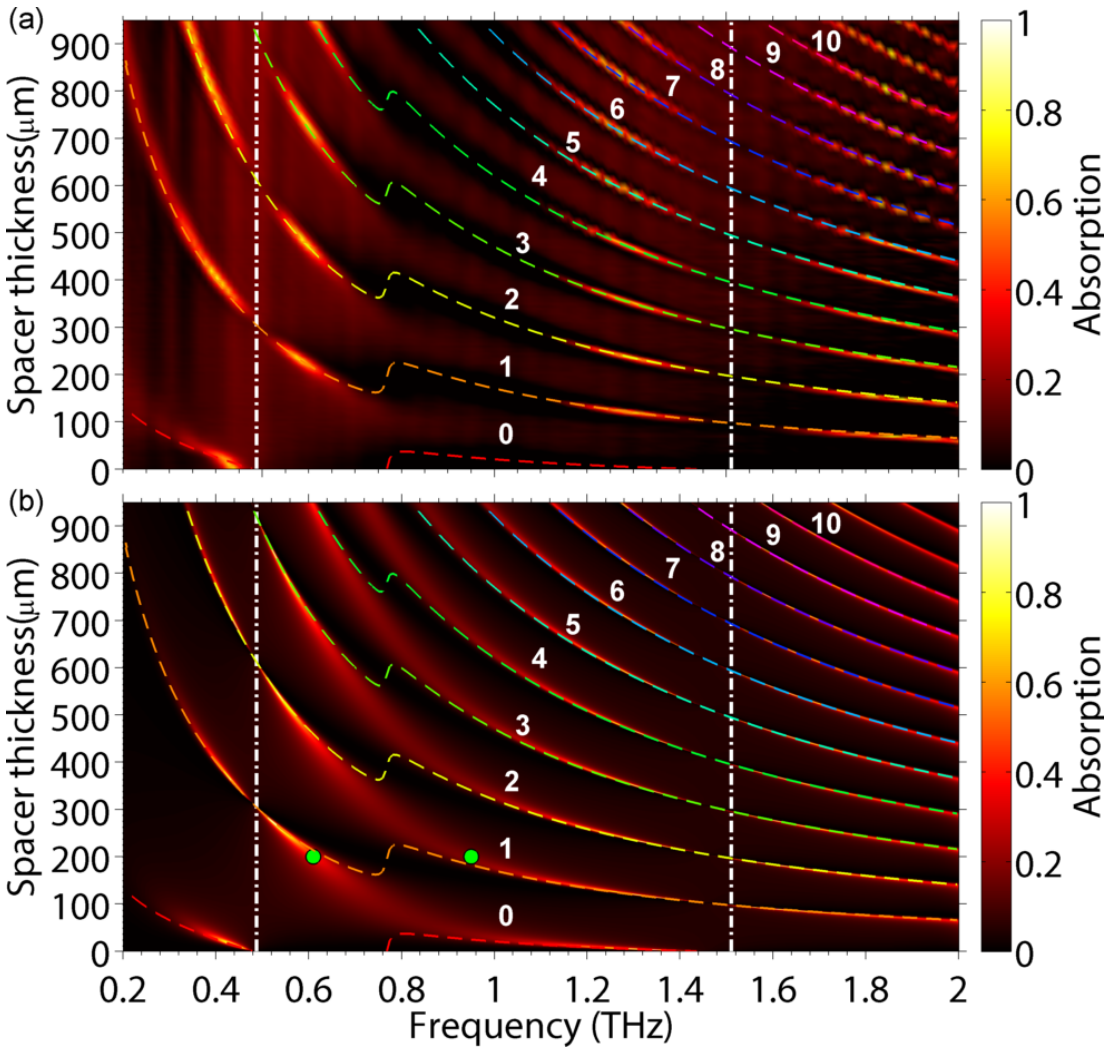

Figure 4.4: Absorption spectra as a function of spacer layer thickness from a) experimental THz-TDS reflection measurements and b) interference theory. The LC and dipole resonance frequencies of the isolated MM layer (i.e., see Figure 4.3) are marked with vertical dashed white lines, where absorption is strongly suppressed due to the large reflection from the SRR/SiN_x. The *m*-curves and their associated value of m are marked with colored dashed lines. The green dots refer to the discussion associated with Figure 4.6.

As the air spacer thickness increases from zero, there is a dramatic redshift in both absorption bands, and additional bands emerge at higher frequencies. The emergence of these bands can be understood as a result of the phase delay within the spacer layer approaching integer multiples of 2π. Using Eq. 4.9, we can identify the air spacer thicknesses, that result in an absorption band. The result is a series of m-curves, shown with colored dashed lines in Figure 4.4a and 4.4b. Each

is associated with a different integer value of m (shown) and thus $2m\pi$ phase accumulations within the spacer layer. The m-curves show excellent agreement with the analytical and experimental results.

Figure 4.5 compares the analytical [i.e., Eq. 4.8] (dashed blue lines), experimental (orange lines), and FEMFD simulated (dotted purple lines) absorption spectra for several choices of spacer layer thicknesses. Each absorption band is labeled with the value of its corresponding m-curve (determined by examining the relevant horizontal cross-sections of Figure 4.4). When $d = 74\mu m < k/4$ (Figure 4.5a), the spacer layer thickness and thus the entire unit cell are of deeply subwavelength corresponding to the metamaterial regime. The absorption bands associated with the 0th and 1st m-curve are visible. As the spacer layer thickness increases, absorption peaks associated with larger values of m begin to emerge. In this regime, very good agreement between the simulation, experimental, and interference theory results is apparent for each of the absorption bands. At $d = 730\mu m$ (Figure 4.5d), absorption peaks associated with m-curves 1 through 8 are all visible. The absorption peak amplitude is largest when the spacer layer is optimized for complete destructive interference of the reflected light for a specific frequency, but this condition is highly sensitive to the spacer thickness d; so, many of the peaks are well below unity absorption. For all spacer thicknesses, all three results (interference theory, FEMFD simulations, and experiment) show very good agreement. The experimental results show consistently smaller absorption amplitudes, not only due in part to imperfect referencing but also owing to the limited frequency resolution, which is evident for the narrowest absorption bands in particular. The other striking discrepancy between simulation, experiment, and interference theory occurs in the vicinity of 0.75 THz. Both the interference theory and the simulations show peaks which are more prominent relative to the experimental data. These peaks lie in a region where the phase of the reflection h in Eq. 4.9 rapidly increases by $\sim pi$, and the m-curves all increase by $\frac{p}{2k}$ accordingly. As such, interference theory is sensitive to any discrepancy in the input parameters, in particular those related to losses in SiN_x and Au. As a result, peaks occur without any clear correspondence to one

of the *m*-curves.

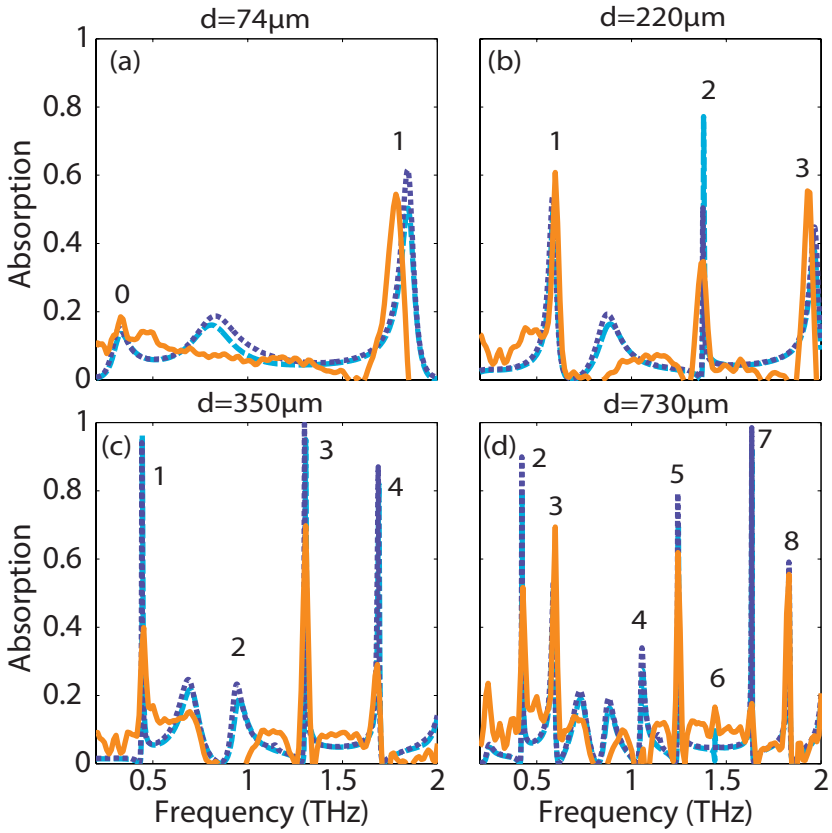

Figure 4.5: Absorption spectra at several spacer layer thicknesses from interference theory calculations (dashed blue lines), experiments (solid orange lines), and FEMFD simulations (dotted purple lines). The value of the corresponding m-curve is noted for each peak.

4.4 Discussion

In addition to the high degree of tunability and resulting emergence of multiple absorption bands, the dielectric properties of the air spacer also play an important role in the observed absorption characteristics. Whereas any ordinary dielectric layer has a real permitivity $\varepsilon_r > 1$ and a finite imaginary part ($\varepsilon_i > 0$) indicating losses, in this case $\varepsilon = 1$ and is entirely real and thus entirely lossless. This has profound consequences for both the mechanism and the characteristics of the absorption[73]. Already we have seen that the application of the interference theory is

dramatically simplified by as well as the resulting expressions for the total reflection and the critical spacer thicknesses in equation 4.8 and 4.9 respectively. But it is important to consider the physical ramifications as well. Most obvious is that whereas in an ordinary three layer MPA, losses in the dielectric layer contribute to the absorption of incident light, here no such absorption occurs. Essentially 100% of the absorbed light is absorbed by ohmic lossess in the metals of the *SRR* layer and ground plane. Furthermore the absence of any material in the spacer layer means this space is available to be filled with gaseous or liquid species. In doing so, the dielectric environment of the spacer layer would be altered, in turn changing the observed absorption spectra. This approach can be employed as a highly sensitive probe in order to detect gasses, chemical, or biological. species[103][104][15]. Furthermore, the lossless dielectric layer reduces the linewidth of the absorption peaks in general. Compared to an ordinary three-layer absorber, the Q-factor of a air-spacer MPA is larger by a factor of $\simeq$2, owing to the reduction absence of dielectric losses[73]. This enhances the sensitivity for the aforementioned applications, but is worth investigating fully in its own right.

To that end we have also investigated the dependence of the absorption peak linewidth on the spacer layer thickness. In Figure 4.6, the Q-factor of the absorption peaks is obtained from the interference theory result and plotted as a function of spacer layer thickness d for a number of different m-curves, with each value of m indicated with a different color (as shown by the dashed lines in Figure 4.4. We define the quality factor as $Q = f_a/\Delta f_a$, where f_a is the frequency of the absorption maxima and Δf_a is the full width at half maximum of the resonance, although it should be noted that many of the absorption peaks, particularly at larger values of d, are highly asymmetric. Likewise, note that the frequency of the absorption bands for a given value of m is inversely related to the spacer thickness d (see Figure 4.4).

For absorption bands along each m-curve, a similar pattern emerges. It is therefore instructive to examine the Q-factor associated with $m = 1$ (orange dots) in detail, as this description can be generalized to all other values of m. The $m = 1$ curve first appears at $d = 70\mu m$ and $Q = 15$

in Figure 4.6, corresponding to the band emerging at 2 THz which is marked with an orange dashed line in Figure 4.4. As d increases, the Q-factor reaches a maximum value of $Q = 115$ at $d = 95\mu m$. This corresponds to the m-curve crossing f_{dipole}. The Q-factor then decreases and vanishes as the absorption bands become indeterminate, corresponding to the previously mentioned jump in the m-curves. The band reemerges at $d = 200\mu m$ and $Q = 9$. A similar behavior follows as a function of increasing d; the Q-factor first increases to a maximum of $Q = 99$ at $d = 296\mu m$ (this time corresponding to the m-curve crossing f_{LC}), and then decreases and vanishes.

The m-curves are multi-valued as a function of d due to the previously discussed jump in the m-curves at $\sim$0.75 THz. As a result, multiple Q factor values can occur for a single value of d and m. In the case of $m = 1$, at $d = 200\mu m$, both branches of the m-curve have the same value of Q (see the black square in Figure 4.6), but these absorption bands are distinct and occur at different frequencies (see the green dots in Figure 4.4b). For all m-curves, there is generally a low-Q branch associated with lower frequencies and larger values of d and conversely a high-Q, high-frequency, low-d branch. Overall, the Q-factor increases with the values of m, reaching Q factors in excess of 400 for $m = 710$. We note that when the peaks become this narrow, the spectral resolution limits the magnitude of Q which can be resolved, given the spectral resolution of the simulation upon which the interference theory result is based. This constitutes a Q factor far larger than that of comparable THz MM absorbers although in this regime, the spacer layer thickness d is no longer of subwavelength.

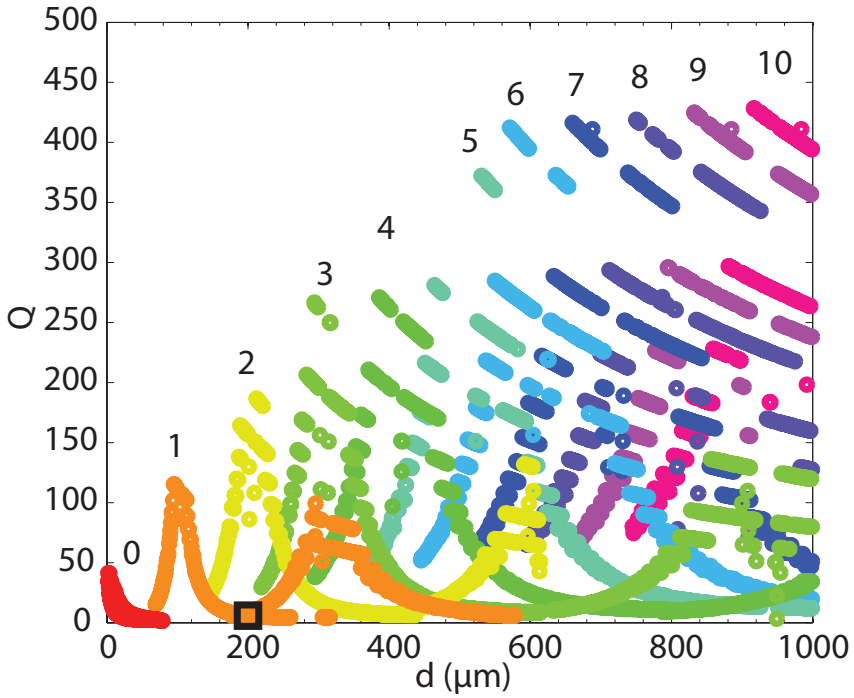

Figure 4.6: Q factor of absorption peaks as a function of spacer layer thickness d for values of m between 0 and 10 as determined from interference theory [using Eq. 4.8]. Each color corresponds to a different value of m (see Figure 4.4). The black box highlights a region where more than one absorption can occur for a given value of m and $d$see the green dots in Figure 4.4 corresponding to this highlighted region.

4.5 Conclusion

We have experimentally realized a metamaterial-dielectric-metal absorber with a broadly tunable air dielectric layer. It has been demonstrated that the characteristics of the VAS-MPA can be accurately predicted using the interference theory of perfect absorbers, and we have comprehensively experimentally verified the evolution of the absorption bands of the absorber as a function of dielectric spacer layer thickness with THz-TDS. These measurements exhibited a high degree of agreement with both numerical simulations and analytical predictions. We characterized the observed absorption bands in relation to the m-curves predicted by interference theory. Finally, we examined the role of the spacer thickness in the absorption peak Q-factor, finding extremely large values in excess of $Q = 400$ for large spacer thicknesses and large values

of m.

Our approach realizes an absorber device that, with relatively modest tuning of physical parameters, is capable of achieving a plethora of absorption characteristics: broad or narrow absorption bands, few or several absorption bands within the 02 THz regime, continuous frequency tunability, and continuous tuning of the absorption peak amplitude. While the practicality of this device is limited by the bulky translation stage, a micromechanically actuated analogue of the VAS-MPA could achieve a similar degree of tunability in a far smaller form factor. Likewise, it should be noted that all the results and analysis herein depend on the optical path length of the dielectric spacer layer, and thus, similar results can be achieved by modulating the refractive index of the dielectric layer rather than (or in addition to) its thickness d, which opens further possibilities for realization of practical devices. More generally, our results inform the design of metamaterial absorber devices where a high sensitivity to the dielectric environment, a wide degree of tunability, or a variable number absorption bands is desirable.

4.6 Acknowledgements

This research is in part is a reprint of the material as it appears in Applied Physics Letters 2018. Jacob Schalch, Guangwu Duan, Xiaoguang Zhao, Xin Zhang, and Richard D. Averitt, American Institute of Physics, 2018. The dissertation author was the primary investigator and author of this paper.

We acknowledge support from the National Science Foundation (NSF) (ECCS-1309835) and Army Research Office (ARO) (W911NF-16-1-0361). We thank Boston University Photonics Center for technical support.

Chapter 5

Broadband electrically tunable VO_2 metamaterial terahertz switch with suppressed reflection

Devices designed to dynamically control the transmission, reflection, and absorption of terahertz (THz) radiation are essential for the development of a broad range of THz technologies. A viable approach utilizes materials which undergo an insulator-to-metal transition (IMT), switching from transmissive to reflective upon becoming metallic. However, for many applications, it is undesirable to have spurious reflections that can scatter incident light and induce noise to the system. We present an electrically actuated, broadband THz switch which transitions from a transparent state with low reflectivity, to an absorptive state for which the reflectivity and transmission is strongly suppressed. On one side, our device consists of a patterned high resistivity silicon metamaterial layer which provides broad band reflection suppression by matching the impedance of free space. The other side is a VO_2 ground plane which undergoes an IMT by means of a DC bias applied to an interdigitated antenna. THz time domain spectroscopy measurements reveal an active bandwidth of 0.7 THz with suppressed reflection and more than 50% absorption modulation

with a low insertion loss. We utilize finite difference time domain simulations (FDTD) in order to examine the loss mechanisms of the device, as well as the sensitivity to polarization and incident angle. This device validates a general approach towards suppressing unwanted reflections in THz modulators and switches which can be easily adapted to a broad array of applications through straightforward modifications of the structural parameters and IMT mechanism.

5.1 Introduction

In recent years, the terahertz (THz) region of the electromagnetic (EM) spectrum has attracted enormous interest to study fundamental physical phenomena at meV energy scales [105][106][107][108][109] and, more recently, interest from a broader community as THz technologies become more available for applications in wireless communications[110][111], security[14], imaging[112], and biosensing[50] among others. With the proliferation of THz technologies, there is a continuing demand for better means of modulating and otherwise manipulating THz light. One promising route for the realization of active control of THz waves has been metamaterials (MMs)[5][113], which are periodic artificial structures with subwavelength dimensions. The effective optical properties of these media are determined primarily by their subwavelength geometry and constituent materials. Tunable THz MMs have been realized by a variety of methods, including micro-electro-mechanical systems[114][115][116][117], photoexcitation[118][119][120], and electrical actuation[121][122].

Additionally, metamaterial absorbers, designed to achieve near unity absorption, have been realized by a various means[123][124] and are important for a number of applications including energy harvesting[125], detection[61], sensing[126], and electromagnetic concealment. Metamaterial absorbers can achieve high absorption in part due to the ability to match the impedance of free space, thus suppressing reflections at their surface[127]. However, metamaterial absorbers are generally narrowband devices, and many of these devices operate by entirely

suppressing transmission through the device with a metallic ground plane. This in turn limits their usefulness in applications where broadband operation is required, or where it is desirable to have tunable transmission through the device. Conversely, many traditional modulators and optical switches utilize phase-transition materials which go from transmissive in their insulating state to reflective in their metallic state under proper external stimulation[128][129][130][131]. While this is an effective means for modulating transmission across a broad spectral range, significant reflection in the insulating state will still exist due to impedance mismatch with free space, and in the metallic state, nearly all incident light will be reflected. This can be detrimental in devices where scattered light impedes performance or even causes irreversible damage, i.e. in sensors and sensitive bio systems[30][132][133]. Common THz modulators based on IMT materials typically consist of a thin IMT layer on a substrate (Figure 5.1a). When this type of device is in the insulating state, losses in both the substrate and IMT material are low, and the device will be largely transparent, with some light being reflected due to impedance mismatch at the interface between the device and free space. Upon transitioning into a metallic state either by heating, optical excitation, or other means, the device becomes mostly reflective, though depending on the thickness and conductivity of the IMT layer, some transmission and absorption may persist. While effective at creating a dramatic modulation of the transmission amplitude, the light reflected from the modulator in both its transmissive and opaque state is undesirable for many applications. Alternatively, if an impedance matched layer is introduced to the device, it can dramatically reduce reflections from the surface when the IMT material is in the insulating state. The result is a device with high transmission and very low reflection (Figure 5.1b). With judicious design choices, this same layer can act to trap light inside of the device allowing the light to be dissipated into heat. In this state, both the transmission and reflection are very low, with nearly all of the incident light absorbed. In the following sections we demonstrate the realization of such a device.

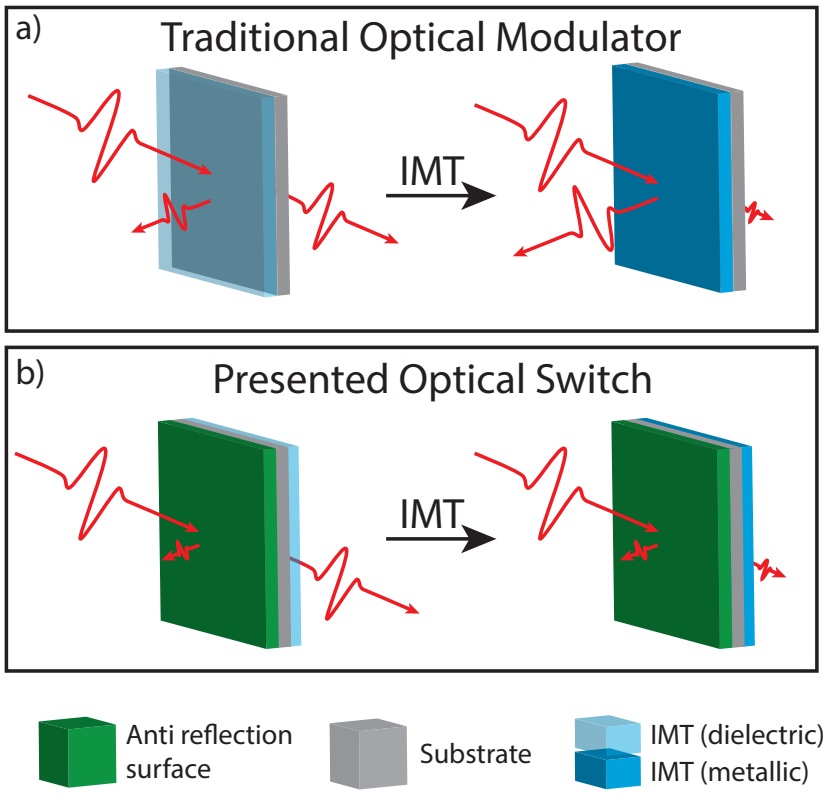

Figure 5.1: (a) A traditional optical modulator based on phase change materials goes from a partially reflective, mostly transmissive state to a mostly reflective, partially transmissive state upon undergoing an IMT. (b) By contrast, introducing an anti-reflection surface allows the device to transition from a transmissive state with little reflection, to an absorbing state with simultaneously suppressed reflection and transmission, offering significant operational advantages.

5.2 Experiment

We realize an electrically actuated, broadband THz switch which can be actuated by means of a modest applied voltage. In the absence of a bias, the device is transparent, with very low reflectivity. With a bias of 2.5V, the device acts as a broadband THz perfect absorber, with nearly all incident light being neither transmitted nor reflected, but absorbed and dissipated as heat. The device consists of four layers (Figure 5.2a). The first is a periodic metamaterial array of double-step high resistivity silicon cylinders. These cylinders act as a broadband THz

metamaterial layer to closely match the impedance of free space in order to minimize the reflection of incident light, as well as to trap back reflected light within the device[134][135][136]. The second layer is a high resistivity silicon substrate which supports the device, and out of which the metamaterial layer is etched. Next is a layer of VO2, a phase change material which undergoes an IMT slightly above room temperature at 60C. Finally, the bottom layer consists of a gold interdigitated antenna which, with an applied bias, induces the IMT in the underlying VO_2 via Joule heating.

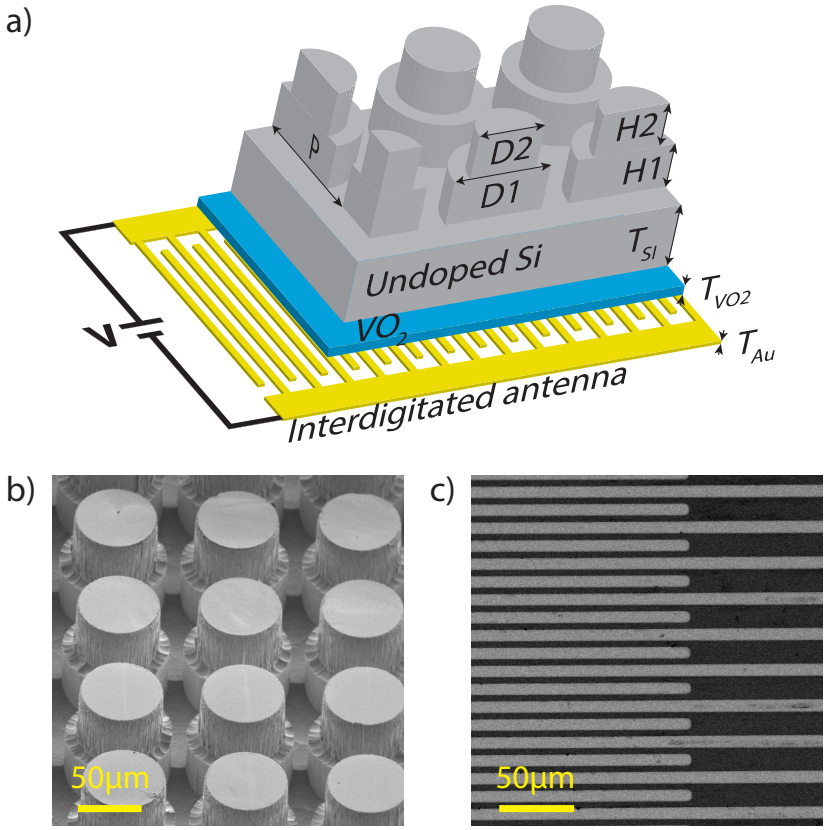

Figure 5.2: Schematic and SEM images of broadband THz switch. (a) The top of the device consists of a double layer metamaterial patterned into the high resistivity silicon where D_1=92μm, H_1=30μm, D_2=74μm, and H_2=45μm. The thickness of the Si substrate is T_{SI}=410μm, the thickness of the VO_2 is T_{VO2}=0.2μm, and the thickness of the Au interdigitated antenna is T_{Au}=0.15μm. The linewidth and separation of the antenna fingers are both 6μm. (b) and (c) are SEM images of the MM patterning on the top of the device, and the interdigitated antenna on the bottom of the device, respectively.

5.2.1 Fabrication

The fabrication of the sample began with a high resistance intrinsic silicon wafer with a resistivity of 3000 cm and a thickness of 500m. We then pattern a one side of the wafer with a MM anti-reflection surface, the unit cell of which consists of a double-step cylinder on a square lattice (See Figure 5.2). To perform this patterning, we utilize inductively coupled plasma (ICP) etching technique: First, a 3um thick SiO2 mask layer is deposited by thermal oxidation on the unpatterned Si surface. Next, a silica mask with circular pores is printed onto the SiO2 mask by photolithography. The first ECP etching creates large cylinders with height H1 and diameter D1. Next a second mask applied in a similar fashion, and the top half of the cylinders are further etched down to diameter D2 and height H2.

The VO_2 thin film is deposited on the other side of the Si wafer by a reactive magnetron sputtering method from a metal vanadium, as we reported in ref[137]. In order to obtain a high quality VO_2 film on Si substrate, the substrate temperature is precisely controlled and quenched in a specific process. In our experiments, the substrate temperature fixed at 600. After the film deposition, the sample/substrate temperature was sequentially decreased to 450 and then 200, being held at each temperature for 30 minutes before naturally cooling to ambient temperature. The Au coplanar interdigital contacts were patterned by a typical lift-off procedure, and the linewidth and separation of the antennas are both 6m.

5.2.2 Measurement

We utilize a dual-mode THz-TDS system to measure the complex reflection and transmission coefficients of our broadband THz switch[101]. A titanium sapphire laser generates 800nm, 20fs pulses at a repetition rate of 80 MHz, which is used to generate and detect the THz pulses using photoconductive antennas. The THz pulses impinge on the sample at normal incidence and both transmission and reflection are measured. In the present case, the THz pulses are incident

on the patterned silicon side of the sample, with the electric field polarized perpendicular to the interdigitated antenna arms. We perform a reference measurement using air (a gold-coated silicon wafer) as the reference for transmission (reflection) measurements.

5.3 Results

The time domain sample and reference pulses are Fourier transformed to obtain the frequency domain transmission and reflection spectra. We verify our experimental results with the finite difference time domain (FDTD) solver CST Microwave Studio 2016[138]. In the simulation, we replicate the geometry of a unit cell and apply periodic boundary conditions where gold is modeled with a conductivity of 4.56x105 $(\Omega cm)^{-1}$, and the Si as a lossy dielectric with a relative permittivity of $\varepsilon = 7.6(1+0.0053i)$. In its insulating state the VO_2 is modeled as a dielectric with permittivity $\varepsilon_r = 10$, whereas in the metallic state it is modeled with a real permittivity $\varepsilon_r = 10$ and a conductivity of 2000 $(\Omega cm)^{-1}$.

We performed THz-TDS measurements in reflection and transmission to characterize the broadband THz switch as a function of applied bias (Fig 3). In the low voltage state (blue lines) reflection from the patterned side of the device is low across a wide bandwidth as shown in Figure 5.3a. Specifically, the reflectivity is below 10% from 410 GHz to 1.47 THz. For comparison, the reflectivity of an unpatterned but otherwise identical silicon parent wafer (black line) exhibits 30% reflectivity across the entire measured spectrum. Meanwhile, the transmission (Figure 5.3b) is above 50% from 220 GHz to 930 GHz with a maximum transmission of 75% at 550 GHz. In the high voltage state (red lines), the reflectivity (Figure 5.3a) is essentially unchanged, but the transmission is reduced to below 6% across the entire measured range (Figure 5.3b). The absorption (Figure 5.3c) is A=1-R-T where R is the reflection coefficient and T is the transmission coefficient. Between the low voltage state (blue line) and high voltage state (red lines), there is a considerable change in absorption across a large bandwidth. FDTD simulations are in excellent

agreement with experiment (Figure 5.3 dashed lines).

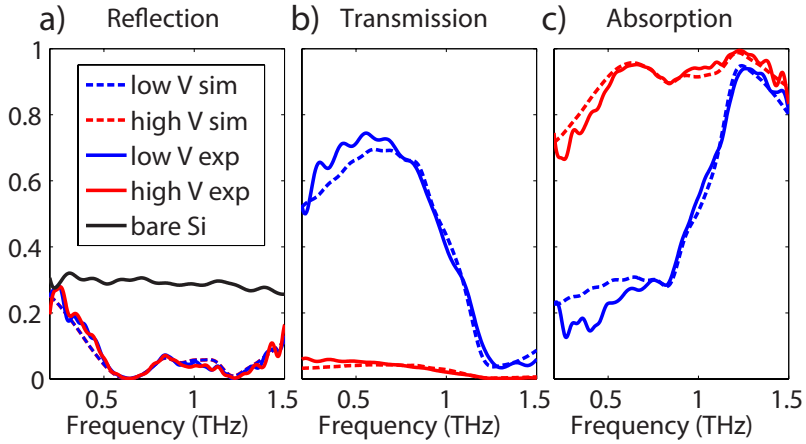

Figure 5.3: THz-TDS measurements (solid lines) and corresponding FDTD simulations (dashed lines). (a) Reflectivity, (b) transmission and (c) absorption of the broadband THz switch in the low voltage (blue) and high voltage (red) state. For comparison, the black solid line in (a) shows the reflection of an identical but unpatterned Si wafer. It is clear that the metamaterial device has much lower reflectivity.

We analyze the absorption modulation performance in further detail in the inset of Figure 5.4. For applications which require a minimum modulation depth of only 0.5, the effective bandwidth of the device is 0.7THz (blue line) with the band centered at 0.57THz (green line). As the minimum modulation depth is increased, the effective bandwidth decreases band center frequency increases. At for a modulation depth of 0.65, the effective bandwidth is 0.13THz centered at 0.63THz. Figure 5.4 shows the absorption of the THz switch measured at this frequency as a function of the voltage applied to the interdigitated antenna. As the voltage increases from 0 to 2.2V, the VO_2 retains its insulating state and there is little change in the absorption. But between 2.3 and 2.4, the absorption dramatically increases from 25% to 92% as the VO_2 undergoes its IMT. As the bias is reduced from its maximum value, the transition does not occur until between 2.1 and 2.0V, showing a clear hysteresis with a width of 0.2V. This indicates that within this voltage region, the switch can act as a memory device; retaining its previous state in spite of modest changes in the applied voltage.

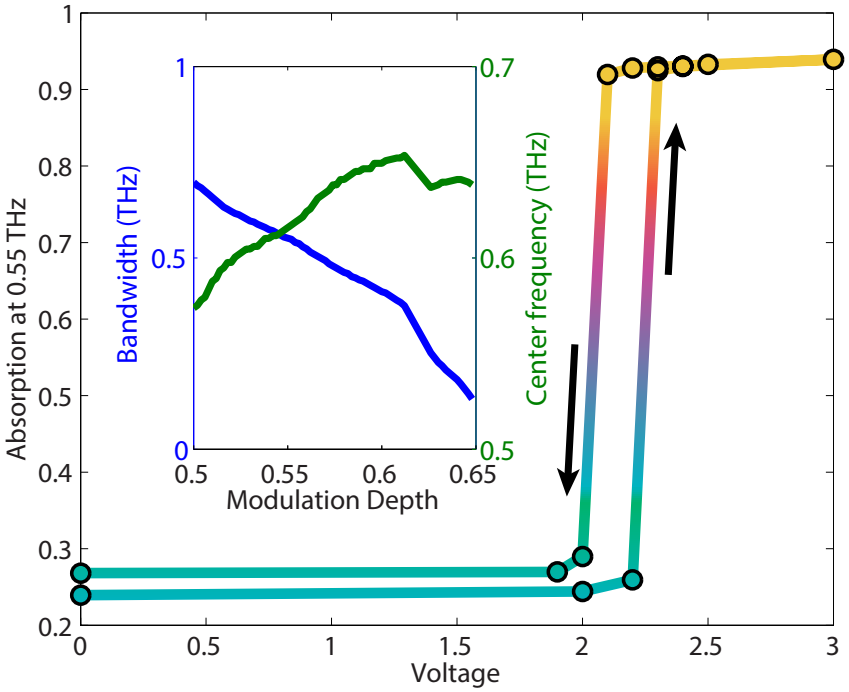

Figure 5.4: Absorption at 550GHz as a function of applied bias with increasing and decreasing voltage indicated by arrows. Inset: Absorption bandwidth (blue) and center frequency (green) as a function of the minimum absorption modulation depth ADepth AHighV-ALowV.

5.4 Discussion

5.4.1 Reflection suppression mechanism

The mechanism of suppressed reflection and strong absorption can be elucidated by inspecting the distribution of electric fields from FDTD simulations, presented in Figure 5.5a and b. The broad-band response of the double-step cylinder metamaterial layer can be understood as a superposition of the response of the large bottom cylinder array and the top cylinder array[139]. The former contributes primarily through a local air gap resonance mode, apparent in the strong field enhancement in the small gaps in between the large cylinders. This mode is largely responsible for the low frequency portion of the absorption band. The top small cylinder array contributes primarily at higher frequencies; the response can be interpreted as a HE mode in the top cylinders[140]. This can be seen in particular in the low voltage (high transmission) state

(Figure 5.5a) by the field enhancement at the top of the small cylinder. the small and large cylinder lattices also contribute to a 1st order diffraction mode which is determined by the periodicity of the metamaterial unit cell. This mode can be seen qualitatively in the electric field distributions both in the high and low voltage state. In the Si region of the device interference between adjacent unit cells creates an angular perturbation to the fields, which would otherwise appear as plane waves. These modes reduce the reflectivity and trap THz waves within the Si when the device is in its high voltage state. That being said, these modes do not play a direct role in the strong absorption of the THz waves. FDTD simulations reveal that when the VO_2 is in its insulating state, of the modest absorption that occurs, 90.5% occurs as ohmic loss in the gold while only 6.5 % and 3% occur in the VO_2 and Si respectively. However, once the VO_2 transitions to a metallic state, it acts as a bad metal. In this state 99.5% of the material losses occur in the VO_2, revealing its nearly exclusive role in the broadband absorption of the incident THz light. Notably, this means that the performance of the switch is largely independent of the thickness of the Si substrate (TSi). Though this implies that a far thinner form factor is possible, Fabry Prot modes should be considered.

5.4.2 Angle of Incidence

For consideration of applications with non-normally incident radiation, the reflectivity of the isolated metasurface are calculated by frequency domain simulations. The reflectivity as a function of frequency and incident angle is illustrated in Figure 5.5c and d for TE and TM polarizations respectively. For TE illumination, the reflectivity is below 20% across a wide band and below 40 degrees angle of incidence. The performance degrades at larger angles, especially at low frequencies. Performance under TM illumination is much better, with no significant reduction in the anti-reflection properties except at glancing incidence. The reflectivity across nearly the entire sampled frequency range is below 10% until the angle of incidence is greater than 70 degrees. The metamaterial layer is fourfold symmetric and a result its performance is

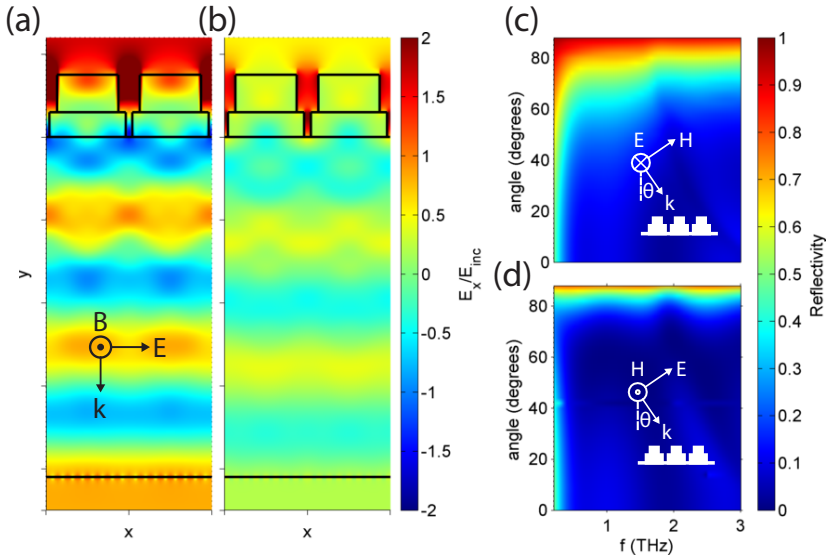

Figure 5.5: The x-component of the electric field normalized to the incident electric field for the broadband THz switch simulated in the (a) low and(b) high voltage states using FDTD simulations. The reflectivity for (c) TE and(d) TM polarized waves on the patterned Si MM surface as a function of incident angle (see insets) as determined from frequency domain simulations.

independent of the azimuthal angle of illumination. However, the interdigitated antenna on the opposite face of the device is not. It acts as a polarizer. When the light polarization is orthogonal to the antenna arms, the antenna has a negligible effect on the transmitted light, but when the polarization and antenna arms are parallel, the transmission is strongly suppressed. This limitation could be eliminated by the introduction of a DC conductive but THz transparent material for the antenna, such as MoS_2[141][142]. This would allow the device to operate under large angles of incidence as shown, and would also make the response independent of azimuthal polarization angle.

5.4.3 Switching Speed

VO_2 has attracted considerable attention because its IMT occurs near room temperature (60C), and because it is fairly frequency independent over from THz to IR. At THz frequencies, the VO_2 is nearly completely insulating, whereas upon transitioning to the metallic state, it has

a conductivity of approximately 2e3(Ωcm)$^{-}$1[143]. In this device, the sudden transition to the metallic state is dominated by joule heating. As the interdigitated antenna is biased, small currents flow through the VO_2 and heat it above the IMT temperature. Above the critical voltage, the resulting decrease in resistance and increase in current results in a quick transition into the metallic state. As the voltage is decreased, the heat must be radiated away before the VO_2 transitions back into its insulating state. As a result the transition is slow, on the order of seconds.

While the mechanism in this device is slow, there are a variety of means by which the switching speed may be increased to MHz frequencies and beyond. One such approach leverages the well studied field-induced generation of carriers in VO_2[144]citearXiv:1804.09275. While there is still some debate over the exact nature and mechanism of the transition is generally considered to be an autoionization process resulting from coulomb barrier lowering, analogous to the Poole-Frenkel effect[145]. Relative to a purely thermally induced phase transition, these electrical effects can occur on a much shorter timescale, on the order of 1s[146]. Though this generally requires fields on the order of kV/cm, the field enhancements provided by micro-scale plasmonic structures can significantly enhance the fields on the VO_2. In particular, large transient THz fields enhanced by metamaterials could be used to transiently induce the IMT. This opens the possibility device to act nonlinearly; with the absorption increasing as the incident fluence is increased on very short timescales. This would be particularly useful for use as an optical limiter, where large incident fields would induce the absorptive state in the THz switch in order to protect sensitive components.

Additional functionalities, dynamics, and switching behaviors could be realized by modifying the VO2 used, or by replacing it with another phase change material. For instance introduction of vacancies into the VO_2 generally decreases the critical temperature and broadens the hysteresis. Thus the absorbing state could be initiated at a lower temperature or voltage. A broadened hysteresis would enable the realization of devices which retain their previous state in the absence of an applied voltage, even at room temperature. Likewise, a broadened hysteresis would enable

easier continuous tuning of the transmission due to a less abrupt phase change. Though switching in VO_2 is generally slow, substituting the VO_2 with alternative IMT materials, and with other means of switching far faster dynamics could be realized. Femtosecond optical excitation of a high mobility semiconductor such as InAs would allow for ultrafast control of the switching, though this would introduce the complication of needing a suitable light source. Ultimately the THz absorption mechanism requires only a sufficiently transparent and opaque IMT for the transmissive and absorptive state respectively. Any number of different materials and mechanisms may be chosen interchangeably depending on the demands of the application at hand.

5.5 Conclusion

We have experimentally demonstrated an electrically actuated, broadband THz switch using a high resistivity silicon wafer patterned with a double-layer metamaterial structure, activated by an interdigitated antenna which initiates an IMT in an underlying VO_2 film. Compared to ordinary modulator designs, this device has very low reflection in both its transmissive and opaque state, which is advantageous in applications where back reflected light may interfere with device performance. We have performed THz-TDS measurements of the reflection and the transmission to determine the total electromagnetic absorption of the device at low and high voltage states. We have demonstrated a bandwidth of 700 GHz over which the absorption is tuned by at least 50%. The device enters its absorbing state with an applied voltage of 2.3V and returns to its insulating state once the voltage is decreased below 2.1V, demonstrating a hysteresis with a width of 0.2V. We have used frequency domain simulations to assess how multiple modes in the Si metamaterial act to suppress reflection and trap THz waves. We also demonstrate its robustness to large angles of incidence in both TE and TM polarizations. With this work as a proof of concept, there are ample opportunities to expand the functionality of and improve the performance of this device. We have suggested modifications which would

allow the THz switch to retain its performance while reducing the thickness and/or making it azimuthally polarization insensitive. Likewise, modifying the VO_2 or replacing it with another phase change material would allow for the realization of many different transition characteristics. These include variable actuation voltage or temperature, faster switching, or switching with other stimuli. Similarly, taking advantage of nonlinear effects in VO_2, new functionalities on very short timescales could be realized. By introducing the appropriate modifications, the operating principle of the device presented in this manuscript can be used to inform the development of a wide variety of modulators, optical switches, optical limiters, and absorbers for THz applications.

5.6 Acknowledgements

This work in part is currently being prepared for submission for publication of the material. Jacob Schalch, Yahua Tang, Hao Zhang, Xiaoguang Zhao, Xin Zhang, Qiye Wen, Richard D. Averitt. The dissertation author was the primary investigator and author of this material.

This work is supported by Natural Science Foundation of China under Grants 51572042, Science Challenge Project under Grant No. TZ2018003 and International Science and Technology Cooperation Program of China under Grant No. 2015DFR50870.

We acknowledge support from the Department of Energy Basic Energy Sciences(DOE-BES) (DE-SC0018218). We thank Boston University Photonics Center for technical support.

Chapter 6

Strong metamaterial-Josephson Plasma Resonance coupling in superconducting $La_{2-x}Sr_xCuO_4$

6.1 Introduction

Terahertz spectroscopy of the c-axis Josephson plasma resonance (JPR) in high temperature superconducting cuprates is an insightful probe of the superconducting condensate. We investigate electromagnetic coupling between metasurface arrays of split ring resonators (SRRs) and the JPR of a $La_{2-x}Sr_xCuO_4$ single crystal ($T_c = 32K$). This is accomplished by applying a series of interchangeable metamaterial tapes. Specifically, the metasurface LC resonance frequency (ω_{MM}) is swept through the JPR frequency ($\omega_{JPR} = 1.53THz$) using a series of tapes applied to the same single crystal with ω_{MM} determined by the SRR geometry. THz reflectivity measurements on these hybrid superconducting metamaterials (HSMMs) reveal anti-crossing behavior characteristic of strong coupling. The experimental results, validated with numerical simulations, indicate a normalized Rabi frequency of $\Omega_R = 0.29$. Further, we show that HSMMs

with $\omega_{MM} > \omega_{JPR}$ provide a route to couple to hyperbolic waveguide modes in c-axis cuprate samples. This work informs future possibilities for optimizing the coupling strength of HSMMs and investigating nonlinear superconductivity under high field terahertz excitation. Finally we present preliminary nonlinear THz spectroscopy of HSMMs with optimized coupling strength and explore the possible origins of these nonlinear interactions.

6.1.1 Introduction to Coupling: Classical Picture

We will begin with an introduction to the basic basic phenomenology of coupling, for which it is useful to return to an entirely classical mechanics example. Recall our discussion of a simple harmonic oscillator, a mass on a spring, in section 2.1.1. We will now add a second mass and spring, and connect the two masses by a third spring of spring constant κ (Figure 6.1a). In the absence of any driving force, the equations of motion for the two masses are

$$\ddot{x}_1 + \gamma_1 \dot{x}_1 + \omega_1^2 x_1 - \Omega^2 x_2 = 0 \tag{6.1}$$

$$\ddot{x}_2 + \gamma_2 \dot{x}_2 + \omega_2^2 x_2 - \Omega^2 x_1 = 0 \tag{6.2}$$

where x_j, $\omega_j = \sqrt{k_j/m_j}$, and $gamma_j$ for $j = 1,2$ are the equilibrium displacement, eigenfrequency, and loss rate of the the jth oscillator respectively and $\Omega = \sqrt{\kappa/m_r}$ is the coupling rate between the two masses. For simplicity, we will first consider the symmetric case, i.e. $m_1 = m_2 = m_r = m$, $k_1 = k_2 = k$, such that $\omega_1 = \omega_2 = \omega_0$ and $\gamma_1 = \gamma_2 = \gamma$. Here we will also focus on the under damped case ($\gamma/2 < \omega_0$) but a through discussion of the overdamped case can be found in reference [147]. We can make some initial intuitive observations about this system. First, the system has two eigenmodes. In the symmetric mode, $x_1(t) = x_2(t)$ and the two masses oscillate in phase with each other. In this mode, the eigen frequency is simply that of a single

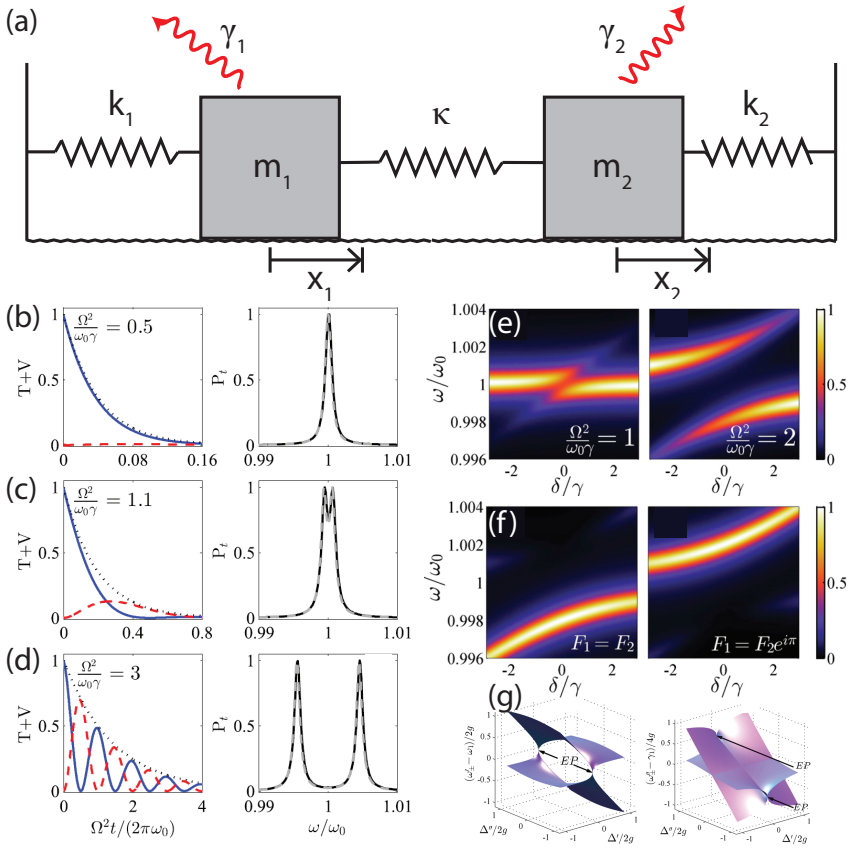

Figure 6.1: a) A coupled harmonic oscillator consisting of two SHOs connected by a spring. left side b-d) The total (kenetic+potential) energy contained in oscillator 1 (blue solid line), oscillator 2 (red dashed line), and both oscillators (black dotted line) as a function of normalized time for normalized coupling of $\Omega = 0.5, 1.1$ and 3 respectively. right side b-d) The frequency domain integrated dissipated power spectrum of the coupled harmonic oscillators. The black line represents an initial condition in which only one mass is perturbed, while the grey line represents steady state power dissapation when only one oscillator is driven with a harmonic force. e) The steady state total power absorption by two CHOs as a function of detuning for a normalized coupling strength of $\Omega^2/\omega_0\gamma = 1$ (left) and 2 (right) showing avoided resonance crossing behavior. f) The same power absorption but where both oscillators are driven in phase (left) and with a phase difference of π (right). g) the real (left) and imaginary (right) parts of th non-Hermitian Hamiltonian eigenvalues as a function of the real (Δ') and imaginary (Δ'') parts of the complex detuning parameter. The exceptional points are marked.

mass $\omega_0 = \sqrt{k/m}$, and the coupling spring plays no role in the dynamics. If masses are exactly out of phase ($x_1(t) = -x_2(t)$, the anti symmetric eigenmode results with a frequency given by $\omega_0 = \sqrt{(k+2\kappa)/m}$. If either of these modes are enforced by the initial conditions, the total energy of each subsystem will remain the same as the system gradually rings down, remaining in

that eigenmode the entire time.

But what if neither of these eigenmodes are initially excited? We can instead consider a situation where only one mass is initially displaced from equilibrium ($x_1(0) \neq 0, x_2 = 0$). In some sense this is a superposition of the two previously mentioned eigenmodes; where as we previously considered a phase difference in the motion of the masses of 0 (symmetric) and π (antisymmetric), we now consider $\pi/2$. It is useful to use the total mechanical energy of each subsystem $T_j + V_j = m\dot{x}_j^2/2 + kx_j^2/2 (j = 1,2)$ in order to evaluate the dynamics. With our initial conditions, all of the energy starts with the $j = 1$ oscillator. In Figure 6.1b-e the total mechanical energies are plotted as a function of a dimensionless time constant $\Omega^2 t/(2\pi\omega_0)$ for three choices of $\Omega^2/\omega_0\gamma$. When this ratio is less than 1, the system losses are dominant, and oscillator 1 rings down before exchanging any significant amount of energy with oscillator 2. We can evaluate this behavior in the frequency domain by evaluating the fourrier transformed power spectrum:

$$P_j(\omega) = \frac{\omega_j^2 \gamma_j}{2\pi} \left| \int_{-\infty}^{\infty} x_j(t) e^{-i\omega t} dt \right|^2 \tag{6.3}$$

Unsurprisingly, this weak coupling case amounts to a single peak at ω_0, corresponding to the dynamics of a single, uncoupled SHO (i.e. Ω=0, see Figure 2.2). When the coupling is increased, to $\Omega^2/\omega_0\gamma = 1.1$, the result is a perturbative variation of the former case: some of the energy initially supplied to oscillator 1 is transferred into oscillator 2 before the system rings down, but only one such transfer occurs. In the frequency domain, a large peak at ω_0 is still visible, but there is a small bifrucation into two distinct maxima.

When the coupling constant is high $\Omega^2/\omega_0\gamma = 3$, entirely new behavior appears. In the time domain, we see that energy is exchanged between the two subsystems with a frequency of $\Omega^2/\omega_0)$ for multiple cycles, indicating that this this exchange of energy occurs faster than the two oscillators dissipate energy. This is the so-called strong coupling regime. In the frequency domain, the power spectrum separates into two distinct peaks. This effect is typically referred

to as 'Rabi splitting' and is regarded as the spectral signature of strong coupling. It is notable that the boundary between weak and strong coupling ($\Omega^2/\omega_0\gamma \simeq 1$) is is a smooth one with no distinct transition. One consequence of this is that there are a variety of definitions of strong coupling depending on the context and system considered. Of course this degenerate example is the simplest possible, and there are many factors which complicate both the observation and definitions of strong coupling as we will now see.

Whereas previously we have considered a transient system, we now introduce a driving force to oscillator 1 of amplitude F and frequency ω. We also assume a harmonic steady state solution for both masses and rewrite equation 6.2 in matrix form:

$$\begin{bmatrix} \omega_1^2 - \omega^2 - i\gamma_1\omega & -\Omega^2 \\ -\Omega^2 & \omega_2^2 - \omega^2 - i\gamma_2\omega \end{bmatrix} \begin{bmatrix} x_1 \\ x_2 \end{bmatrix} = \begin{bmatrix} Fe^{-i\omega t} \\ 0 \end{bmatrix} \tag{6.4}$$

Rather than examining the integrated power spectrum of the motion, the enforcement of a steady state solution can be exploited to show that the steady state power dissipation by a given oscillator driven at frequency ω is given by $P_j = \omega^2\gamma_j|x_j(\omega)|^2$. Generally these give nearly identical results as the transient case (See dotted lines Figure 6.1b-d). We will also now relax the degeneracy of the example, considering situations in which, the spring constants, masses, and/or damping rates may be unequal. We define the dimensionless quantity $\Omega^2/\omega_m\Delta$ where $\omega_m = (\omega_1 + \omega_2)/2$ and $\Delta = (\omega_1 - \omega_2) - i(\gamma_1 - \gamma_2)/2$, the complex detuning parameter.

First let us examine the case where only the eigenfrequencies (real part) are detuned ($\Delta = \delta = \omega_1 - \omega_2$, $\omega_1 = \omega_0$). Figure 6.1e and f show the power spectrum as a function of δ for a coupling of $\Omega^2/\omega_0\gamma = 1$ and 2 respectively. In both cases at zero detuning, the two resonances anticross. This constitutes an avoided resonance crossing (ARC) that is considered a hallmark of strong coupling effects. The separation between the two peaks at zero detuning is the Rabi splitting frequency. In the low coupling case, the spectrum of the single oscillator resonance will quickly recover as the detuning becomes finite. In the large coupling case, the ARC is far

more dramatic. At large negative detuning, a peak only slightly shifted from ω_0 appears, but as detuning approaches zero, this band approaches the $\omega = \omega_2$ diagonal. Simultaneously, a peak at low frequency emerges along this diagonal, and asymptotically aproaches ω_0 for large positive detuning. Thus over a large region of detuning, a significant quantity of energy is being coupled into the second resonator. Keep in mind that so far we have only considered the case where 1 is being driven. This is why, so we see no spectral features along the $\omega = \omega_2$ diagonal for large detunings, or even small detunings in the case of weaker coupling (Figure 6.1b). These spectral features change dramatically when both oscillators are driven depending on the phase. Figure 6.1c,d show the same spectra, but now with a driving force applied to both masses and a phase difference of 0 and π respectively. When the phase difference is zero, only the lower branch is strong, whereas whereas for a phase difference of π, the upper branch appears. The weaker branches in both cases are present, but note that at zero detuning, we excite ONLY one branch, because the driving force strictly excites one of the eigenmodes of the system, as mentioned previously in our discussion of the degenerate and transient case.

6.1.2 Introduction to Coupling: Quantum Picture

Mapping this simple coupled oscillator to a two-state Non-Hermetian Hamiltonian (NHH) gives a straightforward glimpse at how a similar problem can be treated in quantum mechanics. The most important distinction as we will see is that the energy spectrum of the resulting Eigen states are complex. where the real part is connected to the energy and the eimaginary part to the loss. We start by writing Equation 6.2 by dividing the first and second row by $(\omega_1 + \omega)$ and $(\omega_2 + \omega)$ respectively to get:

$$\begin{bmatrix} \omega_1 - \omega - \frac{i\gamma_1\omega}{\omega_1+\omega} & -\frac{\Omega^2}{\omega_1+\omega} \\ -\frac{\Omega^2}{\omega_2+\omega} & \omega_2 - \omega - \frac{i\gamma_2\omega}{\omega_2+\omega} \end{bmatrix} \begin{bmatrix} x_1 \\ x_2 \end{bmatrix} = \begin{bmatrix} 0 \\ 0 \end{bmatrix} \tag{6.5}$$

Given that we are interested in behavior when both oscillators or near resonant, we can make the substitution $\tilde{\omega} \simeq (\omega + \omega_{1,2})/2$. This turns the above equation into a characteristic equation of the form $|H - \omega I| = 0$ where I is the identity matrix and

$$H = \begin{bmatrix} \omega_1 - \frac{i\gamma_1}{2} & g \\ g & \omega_2 - \frac{i\gamma_2}{2} \end{bmatrix} \tag{6.6}$$

is the hamiltonian with $g = -\frac{\Omega^2}{2\tilde{\omega}}$ is the effective coupling constant. Diagonalization yeilds the eigenvalues of the NHH:

$$\omega_\pm = \tilde{\omega} \pm \frac{\Delta}{2}\sqrt{1 + \left(\frac{2g}{\Delta}\right)^2} \tag{6.7}$$

where $\tilde{\omega}$ is the average complex frequency for the bare states and Δ is the complex detuning as defined previously. This classical-quantum equivlance suggests that the non-Hermitian nature of this hamiltonian is roughly equivelant to introducing damping in the classical mechanical case. However there are some important distinctions as we will now see. In the analysis of the complex eigenfrequencies $\omega_\pm$ it is useful to Taylor expand the square root about $\frac{2g}{\Delta} = 0$:

$$\omega_\pm \simeq \tilde{\omega} \pm \frac{\Delta}{2}\left(1 + \left(\frac{2g}{\Delta}\right)^2 - \left(\frac{2g}{\Delta}\right)^4 + ...\right) \tag{6.8}$$

From this form, we see that if only the first term is retainied, the role of the coupling constant g is on the eigenfrequencies is negligable as Δ becomes large. We also see frome equation 6.7 that a pole appears at $2g/\Delta = \pm i$. This indicates that for $|2g/\Delta| < 1$, the sum converges and the powers of $2g/\Delta$ can be treated as a perterbation series. But for $|2g/\Delta| \geq 1$, $\omega_\pm$ connot be calculated analytically using perterbative methods. Unlike the previous classical case, this creates a sharp boundary between the weak and strong coupling regime; the latter characterized by its non-perterbative solutions. Among other things, this also implies that unlike the previous case,

there is no requirement for energy exchange cycles nor any limitations imposed relative to the loss rates of individual oscillators nor their sum; by this definition highly lossy systems may still meet this definition of coupling while failing to meet the classical one.

Figure 6.1g shows the solutions of $\omega_\pm$ in the complex Δ plane. Most notable is that for $\Delta''/2g = \pm 1$ and $\Delta' = 0$ the solutions of $\omega_\pm$ coalesce. This is called the exceptional point and defines the boundary between strong and weak coupling. This implies that the eigenvalues of the NHH are continuations of one another via the exceptional point. In most realistic experimental scenarios, the real and imaginary detuning cannot be independently controlled and in the ARC we see what appear to be two separate absorption bands. But with control of the loss detuning as well, it is possible to access this point, and see that in fact, the two branches are manifestations of the same solution[148][149].

We have thus far discussed the simplest classical example of mechanically coupled oscillators and seen that the distinction between weak and strong coupling is smooth, and marked by at least one cycle of energy exchange between the oscillators before the energy is dissipated from the system. We saw how this leads to ARCs in a continuously driven case. Next we saw that in the language more natural for quantum mechanics: a two state NHH. In this context, strong coupling is instead distinguished by $|2g/\Delta| \geq 1$ and is independent of damping rates. While both definitions will agree in the most extreme cases, this does create the possibility for systems which are strongly coupled in one definition but not in others. In this section we have considered examples in which damping, resonant frequencies, and coupling strengths are arbitrary. Furthermore it is easy to see how tuning of such parameters may be accomplished in a real experiment by changing the frictional environment, the masses of the blocks, or the spring constant of the central spring respectively. But when attempting to couple photons to excitations in matter, the tuning knobs are less accessible and strong coupling is both more difficult to attain and to understand. In the next section I will introduce light matter coupling and some of its unique challenges and consequences.

6.1.3 Introduction to Light Matter Coupling

Our discussion of strong coupling has been limited to ones where the mechanism of the coupling is intuitive and obvious (i.e. a spring), or completely unspecified and abstract. It is far less obvious how these phenomena can be connected to the world of condensed matter physics and optics. In this section I will introduce the concept of light-matter interaction and how it can be modified and strengthened to the strong coupling regime and beyond.

Interactions between light and matter are typically described intuitively in the language of emission, absorption, and scattering processes between a photon and an electron. In quantum electrodynamics (QED), the strength of the "spring" that couples photons to electrons is given by the fine structure constant α. As before, this coupling constant determines the strength of these interaction (i.e. how likely it is that a photon and electron will undergo one of these processes). This constant must be experimentally determined, and does not fall directly out of the formalism the standard model of particle physics. Never the less, it is fundamental and can be calculated by a number of means to be $\alpha \simeq \frac{1}{137}$. Due to the small size of α, in a perturbative treatment of QED the only photon-electron interactions which must be taken into account are first-order (absorption and emission) and second-order (scattering) to capture most electron-photon interactions we see in nature.

But while the value of α is fundamental, early experiments by Purcell in 1946 showed that interaction between photoemitters and light can be modified by their electromagnetic environment [150]. In short, the light-matter interaction strength set by nature could be altered if the right conditions were created. These experiments spawned the entire field of cavity quantum electrodynamics (CQED), which sought to exploit photonic resonators to control the coupling of light to matter. We can make use of the topics already discussed for an intuitive understanding of how these interactions work: the cavity acts as a reservoir of photons which can repeatedly exchange energy with matter inside of that cavity. The result is a state in which the contributions of both systems cannot be disentangled and in which entirely new properties emerge.

These early experiments revolved around placing an atom in an optical cavity (Figure 6.2a). The atom could be adequately approximated as a two level system while the photon energy of the light is determined by the resonant condition of the cavity, i.e. its size. The behavior of such a system can be modeled with the quantum Rabi model (QRM). The Hamiltonian is given by:

$$H_{Rabi} = \omega_c a^\dagger + \frac{1}{2}\omega_q \sigma_z + H_{int} \tag{6.9}$$

$$H_{Rabi} = gXY' = ig_1(ab^\dagger - a^\dagger b) + ig_2(a^\dagger b - ab) \tag{6.10}$$

where ω_c is the cavity frequency, ω_q is the energy level difference in the two level system, a ($a^\dagger$) is the annihilation (creation) operator for the cavity mode and σ_+ (σ_-) is the lowering (raising) operator between the ground state and excited state of the two level system. In this hamiltonian the cavity photons act as a single-mode bosonic field with a population determined by creation and annhiliations of cavity photons, while the state of the two level system is determined by the raising and lowering operators. The two systems are connected by the interaction term, where g denote the light matter coupling.

Purcell's early experiments saw modifications in the photoluminescence of atoms in a cavity; ultimately the effect of the coupling in this case was a small modification of the losses. But with ever higher Q-cavities, it was eventually possible achieve coupling which exceeded the losses in the system, meeting the first definition of strong coupling discussed previously, i.e. $\Omega^2 > \omega_0\gamma$. This strong coupling was demonstrated with single atoms in a microwave [154] and optical [155] cavities, as well as 2D electronic excitations in semiconductor microcavities [156][152], and in superconducting circuits [157]. In this strong coupling regime, it is possible to observe multiple exchanges of energy between the light and matter before the energy dissipates. These exchanges are called vacuum Rabi oscillations, and occur at a frequency g. Still, these

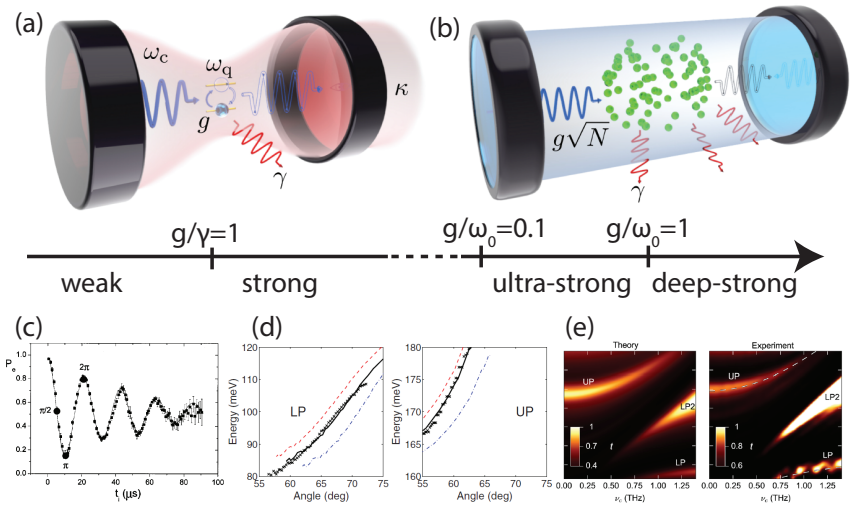

Figure 6.2: The regimes and history of light matter coupling a) A single dipole in a cavity can strongly couple to light with coupling constant g . b) multiple dipoles coupled to a single cavity mode have their coupling constant modified by the number of dipoles to $g\sqrt{N}$ (From [151]). c) observation of Rabi oscillations in entangled dipoles in a cavity (From [152]). d) The first observation of ultra-strong light-matter coupling in a quantum well microcavity with coupling to many electrons (From [153]). e) The first experimental observation of deep-strong coupling. This system couples the resonant modes of a SRR to cyclotron resonances in a stack of 2DEG quantum wells which can be tuned with an applied magnetic field.

experiments could adequately be described with first order perturbation theory, because relative to the bare frequencies of the cavity or excitation, the coupling strength was very small; on the order of 10^{-3} to 10^{-6}.

It took decades of development across different fields and approaches before it was possible to strengthen the coupling by several orders of magnitude in order to demonstrate coupling frequencies which approached the bare excitation frequencies of the systems. The key innovation which allowed this barrier to be overcome was the simultaneous coupling of couple many excitations (atoms) to the cavity mode. This leads to a result predicted by Dicke [158]; the coupling g is enhanced to $g\sqrt{N}$, where N is the number of atoms in the cavity (Figure 6.2b). The first realization of the ultrastrong-coupling (USC) regime occured in 2009 in a semiconductor microcavity embedded with quantum wells[153]. This system took advantage of the large number of electrons occupying parallel sub-bands in the quantum well which could be collectively excited

and demonstrated a normalized coupling $g/\omega_0 = 0.11$, slightly above what has become the nominal threshhold for USC of $g/\omega_0 = 0.1$, noting that now we compare the coupling frequency directly to the frequency of the excitation rather than to the loss rate of that excitation. These experiments and those that followed led to an explosion of interest in USC.

When coupling frequencies begin to approach and even exceed the bare frequencies of the coupled excitations, strange behavior begins to emerge. Formally, this is where first order perturbation theory breaks down and where higher order and even non-perturbative effects must be taken into account. the rotating-wave approximation of light-matter interactions is no longer effective and anti-resonant coupling terms must be considered in order to account for terms describing the simultaneous creation of correlated light and matter excitations. More intuitively, the matter excitations and resonant photons hybridize into polaritonic states who's characteristics can no longer be fully disentangled[159][151].

Initially, strong light-matter coupling in cavities and the like were primarily confined to the realm of atomic and molecular physics. In these systems, USC has been leveraged for applications such as high-precision measurement and quantum information processing. But the general principles of strong coupling have since been applied to a wide variety of systems, using various means to create resonant photons and to couple them to an array of different excitations in matter. In particular, advances in fabricating micron scale plasmonic structures, microcavities, and probing the resultant properties have opened up new possibilities for dressing quantum materials in order to achieve strong coupling effects. Metasurfaces, typically consisting of arrays metallic split-ring resonators (SRRs), gained initial fame for manipulation of electromagnetic (EM) waves in the far field[5][113], and can be fabricated by standard lithographic techniques on any surface of sufficient quality. Importantly, the strong resonant enhancement and localization of EM waves in the near field of SRRs provide a route for coupling to nearby materials[68].This strategy has been employed to demonstrate coupling to cyclotron resonances[71], phonons[160], and electronic transitions in semiconductors[161]. A telltale behavior of the strong coupling between

the metamaterial resonator and the quantum state is the appearance of polariton modes split by the Rabi vacuum frequency Ω_R[162]. The splitting provides a direct measure of the coupling strength, and corresponds to the frequency at which virtual photons are exchanged between the constituents comprising the coupled system[156][163]. Recent work in which metamaterials couple to the cyclotron resonance (ω_c) of semiconductor 2DEGs achieved the normalized coupling of $\Omega_R/\omega_C = 0.87$[164], and even reached beyond unity coupling of $\Omega_R/\omega_C = 1.43$ into the so-called deep-strong regime (Figure 6.2e)[165]. In the ultra-strong coupled systems, new possibilities for the manipulation of dressed quantum states are possible, including the observation of correlated virtual photon pairs[166], non-classical radiation from thermal sources[167], and sideband cooling of quantum order parameters[168] among others. Superconductors have emerged as another type of system fruitful for the study of light-matter coupling[157] offering a pathway to interrogate or manipulate superconductivity[169].

6.1.4 Superconductivity

Since its discovery, superconductivity has remained one of the most important topics in condensed matter physics. Superconductivity is a phase of matter which is purely purely quantum mechanical in nature, and occurs in some materials below a critical temperature T_c. Though many different types of materials display superconductivity and with many different critical temperatures, the state is characterized by several properties which are identical in all supercondcutors. The most conceptually straightforward of these is zero direct current (DC) electrical resistance. That is, below T_c a superconductor will transport electrical current with zero losses, even maintaining a current in the absence of any driving voltage. Superconductors are also characterized by a distinct phase transition; that is, a critical temperature T_c where superconductivity suddenly emerges. This phase transition is associated with the sudden appearance of a superconducting order parameter Ψ who's magnitude is related to the density of superconducting electrons. Third, the Meissner effect is a phenomena whereby magnetic fields penetrating a superconductor are

expelled entirely from that material once it becomes superconducting. The infinite conductivity and Meissner effect of superconductors are truly bizarre quantum phenomena, which have been leveraged for a broad array of both scientific and practical applications, with the promise of many more to come. Owing to the lossless transport of DC currents, superconductors have been

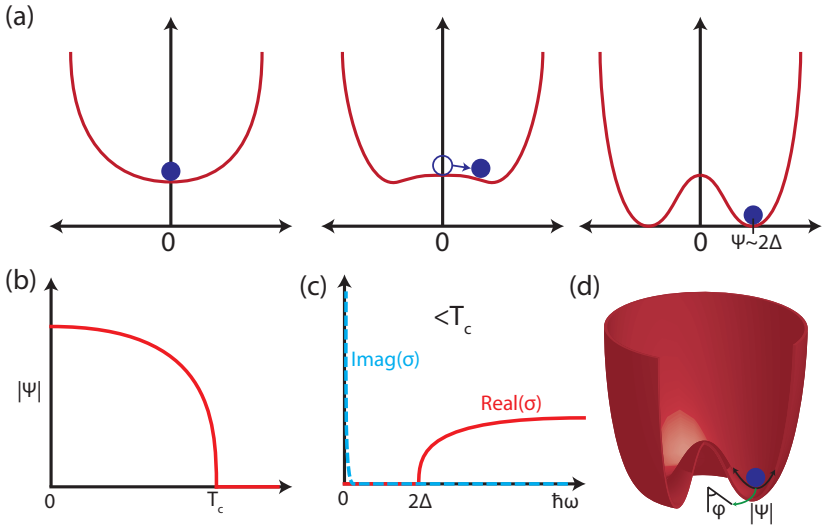

Figure 6.3: The superconducting order parameter and energy gap. a) The free energy diagram of a second order phase transition. As the potential landscape changes, the order parameter becomes finite. b) The order parameter as a function of temperature. c) The signature of optical conductivity in optical experiments: a gap opens in the real part of the optical conductivity σ while the spectral weight collapses to a delta function at zero frequency in the imaginary part. d) The complex order parameter Ψ has both amplitude and phase ϕ. An excitation of the amplitude is the Higgs mode, while an excitation of phase is the Goldstone mode.

employed to create the most powerful electromagnets in the world, in use both for scientific endeavors like particle accelerators and plasma reactors, but also in magnetic resonance imaging (MRI) devices and the like. They have been used to build superconducting circuits for computers and sensitive magnetometers where their sensitivity to magnetic fields can be leveraged. But the low temperature operation of supercondcutors remains the biggest obstacle to an entire world of other possibilities, from lossless power transmission to levitating transportation. While many of these applications are possible now, it is simply not practical in most cases to use expensive and non-renewable cryogens or power hungry refrigerators to maintain the supercondcting state. As

such, an enormous amount of effort has been directed towards a better understanding of superconductivity, higher T_c materials, and other means whereby superconductivity can be modified and controlled.

Microscopically, the mechanism of superconductivity is explained by the Bardeen, Cooper, and Schrieffer (BCS) theory [170]. Electrons are fermions and more than one cannot occupy a single state specified by a given set of quantum numbers. But in a superconductor, pairs of electrons with equal and opposite momentum and spin combine into a quasi-particle known as a Cooper pair. This Cooper pair conversely obeys Bose Einstein statistics, and as a result, many can occupy the same quantum mechanical state. The cooper pairs collapse into a single bosonic ground state at zero energy, where individual electron pairs become indistinguishable from one another. These cooper pairs have a binding energy of 2Δ, thus an excitation of at least that energy, either by a photon, phonon, or the like is required in order to break the cooper pair and return it's constituent electrons to their normal state. While in a normal metal, electrons in motion are in distinct states and scatter from ions in the crystal lattice. But in a superconductor, no scattering event below the gap energy is possible, and the cooper pairs will flow as a superfluid; without dissipation.

In optical experiments of isotropic superconductors, the signature of superconductivity is the appearance of the 2Δ energy gap at low energies: Below T_c, the real part of the optical conductivity goes to zero at low energies and is finite above 2Δ (Figure 6.3c). In practice this tells us that photons below the gap energy will not interact with the material, while photons above the gap will break cooper pairs and increase the normal state electron population of the superconductor. Meanwhile, in the imaginary part of the conductivity, the density of states below the gap collapse into a delta function at zero frequency, that is to say, the conductivity at zero frequency is infinite. Thus the Meissner effect and zero resistivity is manifestly a DC effect.

The 2Δ energy gap in optical conductivity is directly related to the emergence of a superconducting order parameter Ψ in Ginsburg-Landau theory [171]. This theory is an evolution

of the theory of second order phase transitions: as a potential surface with a minimum at $\Psi = 0$ is continuously deformed, the minimum becomes an unstable equilibrium as another minimum emerges at finite Ψ (Figure6.3a). The magnitude of this order parameter, as the eigenvalue of a Hermetian operator, is an observable, and while its precise meaning is complicated, it is related both to the proportion of electrons in the superconducting state, and to the binding energy of the cooper pairs. Figure 6.3b shows a prototypical magnitude of the order parameter as a function of temperature. But it is important to recal that as with any order parameter in quantum mechanics, Ψ has not only a magnitude but also a phase: $\Psi = |\Psi|e^{j\theta}$. While the former is measurable as we have seen, the latter is not. Furthermore, the potential surface which characterizes the free energy is completely degenerate in θ. Thus it forms the farmiliar "mexican hat potential" where the magnitude of Ψ is the same for any value of θ (Figure 6.3d). Due to this degeneracy, and the nature of the second order phase transition, there is no telling what value of θ the system will adopt upon crossing the superconducting thresh hold. While this may seem meaningless (after all, the phase cannot be measured), the value of θ does determine how the superconducting condensate will interact with other quantum systems.

6.1.5 The Josephson Effect

The Josephson effect is a direct and macroscopic manifestation of the interaction of two nearby superconducting condensates. A Josephson junction is formed when two superconducting regions with order parameters $\Psi_1 = |\Psi_1|e^{j\theta_1}$ and $\Psi_2 = |\Psi_2|e^{j\theta_2}$ respectively, are separated by an insulating region (Figure 6.4a). As the superconducting condensate collectively occupies a single bosonic state, its coherence length is relatively long, and the tails of the wave function reach well into the dielectric function and even into the adjacent superconducting region. The result is that for a small enough insulating layer, there is a significant overlap of the wave functions of Ψ_1 and Ψ_2 (Figure 6.4b). This overlap can result in the quantum tunneling of cooper pairs across the gap from one superconducting region to the other. While macroscopic scale quantum tunneling is exciting

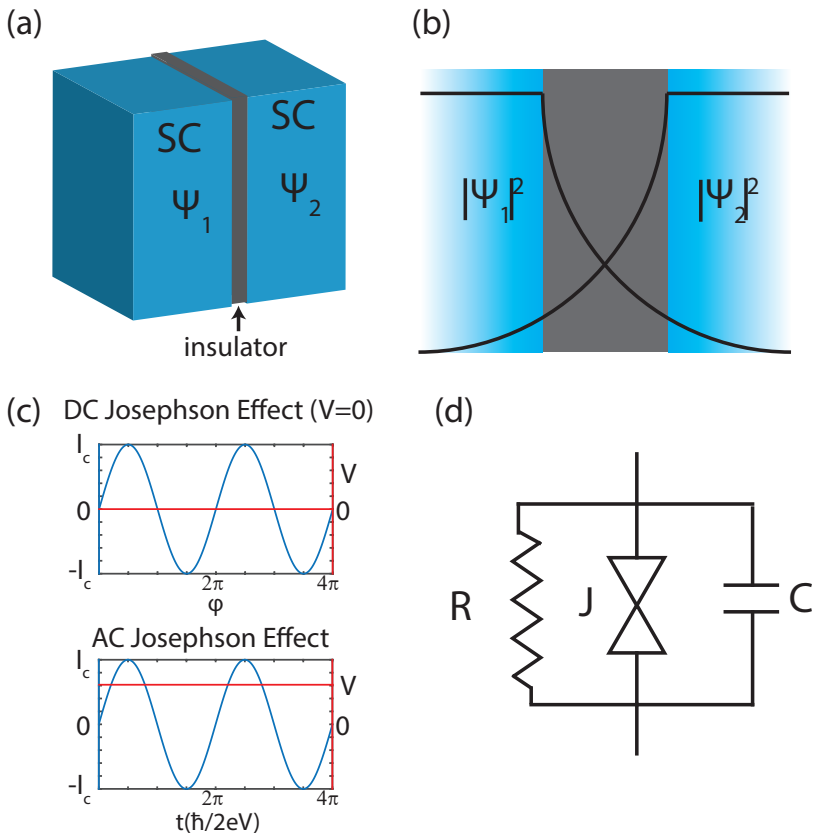

Figure 6.4: a) A schematic of a josephson junction; two superconducting reigons with order parameters Ψ_1 amd Ψ_2 separated by a thin insulating regions. b) The long coherance lenth of the superconducting condensate result in significant overlap of the wave functions across the insulating gap. c) Top: The DC josephson effect: in the absence of an applied voltage, a DC current will be generated which depends sinusoidally on the phase difference between the two superconducting reigons. Bottom: The AC jospehson effect: A constant applied voltage results constant rate of change of the phase difference, in turn resulting in an oscillating tunneling current. d) A Josephson junction can be approximated as a circuit with capacitance, resistance, and kenetic inductance.

in an of it's self, the Josephson effect has applied in a wide variety of contexts in both scientific and practical applications. For the former, Josephson junctions have been studied for a variety of purposes, and as has already been mentioned, in many of the pioneering experiments involving strong light matter coupling[157]. Likewise the unusual properties of the Josephson junction give them exceptional properties for applications where the a sensitivity to stimuli approaching the theoretical limits set by quantum mechanics are necessary. They have been put to use in

superconducting quantum interference devices[172], highly sensitive transistors[173], digital electronics[174], and others, with the promise of many others to come. As with superconductivity in general, the chief impediment to adoption in technology is the cryogenic temperatures required to maintain the superconducting state.

The the Josephson effect arises due to the difference in phase between the two superconducting order parameters in the two superconducting regions $\theta_1 - \theta_2 = \phi$. The result of this phase difference is a superconducting tunneling current across the junction, and is captured in the so-called first Josephson equation:

$$I(t) = I_c sin(\phi(t)) \tag{6.11}$$

Where I_c is the critical current. This expression tells us that the current across the Josephson junction will vary sinusoidally with the phase difference between the two sides. Counter intuitively, this implies that a DC current can flow through the junction even in the absence of any applied voltage (Figure 6.4c top). This is the DC Josephson effect. The second Josephson equation tells us how the phase difference ϕ evolves over time:

$$\frac{\partial \phi}{\partial t} = \frac{2e}{\hbar} V(t) \tag{6.12}$$

where $V(t)$ is a voltage applied across the junction. This indicates that the phase will advance linearly in time as a DC voltage is applied. Considering this situation in the context of equation 6.11, this indicates (again counter intuitively) that when a DC bias is applied, the result will be an oscillating current across the junction. This is the AC Josephson effect (Figure6.4c bottom) and thus a Josephson junction can act as a near perfect DC-AC transducer.

While the consequences of the Josephson effect are many fold, it is useful for illustrative purposes to put these effects into a more farmiliar context: a RLC circuit. Beginning with a re-aragement of the definition of inductance $V = L\frac{dI}{dt}$, we can plug in equation 6.11. Arriving at

$V = LI_c cos(phi(t)) \frac{\partial \phi}{\partial t}$ we can plug insert equation 6.12 and rearrange to finally arrive at:

$$L = \frac{\hbar}{2eI_c} sec(\phi(t)) \tag{6.13}$$

This amounts to an unusual nonlinear inductance. It is worth noting that this inductance does not originate from energy stored in a magnetic field as it does in a more typical situation. Instead this inductance derives from the kinetic energy of the tunneling pairs. Their inertia effectively takes on the role of lenses law, resisting changes to the flow of electrons. The origin of the capacitance in this situation is much more straightforward. A josephson junction is simply two conducting plates separated by an insulator, and as such, the capacitance is determined in the ordinary way. Though the superconducting currents are ostensibly lossless at zero frequency, dissipation effects in the finite voltage regime can be captured with a resistor when the currents exceed the critical current I_c and normal state quasiparticles emerge. The result is a parallel, nonlinear RLC circuit, or more accurately a resistively and capacitively shunted junction as depicted in Figure 6.4d. The total current across the junction then becomes:

$$I = I_c sin(\phi) + \frac{V}{R} + C\dot{V} \tag{6.14}$$

This can be written in the form of a nonlinear differential equation with a form similar to those we saw earlier in section 2.1.1.

$$\ddot{\phi} + \beta_c \dot{\phi} + sin(\phi) = \frac{I}{I_c} \tag{6.15}$$

Where $\beta_c = \omega_J RC$ determines the damping and the characteristic resonant frequency is $\omega_J = \sqrt{2eI_c/\hbar C} = 1/\sqrt{L_0 C}$. This LC resonance corresponds to the resonance of the nolinear circuit in the limit where phase differences are small. Thus through equation 6.15 we have a more farmilar way of adressing the electrodynamics of a Josephson junction. It is worth noting that this

differential equation has a mechanical analogue in the form of an unusual pendulum, and while I will not discuss it here, it is useful for understanding the dynaics of the josephson junction, particular under large biases [175].

As it turns out, Josephson junctions are not strictly artificial constructions nor are they always of macroscopic construction. In many cases, the crystal structure of superconductors create intrinsic Josephson junctions, where the unit cell of the crystal result in superconducting reigons seperated by effectively insulating barriers.

6.1.6 High T_c Superconductivity in Layered Cuprates

Initially superconductivity was only thought to exist in a hand full of elemental metals and only at extremely low temperatures; just a few Kelvin. These "type 1" superconductors such as Sn, Al, Pb, and Hg displayed perfect diamagnetism up to a critical magnetic field H_c. For most of the 20th century, it was believed that BCS theory disallowed superconductivity above 30K. In 1986, Bednorz and Muller discovered superconductivity at a previously unheard of 35K, $La_{5-x}Cu_5O_{5(3-y)}$, a Lanthanum based perovskite[176]. This discoverery resulted in a renewed frenzy of scientific and popular attention as theorists scrambled to understand how this result was possible, and as hope for more practical and even room temperature superconductivity was renewed. In these type II superconductors, all magnetic fields will be expelled from the superconductor until a critical field value H_{c1} is reached. At this point, individual quanta of magnetic field will penetrate though the superconductor, with more and more appearing as the fields are increased. Upon reaching the second critical field value H_{c2}, the superconductivity will fail and the material will enter its normal state. Superconducitivity has remained one of the major focuses of condensed matter physicsists the world over new means of understanding and controlling superconductivity have been developed. Efforts to create a higher T_c have driven ever more sophisticated synthesis and crystal growth and treatment techniques employing epitaxial strain, heterostructures, unconventional superconductor searches and beyond. But so too have the

efforts to manipulate superconductivity by other means, in particular, the use of light.

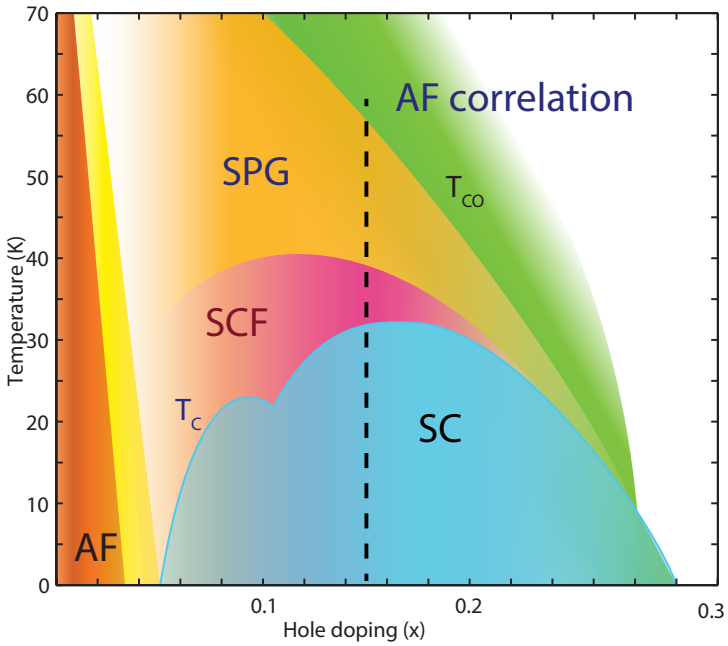

Figure 6.5: The phase diagram of hole doped $La_{2-x}Sr_xCuO_4$. The experiments presented later in this section use a crystal with x=0.15 for which T_c is 32K. It is marked with a dashed vertical line.

Specifically, layered high-T_c superconducting cuprates such as $La_{2-x}Sr_xCuO_4$ (LSCO) have demonstrated complex phenomena associated with interlayer Josephson effects[109][177]. The phase diagram of LSCO as a function of hole doping x and temperature is shown in Figure 6.5 and a unit cell of LSCO is shown schematically in Figure 6.6a. LSCO has a perovskite crystal structure. In each unit cell there is a single CuO_2 layer (top and bottom) which lies on the plane parallel to the a and b-axes. This plane consists of Cu^{2+} at the center of a square of O^{2-} ions. With the addition of another oxygen ion above and below, the copper, the oxygen forms an octahedral cage around the copper ion. Along the c-axis, adjacent CuO_2 plane are separated by La^{3+} and Sr^{2+} ions such that the CuO_2 planes become relatively weakly coupled.

As shown schematically in Figure 6.5, At x=0, the undoped parent compound La_2SrCuO_4 is an mott-insulator with antiferromagnetic ordering at low temperatures. As trivalent La is

replaced with divalent *Sr*, mobile holes are introduced into the CuO_2 planes which lead to conductivity. For doping above 5% the material becomes superconducting at very low temperatures. As the hole doping is increased further, the superconducting phase grows. At approximately 1/8th doping, the superconducting dome grows considerably and T_c reaches a maximum at 32K at about x=0.15 (the doping of the crystal we will be examining later). In this superconducting phase, cooper pairs move without resistance in the CuO_2 (ab) plane, but not along the perpendicular c-axis. In this direction, the electrodynamics are dominated by quantum tunneling between the CuO_2 layers, i.e. the Josephson effect.

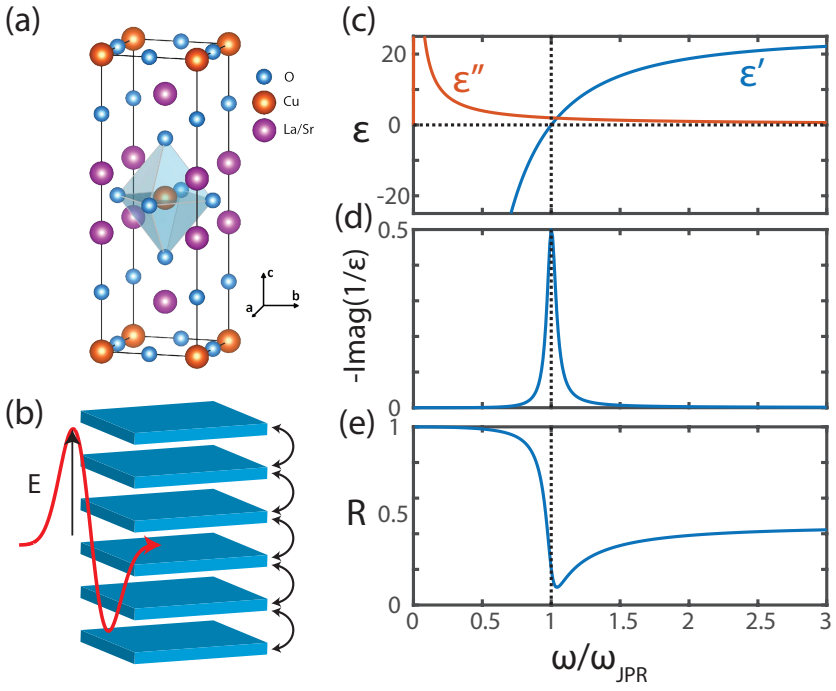

Figure 6.6: The Jospehson effect in layered cuprates. a) The unit cell of $La_{2-x}Sr_xCuO_4$. Below T_c it effectively consists of a stack of CuO_2 planes weakly coupled along the c-axis. b) This crystal structure effectively forms an intrinsic stack of Josephson junctions along the c-axis. Applying an electric field along the c-axis by mean of illumination with a THz pulse drives collective oscillations in the superconducting order parameter between layers. c) The real (blue) and imaginary (orange) parts of the c-axis permittivity of a prototypical layered cuprate superconductor. The real part of epsilon (ε') crosses zero at the JPR. d) the loss function peaks at the JPR. e) The reflectivity of a layered cuprate with the field polarization parallel to the c-axis. Around ω_{JPR} there is a characteristic Drude-like plasma edge which is the telltale spectroscopic signature of the JPR.

Below T_c, LSCO can be modeled as a stack of superconducting CuO_2 layers weakly coupled along the c-axis (Figure 6.6b). The system behaves as a series of Josephson junctions, exhibiting a collective phase oscillation at the Josephson Plasma Resonance (JPR) frequency. The behavior of a semi-infinte stack of Josephson junctions requires a more sophisticated approach than that presented in the previous section. Such an approach can be found in [178] and [179]. Fortunately, in the limit of uniform phase differences along the c-axis, the nonlinear differential equation which governs the evolution of ϕ on the layers is very similar to the one we have already seen in equation 6.15. This leads to a natural frequency of $\omega_J = c/(\lambda_c\sqrt{\varepsilon_r})$, the so called Josephson plasma resonance (JPR). Here, $c/\sqrt{\varepsilon_r}$ is the light velocity along the c-axis while λ_c is the c-axis penetration depth. In order to probe this collective oscillation of tunneling electrons, it is necessary to apply a resonant alternating bias to the c-axis of the layered cuprate.

Fortunately, the JPR typically lies in the THz regime and is thus accessible with the THz techniques that have been discussed previously in 3.3.1. The simplest model which adequately captures the c-axis response of superconducing layered cuprates is the "two fluid" model. This model is a modification of the farmiliar Drude model of electrical conduction; a simple and fully classical theory which describes free electrons in a conductor as being classical particles which undergo elastic collisions with the static ions. In this model, resonant excitations of the electron plasma occur at $\omega_p = \sqrt{\frac{ne^2}{\varepsilon_0 m}}$ where n is the number density of electrons, e is their charge and m is their effective mass. In the two fluid model, there are considered to be two seperate electron gasses. The superconducting electrons are treated as a lorentzian oscillator which peaks at zero frequency and has no damping, while the normal state carriers are approximated as a second lorentzian oscillator with finite damping. From the drude model, the frequency dependent dielectric function along the c-axis is approximated as:

$$\varepsilon_c(\omega) = \varepsilon_\infty - \frac{\omega_s^2}{\omega^2} - \frac{\omega_n^2}{\omega^2 + i\gamma_{st}\omega} \tag{6.16}$$

Where ε_∞ is the high frequency dielectric constant, ω_s and ω_n are the superfluid and normal carrier plasma frequencies respectively, and γ_{st} is the damping frequency of the normal carriers. The real (blue) and imaginary (red) part of such a dielectric function are shown in Figure 6.6c. Because both oscillators peak at zero frequency, the real part of ε_c is singular and negative at ω=0. However, as the frequency increase, it crosses zero before asymptotically approaching the high frequency permittivity ε_∞. This zero crossing corresponds to a longitudinal resonant mode and occurs at approximately $\omega_s/\sqrt{\varepsilon_\infty}$. This is the Josephson plasma resonance. It can be unambiguously identified by a peak in the loss function $-Imag(1/\varepsilon_c)$ shown in Figure 6.6d. But in a more realistic experimental scenario in which the c-axis of a layered cuprate is illuminated with light polarized parallel to the c-axis, the JPR can be identified by a characteristic plasma edge in reflection measurements (Figure 6.6e). This plasma edge is qualitatively identical to those which occur at metallic plasma frequencies in gold, aluminum, and the like, albeit at a far lower frequency.

The JPR in LSCO has been studied extensively, and manipulation of the superconducting phase via optical excitation of the JPR has been accomplished by microwave cavity cooling[180], optical pumping[181], and high field THz excitation[182]. However, dressing of the JPR with microstructures has remained elusive[183]. Epitaxial thin films of LSCO which would be suitable for the deposition of metamaterials have an exposed ab-plane, precluding the possibility of coupling incident light to the c-axis JPR[184]. Fortunately, large single crystals of LSCO can be grown and cut to expose a large c-axis surface. However, direct fabrication of metasurfaces on such precious samples using photolithography would make it challenging to perform systematic studies of light-matter coupling in order to perform a parametric sweep necessary to observe an avoided crossing.

6.2 Metamaterial Coupling to the JPR: Preliminary Measurements

In our inital measurements, we identify evidence of strong coupling between the c-axis JPR of LSCO and the inductive-capacitive (LC) resonance of a metamaterial through observation of an avoided resonance crossing; a signature of strong coupling. At 15% Sr doping, and well below T_c=32K (8K) the JPR resonance frequency is $\omega_{JPR} = 1.53THz$. In order to parametrically sweep the LC resonance frequency across the JPR we fabricated a series of flexible and interchangeable metasurface tapes and adhered them to the c-axis of the LSCO. We fabricated three tapes: One with a resonant frequency $> \omega_{JPR}$, one near ω_JPR, and one below ω_{JPR}. We performed FTIR spectroscopy measurements in reflection on the resulting hybrid superconducting metamaterials (HSMMs) and validated the results with numerical simulations, indicating a normalized Rabi frequency of $\Omega_R = 0.29$. Furthermore, we use these simulations to extend these results for arbitrary metamaterial resonance frequency in order to unambiguously delineate the avoided resonance crossing, explore the nearfield behavior of the HSMMs, and investigate routes toward excitation of hyperbolic waveguide modes in the LSCO.

6.2.1 Fabrication

The metamaterial tapes consist of a flexible polyimide tape patterned with 200 nm thick Au SRRs, where the linewidth, periodicity, gap size, and edge length of the SRR is scaled uniformly to achieve the three desired frequencies (Figure 6.7). The fabrication process is similar to the process described in section 3.2.1. It begins with polyimide spin coated (thickness of $8\mu m$) onto a silicon wafer coated with a sputtered silicon nitride film to facilitate the removal of the polyimide from the substrate[185]. Subsequently, the periodic array of SRRs consisting of 200 nm thick gold is patterned using direct laser writing. The nominal dimensions of the three metamaterial tapes are shown in table 6.1. The metamaterial (MM) tapes can be peeled off of the

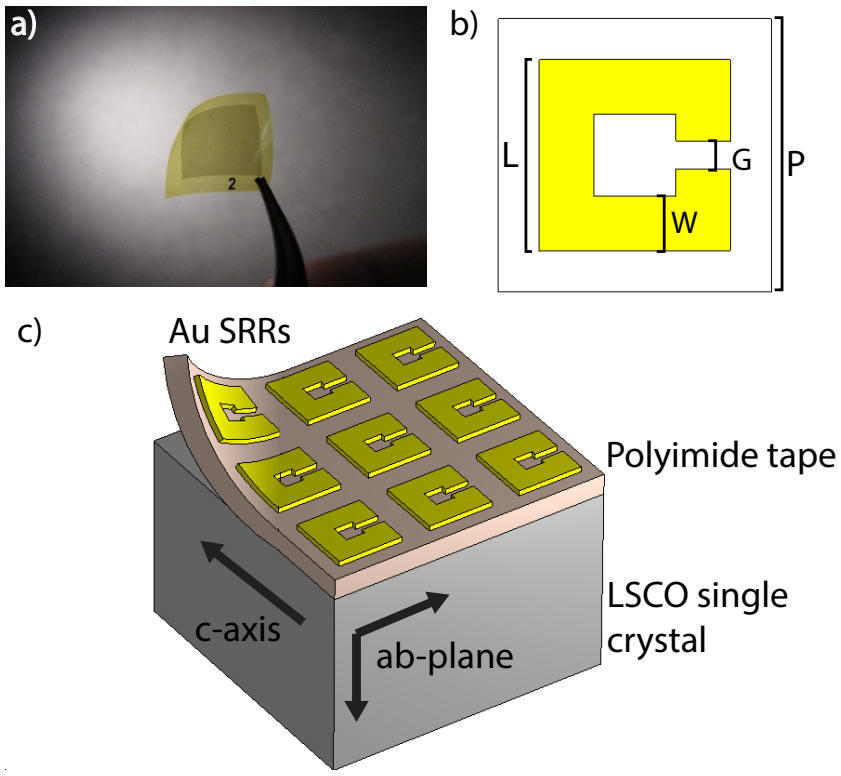

Figure 6.7: a) A photo of the polyimide tape with SRRs. b) Schematic of metamaterial unit cell. c) Schematic of hybrid superconducting metamaterial.

substrate (Figure 6.7a), and pressed onto the LSCO such that the capacitive gap is parallel to the c-axis. Figure 6.7c shows a schematic of the HSMM. In this geometry, the polyimide serves as a dielectric spacer layer between the SRR and LSCO, preventing the LSCO from shorting the plasmonic resonance of the SRR. The LSCO single crystal was grown by the travelling-solvent floating-zone method[186]. The large single crystal is oriented by LAUE diffraction and cleaved along the a-c plane. We perform reflection spectroscopy measurements of the LSCO and HSMM samples with the polarization parallel to the c-axis using a Bruker FTIR IFS-66 spectrometer.

6.2.2 Measurement

The LSCO JPR response was first characterized in the absence of the MM tapes. At T=8 K (well below T_c=32K) the characteristic reflectivity feature associated with the JPR occurs at

Table 6.1: The dimensions of the three metamaterial tapes.

	P (μm)	L (μm)	W (μm)	G (μm)	ω_{LC} (THz)
Tape 1	20	14	3.8	2.0	2.9
Tape 2	36	25.2	8.5	3.6	1.9
Tape 3	52	8.5	11.5	5.2	1.24

ω_{JPR}=1.53THz as shown by the black dots in Figure 6.8a. The c-axis response of layered cuprates can be expressed using the two-fluid model of the permittivity

$$\varepsilon_c(\omega) = \varepsilon_\infty - \frac{\omega_s^2}{\omega^2} - \frac{\omega_n^2}{\omega^2 + i\gamma_{st}\omega} \tag{6.17}$$

where ε_∞=27 corresponds to the high frequency dielectric constant, ω_s = 8THz is the plasma frequency of the superconducting carriers, ω_n = 21.3THz and γ_{st}=150THz are, respectively, the plasma frequency and the scattering rate of normal state carriers. The numerical values are suitable at T=8K[109]. In general, the plasma frequency ω_s^2 is strongly temperature dependent. Furthermore, it is well known that in near optimally doped cuprates, spatial inhomogeneities result in a distribution of JPR frequencies. This in turn results in a broadened loss function and associated JPR plasma edge. We broaden the JPR with a Gaussian distribution with a width of 0.5THz in order to more closely model the experimentally observed response[187]. The solid black line in Figure 6.8a shows the fit to the reflectively computed from this model. Some discrepancies between the model and the measurements persist due to imperfect referencing.

Subsequently, the MM tapes were adhered to the LSCO crystal and room temperature FTIR measurements were performed to identify the resonant frequencies of the MM tapes in the absence of the JPR (Figure 6.8b-d). The LC resonance is the lowest frequency resonance of the metamaterial, corresponding to the reflection maxima which occur at ω_{MM1} = 3 THz, ω_{MM2} = 1.9 THz, and ω_{MM3} = 1.2 THz for MM tape 1, 2, and 3, respectively. Likewise, this is the frequency for which the enhancement of the incident EM fields in the capacitive gap of the SRR will be

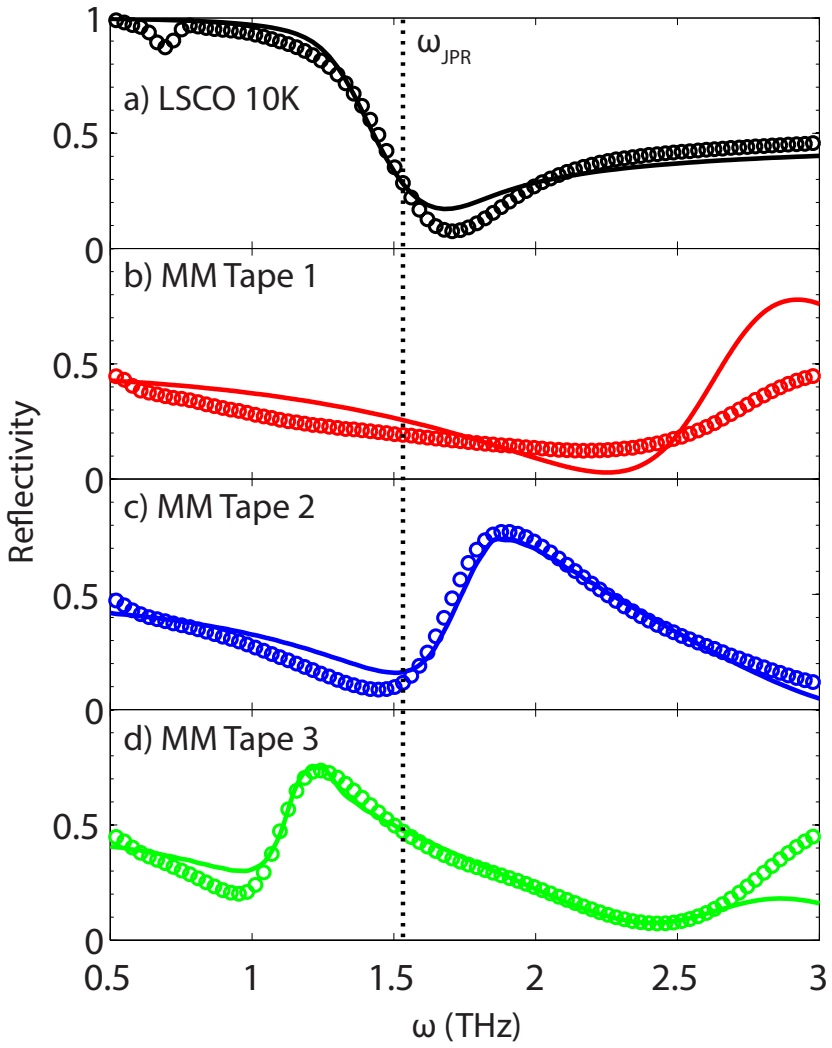

Figure 6.8: a) Reflection spectroscopy of LSCO at 10K (circles) with a two fluid model fit (solid line), and MM Tapes b) 1, c) 2, and d) 3 on LSCO at 300K (red, blue, and green circles) and FDTD simulations (solid lines).

largest. We model these results using the commercial finite difference time domain (FDTD) solver CST[138] and find good agreement (solid lines). In these simulations, gold is modeled as a lossy metal with conductivity σ = 4.56e7 S/m, polyimide as a lossy dielectric with permittivity ε_{PI} = 3.5+i0.01, and the LSCO above T_c is modeled as an isotropic dielectric with permittivity of $\varepsilon = \varepsilon_\infty = 27$. Overall, the agreement between experiment and simulation is reasonable and demonstrates that, above T_c, the electromagnetic response is what is expected for SRRs placed on

top of a nominally dielectric substrate (i.e. the c-axis is effectively dielectric and dominates the overall electromagnetic response, while conductivity in the ab-plane has little effect).

The reflectivity of each of the HSMMs was measured at 8K (¡ T_c = 32K) as shown in Figure 6.9(a) (c). In the presence of the MM tapes, the JPR is redshifted because of the polyimide to $\omega_{sJPR} = \omega_s/\sqrt{\varepsilon_{infty} + \varepsilon_{PI}}$=1.44 THz (Figure 6.9 vertical line). HSMM 1 (red circles) shows a resonant reflection peak at 3THz= ω_{MM3}, well separated from the Josephson plasma edge at ω_{sJPR}. This is a typical response for a SRR on a dielectric substrate (see 6.8b), since well above ω_{sJPR} the c-axis of the LSCO acts as a lossy dielectric. In Figure 6.9b, the results for HSMM 2 (blue circles) are shown. There is a reflection maxima characteristic of a MM resonance at 1.9 THz (similar to the room temperature case in Figure 6.8c) and, additionally, a plasma-like edge at 1.3 THz which is clearly red-shifted relative to ω_{sJPR} = 1.44 THz. This is indicative of coupling between the MM tape and the LSCO as discussed in greater detail below. For HSMM 3 (green circles, Figure 6.9c), the Josephson plasma edge is again obvious, but there is a clear reflection minimum at 1THz. At this frequency, the c-axis LSCO surface is highly conductive exhibiting near unity reflection. As a result, this narrow absorption band can be intuitively understood using the same formalism as for metamaterial perfect absorbers; near the resonance frequency of the MM, destructive interference between light initially reflected from the MM surface and light which is transmitted through, reflected internally by the LSCO, and subsequently transmitted through the MM surface results in a strong and narrow absorption feature[99].

We compare these results to full wave FDTD simulations (solid lines). In these simulations the gold and polyimide are modeled as in the previous section, whereas the LSCO at 8K is modeled as an anisotropic superconductor. This c-axis response is as described above while the ab-plane permittivity used in the simulation is determined from experimental measurements[188]. For the c-axis complex permittivity we use the parameters used to the fit Figure 6.8a with Equation 6.17 including the Gaussian broadening previously mentioned. We find fair agreement between the experimental reflectivity and simulations with much of the discrepancy likely due

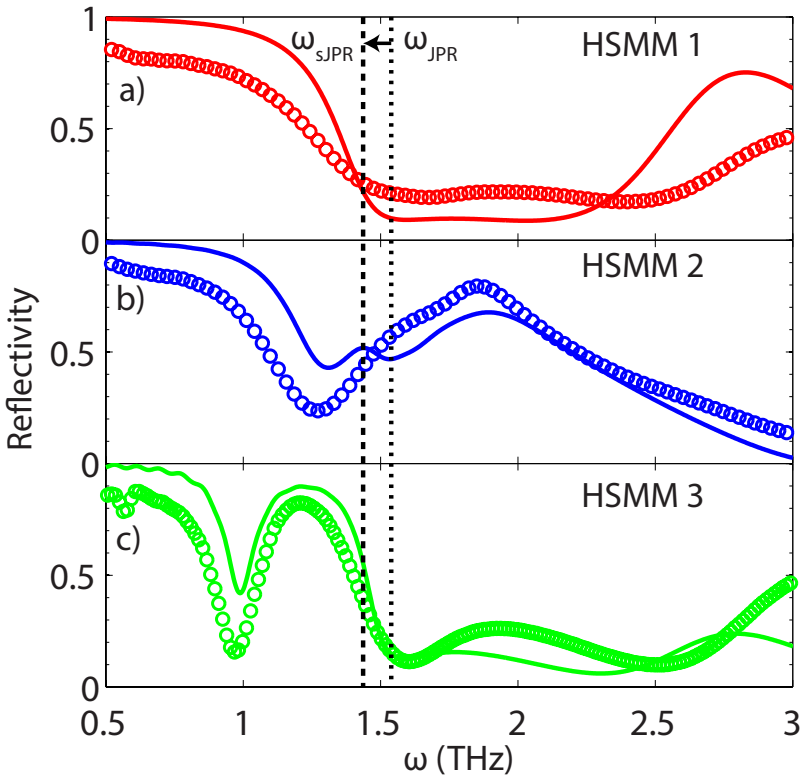

Figure 6.9: Reflectivity of MM tapes on LSCO at 8K for MM tape a) 1, b) 2, and c) 3 (circles), and corresponding FDTD simulations (solid lines). A dotted vertical line indicates the screened JPR at ω_{sJPR} = 1.44THz.

to the disagreement between the modeled and measured c-axis properties (See Figure 6.8a). Nonetheless, the agreement is sufficiently good such that we can investigate the electrodynamic response in greater detail using simulations with a finer sweeping of the SRR geometry (and therefore the resonance frequency) than is possible in experiment.

6.2.3 Discussion

We performed additional simulations as shown in Figure 6.10 to retrieve reflectivity spectra for MM tapes of arbitrary resonant frequency in order to more fully understand the experimental results. Here, MM denotes the frequency of the metamaterial resonance on LSCO

above T_c where ε= 27. The diagonal dashed white line tracks $\omega_{MM} = \omega$. The horizontal lines at ω_{MM1} (red), ω_{MM2} (blue), and ω_{MM3} (green) correspond to the three resonance frequencies for which experimental measurements were performed (i.e. Figure 6.9a-c). The vertical dotted line denotes ω_{sJPR}= 1.44THz. At frequencies higher than the JPR, the LC resonance manifests (as expected) as a broad reflection maximum. But as ω_{MM} approaches at ω_{sJPR}, this reflection feature is suppressed, and an avoided crossing occurs. For $\omega < \omega_{sJPR}$, a narrow absorption band emerges, indicative of the LC resonance of a metamaterial in the presence of a conducting ground plane. This reflection minima emerges from the plasma edge at ω_{sJPR} = 1.44THz, and diverges from it, eventually asymptotically approaching $\omega_{MM} = \omega$ for small values of MM. For lower values of ω_{MM}, additional polaritons emerge below ω_{sJPR} first at ω=1.3 and ω_{MM}=0.9 and again at ω=1.3 and ω_{MM}=0.5. These are associated with the higher order dipole and quadrupole modes of the MM, respectively. Clearly, a rich electromagnetic response is observed upon sweeping ω_{MM} from 0.5 to 3.0 THz.

To interpret the observations, we modify Equation 6.17 as follows. The optical response of the HSMM is assumed to be the sum of two oscillators; a Drude response representing the Josephson plasmon , and a Lorentzian oscillator corresponding to the MM tape. The contribution of the normal carriers is adequately captured by adding an effective damping term to the Josephson plasmon. The total effective permittivity parallel to the c-axis can be expressed as:

$$\varepsilon_c = \varepsilon_{eff} - \frac{\omega_s^2}{\omega^2 + i\gamma_a\omega} + \frac{F}{\omega_{MM}^2 - \omega^2 - i\gamma_b\omega} \tag{6.18}$$

where $\varepsilon_{eff} = \varepsilon_\infty + \varepsilon_{PI}$ =30.5 is the effective permittivity at high frequency. The second term is the Drude response of the Josephson plasmon, with ω_s=8 THz and γ_a=0.28 THz. We represent the JPR with a single Drude response rather than the two-fluid model used previously in Equation 6.17; this simplified model is adequate for the present purposes to understand the effective response of the HSMMs. ω_{MM} is the LC resonant frequency of the MM tape while the damping

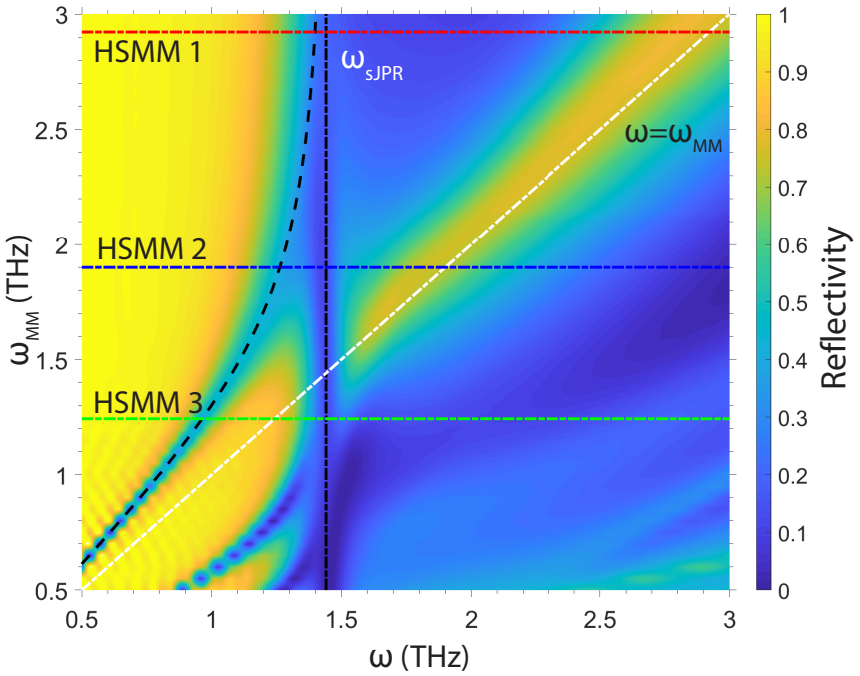

Figure 6.10: Extended FDTD simulation results showing reflectivity as a function of arbitrary metamaterial tape resonant frequency. MM tape frequencies used in experimental measurements are marked by dotted horizontal lines in red, blue, and green for tape 1, 2, and 3 respectively. A vertical black dotted line marks sJPR, and a diagonal line tracks $\omega = \omega_{MM}$. Black dashed line tracks the low frequency polariton of the dielectric function from Eqn. 6.19.

rate is given by γ_b =0.8 THz. $F(\omega_{MM})$ acts as a fitting parameter but generally represents the MM oscillator strength which is related to the geometry and the filling fraction of resonators[32][68].

The Lorentzian MM response has a pole at $\omega_{MM} = \omega$, corresponding to a transverse mode associated with the resonance of the metamaterial. The JPR response (i.e. the first two terms of Eqn. 6.18) has no finite frequency transverse modes, but exhibits a longitudinal mode when the sum of the terms equals zero, which occurs at the screened JPR ω_{sJPR}=1.44 THz. This is analogous to the situation that occurs in a doped semiconductor where the plasma frequency overlaps with an optical phonon mode[189][190]. Coupling leads to mode splitting and the emergence of a new longitudinal (polaritonic) mode. A similar coupling arises in HSMMs.

To obtain the longitudinal mode coupling, we simply set tot=0, and solve to obtain the

roots:

$$\omega_{\pm} = \frac{1}{\sqrt{2}}\left[\omega_{MM}^2 + \frac{\omega_s^2 + F}{\varepsilon_{eff}} \pm \sqrt{\left(\omega_{MM}^2 + \frac{\omega_s^2 + F}{\varepsilon_{eff}}\right)^2 - \frac{4\omega_s^2\omega_{MM}^2}{\varepsilon_{eff}}}\right]^{\frac{1}{2}} \tag{6.19}$$

We use F as a parameter to fit the solution for the lower polariton ω_- plotted as a black curved line in Figure 6.10. For large values of MM the polariton follows the longitudinal mode of the LSCO at ω_{sJPR}. But as ω_{MM} decreases and approaches $\omega_{MM} = \omega_{sJPR}$, the polariton undergoes an avoided crossing, before asymptotically approaching the MM transverse mode along $\omega = \omega_{MM}$. By evaluating the polariton frequencies at ω_{MM}=ω_{sJPR}, we can also estimate the strength of the normalized coupling constant as:

$$\frac{(\omega_+ - \omega_-)}{2\omega_{sJPR}} = \Omega_R = 0.29 \tag{6.20}$$

This splitting and coupling can be viewed classically as a simple consequence of the linear absorption and dispersion of the effective dielectric function, or as a manifestation of vacuum Rabi splitting[191][192][193]. Making a clear-cut distinction between weak and strong coupling in this scenario is difficult, particularly due to the frequency dependent damping of the MM. That being said, a normalized coupling constant of Ω_R=0.29 falls within the strong coupling regime as defined by[194] even for conservative choices of oscillator parameters.

This approach provides some insight regarding the nature of the avoided crossing as well as the role that various parameters play in the observed spectra as well as the coupling. The terms under the square root determine the magnitude of the splitting between the coupled modes, and thus the coupling strength. In particular, the oscillator strength of the MM tape, F, is dependent on the design parameters of the MM and thus, can be optimized for stronger coupling. This approach does not, however, account for higher frequency modes of the SRRs, which are apparent at small values of ω_{MM}. We note that the upper and lower polaritons are highly asymmetric, with the latter appearing to have a far larger coupling constant (as evidenced by the rapid divergence

from ω_{sJPR} as ω_{MM} decreases). This is not unusual in coupled systems where radiative losses depend strongly on frequency[195]. In HSMMs in particular, above ω_{sJPR} (where the c-axis of the LSCO acts as a dielectric), the resonance has a low quality factor as is typical for SRRs above a dielectric material. Thus coupling is strongly suppressed. Conversely, below ω_{sJPR}, the c-axis is metallic and the quality factor of the resonance is significantly higher (as is typical for SRRs above a metallic surface i.e. metamaterial perfect absorbers) and thus the polariton is clear. We note that this simple effective medium model is intended to provide a simple and intuitive analytical approach to understanding the response observed in experiment and in the full wave electromagnetic simulations. A more complete analytical analysis is possible, but is beyond the scope of the present work [196][197][198].

An observant reader may wonder at this point why the interference theory of metamaterial absorbers which was put to use so effectively in chapter 4 has not been summoned here. Though strictly speaking, the interference theory and equation 4.6 is correct only for a perfectly metallic and dispersionless ground plane, we can easily modify the equation to account for a ground plane surface with arbitrary complex reflectively (shown schematically in the inset of Figure 6.11):

$$r = r_{12} + \frac{t_{12}^2 r_{23} e^{i\beta}}{1 - r_{23} r_{21} e^{i\beta}} \tag{6.21}$$

Where here r_{23} is the complex reflection coefficient of the c-axis of the LSCO modeled by equation 6.17 in conjunction with the Fresnel equations. The complex transmission t_{12} and reflection r_{12} and r_{21} are retrieved from FEM simulations. The result of this interference theory calculation is shown in figure 6.11. At first glance, this result seems to qualitatively reproduce the full wave simulation, particularly for large detunings of the metamateiral tape. But in the vicinity of zero detuning, where $\omega_{JPR} \simeq \omega_{MM}$, there are considerable differences. First, the low frequency absorption band appears to approach much closer to the crossing point before veering off towwards low frequency. But more prominently, the reflection peak at higher frequency

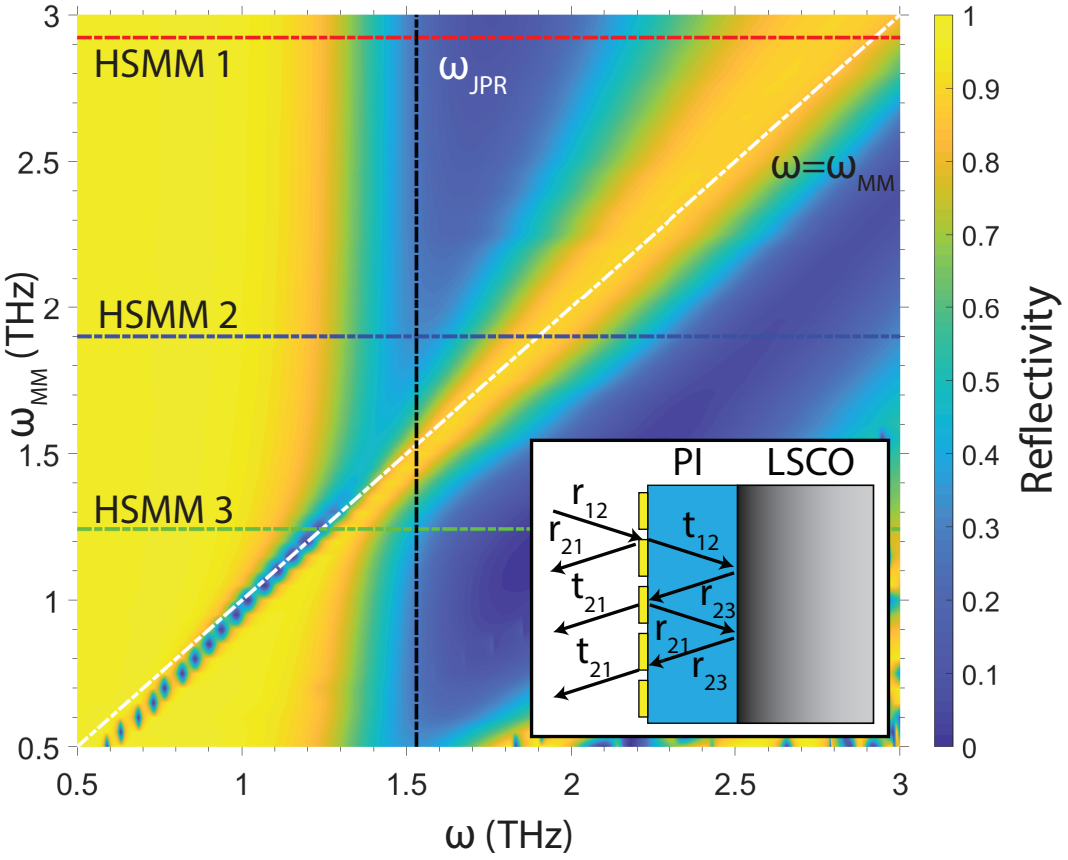

Figure 6.11: The interference theory of metamaterial absorbers applied to the HSMM. Inset: The interference theory is modified to account for a frequency dependent and complex reflection coefficient. The complex reflection and transmission of the MM layer are retrieved from simulations while the reflectively of the LSCO surface r_{23} is calculated from the two fluid model. The result is significantly different than the full wave simulation. While some regimes appear qualitatively similar, this approach fails in particular in the vicinity of the avoided resonance crossing: The reflectively at $\omega_{MM} = \omega_{JPR}$ is close to unity.

remains present as ω_{MM} is tuned down and past the JPR. There is no avoided crossing of this peak. It requires only cursory inspection of the interference theoy schematic to see why: When the metamaterial layer is resonant, r_{12}=1 and t_{12}=0. Thus at ω_{MM}, all light incident upon the HSMM will be reflected from the first surface; it does not matter what materials lie further beyond the MM layer because no light will reach them. This is not what we see in the experiments nor the full wave simulations, so clearly something more complex is occurring.

To gain further insight into JPR/SRR coupling, it is useful to examine the near field. We

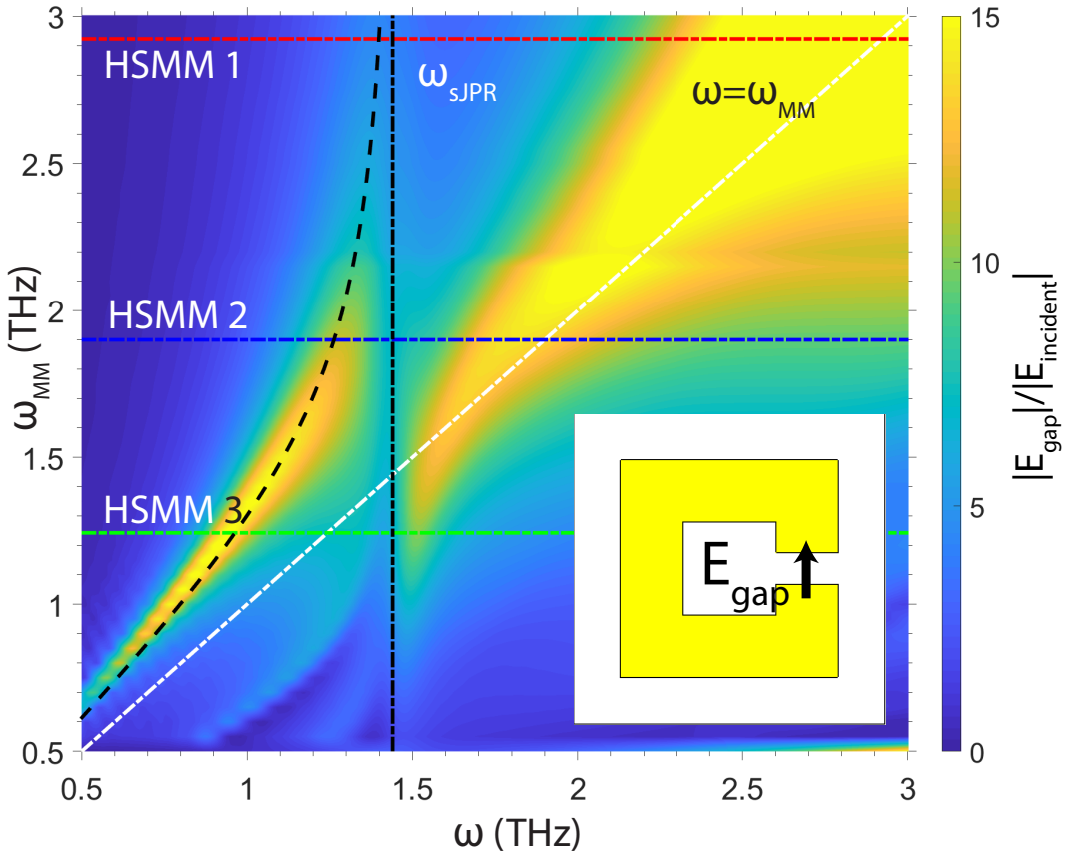

Figure 6.12: The field enhancement in the metamaterial capacitive gap as a function of frequency and metamaterial resonant frequency. Unlike the reflectively, polaritons both above and below ω_{sJPR} appear as local maxima in the field enhancement allowing for unambiguous identification of the avoided crossing. Inset: The location on the SRR where the fields are being probed.

performed FDTD simulations to probe the fields in the SRR gaps as a function of metamaterial tape frequency ω_{MM}. We present the result in Figure 6.12. Because this field enhancement is at a maximum when the SRR is resonantly excited, it can serve as a useful proxy to identify the coupled polaritons of the HSMM. This approach is less ambiguous than examining the reflectively as both above and below the JPR, the resonances appear as maxima in the field enhancement. This approach unambiguously shows a broad peak which begins at high frequencies and approaches ω_{sJPR} as ω_{MM} is decreased. But at the crossing the peak is strongly suppressed. Meanwhile, below the JPR, field enhancement peak emerges close to ω_{sJPR} but avoids the crossing point by a far larger margin before asymptotically approaching ω_{MM} at low frequencies. Witih this

approach, an asymmetric avoided crossing is obvious and validates our previous interpretation of the evolution of the HSMM reflection spectra.

We can further support this interpretation by examining the surface currents and electric field distributions elsewhere in the HSMM at specific frequencies (Figure 6.13). In Figure 6.13a we show the magnitude of the electric field measured at the center of the SRR gap, normalized to the magnitude of the incident electric field for each of the three HSCMMs that were experimentally investigated. Across much of the spectral region for all 3 HSCMMs, there is a significant enhancement of the incident field, due to resonant accumulation of charges on the opposing sides of the capacitive gap. The peaks in the local field enhancement occur at nearly the same frequencies where features in the far-field spectroscopy appear. For each of the HSCMMs, open (closed) circles in Figure 5a indicate frequencies at which minima (maxima) in the experimental reflectivity spectra occur that, as previously discussed, are tied to the lower (upper) polaritons. Identifying the polariton modes through the local electric field, where both lower and upper polaritons appear as local maxima, simplifies their identification, and their close correspondence to spectral features lends additional evidence to our interpretations of the experimental spectra.

Figure 6.13 b and c show the electric field distributions in the LSCO and the surface currents on the SRRs for HSMM 2, where the MM resonance is tuned close to the JPR and, as described above, Ω_R=0.29. Figure 5b shows the fields and currents for HSMM 2 sampled at the lower polariton frequency (1.3 THz), corresponding to the open blue circle in Figure 6.13a. The current (black arrows) circulate around the SRR, characteristic of the LC resonance. At this frequency (1.3 THz $< \omega_{sJPR}$) the c-axis is metallic while the ab-plane is superconducting meaning that only evanescent waves are supported. The electric field parallel to the c-axis (color) decreases exponentially into the LSCO, and is confined to the first few microns of the crystal. Figure 5c shows the fields and currents for HSMM 2 sampled at the upper polariton frequency (1.9 THz), corresponding to the closed blue circle in Figure 6.13a. Though well separated

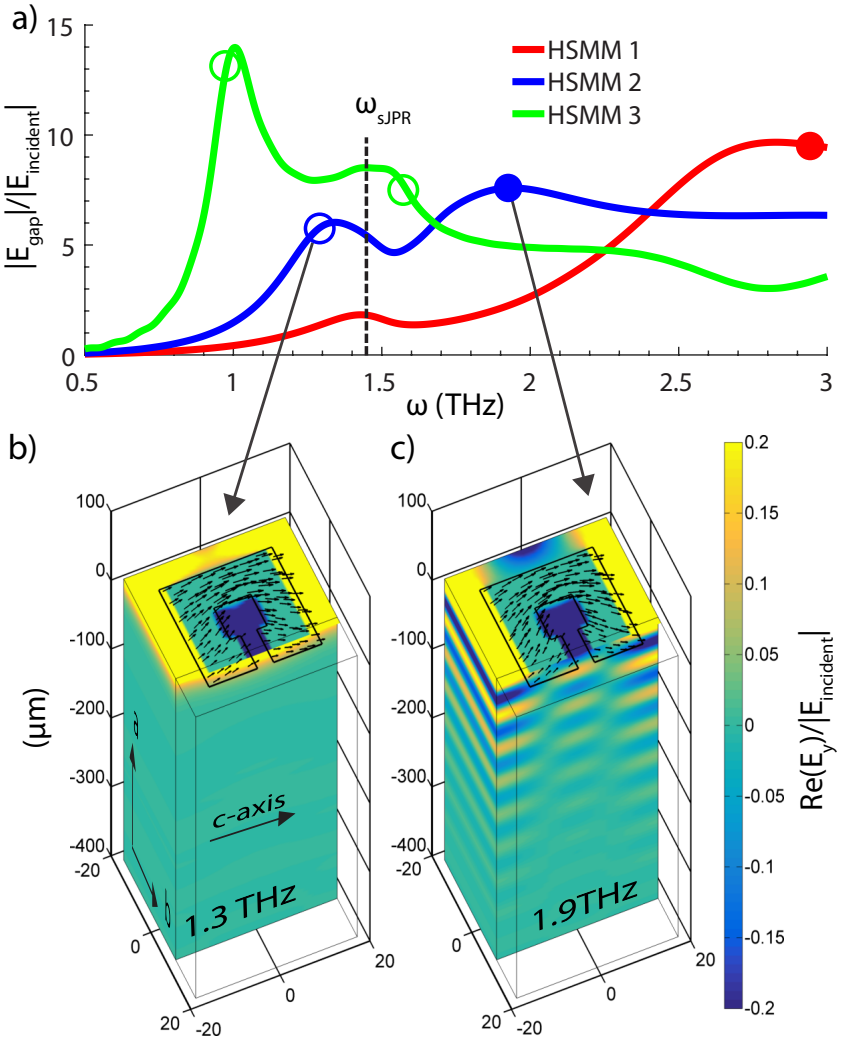

Figure 6.13: a) The field enhancements relative to the incident field at the SRR gap for each of the tested HSMM 1 (red), HSMM 2 (blue), and HSMM 3 (green). Open circles correspond to frequencies of local minima in experimental results while closed circles indicate local maxima. (Top) surface current densities (black arrows) and electric fields parallel to the c-axis (color) for HSMM 3 sampled at 1.3 (b) and 1.9 THz (c), corresponding to the circled features in the spectrum.

from the lower polariton, the currents on the SRR are circulating as before. This indicates that though this frequency corresponds to an entirely different spectroscopic feature, the LC nature of the SRR resonance is nevertheless retained. However, inside the LSCO at this frequency, the electrodynamics are entirely different for the 1.3 THz resonance. Namely, a propagating mode is observed with pronounced subwavelength structure, persisting over a considerable propagation

distance. Two planar nodes in the electric field appear parallel to the ab-plane. Though coupling in this regime is nominally weak due to the high loss rates in the MM, the electrodynamics warrants further investigation.

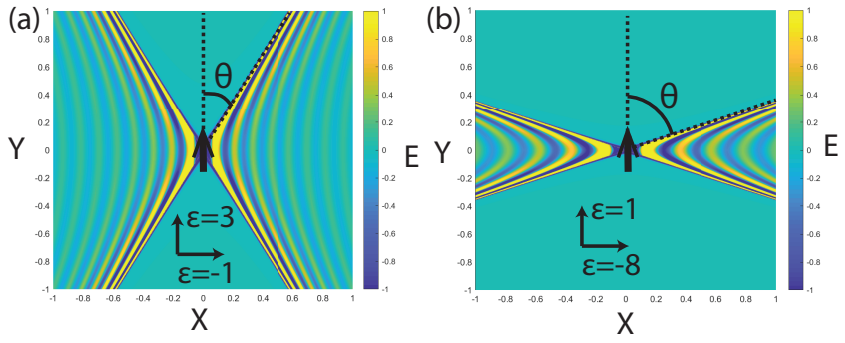

Figure 6.14: An illustration of wave propagation from finite sources in hyperbolic media. a) Field propagation from a dipole parallel to the axis of anisotropy, where the axis of anisotropy has ε=3 and the perpendicular plane has ε=-1. b) When the ratio is increased to $\frac{-8}{1}$, the angle over which the fields are excluded grows larger, and the fields propagate along an increasingly planar region.

Above ω_{sJPR} the c-axis permittivity is positive, while the ab-plane permittivity remains large and negative (i.e. superconducting). Thus, above the JPR resonance, LSCO constitutes a hyperbolic medium; one in which $\varepsilon_{ab}\varepsilon_c < 0$. In a hyperbolic medium, EM waves from finite sources (i.e. a dipole) propagate in an unusual fashion which depends on both the relative signs of the permittivity on the axis of anisotropy (the c-axis in this case) and other axes, as well as the polarization of the source relative to the axis of anisotropy[199][200]. These are known as hyperbolic waveguide modes (HWM). When the axis of anisotropy has positive permittivity and a dipole is oriented parallel to it, the hyperbolic media support radiating waves similar to that of a point dipole in an ordinary dielectric, but with conical regions above and below the dipole in which fields are entirely excluded. The field distributions for such a system are shown schematically in Figure 6.14. Relative to the axis of anisotropy, the angle of this excluded region is given by $\tan^2\theta < -\varepsilon_{ab}/\varepsilon_c$. For a modest ratio of permittivities, the angle is close to 45$\circ$ (Figure 6.14a) while as the ratio increases, the angle becomes increasingly large, and the fields

propagate across an increasingly flat region (Figure 6.14b). the In the case of LSCO at 8K and at 1.9THz, $\theta \simeq \pi/2$, so fields propagate almost exclusively along the ab plane with minimal angular dispersion.

Returning to metamaterial, we consider a cross-section parallel to the c-axis and through the capacitive gap of the SRR. The segment spanning the capacitive gap of the SRR constitutes an extended dipole oriented parallel to the axis of anisotropy (c-axis). Similarly, the segments between the edge of the SRR and the unit cell boundary (i.e. between SRRs in adjacent unit cells) acts as a similar dipole, but with a phase shift of π. In Figure 6.13c we can understand the checkerboard pattern of fields which propagate into the LSCO as being a highly directional projection of the fields produced on the plane of the SRRs. After dispersing slightly in the polyimide, the field distribution which reaches the LSCO surface is locked-in, and propagates a significant distance parallel to the ab-plane, while retaining its sub-wavelength structure. It should be noted that this phenomenon does not appear in a metamaterial over an ordinary dielectric substrate nor in an isotropic medium with a Drude response; though the fields in the vicinity of the SRR have fine structure as previously described, the wave decays to a uniform plane wave over a very short propagation distance. These interesting nearfield phenomena could inform methods whereby HWMs are launched from a MM excited by a far field pulse. Such modes propagate over a distance exceeding 100μm, so conceivably they could be measured on the opposite side of a thin crystal. It should also be noted that rich dispersive properties emerge in the case of arrays of dipoles in the vicinity of a hyperbolic media, but this is beyond the scope of the current work[201].

6.2.4 Conclusion

Our initial measurements on HSMMs demonstrate the viability of achieving strong light matter coupling between the Josephson plasmon in LSCO with interchangeable metamaterial tapes. We have demonstrated spectroscopic evidence of strong coupling with a normalized

coupling of Ω_R=0.29 and performed simulations both to extend the spectroscopic results as well as examine the nearfield electromagnetic field distributions and interactions between the LSCO and MM tapes. In the nearfield simulations, we have observed evidence of hyperbolic waveguide modes emerging in the LSCO. In general, this work demonstrates the utility of using removable MM tapes for achieving interactions between the MMs and solid state systems. This may prove particularly useful in situations where the availability, surface quality, or sensitivity of a crystal make direct deposition of MMs onto its surface (i.e. through lithography) untenable. Our results offer guidance for the design of future iterations of HSMMs that aim to achieve higher coupling constants through tailoring of the spatial and temporal characteristics of the hybrid mode. Furthermore, due to the intrinsic nonlinearities associated with Josephson plasma oscillations, we can apply this approach in conjunction with high field THz excitation in order to explore the complex nonlinear interactions in HSMMs that are likely to emerge[168][202]. Likewise, this could provide an exciting avenue for the direct experimental observation of hyperbolic waveguide modes using nearfield techniques, for instance with THz nearfield microscopy[203][169].

6.3 Metamaterial Coupling to the JPR: Nonlinear Effects

6.3.1 Introduction

As we have seen, Josephson junctions and by extesnion layered superconducting cuprates are intrinsically nonlinear systems. Before considering the consequences of nonlinear excitation of hybrid superconducting meteamaterial systems, it it will first be useful to examine theoreticaly and experimentally how LSCO behaves under large THz fields. To build some basic intuition, we can return to the Josephson equations in the presence of harmonic applied voltage. Consider an oscillating electromagnetic field incident polarized parallel to the c-axis of Josephson junction given by $E(t) = E_0 sin(\omega_{THz} t)$. Plugging this into the voltage in the second Josephson equation (Equation 6.12) where $V(t)$ is replaced with $dE(t)$. Here d corresponds to the inter layer spacing

between the CuO_2 planes, about $1nm$. The inter-layer phase difference from Equation 6.11 is given by $I(t) \propto sin(cos(\omega_{THZ}t))$. This leads to a renormalization of the super fluid density, and with it, the Josephson plasma frequency. The JPR is shifted to $\omega_{JPR}^2 = \omega_{JPR0}^2 cos(\phi_0 cos(\omega_{THz}t))$ where $\phi_0 = 2edE_0/\hbar\omega_{THz}$. Thus as the strength of the THz fields are increased, we see a red shift of the JPR, similar to what we would see if we decreased the order parameter through an increase in temperature.

Nonlinear excitation of a layered cuprate can also result in the generation of the third harmonic of the incident pulse. Again assuming an oscillating applied field considered previously, we can plug in the phase $\phi(t) = \phi_0 cos(\omega_{THz}t)$ to the first josephson equation where we arrive at: 6.11):

$$I(t) = I_c sin(\phi_0 cos(\omega_{THz}t)) \tag{6.22}$$

$$= I_c \left[\phi_0 cos(\omega_{THz}t) + \frac{\phi_0^3}{6} cos^3(\omega_{THz}t) + ...\right] \tag{6.23}$$

The second term in equation 6.23 indicates that THz light at $3\omega_{THz}$ will be produced if a sufficiently THz source is used. These phenomena have already been observed in experiments on a similar High T_c cuprate LBCO [202]. Observation of this THz emission can be leveraged as a powerful tool to probe cuperconducting and other hidden correlations in these complicated systems. Furthermore, experimental evidence of parametric amplification of Josephson plasma waves have been observed in the same system in a high field THz pump-THz probe geometry[182]. Though parametric amplification of THz photons based on nonlinear optics is relatively common at this point, the consequences of this discovery may be profound: It suggests that with the right large field THz excitation, coherent parametric control may be leveraged over the superconducting condensate. This brings closer to reality the possibility of performing precise manipulation of the superconducting condensate, including sideband cooling.

In this section, we build on our previous study of strong coupling between THz meta-

materials and the c-axis josephson plasmon of an LSCO crystal. We apply a variety of second generation metamaterial tapes LSCO crystal and illuminate them with high-field single cycle THz pulses in order to perform nonlinear THz spectroscopy at low temperature. We use metamaterials fully enclosed in a dielectric tape in order decrease the distance between the LSCO surface and the metamaterial to only 200nm, significantly increasing the enhancement of incident fields at the LSCO surface. We take several different approaches towards metamaterial design in order to optimize the enhancements of the incident field and the coupling strength, and to allow for easier identification of the coupled polaritons. We see clear and dramatic nonlinear behavior for all metamaterial tapes and at all temperatures. Though analysis is in its nascent stages and further experiments will be required to disambiguate the observed dynamics, these early measurements are likely to reveal the rich interplay between metamaterial coupling and nonlinear Josephson physics.

6.3.2 Experiment

As the thickness of the dielectric layer separating the LSCO crystal from the metamaterials are decreased, the field enhancement within the SRR gap generally decreases, but the field enhancement at the LSCO surface increases. An illustrative simulation result is shown in Figure 6.15a. This in turn enables the possibility of larger coupling strengths. To this end, our second generation metamaterial devices consist of metallic resonators sandwiched between two layers of polyimide (Figure 6.15b). The polyimide layer on one side is $7.5\mu m$ thick and primarily provides structural support, while the layer on the opposite side is only 200nm thick. This side of the tape is adhered to the LSCO, dramatically enhancing the possibility for coupling.

The tapes are fabricated in a similar fashion as described in the previous section: It begins with polyimide spin coated (thickness of $8\mu m$) onto a silicon wafer coated with a sputtered silicon nitride film to facilitate the removal of the polyimide from the substrate[185]. Subsequently, the periodic array of metamaterials consisting of 200 nm thick gold is patterned using direct

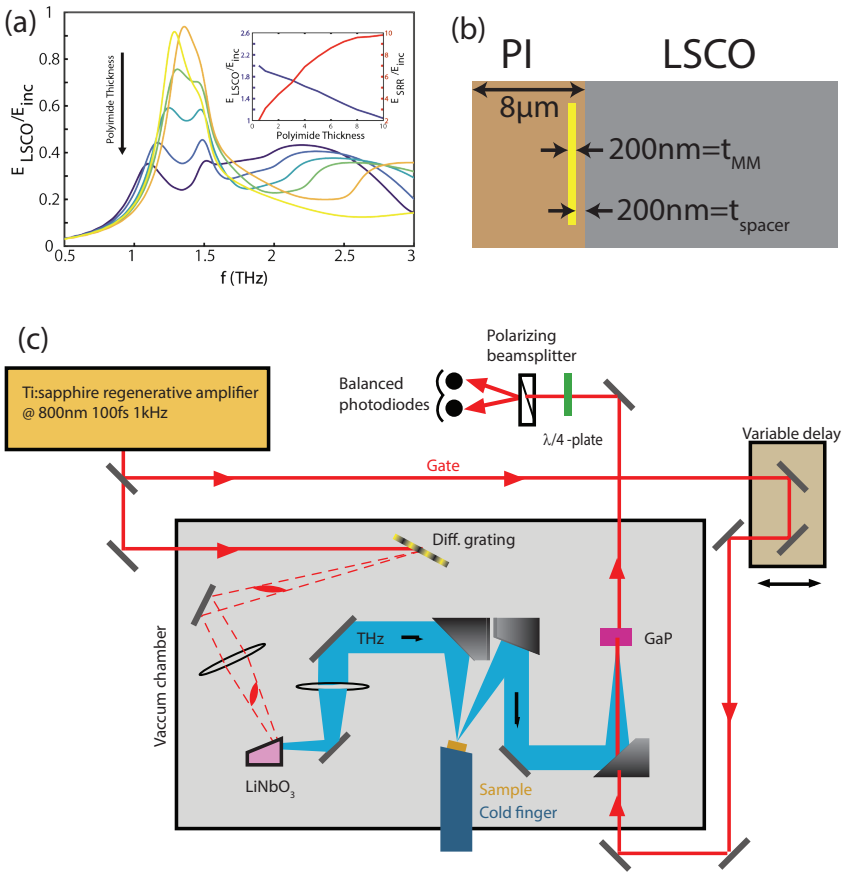

Figure 6.15: A schematic of the instrument for high field nonlinear THz time domain spectroscopy. a) As the thickness of the polyimide layer seperating the metamaterial from the LSCO is decreased, the field enhancement at the LSCO surface increases dramatically. Inset) The peak fields at the LSCO surface increase with decreasing polyimide thickness while the field enhancement in the SRR gap decrease. b) The cross section geometry of the HSMMs shown in this section. The metamaterial layer is 200nm thick and surrounded by polyimide, with only 200nm of polyimide seperating it from the LSCO surface. c) A schematic of the experimental apparatus used for high field nonlinear THz TDS. It is a single beam experiment similar to that presented in section 3.3.2, but adapted for reflection.

laser writing. Once completed, a second layer of $1\mu m$ polyimide is spin coated on top of the metamatierals. Spin coating offers too little precision in the control of the thickness, so in order to achieve the desired 200nm thickness, this layer is subsequently etched by RIE as described in section 3.2.1. The result is a free standing polyimide tape with a metamaterial array embedded just 200nm beneath one of the surfaces.

Figure 6.15c) shows a schematic of the high field nonlinear THz TDS used for these

measurements. A regeneratively amplified Ti:Saph laser outputs 800nm pulses with a 200fs pulse duration and a repetition rate of 1KHz with a total power of 5W (5mJ per pulse). The THz generation is accomplished using the tilted pulse front method with LbNiO3 as described previously in section. The 2.5uJ THz pulses are focused onto the sample resulting in a maximum peak pulse electric field of 90kV/cm. The reflected light is collected by an OAP and focused onto a 100um GaP(100) crystal fused to a 1mm GaP(110) crystal. The thin active crystal on a thicker index matched crystal provides electro-optic signal while avoiding saturation effects as well as etalons from multiple internal reflections in the crystal. A gate beam is introduced with a pellicle beam splitter and focused onto the detection crystal. The resulting rotation of the gate beam is measured by balanced photodiodes. A reference signal from a gold mirror, and the sample signal is collected for each fluence, with the position of each adjusted to the THz focal plane for each measurement.

6.3.3 Results

We begin with nonlinear spectroscopy of the LSCO crystal in the absence of any meta-material tapes. Figure 6.16a shows the reflectivity of an LSCO crystal at 10K for a variety of THz field strengths. Lineaer spectroscopy is performed above and below T_c with ZnTe generation crystal (black solid lines). A literature value is shown for comparison (dashed black line). These linear spectroscopic results show good agreement to both literature values and those presented previously in Figure 6.8a. The colored lines are measured using large THz fields from $LiNbO_3$. Even at the lowest fluence measured (purple line). It is clear that there is a significant red shift of the JPR relative to the linear result. This red shift continues to increase with the field strength, as is predicted by the discussion in the previous section. Meanwhile, above the JPR at 2Thz, a small peak begins to appear, most prominently between the 82kV/cm (yellow) and 90kV/cm (red) line. With the peak of the incident THz spectrum occuring at about 0.65THz, the appearance of this peak is highly suggestive of third harmonic generation from the incident THz pulse, as discussed

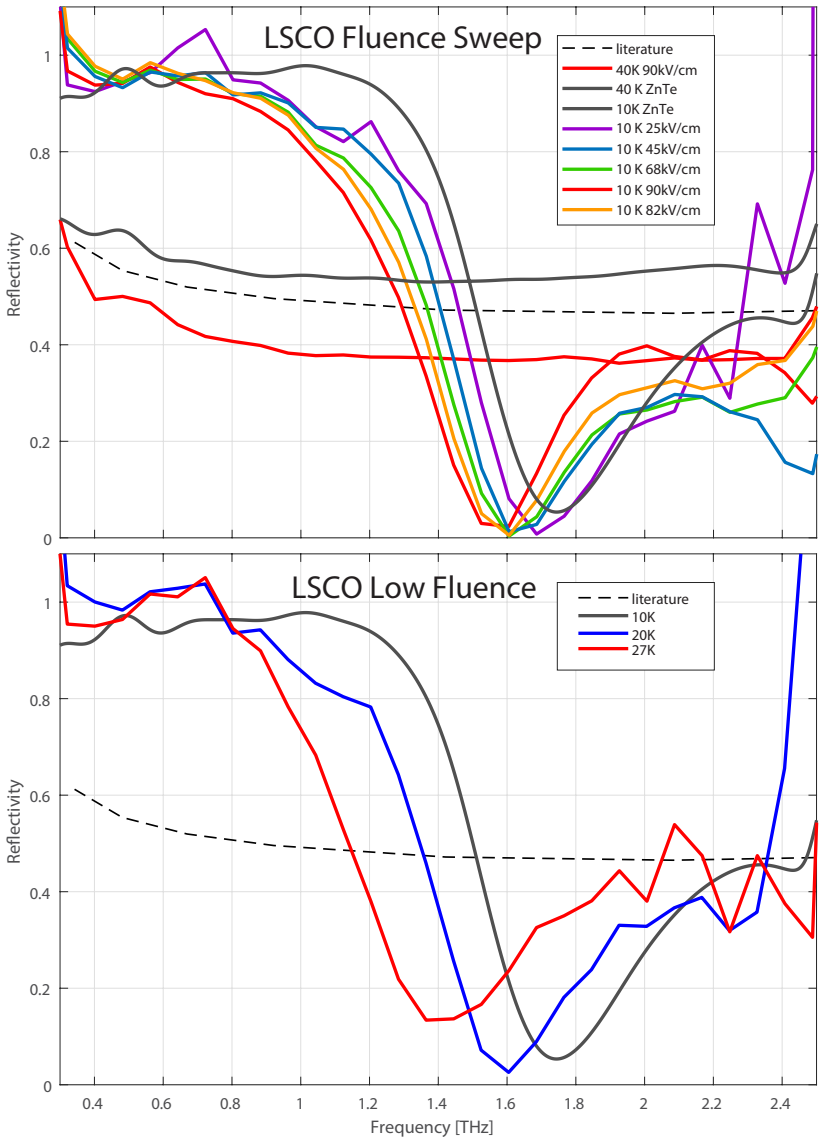

Figure 6.16: Nonlinear THz TDS of LSCO at low temperature. a) Spectroscopy as a for several choices of peak THz field strength at 10K. The black line shows linear spectroscopy of the same crystal at 10K. It is clear that even for the minimum fluence in this experiment, we are seeing nonlinear effects. 300K data at high and low field as well as literature values (dotted) are presented. b) Low fluence measurements as a function of temperature illustrate the suppresion of the superconducting order parameter and with it the JPR frequency. However in this situation, no 3rd harmonic signal appears as the JPR shifts to lower frequency.

previously. For comparison, low fluence measurements of the LSCO crystal at several different temperatures are presented in Figure 6.16b. As the temperature is increased, we observe a blue shift due to the reduction of the magnitude of the superconducting order parameter. Qualitatively,

this appears to be similar to the effect of increasing the LSCO fields at 10K, but no clear 3rd harmonic signal is apparent at higher temperatures.

The first HSMM we measure consists of complimentary split ring resonators (CSRR) (which were discussed previously in section 2.3) embedded in polyiide and adhered to the LSCO crystal. Figure 6.17a is a simulation showing the evolution of the reflectivity spectra of these HSMMs as a function of the metamaterial frequency ω_{MM}. The inset shows SEM images of the MM tape. The most striking difference in these spectra as compared to those presented previously in Figure 6.9 is that in this situation, the coupled polaritons both above and below the JPR appear as minima in the reflection. Furthermore, the reflection feature of the JPR its self is almost entirely suppressed. These traits make the evolution of the spectra far less ambiguous: At $\omega_{MM} = \omega_{sJPR}$ (solid blue line), the lower polariton appears at 1.2 THz whereas the high polariton appears at 1.8THz. An avoided crossing is apparent. In this situation ARC splitting is relatively small. At 0.24THz this corresponds a normalized coupling frequency of only Ω_R=0.16. As ω_{MM} Is decreased, a second order low frequency polariton appears at ω_{MM}=1THz and ω=1.4 THz. This should not be confused with a continuation of the first order high frequency polariton. Though they appear to intersect, inspection of the near field in simulations reveal that they do not, in fact, correspond to the same MM resonant mode.

Figure 6.17b shows experimental nonlinear reflectivity measurements of a HSMM tuned to $\omega_{MM} = \omega_{sJPR}$=1.44THz (Indicated with a solid blue line in Figure 6.17a) and measured at 20K. The result is striking. At 10kV/cm (red line), there is a very broad absorption feature centered at ω_{sJPR}. But when the incident fields are increased only marginally to 20kV/cm (yellow line), there is a dramatic narrowing of the feature. Further increases of the field result in a modest redshift of this reflection minima, and a slight broadening. This narrowing most likely indicates that the excited mode is becoming less lossy with increasing THz fields; that is, it is radiating away energy more slowly. While this is generally inconsistent with typical trends in nonlinear systems, it is reminiscent of some strong coupling experiments including Purcell's in which the radiation rate

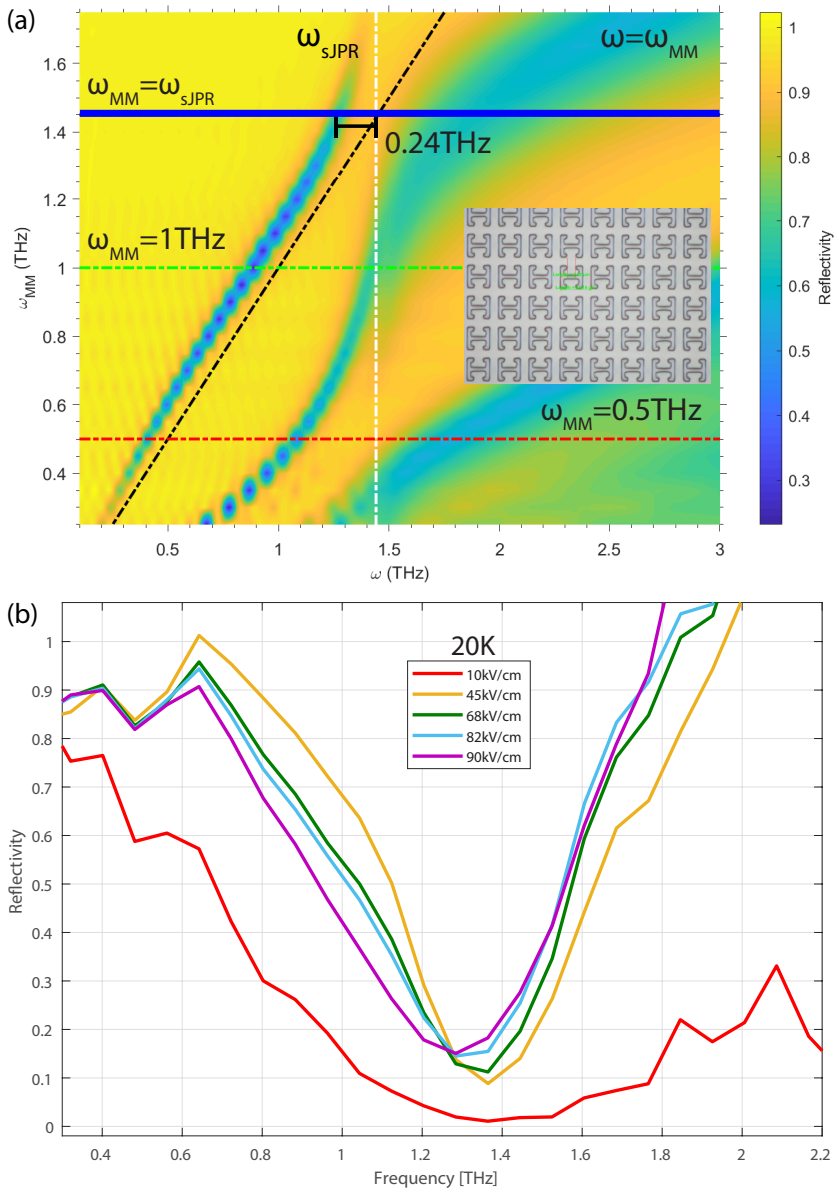

Figure 6.17: A result summary for complimentary split rings coupled to the Josephson Plasmon. a) A surface plot showing simulated reflectivity as a function of frequency and metamaterial frequency. The solid blue line indicates the sample for which experiments were performed. Inset) A SEM image of the metamaterial. b) The nonlinear response at 20K shows a dramatic narrowing of the absorption band as the THz fields are increased.

of an atom is suppressed[150]. That being said, at present it is difficult to make strong claims about the origin of this phenomena. Among other things, our previous measurements on the LSCO crystal indicate that even at 10kV/cm the nonlinear regime is easily reached. Doubly so

due to the local field enhancements of the metamaterial. Linear spectroscopy of this HSMM will assist in understanding this fascinating behavior, as will additional numerical and analytical analysis.

We also measure a second HSMM with a metamaterial consisting of d-ESRRs (also discussed previously in section 2.3). Figure 6.18a. Shows the simulated reflectivity as a function of ω_{MM} as before. The inset shows a SEM image of one of the MM tapes. These spectra are qualitatively similar to those presented in 6.9, but with several crucial differences. At 200nm as compared to 8μm, the proximity of the SRRs to the LSCO surface dramatically red shifts the resonance, requiring a far smaller resonator to achieve the same ω_{MM}. Also, above the JPR, the reflection peaks of associated with the polaritons are relatively weak. Otherwise this MM shows qualitatively similar features: At zero detuning ($\omega_{MM} = \omega_{sJPR}$) there is a first order polariton at low frequency (0.5THz). This corresponds to a splitting of 0.8 THz, resulting in a normalized Rabi frequency of Ω_R=0.55. This is considerably larger than those seen in section 6.2. A second order polariton appears at lower ω_{MM}=1.2Thz and ω=1.4 THz.

Figure 6.18b shows the nonlinear reflectively of a HSMM corresponding to ω_{MM}=1THz (Shown with the solid green line in Figure 6.18a) and measured at 20K. Here we see an interesting an non-monotonic behavior as a function of increasing incident field strength. At the lowest measured field of 5kV/cm (red line), the JPR plasma edge is apparent, with an additional reflection minima at 0.5THz (polariton below JPR) and a reflection maxima at 2 THz (polariton above JPR). As the incident field is increased, the peak at 2THz grows dramatically until reaching a maximum for 17kV/cm (green line). Meanwhile, the other features undergo marginal changes. But then as the incident fields are increased further, the peak is suppressed, until at 100kV/cm (purple line), the reflectively of the HSMM is similar to that at the lowest fluence, but with a significantly red shifted JPR plasma edge.

It is likely that this behavior indicates a competition between two nonlinear effects, which onset at different fluences. The nonlinearities in LSCO have a very low onset as we have already

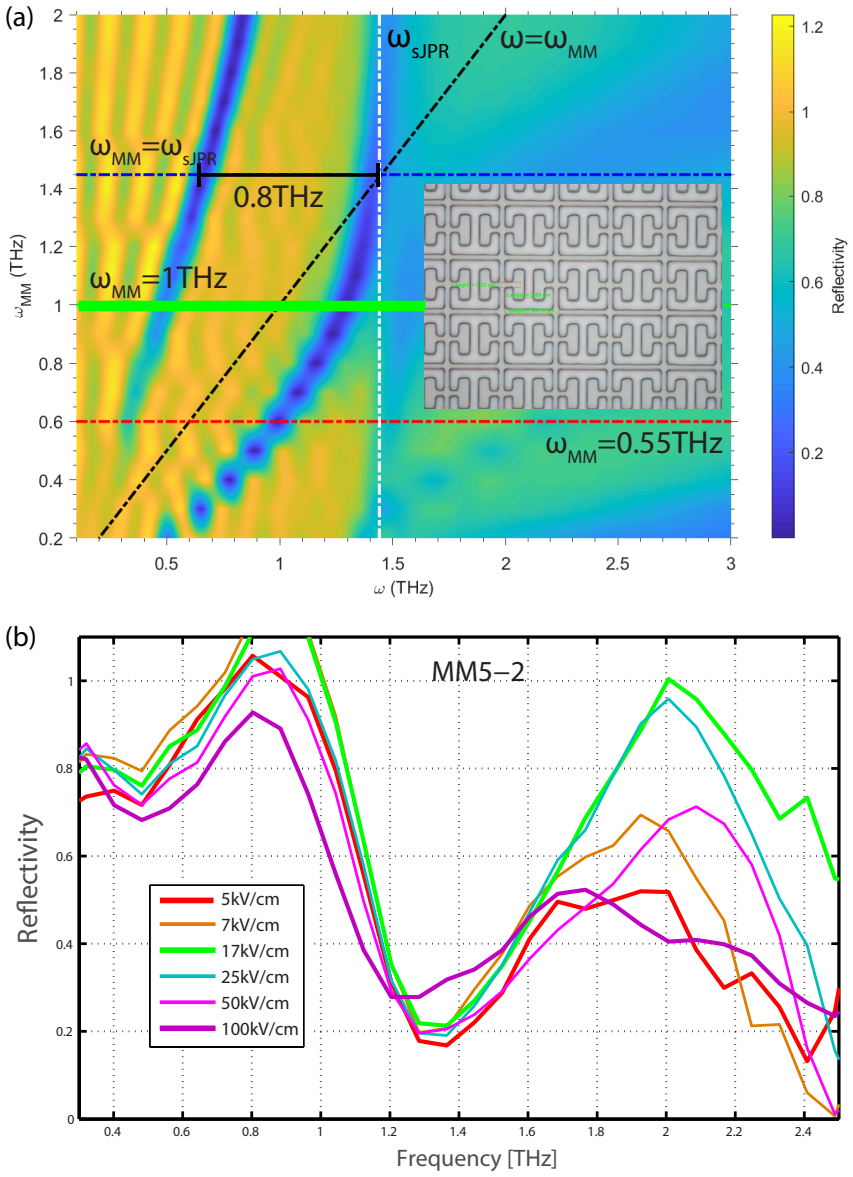

Figure 6.18: A result summary for double split rings coupled to the Josephson Plasmon. a) A surface plot showing simulated reflectively as a function of frequency and metamaterial frequency. The solid blue line indicates the sample for which experiments were performed. Inset) A SEM image of the metamaterial. b) The nonlinear response at 10K. This HSMM displays an interesting saturation effect in which the reflectively is first enhanced, and then suppressed as the incident fields are progressively increased.

seen in Figure 6.16b, so this could be the dominant factor for the nonlinear effects at the lower fluences. But SRRs under very large excitations have nonlinear behavior of their own as dielectric

breakdown, impact ionization, and other high field effects begin to onset [31]. This may be responsible for the reversal of the earlier trends as we approach the maximum field. This is of course to say nothing of complex interactions between the two systems. As with the previously discussed HSMM, it is likely that even for the lowest fluences attainable with this system, we are well into the nonlinear regime. In fact, SRRs generally produce significantly greater field enhancements than CSRRs. Linear spectroscopy will be a great aid in understanding the observed spectra, as will additional nonlinear measurements, and numerical and analytical analysis.

6.3.4 Conclusion

These brand new measurements and HSMM systems represent an exciting step into the world of nonlinear coupled Josephson plasmonics. We performed preliminary linear measurements on a series of HSMMs and in conjunction with numerical simulations, identified evidence of strong coupling with a normalized Rabi frequency of Ω_R=0.29 and breaching the ultrastrong coupling regime. We took both numerical and anlytical approaches in order to model the experimentally observed behavior and examine the interesting near field interactions which occur in the HSMMs. Using these results, we endevored to create a second generation of HSMMs in order to generate more unambiguous spectral signatures of strong coupling, and dramatically increased coupling strengths. We presented two such HSMMs, one which integrates CSRRs in order to produce an unambiguous spectral signature of the avoided resonance crossing, and another integrating dESRRs which appears to produce a coupling frequency nearly double that of the HSMMs explored in section 6.2 at Ω_R=0.55. We performed high field THz TDS on these samples using a $LbNiO_3$ THz system. The results are both fascinating and puzzling with dramatic nonlinear behaviors observed for all samples and at all temperatures. While it is too early to definitively speculate about the origins of the observed behaviors, it is clear that this complex system hosts a variety of interesting and unusual nonlinear characteristics. Additional nonlinear measurements, linear measurements, and analytical and numerical analysis will soon follow with

the hopes of unpacking the dense physics in this system. With additional work it should become clearer the ways in which the strong coupling and the exotic nonlinear phenomena already known to exist in Josephson systems interact to result in the behavior we observe.

6.4 Acknowledgments

This work in part is currently being prepared for submission for publication of the material. Jacob Schalch, Kirk Post, Guangwu Duan, Xiaoguang, Zhao, Young-Duck Kim, James Hone, Michael Fogler, Xin Zhang, Dimitri Basov, and Richard D. Averitt. The dissertation author was the primary investigator and author of this material.

We acknowledge support from the Department of Energy Basic Energy Sciences(DOE-BES) (DE-SC0018218) for work performed at UC San Diego and Columbia University. We thank Boston University Photonics Center for technical support.

Chapter 7

Conclusion and Future Directions

Though the field of metamaterials is not even 20 years old, there is a feeling among many that, at least in the context of physics research, there is not much left to do. This argument is not without merit. Indeed many physics researchers have been winding down their research into the field while engineers researchers wind it up: in terms of simple dielectric and metallic metamaterials, the hard problems now are mostly in the realm of engineering; optimization, fabrication, bandwidth, etc. rather than problems of fundamental physical understanding. The low hanging fruit has been plucked. Practical metamaterial devices have even made major forays in to the commercial world; a milestone that traditionally causes physicists to lose interest immediately. But I hope that this document will serve as a testament to the contrary. While the easy problems may have been solved, physics has never been about the easy and there exists an entire world of mostly untapped and fascinating problems which can be approached with metamaterials.

In chapter 2 I introduced the basic operating principles of metamaterials, at first using the split ring resonator as an illustrative example to explore in depth. I discussed the modes and the near and far field electromagnetic properties, and the various ways in which the response of a metamaterial is understood via effective medium theory. Following this extended exploration, I briefly introduced the enormous variety of metamaterials and their operating principles which

have been developed over the short life of the metamaterial field.

Throughout this dissertation, I have alluded to the serendipitous confluence of progress in computational, micro-fabrication, and THz technologies in order to enable the particularly meteoric rise of THz metamaterials. In chapter 3 I explored each these tools, loosely following the order of operations by which a THz metamateiral study is executed. I began with a discussion of the powerful computational techniques which are leveraged for designing metamaterials and for accurately predicting their interactions with electromagnetic fields. In section 3.2 I surveyed some of the techniques which come together to bring a metamaterial design into the material world with nanometer precision. Finally I discussed ultrafast optics and experimental THz techniques. I over viewed some of the challenges inherent in working in this frequency range and how they can be overcome with THz time domain spectroscopy, and other large fluence nonlinear and pump-probe techniques.

From there I presented several original research projects. In chapter 4 I presented a metamaterial absorber with a continuously tunable dielectric layer made of just air. We demonstrated dramatic tunability and excellent agreement with numerical and analytical predictions. This work served as a comprehensive verification of the analytical interference theory of metamaterial abasorbers, but also served as a proof of concept; an avenue towards massively tunable and high-Q metamaterial absorbers.

In chapter 5 I presented a research project geared towards practical device applications; Broadband electrically tunable VO_2 metamaterial terahertz switch with suppressed reflection. We show that this device is capable of switching from a transmissive state with low reflection to a fully absorbing state, all across a substantial bandwidth of operation and with the application of only a few volts. With validation of this general approach, this design concept can be adapted to a wide variety of applications including optical limiters, switches, modulators, and the like.

In chapter 6 we explored the the deep and complex physics of layered high T_c cuprates coupled to metamaterials. In preliminary experiments we performed linear spectroscopy of hybrid

superconducting metamaterials consisting of flexible polyimide tapes with embedded materials adhered to a $La_{2-x}Sr_xCuO_4$ crystal cut along the interlayer c-axis. We observe evidence of strong coupling and explore simulated nearfield response including evidence of hyperbolic waveguide modes. We followup with new nonlinear thz spectroscopy on second generation HSMMs and observe complex nonlinear behavior. While the analysis of this data is ongoing, it is likely to be a promising route towards nonlinear coupled phenomena.

While the introductory chapters of this dissertation should serve as a useful guide to individuals interested in or beginning a career in metamaterials research, the latter chapters should illustrate the variety and complexity of the problems in metamaterials physics that have yet to be explored. Terahertz metamaterials remain a particularly young and vibrant field with the promise in both academic and practical spheres as complex condensed matter systems are further explored and THz technologies are further developed respectively. My hope is that this work serves as both a guide and a reference to newcomers to the field as well as a contribution in and of its self to the greater world of THz, condensed matter, ultrafast, and metamaterial physics.

Appendix A

Photoconductive THz TDS User Guide

In this section I will attempt to provide a guide for the setup, use, and troubleshooting of the dual-mode photoconductive THz TDS system which I constructed, and which was used for many of the measurements throughout this thesis, and many others not presented. While not the most glamorous ultrafast instrument, this system is a true workhorse, capable of quickly performing low noise and high resolution time domain spectroscopy of samples at normal incidence in both transmission and reflection mode, with only a few seconds of effort required to switch between the two. Many subsystems come together to make this system work. I will attempt to mention them all in the order in which they are encountered, some of the common issues and solutions for each, as well as more detailed application notes when warranted.

A.1 Merlin M25 Chiller

This water chiller provides cool water to the Spectra-Physics Millenia pro laser. It is vital for the temperature regulation of the phase matching in the laser (metnioned earlier in section 3.3.1) and due to repeatability issues during thermal cycling, the chiller should be left running AT ALL TIMES, even when the laser is off. The set point should be 18C and the readout should never deviate from this. If it does, turn off the laser immediately and before evaluating the chiller.

The manual has some useful information but not much. The operation is mostly self explanatory. Do not use transparent tubing for the water. This could promote the growth of photosynthetic biological contaminants.

A.1.1 Maintenance

Every 6 months, the water in the chiller should be replaced. Distilled water is the only type which should be used in this chiller. Not DI, not filtered, not purified; distilled. There is a siphon valve on the lower back side of the chiller that can be used to siphon/drain the water. Running the pump will accelerate this process, but the pump should not be run on an empty/low reservoir. This is the only regular maintenence that the chiller requires. Often the drained water will have fine black particles floating in it. This is normal, but if it is very dark this could indicate a problem with the pump.

This is also a good opportunity to flush clean the system, though every 6 months is probably overkill. Flush the system with a 1:1 mixture of acetic acid and distilled water (alternatively a 1% mixture of glacial acetic acid and water). After running the pump with the cleaning mixture, drain it, run it with pure distilled water several times, and then fill it with distilled water.

A.1.2 Trouble Shooting

There is only one failure mode of the chiller that I have seen so far, though I have seen it twice. If the temperature above its set point, and/or there are unusual noises coming from the chiller or the drained water is very dark, this is likely a problem with the pump and/or the coupling between the pump and the motor that drives it. Though it requires some disassembly, the pump can be removed and replaced. It is difficult to usefully evaluate the actual health of the pump once removed; turning the drive with your fingers is easy and smooth on a new one while more halting and difficult on an old one, but I don't know whether this indicates a broken

pump. In both failures I have seen it is the nylon coupling between the large motor and the pump which has broken. The 1 inch cylindrical piece has a male end and a female end. In both cases the paddle on the male end was disconnected and partially ground to dust. In this scenario, I obviously recommend replacing the coupling (part #1145128) and the pump (part #NC0389902).

A.2 Millenia Pro Diode Pumped Laser

The next stop towards in the line is the 5W CW 532nm Diode-Pumped Spectra Physics Millenia Pro laser. Fortunately, this piece of equipment is also very user friendly and rarely requires maintenance. When it does however, most of these procedures should not be attempted by the end user. Though the manual covers everything in depth and should be referred to for detailed operating instructions, I will briefly mention some considerations for regular use of the laser. Typically, operating at 3W output power, diode current will be about 39A with a temperature T1 of 26.5 degrees. If the temperature or current is significantly hgiher than this, something may be wrong.

A.2.1 Daily Operation

The power supply for the Millenia Pro should be left on at ALL TIMES for the same reason as the chiller: it provides heat to the SHG phase matching mechanism and thermal cycling will disrupt the pointing and power stability of the laser. That being said, the diode has a finite lifetime, so the laser its self should not be left on for extended periods of time when it is not in use (for instance over night when no measurements are in progress). In order to start the laser, hold the power button on the controller box. After a few seconds the ”laser emission” light should be solid, and a white light should appear on top of the laser head box. The shutter is closed and will not open until the laser reaches its power set point. For this reason it is often best to use a low power setpoint (10mW) when starting the laser. The power should reach this setpoint

(often taking about 15 seconds) at which point the shutter can be opened, and the operating power setpoint (several watts) can be selected.

The laser should be left running at the power which you intend to use for about 1 hour to allow it time ”warm up” and allowing the pointing to settle. For rough alignment the laser should be used at a low power setpoint. At 10mW it is safe to place a piece of paper or your skin for instance in front of the beam, though of course appropriate laser safety goggles should still be used. At typical operating powers (3-5W) the beam will immediately burn almost anything in its path, including skin. Nothing other than optical components should be placed in front of the beam at this power, and the power should not be increased to this level until rough alignment has been done and the beam path is safe and free of scattering.

A.2.2 Troubleshooting

Often times the only clear evidence of a problem with the Millenia Pro is the laser failing to reach its set-point power, or showing fluctuations in the power reading. An unusually high diode current given the laser power may also indicate a problem. Other issues often only manifest as downstream effects in which there are no obvious problems with the laser its self. For instance, slow power drift or mode locking stability issues from the 800nm oscillator could be a matter of power or beam pointing drift from the 532nm beam rather than an issue with the oscillator. Fortunately, these types of issuse are uncommon, but unfortunately there is little the end user can do to rectify them.

The only real troubleshooting that the end user can perform is optimization of the SHG temperature. In this process the temperature and thus phase matching condition of the SHG crystal is optimized in order to improve the conversion efficiency of the 532nm beam, and thus decrease the amount of diode current required to reach a given output power set point. Before beginning this procedure, the lase should be run at its maximum power for an hour. This optimization can be performed in automatic or manual mode. The manual comprehensively details both procedures,

but afterwards, the diode current at a given output should be at least slightly reduced.

Any other problems will require a consultation with spectra-physics. Most notably, the diode has a finite lifetime, and will eventually fail and need to be replaced. In general the diode current required to achieve a certain power output will increase as the diode degrades. Though SHG crystal temperature optimization and cavity alignments can improve things to some degree, eventually the diode will no longer be serviceable.

A.3 KML Ti:Sapphire Laser

The KML Ti:Sapphire modelocked laser oscillator is at the heart of the photoconductive system and unlike the previous components, must be set up and tuned manually. The parameter space of adjustments is large, and the window in which a reliable, efficient modelocked can be achieved is small and challenging to find. Sometimes this process seems like more of an art than a science. Even identifying high quality mode lock requires a number of different diagnostic tools. Specifically, the aim is to have a reliably modelocked output with an average power of 800mW, centered at 800nm with a 60nm FWHM, and a clean, consistent train of pulses seperated by 12.5ns. Though the pulse duration is also important, it is difficult to optimize simultaneously, and the pulses will be compressed by a seperate pulse compressor later. For our purposes, a 100fs pulse is perfectly acceptable. The manual for the KML oscillator is quite thorough, and should be used as a primary reference, but in the following sections I lay out a few tips and strategies not covered in it.

A.3.1 Diagnostic Tools

The first tool that will be necessary for setting up and tuning the KML oscillator is a power meter. It should at least 20cm from the laser apeture where the light is not too tightly focused. As you work on tuning and optimizing the oscillator, keep in mind that the pointing of

the output beam will change slightly, so remember to periodically move the power meter in order to optimize the power it reads out.

The second tool is a fast photodiode connected to a oscilloscope. Be careful to use a photodiode which is rated for the power that will be in use (¡800mW), or alternatively, use a neutral density filter to attenuate the light to an acceptable level for the photodiode. The photodiode can be sensitive to align, but do so by optimizing the signal in the oscilloscope. In CW lasing mode, the signal will of course be flat, but when modelocked, there will be a pulse train. In addition to simply providing evidence that the laser is modelocked, viewing the pulse train on a short time scale will allows for the identification of double puling (though only when the pulses are well separated). On a longer time scale, periodic variations in the amplitude of the pulses can suggest instability or self q-switching issues. Keep in mind that as with the power meter, tuning the laser by optimizing the amplitude of the pulses is not a good idea, as the pointing of the laser also contributes to the observed signal on the oscilloscope.

Third is the spectrometer. The head of the spectrometer should be covered with a white diffusing object both in order to attenuate the incoming light as well as to disperse it, making it less sensitive to alignment. A strip of paper is one simple solution, but I have found that pressing a small piece of packing foam onto the spectrometer is both convenient and reliable. The spectrometer requires very little power to operate effectively. In CW mode, there will be a very narrow signal which will almost certainly saturate the detector. In a good modelock, this will turn into a broad gaussian shaped pulse with a FWHM of tens of nanometers. As with the photodiode, this provides an unambiguous indication of modelocking, but also offers other information. Lopsided, boxy, excessively broad, excessively narrow, or wavy lineshapes can all indicate various types of issues with the modelock. Though some common issues will be discussed later, a more comprehensive troubleshooting guide can of course be found in the manual.

The final diagnostic tool is the autocorrelator which allows the pulse duration to be

measured. It is in my opinion not neccessary to measure the pulse duration directly out of the oscillator. After all, the next stop for the pulses is a pulse compressor, and even then, as we have seen previously in section 3.3.1, the dynamics of the PC THz-TDS system are dominated by other factors so long as the 800nm pulses are relatively short. Never the less, short pulses are ideal, and after compression it should be possible to achieve 20 fs pulses. That being said, I have found it to be extremely difficult to find a signal from the oscillator with the autocorrelator. The manual for the Minioptic delta single shot autoccorelator is quite good and comprehensive. Follow it to a T and use as much power as possible. Seeing the SHG light in the autocorrelator will never the less be extremely difficult, even in an utterly darkened room though it is possible. In order to optimize the very weak and noisy signal, I often will move the delay stage back and fourth until my eye can pick up a small bump moving back and fourth. Once identified, this bump can be iteratively strengthened by optimization, and eventually a large but very narrow peak should emerge.

During the setup and optimization of the oscillator you will constantly have to switch between the power meter, photodiode, and spectrometer. This can be tedious so given the various levels of alignment difficult for each tool, I recommend the following: Set up the photodiode about 30-40cm from the oscillator and align it such that the beam partially reflected from its sensor is well separated from the path of the incident beam. Place the spectrometer somewhere in front of this beam. This way the pulse train and spectrum can simultaneously be measured. The power meter has the largest aperture and is the least sensative to alignment so place it on a magnetic mount such that it can be easily slid in and out of the beam path in front of the photodiode.

A.3.2 Initial Alignment

The Millenia laser MUST be run at its minimum power setting until the the initial alignment of the KML laser cavity is complete in order to ensure that there are no dangerous stray beams. Wear appropraite sfety goggles at all times.

Keep in mind that the Millenia is p-polarized, but the KML requires an s-polarized input beam. The beam going into the KML should also be abel to be steered precisely, and must be as stable as possible. For these reasons, a periscope to rotate the polarization, followed by two high stability mirrors on large solid mounts should be used to route the beam from the Millenai to the KML. This beam path should also as short as possible to maximize stability.

With the laser at minimum power, perform the initial alignment procedure as detailed in the user manual. The prisms should be positioned such that the beam center passes through the prisms about 2mm from the apex of the prisms. The high reflector and the output coupler should be aligned such that the beams are reflected back along the same path. If there are multiple spots where a beam passes through one of the optics, this a misallignemnt of one of the two is likely the cause. If there is a significant amount of diffracted light scatted from the crystal, the beam may be focused onto a damage spot and may need to be translated slightly to find a new spot.

Once the visual alignment through the irises is as good as possible, remove/open them, ensure you are wearing safety goggles and increase the pump power to its nominal operating value (3W). At this power level, never place anything (i.e. an alignment card, paper, or your finger) directly into the 532nm pump. It will burn whatever you put into the path, including your skin, and will cause soot to be deposited on the optics. Set up a power meter and open the KML shutter. With luck the power should be lasing, but even if it is not, there will be some amount of power that should be detectable on the power meter even if it is only a few microwatts. Make adjustments to the high reflector and output coupler to maximize this reading. Once the lasing thresh hold is met the power will shoot up.

At this point optimize the power in CW mode as much as possible. Spend a LONG time on this; even when it seems impossible, more power can almost always be squeezed out of the laser. Keep in mind as you perform the optimization that the pointing of the laser will be changing slightly. As a result, make sure to periodically ensure that the beam is still well aligned to the power meter. The vast majority of this optimization should be performed by adjusting the output

coupler and high reflector, but other parameters may be adjusted as well. Below is the hierarchy of degrees of freedom that should be adjusted. Items closer to the bottom of the list should more or less not be adjusted from their nominal positions.

- Output coupler/High reflector (almost all of the optimization)
- Turning mirrors (between Millenia and KML. Make only minuscule adjustments)
- Lens (to optimize focus in crystal)
- Curved mirror
- Prisms (sometimes power increased by putting the beams through a lot of prism glass, but this is ultimately unproductive. Try and keep the beam 2mm from the apexes of the prisms.
- Crystal

With a pump power of 3W, it should be possible to reach a CW power output of at least 600mW. Once you are satisfied with the power, keep working at it anyway. It is tedious but this will pay dividends later in stability and available power.

A.3.3 Mode Locking

Before looking for a mode lock, set up all of your diagnostics as well as possible. You will be switching between looking at the power, spectrum, and pulse train often, so you want it to be quick and easy. As with the rest of these appendices, keep in mind that the user manual for the various pieces of equipment should be considered your primary instruction for their operation. That being said, modelocking can sometimes be more art than science, so below are my tips for finding a good mode lock.

Make sure that the there is still about 2mm of prism glass in the beam for both prisms. While watching the spectrum, slowly translate the second curved mirror towards the crystal. As

you are doing this, constantly nudge the second prism assembly pressing on the prism base. As you translate the curved mirror forward, the power will drop, and at some point the spatial mode shape of the laser may switch into an oval or a vertical line. This is generally the first place you might start to see hints of mode locking. The spectrum will become jumpy and with nudges to the prism broadband signals may momentarily appear and go away.

There is no guaranteed secret to mode locking sucess and I have found that even exactly reproducing all of the same parameters for the various components from a previous mode lock will not only not guaranteed to work; it almost never works. Follow the manual and look at trouble shooting tips if you have issues. Primarily this procedure involves moving the prisms to find the best compination of positions for a mode lock of the right bandwidth, and moving the curved mirror if no such positions are found. My hirearchy for adjustments are as follows:

- Prism positions: Generally, moving either prism out will result in a easier mode lock but with narrower bandwidth. Move one out and one in in order to keep constant bandwidth while searching for a more stable mode lock.

- Curved mirror: Generally the mode lock position is around 4.11mm but if no modelock can be found, or if the spatial mode or power is not where it should be, tweaks to the curved mirror can help.

- High reflector and output coupler: ONLY adjust these to tweak up the power and ONLY do so when the laser is in CW operation. Adjustments while mode locked will certainly screw up the bandwidth. Sometimes TINY tweaks can get rid of Q-switching and other instability, but that is the only major exception.

- Pump power: if all else fails, try adjusting the pump power. Increasing the power can make a modelock more stable or can help getting into a mode lock if lower powers are not cutting it. Conversely, if it seems impossible to get rid of Q-switching or double pulsing effects, decreasing the power can help.

- Crystal, lens, and turning mirrors: do not touch. If you think they need optimization, go back to the CW maximum curved mirror position to do so.

This process can be long and arduous and there are many failure modes. Below is a list of some of my lessons learned in the many, many times I have gone through this process:

- While the manual describes the circular mode switching into a vertical elliptical mode as the curved mirror is translated inwards (and this used to be the case), I have not seen this behavior recently. More commonly the circle goes directly into a very elongated vertical mode. It is often somewhere in this mode that the mode lock can be found.

- The window for positions of the prisms which will give a mode lock is typically very small, often just a hand full of steps of the motors. That being said, if you find a mode lock but the badndwidth is wrong or it is unstable, try translating both prisms in opposite directions a few steps at a time.

- If there are persistent periodic variations in the pulse train (on the order of μs), this is indicative of Q-switching. If a search for better prism positions is unfruitful, sometimes a tiny adjustment to the high reflector can fix the problem. If they persist never the less, consider slightly increasing the pump power.

- Double pulsing can appear in several different ways. If the pulses are very close together, there will be a periodic variation in the amplitude of the spectrum. If they are very well separated (several ns), they should be visible in the pulse train, often with the second pulse in each pair being substantially smaller than the first. However for certain regimes of pulse separation neither of these diagnostics will work. The problem will however be immediately apparent when you view the THz pulse scan; smaller pulses will appear on either side of the main pulse, separated by 1 to many ps. Look for better prism positions. If all else fails, consider increasing the pump power.

- It is sometimes useful to break the mode lock and tweak up the power using the high reflector and output coupler. Sometimes it can also be useful to return the curved mirror to its CW lasing position to re-optimize the power.

- if there are persistent stability problems, cleaning all of the optics may help, as described in the next section.

- In principle, once the right settings are found, the laser should not require adjustments for many months. Simply run the pump laser for an hour to warm everything up and nudge the second prism to initiate mode locking. In practgice, environmental changes can cause the mode quality or stability to deteriorate, or cause the mode locking condition to be lost entirely. In perticular I have noticed that large cahnges in humidity cause this to happen (the Santa Ana winds for instance).

Ultimately what you are aiming for as a pulse train of 1 pulse every 12.5ns which is stable over all time scales. The spectrum should have a 60nm FWHM centered at 800-820nm. The power will depend on the pump power but should be about 1/2-2/3 of the maximum CW power.

But most importantly the mode lock should be reliable and stable. Every day when you start the laser, you should be able to give the prism one good push and be confident that the laser is correctly modelocked without having to perform any of the diagnostics let alone all of them. If this is not the case, you will loose a lot of time performing all these diagnostics every day. Stick with it until you get it right.

A.3.4 Maintenance

The only regular maintenence that the KML requires is cleaning of the optics which should be done about twice a year. Wear gloves. Use methanol on a many-times folded piece of optical quality cleaning tissue (not a paper towel, not a kim-wipe, use optical quality tissues ONLY). Carefully fold the tissue, clamp it into a pair of forceps, wet it with methanol, and gently

wipe the surface of the optics. Get a new tissue for every single wipe. Do not reuse tissues. Clean every accessible surface that the beam hits, especially the crystal.

Sometimes a spot of the Ti:Sapph crystal will become damaged. The evidence of this is typically diffracted green light scattering across the inside of the cavity in parallel lines and waves. You can avoid the damage spot by making tiny adjustments to the pointing mirror, but often the better choice is to translate the crystal slightly. Perform the initial alignemnt and then loosen the screws which hold the crystal in place and slide it diagonally on its track. Only a tiny adjustment is required to bring it off of the damage spot.

A.4 Single Prism Pulse Compression

As a short pulse passes through dispersive media, the frequency dependent refractive index will ”stretch” the pulse in time; shorter wavelength parts of the pulse will generally fall behind longer ones. The single prism pulse compressor is a simple and effective means of compressing the 200fs pulses coming out of the KML oscillator down to about 20fs. Though not as flexible as more complex compression schemes, it is straightforward to set up and more than capable of achieving the pulse duration required for the PC THz-TDS system. An in depth explanation of single prism pulse compression can be found in reference [204]. Briefly, in this approach, the pulse makes four passes through a single prism. In the first pass, the pulses are spatially separated into their spectral components, with longer wavelengths being bent less and vice versa. On the second and third pass, long wavelengths are sent though the thicker part of the prism while short wavelengths traverse closer to the apex, such that the short wavelength components of the pulse can ”catch up” with the rest of the pulse. On the final pass, the temporally compressed pulse is re-combined spatially.

A.4.1 Alignment

Each of the four passes through the prism in this scheme follow more or less the same path, albeit at different heights. The key alignment criterion is having the prism set at the angle of minimum deviation. This can be determined simply enough. Set up an iris pair and send an alignment beam through into the prism, such that it passes through about 4mm from the apex of the prism about 1/5th of the way up the prism. Rotate the prism slowly, watching the refracted spot on a distant surface. When spot stops and reverses direction, you have just passed the angle of minimum deviation, about 66°.

Next, the retro reflector can be placed in front of the beam about 21" from the prism. The retro reflector will always reflect the light on a parallel line relative to the incident light, so its angular orientation is not terribly important, but the light should be aligned to the vertical center line of the reflector such that the beam will only be displaced in the vertical direction. The reflected beam should be parallel to the incident beam, but at a higher elevation, such that it hits the prism 4/5ths of the way up.

This beam should be aligned to a roof mirror who's height should be adjusted such that the reflected beam returns to the prism 3/5ths of the way up. If the previous steps are performed properly, this beam should then hit the retroreflector and return to the prism at 2/5ths of the way up. After this 4th pass, this beam can be picked off and sent to the rest of the optics.

A.4.2 Pulse Compression Tuning

At this point, the 800nm pulses can be aligned into the system via the iris pair. With the approximate parameters outlined above, the outgoing beam should be compressed fairly well. Once the autocorrelator has been aligned and the signal found, adjustments to the pulse compressor can be made in order to optimize to a transform limited pulse. The best tuning parameter to use is the translation of the retroreflector. Because the retroreflector translation has

little effect on the pointing of the beam, even a large translation, or removing and re-positioning the retroreflector should not cause a loss of signal. In general, the width of the signal from the autocorrelator is related to the pulse duration of the 800nm light. Translate the retroreflector until the signal reaches a minimum in width. If the minimum cannot be easily achieved with translations to the retroreflector, the prism can also be translated further in or out of the beam path, though this will effect the amount of the beam which does not clip the prism, which in turn can effect both spectral content and output power. With some simple adjustments, a pulse duration of about 20fs should be easily achieved.

A.5 Delay Stage and Pointing

After leaving the pulse compressor, the polarization of the beam should be rotated as to be compatible with the photoconductive antenna, and raised to the approximate height of the photoconductive antennas (discussed further in the next section). Both of these tasks can be accomplished with a periscope arranged such that the exiting beam is directed at a 90 degree angle relative to the incident one (though still parallel to the table).

Next, the beam should be split and sent through neutral density filters, allowing the beams going to both the emitter and the detectors to be attenuated. Next, one of these two paths must be put through a delay line (in mine the delay line is on the detector path as seen in Figure 3.8a.

Alligning a delay stage can be tricky but must be performed as precisely as possible. There are various methods for performing that task [205][206], but in general they follow the same pattern; first the beam must be made parallel to the translation stage motion. This can be accomplished with as one would typically align a beam to an iris pair, but where one iris is placed on the stage and translated back and fourth on the stage in order to replicate a ”near” and ”far” iris. Next, a pair of mirrors must be placed on the stage and tuned until they are at exactly 90 degrees to each other such that the exiting beam is parallel to the incident one. I will direct you to

the previously mentioned references for guidance on this task.

IT IS VITAL that 800nm pulses arrive at the detector at the same time as the THz pulse in order for detection to occur. This means that the path lengths of the beams starting at the first beam splitter must be more or less the same: one goes to the THz emitter, through the THz optics and to the detector, and the other goes through the delay stage and to the THz detector. Of course the translation stage provides 20cm of freedom, but never the less these paths should be measured carefully, taking into account the various refractive indices of the materials in the beam path. Ideally this can be achieved while maintaining a minimum possible total propagation distance in order to minimize beam divergence and attenuation. High stability mirror mounts should be used for the two pointing mirrors which come directly before the THz emitters and detectors as these are particularly sensitive components.

A.6 THz Optics Alignment

Next the light comes to the THz optics. In the THz emitter and detector field replacable units (FRUs), the 800nm pulses are focused through a lens and onto the PC antennas generating the THz pulses. On the opposite side of the wafer, a hemispherical Si lens helps to couple the diverging THz light into free space, where it is collected and directed by a series of off axis parabolic mirrors (OAPs). With 5 OAPs, 3 FRUs, and a Si beam splitter, there are an impossibly large number of degrees of freedom for aligning the THz optics, and without everything being close to perfect, no signal will be observed, leaving no way to optimize the THz pulse.

Fortunately there are iterative processes which can be used to align components one at a time, so that everything is in reasonably good shape before ever looking for a THz signal. Before performing the alignment process detailed in the next section it is best to consider the many factors which will inform the placement of various components of the system: The focal point where the sample sits should be directly under a gap in the HEPA filters above the table,

as a cryogen transfer line will need to be brought in from above. The entirety of the THz optics will be enclosed in a plexiglass box so make sure that all of the roughly laid out components will fit within the box while ensuring that the cryostat hole, and holes for the 800nm beam are aligned to the appropriate positions. For any alignment using an iris pair, the further apart the pair is, the more precise it is possible to be; consider this in the placement of the THz optics, in particular for the 800nm beam paths approaching the THz emitters and detectors. Crucially, the only component of this system with a non-adjustable height is the focusing lens in the THz emitter and detectors; as a result, this should set the elevation of all the beam paths for the optics. With enough careful consideration, it should be possible to avoid having to rebuild the THz optics or drill superfluous holes in expensive equipment.

Below I will go through the alignment procedure which I developed through trial and error in order to build the PC THz TDS system. I'm sure it is by no means the easiest, best, or only way to perform this alignment, but it worked for me, and my hope is that in writing it down I will spare future researchers the tedium and time which early mistakes are sure to cost. Aligning a single OAP is a multi-step process in its self, which I will not go into here. Henceforth, every time I mention aligning an OAP I will be referring to the process outlined in reference[207] or some variation of it. Refer to figure A.1 though the following steps.

Before beginning in earnest, it is best to have a movable iris which will serve as a height reference. This height will be determined by the height of the lenses in the emitter and detector FRUs. Start with a level alignment beam and send it through the lens of a partially assembled FRU. Send the level beam through the lens. If the transmitted beam is no longer level (no longer at the same elevation), change the elevation of the alignment beam and try again.

a) Begin by using a HeNe alignment laser to set up two parallel alignment beams though two pairs of irises at the elevation of the reference mirror. Spend some time on this; any imperfections in these alignment beams will compound in every subsequent step. Use the holes in the table. I separated my alignment beams by 1 inch. At this point OAP1 can be

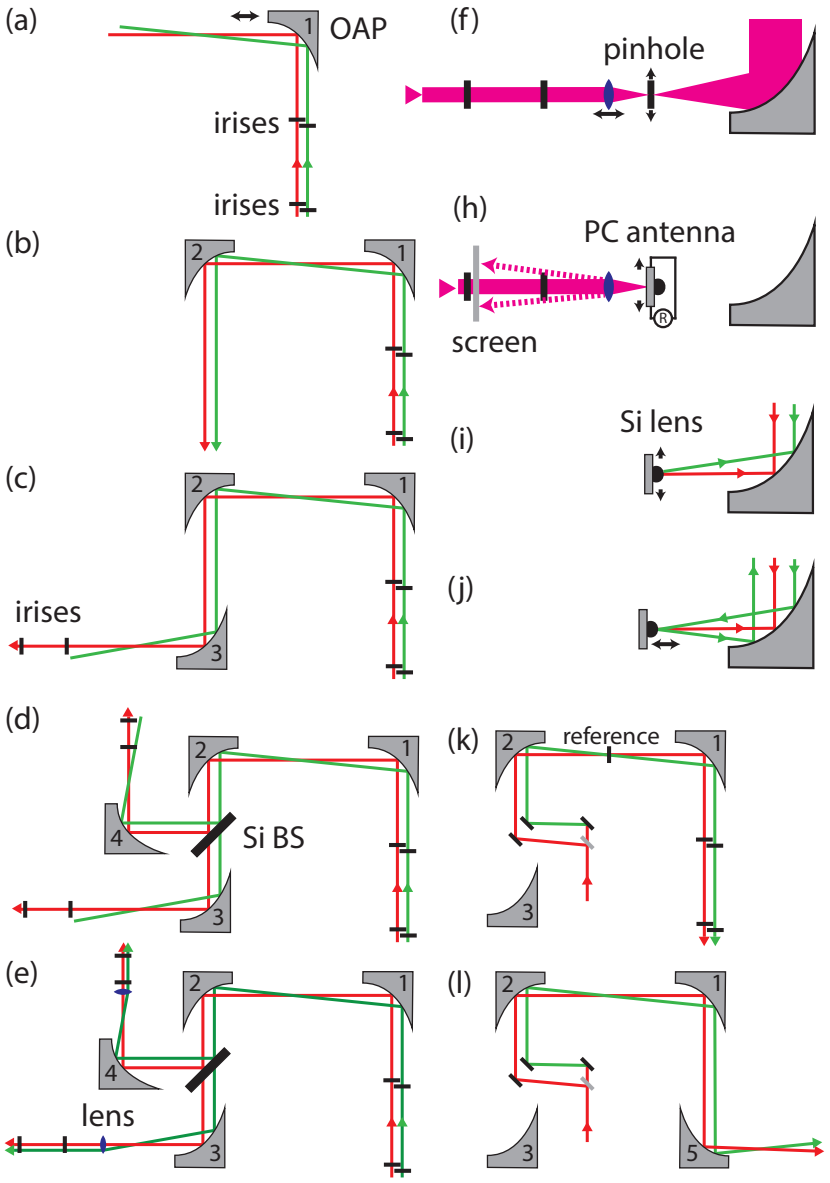

Figure A.1: A guide to the initial setup and alignment of the dual mode photoconductive THz TDS system.

aligned in the fashion described in reference[207]. In a slight variation to this technique, position the OAP such that one of the two beams (red) hits it in its exact center. If done properly, this beam should make a strictly 90deg turns at not only this, but every other mirror it hits. To make this delicate task easier, use blocks fixed to the table and translation stages to push the mirror base back and fourth until this condition is met. This process will

be used for all subsequent components as well. This is also a good time to make note of the focal point of the mirror. This will be the sample position so double check that this is an ideal location.

b) Next, place and align OAP2. Perform all initial alignment steps before placing it in its final location. If aligned properly, the two exiting beams should be completely parallel, both to eachother and to the table. In addition, the separation between the parallel beams should be identical to that of the initial alignment beams (1").

c) OAP 3 comes next. Once aligned the red beam should be parallel to the holes in the table. Place two irises to mark its path. This is the vital advantage of the tedious process of keeping the red beam centered: We will be able to use it to define the path of the 800nm beam later in order to couple the 800nm optics to the THz optics.

d) The large high resistivity silicon beam splitter is expensive and fragile so be careful. It should be used on a magnetic mirror mount so that it can be easily removed and replaced. This will allow for more signal in transmission measurements and aid in aligning. Fortunately the magnetic mounts are extremely repeatable. Thogh the dark Si will attenuate some of the HeNe light, it should still be plenty for alignment. Ensure the red beam is centered and that both beams are parallel to the table holes after they reflect from the beam splitter. Set up OAP4 and two irises in the same fashion as OAP3.

e) Place the emitter and reflection detector FRUs with only the 800nm lens installed. The FRUs are also on magnetic mounts alowing them to be easily removed and replaced. Translate the stage laterally until the introduction of the lens does not divert the beam from its unobstructed path (though of course it will effect the focusing. Ensure that the translation stage they sit on moves parallel to the red beam. Next, translate the FRU parallel to the path of the red beam until both the red and green alignment beams are columnated (i.e. the red beam remains the same diameter and the center of the green beam remains

parallel to it. At this point, the focal points of the OAP and the lens should be aligned. Remove the Si beam splitter and repeat thsi with OAP3 and its FRU.

f) Next we must align the rest of the components of the PC antenna FRU. Start by aligning the 800nm modelocked beam from the oscillator to the iris pair in front of the FRU. Place a pinhole (start with $25\mu m$) in a modified PCB board at the PC antenna location and reassemble the FRU. Place a power meter in the approximate sample position. Next maximize the 800nm power reaching the power meter by iteratively translating the pinhole with the adjustment screws and fine tuning the lens translation with its adjustment screw. It should be possible to get much of the power through. Replace the pinhole with a smaller one and repeat this process. Perform this procedure for the transmitter and reflection detector.

g) We will now install the photoconductive antenna and align the 800nm beam to it. There are two sets of horizontal and vertical adjustment screws on each FRU. One controls the translation of the PC antenna wafer and with it the Si lens, while the other translates the Si lens relative to the PC antenna. In this step we will only use the former. Connect a multimeter to measure the resistance across a chosen PC antenna (alternatively if working with the emitter, a bias can be applied and the photocurrent can be measured). The goal is to ”find” the PC antenna and optimize the signal by minimizing the resistance (maximizing the photocurrent). This can be difficult to do with no other observable, so there is one other useful technique: About 1m in the 800nm path, place a note card in the beam path small hole just large enough to allow the incident light through. Some of the 800nm light incident on the PC antenna will be back scattered through the lens and onto the card forming an image of the Si wafer (though you will need to use an IR scope to see it). You translate the wafer horizontally until an image of the PC antenna comes into view. In the case of the receiver antennas you will also need to translate the wafer vertically in order to find the

bowtie protrusions. Repeat this process for both the emitter and reflection detector.

h) Now we will return to the HeNe alignment beams in order to roughly align hemispherical Si lenses. The hemispherical lenses can be translated perpendicular to the beam path using the second set of adjustment screws, which will adjust the Si lens position but not the PC antenna position. Laterally align the Si lens by getting the red beam to reflect off of it and follow its original path. Though the beam will diverge, it should be possible to get it going back along the path of the original iris pair. If the center of the hemisphere is perfectly at the focal point of the OAP, the green alignment beam should also hit it at normal incidence and it too should retrace its path. If it does not, use the translation stage to translate the entire FRU on its axis in order to get both beams retracing their path.

i) This alignment can be double checked by further translating the entire FRU. When the focal point of the OAP is at precisely the apex of the Si lens, the red beam will retrace its path as before, but the green beam will form a second parallel beam path, 2 inches away from the incident one. After this check, return the Si lens to the state described in the previous step. Repeat this process for both the emitter and reflection detector. At this point the 800nm beam, 800nm lens, PC antenna, and Si lens should all be well aligned to the THz optics.

j) Finally the last OAP and FRU must be placed. This will require the direction of the alignment beams to be reversed. Set up the alignment beam as shown, and lign it such that the beam passes through the two original iris pairs, albeit in the opposite direction. As before it is important that these be as near to perfect as possible. This is a good time to place and align a permanent reference mirror at the sample position. This mirror will serve as a reference while optimizing the system in reflection as well as a way of identifying the proper t=0. Use another removable magnetic mount and place a mirror at the sample position as near to the focal point as possible. Align the mirror so that the reflected beams both retrace their path as well as possible, keeping in mind that adjustments to the mirror

may also translate it away from the true focal point. Hold on to this mirror on its magnetic base and keep it near by. It is just as important as the Si beam splitter.

k) finally, place the OAP5, align it, and set up the transmission detector and beam line using the steps described previously.

Finally the sample stage must be placed and the entirety of the THz optics should be enclosed into a plexiglass box and pumped with dry air. It may be convenient to avoid setting up the box until much of the pulse optimization has been completed, but keep in mind that air moisture will cut the time domain pulse in half, and cause sharp absorptions in the frequency domain.

A.7 THz Generation, Detection, and Optimization

With the THz optics set up, we are almost ready to begin detecting a THZ signal. Before proceeding, adjust the neutral density filters so that only 10-15mW of 800nm light reaches each of the 3 photoconductive antennas. Higher fluences have the potential to damage sensative components. Next we will go through the various electronic equipment necessary for interfacing with the THz optics and the computer and subsequently how to adjust and optimize the THz optics to maximize the THz signal.

A.7.1 Electronics

The lock in amplifier is the heart of the electronics of the PC THz-TDS system. It provides a modulation signal to the emitter power supply and then seeks amplified currents from the detectors which are modulated at the same frequency, resulting in an effectively DC signal which can then be read by the computer as a function of delay time. The lockin should be connected to a computer via a GPIB cable to interface with the software. The reference signal

of the lockin should be set to about 1kHz, being careful to avoid any harmonic of 120Hz (the frequency of US AC power supply). The auxiliary output of the lockin should be connected to the small Zomega HVM-500USB voltage supply. This power supply can then be connected to the THz emitter and we are ready to generate THz light. Open CurrentMon.vi, start the program and select the appropriate input port. A scrolling voltage and current reading should appear. Set the voltage to 100V, and an accompanying photocurrent should appear. Though we will not optimize it yet, a photocurrent of ¿5mA should be possible for a 100V bias and 15mW incident 800nm light.

Next, we must connect the detectors to the electronics. Unforutnately without a second lockin only one can be connected at a time, so make sure that it is convenient to switch between the two detectors. The detector should first be connected to a current amplifier. The bandpass filter should be set to 100Hz-3KHz, allowing a comfortable window for the 1kHz modulation frequency. The sensitivity should be about 20nA/V with a low noise gain mode. The ouptut of the current amplifier should be connected to the input of the lockin. The lock in settings for regular operation should be a 300ms time constant at 24dB and a 50mV sensitivity. Of course some of these settings may need to be changed in order to detect a weak and unoptimized signal. During the optimization process, a multimeter may be plugged into the CH1 output to serve as a more convenient readout of the signal.

The final electronic piece is the delay stage. The time delay stage should be connected to channel 1 and the translation stage which manipulates the sample up and down should be connected to channel 3. The delay stage controller should also be connected via GPIB cable to the computer to interface with the software.

A.8 Software

The preferred LabView software package for controlling this instrument is the home built MultiTHzScanPC.vi. This program is extremely complicated and feature rich but it is resultingly powerful and versatile, and allows for automation of most functions. I will briefly attempt to demystify some of its less obvious features.

The top left box shows time domain (TD) data, the ”THz/PI Signal” tab shows current data as it is being measured, whereas the rest show completed scans of the reference and sample. Below this box is another which shows frequency domain information. ”Magnitude” and ”Current Magnitude” tabs show the Fourier transform of the TD signal for a single scan, and the magnitude ratio (S11 or S21) for sample/reference scans. The other features tabs here allow for a quick calculation of resistivity or conductivity but I do not typically use them.

The top middle of the screen shows a number of options and readouts. The top box allows the selection of the data source (in this case ”SR830”), the next allows you to select either time or delay stage position for the x-axis, and the 3rd box allows you to select which axis you would like to scan (x is the delay stage, y is an auxiliary stage, and z is the sample stage). The next box is crucial as it allows you to select what type of program you would like to run.

1) Single Scan leaves the sample at its current position, and only the gate delay stage while collecting the signal.

2) Multiple Scans moves the sample stage to the reference and performs a delay stage scan, then to the sample position where it does the same. It repeats this for the specified number of runs.

3) Move X, Y, Z-axis allows the selected translation stage (specified in the box above) to be moved to an arbitrary position by entering the number in the below boxes labeled ”Move Delay [ps]” for the X (gate) and Y (auxiliary) stages, and ”Move Z [mm]” for the sample stage.

4) Go to Zero moves the selected translation stage to its zero position.

5) Define Zero zeros the selected translation stage at its current position.

6) Move THz Beam to Sample moves the Z stage to the specified sample position.

7) Move THz Beam to Reference moves the Z stage to the specified reference position.

8) Adjust Z-axis can be used to optimize the zero (reference) position of the Z-axis. When the gate delay is set at t=0, this feature will move the Z-stage around attempting to find the center of the reference (an aperture for instance), before defining this center point as the new Z axis zero. This can be a useful feature but it tends to work poorly with excessively large or small apertures. For transmission use an aperture of around 3-5mm and double check the programs work once it has finished. I do not recommend using this feature in reflection.

I do not use the other options though I'm sure they are useful. Below are boxes that allow the program to be started, continued, or paused. The "Dwell Time" box is the amount of time spent measuring at each delay time, and should be set to 3 times the lock in time constant (0.9sec). X, Y, and Z show the (semi-)real time positions of those axes, while the "Move" boxes allow values to be entered as discussed previously. The "Reset Axes" buttons allow their respective axes to be sent to zero. The next series of boxes show the current parameters of the measurement; run number, temperature set point, sample/reference, the current heater power percentage and range, etc.

The box on the top right has many tabs that allow for defining the parameters of a measurement. Many options I do not use but I will cover the important ones.

1) Controls : The top four switches are primarily for pump probe experiments. For an ordinary THz TDS experiment, they should be set to "Conductivity Data, Chop X or Y", "Pure Conductivity Data", Pure Induced Conductivity Data" and "No" respectively. For a

measurement with a second delay stage (Y-axis), i.e. a pump probe measurement or the measurements performed in chapter 4, they should be set to ”Conductivity Data, Chop X or Y”, ”Time Delay on Induced Conductivity”, ”Time Delay on Induced Conductivity” and ”No” respectively. ”Temperature Mode” enables the temperature controls and interfacing with a temperature controller. ”Current Mode” allows automated interfacing with a Keithley 2420 power supply (See ”Current Settings” tab). The ”X,Y,Z-axis” boxes allow the sign of the axes to be reversed. The Yellow boxes allow the settings of the temperature controller to be changed. Most importantly, to change the heater range, select teh desired range under ”Change Heater Settings”, and press the yellow circle next to it. Enable ”Z-axis Adjustment with Temperature Mode” performs an ”Adjust Z-axis” task after each temperature change in order to compensate for thermal contraction; it has the potential to be a great time and effort saver but again, be cautious using this feature. ”Enable Wait for Sample?” pauses the program after reach run until the user confirms that it should continue.

2) Scan Settings: this is where most the day to day settings are controlled. For each run, a temperature (For temperature mode), current (For current mode), a Y-delay (For time delay on induced conductivity mode), and a number of sample scans can be defined for up to 33 runs. Below, the number of runs can be selected, and the Z-position of the sample can be defined. The reference is always set to zero. ”N Scans Ref” determines how many reference scans will be averaged before each sample run. Other settings deal with the file names. ”Scan File Path” defines the folder where files will be saved. ”Scan File Name” allows the first part of the file name to be defined while all other parts are generated automatically. In addition to this name, the date and temperature will be added to the file name. If ”Current Mode” is active, the current for that run will be added as well. If you wish to record some other value in the current column, you can plug in arbitrary numbers, and use the ”Apply other extension” switch and ”Extension for current” to define a custom extension for the information in that column. Each file ends with either ”Ref” or ”Sig” and a 3 digit number,

starting from zero. Ordinarily the reference scans will be even numbers while the signal scans can be odd. But the start number can also be defined by the user in the ”Choose even file Number to Start” box. This is useful if you wish to do more than 33 runs, but want the files to continue in order. The ”Single Scan settings” apply when the program is run in the ”Single Scan” mode.

3) Conductivity: This tab allows parameters that are used in the calculation of thin film conductivity to be defined. That being said, I have never used it.

4) Current Settings: This tab allows the settings for current mode to be used in order to control a Keithley 2420 voltage supply. Likewise I have never used it and at present I don't think the Averitt Lab has such a device.

5) FFT: This tab allows the parameters of the FFT for the bottom left readout to be changed. I have always found the default to be perfectly satisfactory.

6) Various: Miscelaneous settings and readouts. One key one here is the ”Zero Adjusted Z Position” box which shows by how much the zero of the Z axis has been changed after running the ”Z adjust” mode. Make sure it is more or less what you expected after using this mode.

In the center bottom box, the time start and end times can be defined as well as the time step for one or several different intervals. Below this, is a readout of the expected and elapsed program run time.

A.8.1 THz Signal Optimization

With the THz and 800nm optics aligned, and the electronics and software configured it is time to search for and optimize a THz signal. I recommend starting in transmission mode and performing single scan in the vicinity of the expected t=0 with 0.5ps time steps. If everything

went well, there should be one time delay at the signal peaks. Reset the x-axis zero to this time delay and you are ready to begin optimization.

Once aligned, the OAPs and Si beam splitter should never be touched. Instead, alignment will take the form of iterative adjustments to the PC antennas, the hemispherical lenses, and the turning mirrors sending the 800nm beam into the THz emitters and detectors. Ultimately the goal is to increase the amplitude of the signal, though there are other metrics that are useful to look at as well. Keep in mind that as various dispersive components move, the path length and thus t=0 may change slightly. Manually adjust the delay stage to find the peak periodically in order to compensate for this. Unfortunately moving the antenna also moves the hemispherical lenses, so I recommend the following order.

1) Adjust the emitter antenna position in order to maximize the signal. The PC antenna current can also be used as another metric of the antenna performance which is independent of alignment of other system components and delay adjustment.

2) Adjust the emitter hemispherical lens position. In principle, this adjustment should be in the opposite direction of those made to antenna, compensating for its motion to re-align the hemisphere to the OAP focal point.

3) Adjust the receiver antenna position.

4) Adjust the receiver hemispherical lens position.

5) Repeat this process iteratively. Ideally, during these adjustments, the pulse should move to earlier time, as ideal alignment will send the THz pulse through the thickest part of the hemispherical lens. Be aware that the FRUs are extremely sensitive, and even the touching the knobs may cause electrostatic interference which effects the signal. It may be necessary to keep your hand on the knob until the signal stabilizes, or if not, make small adjustments and remove your hand until the signal stabilizes.

6) Once you are certain the signal cannot be improved further with these adjustments, move on to the turning mirrors. Begin with the emitter antenna. Make a small horizontal adjustment to the first turning mirror and then optimize the signal using the horizontal adjustment of the second. If the signal is better than before then make another small adjustment to the first mirror in the same direction and repeat. Use this method of ”walking” the beam in order to optimize not only the pointing but also the path.

7) Perform the same optimization on the receiver side.

8) repeat steps 1-7 ad nauseam. When the signal can no longer be meaningfully improved, you may take 1D scans and evaluate the time domain and frequency domain characteristics of the pulse. Ultimately, the pulse should resemble a single cycle with a peak around 20mV with some small wiggles afterwards and should have a 10% line at at least 2 THz.

A similar process occurs for optimization of the reflection signal. Place the reference mirror and the beam Si beam splitter into the beam path, connect the reflection detector, and look for T=0. Once found, optimize in the same fashion as described previously EXCEPT make few if any adjustments to the transmitter as, in principle, it should already be well aligned.

The previous steps assume a more or less ideal case. In practice there may be many imperfections, and fortunately there are many degrees of freedom in order to address them. The translation of the entire emitter and receiver FRUs can be adjusted in order to change the location of the hemispherical lens along the beam path. The fine focus of the 800nm lens can be adjusted in order to improve the 800nm beam focusing onto the PC antennas. The transmitter can be adjusted during reflection optimization even after it has already been aligned. These types of adjustments should all be done sparingly only after exhausting other options. Still, the OAPs should NEVER be adjusted.

A.8.2 THz Signal Trouble Shooting

1) There is no THz signal across the entire delay stage range, just noise: While this could be just about anything, if you are confident the Oscillator, electronics, delay stages, etc are performing well and correctly configured, the most likely scenario is that the path lengths were not measured or calculated correctly. Measure again, and eb sure to take into account all of the various indicies of refraction of various components along the way. Remember that the beams must arrive at the DETECTOR at the same time.

2) The main THz pulse is flanked by a symmetric pair of weaker pulses both before and after the main pulse: This is almost certainly caused by double pulsing from the oscillator. These pulses are separated by too small a time delay to be resolved by the photodiode (though they may appear as wiggles in the 800nm spectrum), but are evident in the THz scan. Improve the mode locking condition, possibly by reducing the 532nm pump power.

3) The noise background has a linear slope as a function of delay time especially obvious over broad scans: This is almost certainly caused by poor alignment of the delay stage. As the delay stage moves, the alignment to the PC antennas changes and changes the background signal level.

4) There is a small peak or dip superposed onto the main THz pulse: This is generally a result of bad hemispherical lens alignment. By performing a scan, adjusting one of the hemispherical lens knobs, and performing another scan, the pulse should move relative to t=0. If for instance, there is a small dip during the upswing after the main trough of the pulse, adjust the hemispherical lenses to bring this dip down to the same time delay as the main pulse trough. This should improve the overall signal as well.

5) There is smaller than expected THz bandwidth: There is no magic solution here, only continued, patient, iterative improvement of the alignment of the antennas, hemispherical

lenses, and turning mirrors.

6) There are sharp dips in the frequency domain signal at several frequencies: This is likely water vapor absorption. Ensure that the humidity of the air inside the box is near zero.

A.9 Measurements

In this section I'll briefly describe some basic approaches for taking measurements using the PC THz TDS system. One of the most important factors is the alignment of the sample and reference; both its position on the plane perpendicualr to teh beam path, and along the beam axis. Fortunately, both of these alignments are relatively easily performed due to the ability to do reflection and transmission measurements.

A.9.1 Initial Sample Stage Alignment

In order to initially align the sample stage, use a room temperature sample mount with a copper sample holder with relatively large apertures (5mm diameter) and place it into the sample stage. Start with the instrument configured for transmission and the delay stage set to t=0 (maximum signal). I typically use the top hole in the sample holder as the transmission reference, so attempt to get the beam centered through this hole. We will first center the sample holder relative to the beam on the plane perpendicular to the beam path using the z-stage and one of the delay stage micrometers. The best approach is to choose some signal target value (say, 1/3rd of maximum), translate the stage in one direction until this target is reached, note the position, and then to the same in the opposite direction. The average of these two positions should very nearly be the arpeture center. Do this in both directions and double check. After this, the micrometer dial should rarely need to be adjusted, if ever. The z-stage on the other hadn will need to be adjusted any time the sample holder is changed.

To set the sample mount at the THz focal plane, reconfigure the instrument into transmission mode and find t=0 using the reference mirror on the magnetic mount. Remove the reference mirror and place a the sample holder into the sample stage. You may place thin a mirror over the reference hole position, or, if you are using a typical copper sample mount, simply translate the z-axis 6.5mm up (so the beam hits the copper between the two holes) and use the copper as a mirror. Orient the sample holder as best as possible by eye and adjust the beam axis micrometer dial until the signal is maximum at the reflection t=0. Repeatedly make small adjustments to the sample holder rotation and the micrometer in order to maximize the signal at t=0. At this point, the sample holder should be well aligned in all three axes. While the rotation of the sample holder will need to be carefully adjusted for every reflection measurement, the translation should generally require no adjustments unless a different type of sample holder is used.

A.9.2 Transmission Measurements

Transmission measurements are relatively straightforward. The reference (top) hole in the sample holder should be at the z=0 position and the sample should be placed in the bottom position. On the ordinary ST-300 style copper sample mounts, these holes are separated by 13mm, so set the sample position to +13mm. Samples such as MMs on wafers or thick crystals can typically be mounted simply using double sided tape. That being said, too much adhesion may make the samples difficult to remove without breaking. Place 2-4 tiny strips of double sided tape around the sample position hole and press a gloved finger onto the tape several times to reduce its stickiness. Then orient the sample and press it into place. To remove samples, it is often best to begin by wedging a razor blade underneath the corners in order to carefully pry them up. For other types of samples (for instance flexible metamaterial tapes), nylon cover slips can be screwed down over the sample to hold it in place.

For a typical measurement, start at about t=-5ps with a stepsize of $\Delta t = 0.04 ps$. The end point of the measurement will depend heavily on what is being measured though practically

speaking $t_f = 10 - 15ps$ is generally sufficient for good spectral resolution. In particular thick samples will cause multiple internal reflections (etalons) which will result in a periodic anomaly in the frequency domain data. This can of course be eliminated in post processing but it may be desirable to terminate the scan before the etalon occurs in order to see a nice spectra in real time. In addition, the length of the scan ultimately determines the spectral resolution, so consider the linewidth of the features you expect to observe in your sample spectra. Keep in mind that a thick sample of a high index will delay the arrival of the sample pulse, so terminate the scan accordingly.

Similarly, the more runs or sample scans over which the data is averaged, the better statistics that data will have. Due to long term drift, it is generally best to alternate between sample and reference rather than performing multiple sample or reference scans in a row. Though it may be overkill, I often do 2-3 runs, with one reference measurement and one sample measurement each.

A.9.3 Reflection Measurements

Reflection measurements are significantly more involved, but as before, once things are set up properly, going from one measurement to the next should be easy. For the reference, we wish to use something that approximates a perfect reflection. Generally a gold coated silicon wafer is used. Tape this over the reference hole position and mount the sample in the sample position. It is important that the two be entirely flat relative to one another. If, for instance, there is a bubble or crease in the tape underneath one side of the sample, it will alter the alignment relative to the reference, and reduce the observed reflectively. Place the sample holder into the sample stage and orient it by hand as best as possible. As during initial setup, attractively adjust the rotation of the sample holder and the translation of the sample stage along the beam axis in order to get a maximal signal at t=0. This will ensure that the reference is on the THz focal plane and oriented normal to the incident light. Otherwise the procedure is the same as before. If no

changes are made to the sample holder, it should be relatively easy to reproduce the signal at t=0 simply by rotating the sample holder by hand.

It is likely that the sample and reference will not be perfectly coplanar, so the sample and reference pulses will likely arrive at slightly different times. As long as the difference is not massive (¿10ps) this should not be a problem, but consider this when deciding the start and end times of your scan.

A.9.4 Cryostat/Temperature Controlled Measurements

Adding a ST-300 cryostat requires few additional considerations. Connect the temperature controller to the computer and the cryostat and connect the cryostat to a vacuum pump. Though the vacuum level should quickly reach 10^{-6} Torr, this high of a vacuum level is not strictly necessary. Use a clamp to secure the cryostat to the sample stage to prevent it from rotating or vibrating. Keep in mind that the windows will significantly delay the arrival of the detected pulses depending on their thickness and refractive index.

The Labview code works very well for controlling the cryostat but many experiments, particularly with cryogens should be supervised. Adjust the flow rate such that the cryostat heater can easily reach the desired temperature. Consider that especially at low temperatures, the cold finger and sample holder may contract and the sample position may need to be adjusted. For above room temperature measurements, I have found that the medium heater setting works best up to 370K, and the experiment requires no intervention once initiated.

A.9.5 Typical Operating Parameters and Performance for PC THz TDS System

1) Millenia Pro 532nm Laser

   (a) Output power: 3W

(b) Diode current (D1): 40.3A

(c) Diode temperature: 26.5C

(d) Coolant temperature (TWR): 20.9C

2) KM Laboratories Griffin Oscillator

(a) Curved mirror position: 4.08mm

(b) Crystal position: 6.18mm

(c) Lens position: 4.78mm

(d) Prism 1: 134 (9mm with calipers)

(e) Prism 2: 290 (8.5mm with calipers)

(f) Output Power (CW): 600mW

(g) Output Power (ML): 300mW

(h) Output Wavelength: 810nm

(i) Output Bandwidth (FWHM): 60nm

(j) Pulse Duration (before compression): 200fs

(k) Pulse DUration (after compression): 21fs

3) Current Preamplifier

(a) Input Offset: None

(b) Filter: 6dB bandpass

(c) Filter Frequency: 300Hz-3kHz

(d) Gain Mode: Low Noise

(e) Sensitivity: 20nA/V

4) Lock-in Amplifier

   (a) Time Constant: 300ms

   (b) Sensitivity: 50mV nA

   (c) Reference Signal: sine

   (d) Reference Frequency (to emitter antenna): 1kHz

5) THz Emitter Antenna

   (a) Incident 800nm Power: 10-12mW

   (b) Applied Voltage: 100V

   (c) Photocurrent: 5mA

   (d) Modulation Frequency: 1kHz

6) THz Detection (Transmission w/o Si Beam Splitter)

   (a) Incident 800nm Power: 10mW

   (b) Peak Signal: 18mV

   (c) 10% spectrum peak: 2.1THz

   (d) 100% line $\pm$5%: 2.5THz

   (e) Signal to Noise: 10000

7) THz Detection (Reflection)

   (a) Incident 800nm Power: 10mW

   (b) Peak Signal: 7mV

   (c) 10% spectrum peak: 2THz

   (d) 100% line $\pm$5%: 2.3THz

Bibliography

[1] Guangwu Duan, Jacob Schalch, Xiaoguang Zhao, Jingdi Zhang, Richard D. Averitt, and Xin Zhang. Analysis of the thickness dependence of metamaterial absorbers at terahertz frequencies. *Opt. Express*, 26(3):2242–2251, Feb 2018.

[2] V. G. Veselago. The electrodynamics of substances with simultaneously negative values of and . *Phys. Usp.*, 10(4):509–514, 1968.

[3] D. R. Smith, Willie J. Padilla, D. C. Vier, S. C. Nemat-Nasser, and S. Schultz. Composite medium with simultaneously negative permeability and permittivity. *Phys. Rev. Lett.*, 84:4184–4187, May 2000.

[4] J. B. Pendry. Negative refraction makes a perfect lens. *Phys. Rev. Lett.*, 85:3966–3969, Oct 2000.

[5] D. Schurig, J. J. Mock, B. J. Justice, S. A. Cummer, J. B. Pendry, A. F. Starr, and D. R. Smith. Metamaterial electromagnetic cloak at microwave frequencies. *Science*, 314(5801):977–980, 2006.

[6] Majid Gharghi, Christopher Gladden, Thomas Zentgraf, Yongmin Liu, Xiaobo Yin, Jason Valentine, and Xiang Zhang. A carpet cloak for visible light. *Nano Letters*, 11(7):2825–2828, 2011. PMID: 21619019.

[7] R. Liu, C. Ji, J. J. Mock, J. Y. Chin, T. J. Cui, and D. R. Smith. Broadband ground-plane cloak. *Science*, 323(5912):366–369, 2009.

[8] S. J. Allen, D. C. Tsui, and R. A. Logan. Observation of the two-dimensional plasmon in silicon inversion layers. *Phys. Rev. Lett.*, 38:980–983, Apr 1977.

[9] R Merlin. Generating coherent thz phonons with light pulses. 102:207–220, 04 1997.

[10] Olaf Schubert, M Hohenleutner, F Langer, Benedikt Urbanek, Christoph Lange, U Huttner, D Golde, T Meier, Mackillo Kira, S W. Koch, and R Huber. Sub-cycle control of terahertz high-harmonic generation by dynamical bloch oscillations. 8:119123, 01 2014.

[11] M. Dressel, N. Drichko, B. Gorshunov, and A. Pimenov. Thz spectroscopy of superconductors. *IEEE Journal of Selected Topics in Quantum Electronics*, 14(2):399–406, March 2008.

[12] Christian Jansen, Steffen Wietzke, Ole Peters, Maik Scheller, Nico Vieweg, Mohammed Salhi, Norman Krumbholz, Christian Jördens, Thomas Hochrein, and Martin Koch. Terahertz imaging: applications and perspectives. *Appl. Opt.*, 49(19):E48–E57, Jul 2010.

[13] K. Ishigaki, M. Shiraishi, S. Suzuki, M. Asada, N. Nishiyama, and S. Arai. Direct intensity modulation and wireless data transmission characteristics of terahertz-oscillating resonant tunnelling diodes. *Electronics Letters*, 48(10):582–583, May 2012.

[14] John F Federici, Brian Schulkin, Feng Huang, Dale Gary, Robert Barat, Filipe Oliveira, and David Zimdars. Thz imaging and sensing for security applicationsexplosives, weapons and drugs. *Semiconductor Science and Technology*, 20(7):S266, 2005.

[15] Na Liu, Martin Mesch, Thomas Weiss, Mario Hentschel, and Harald Giessen. Infrared perfect absorber and its application as plasmonic sensor. *Nano Letters*, 10(7):2342–2348, 2010. PMID: 20560590.

[16] R A Lewis. A review of terahertz sources. *Journal of Physics D: Applied Physics*, 47(37):374001, 2014.

[17] M. B. Ketchen, D. Grischkowsky, T. C. Chen, CC. Chi, I. N. Duling, N. J. Halas, JM. Halbout, J. A. Kash, and G. P. Li. Generation of subpicosecond electrical pulses on coplanar transmission lines. *Applied Physics Letters*, 48(12):751–753, 1986.

[18] János Hebling, Ka-Lo Yeh, Matthias C. Hoffmann, Balázs Bartal, and Keith A. Nelson. Generation of high-power terahertz pulses by tilted-pulse-front excitation and their application possibilities. *J. Opt. Soc. Am. B*, 25(7):B6–B19, Jul 2008.

[19] F. Blanchard, L. Razzari, H.-C. Bandulet, G. Sharma, R. Morandotti, J.-C. Kieffer, T. Ozaki, M. Reid, H. F. Tiedje, H. K. Haugen, and F. A. Hegmann. Generation of 1.5 μj single-cycle terahertz pulses by optical rectification from a large aperture znte crystal. *Opt. Express*, 15(20):13212–13220, Oct 2007.

[20] Tobias Kampfrath, Koichiro Tanaka, and Keith Nelson. Resonant and nonresonant control over matter and light by intense terahertz transients. 7:680–690, 08 2013.

[21] D. N. Basov and T. Timusk. Electrodynamics of high-T_c superconductors. *Rev. Mod. Phys.*, 77:721–779, Aug 2005.

[22] Y. Laplace and A. Cavalleri. Josephson plasmonics in layered superconductors. *Advances in Physics: X*, 1(3):387–411, 2016.

[23] R. A. Shelby, D. R. Smith, and S. Schultz. Experimental verification of a negative index of refraction. *Science*, 292(5514):77–79, 2001.

[24] Anthony Grbic and George V. Eleftheriades. Overcoming the diffraction limit with a planar left-handed transmission-line lens. *Phys. Rev. Lett.*, 92:117403, Mar 2004.

[25] Michele Brun, Sbastien Guenneau, and Alexander Movchan. Achieving control of in-plane elastic waves. 12 2008.

[26] Stefan Enoch, Gérard Tayeb, Pierre Sabouroux, Nicolas Guérin, and Patrick Vincent. A metamaterial for directive emission. *Phys. Rev. Lett.*, 89:213902, Nov 2002.

[27] I. Hrebikova, L. Jelinek, and M. G. Silveirinha. Bound states within the continuum a metamaterial-semiconductor analogy. In *2015 9th International Congress on Advanced Electromagnetic Materials in Microwaves and Optics (METAMATERIALS)*, pages 112–114, Sept 2015.

[28] J. B. Pendry, A. J. Holden, D. J. Robbins, and W. J. Stewart. Magnetism from conductors and enhanced nonlinear phenomena. *IEEE Transactions on Microwave Theory and Techniques*, 47(11):2075–2084, Nov 1999.

[29] O. Sydoruk, E. Tatartschuk, E. Shamonina, and L. Solymar. Analytical formulation for the resonant frequency of split rings. *Journal of Applied Physics*, 105(1):014903, 2009.

[30] Mengkun Liu, H Y Hwang, Hu Tao, Andrew Strikwerda, and Kebin Fan. Terahertz-field-induced insulator-to-metal transition in vanadium dioxide metamaterial. 01 2012.

[31] Jingdi Zhang, Xiaoguang Zhao, Kebin Fan, Xiaoning Wang, Gu-Feng Zhang, Kun Geng, Xin Zhang, and Richard D. Averitt. Terahertz radiation-induced sub-cycle field electron emission across a split-gap dipole antenna. *Applied Physics Letters*, 107(23):231101, 2015.

[32] C. . Kriegler, M. S. Rill, S. Linden, and M. Wegener. Bianisotropic photonic metamaterials. *IEEE Journal of Selected Topics in Quantum Electronics*, 16(2):367–375, March 2010.

[33] D. R. Smith, D. C. Vier, Th. Koschny, and C. M. Soukoulis. Electromagnetic parameter retrieval from inhomogeneous metamaterials. *Phys. Rev. E*, 71:036617, Mar 2005.

[34] Kosmas Tsakmakidis. Non-reciprocal plasmonics. 12:378, 04 2013.

[35] S. Sajuyigbe, B. J. Justice, A. F. Starr, and D. R. Smith. Design and analysis of three-dimensionalized elc metamaterial unit cell. *IEEE Antennas and Wireless Propagation Letters*, 8:1268–1271, 2009.

[36] E. Ekmekci, A. C. Strikwerda, K. Fan, G. Keiser, X. Zhang, G. Turhan-Sayan, and R. D. Averitt. Frequency tunable terahertz metamaterials using broadside coupled split-ring resonators. *Phys. Rev. B*, 83:193103, May 2011.

[37] M. Cao and Q. Zhang. Design of broadband multi-layer metamaterial absorber. In *2018 IEEE MTT-S International Wireless Symposium (IWS)*, pages 1–3, May 2018.

[38] N. R. Han, Z. C. Chen, C. S. Lim, B. Ng, and M. H. Hong. Broadband multi-layer terahertz metamaterials fabrication and characterization on flexible substrates. *Opt. Express*, 19(8):6990–6998, Apr 2011.

[39] Christopher M. Bingham, Hu Tao, Xianliang Liu, Richard D. Averitt, Xin Zhang, and Willie J. Padilla. Planar wallpaper group metamaterials for novel terahertz applications. *Opt. Express*, 16(23):18565–18575, Nov 2008.

[40] J. D. Baena, J. Bonache, F. Martin, R. M. Sillero, F. Falcone, T. Lopetegi, M. A. G. Laso, J. Garcia-Garcia, I. Gil, M. F. Portillo, and M. Sorolla. Equivalent-circuit models for split-ring resonators and complementary split-ring resonators coupled to planar transmission lines. *IEEE Transactions on Microwave Theory and Techniques*, 53(4):1451–1461, April 2005.

[41] H. Bahrami, M. Hakkak, and A. Pirhadi. Using complementary split ring resonators (csrr) to design bandpass waveguide filters. In *2007 Asia-Pacific Microwave Conference*, pages 1–4, Dec 2007.

[42] Chéryl Feuillet-Palma, Yanko M Todorov, Angela Vasanelli, and Carlo Sirtori. Strong near field enhancement in thz nano-antenna arrays. In *Scientific reports*, 2013.

[43] Huseyin R. Seren, Jingdi Zhang, George R. Keiser, Scott J. Maddox, Xiaoguang Zhao, Kebin Fan, Seth R. Bank, Xin Zhang, and Richard Douglas Averitt. Nonlinear terahertz devices utilizing semiconducting plasmonic metamaterials. 2016.

[44] D. Sievenpiper, Lijun Zhang, R. F. J. Broas, N. G. Alexopolous, and E. Yablonovitch. High-impedance electromagnetic surfaces with a forbidden frequency band. *IEEE Transactions on Microwave Theory and Techniques*, 47(11):2059–2074, Nov 1999.

[45] Vladimir Shalaev. Optical negative-index metamaterials. *Nature Photonics*, 1:41–48, 2007.

[46] Harish N. S. Krishnamoorthy, Zubin Jacob, Evgenii Narimanov, Ilona Kretzschmar, and Vinod M. Menon. Topological transitions in metamaterials. *Science*, 336(6078):205–209, 2012.

[47] Mario Hentschel, Martin Schferling, Thomas Weiss, Na Liu, and Harald Giessen. Three-dimensional chiral plasmonic oligomers. *Nano Letters*, 12(5):2542–2547, 2012. PMID: 22458608.

[48] Saman Jahani and Zubin Jacob. All-dielectric metamaterials. *Nature Nanotechnology*, 11:23–26, 2016.

[49] R. H. Jacobsen, D. M. Mittleman, and M. C. Nuss. Chemical recognition of gases and gas mixtures with terahertz waves. *Opt. Lett.*, 21(24):2011–2013, Dec 1996.

[50] Thomas W. Crowe, Tatiana Globus, Dwight L. Woolard, and Jeffrey L. Hesler. Terahertz sources and detectors and their application to biological sensing. *Philosophical transactions. Series A, Mathematical, physical, and engineering sciences*, 362 1815:365–74; discussion 374–7, 2004.

[51] C. Kulesa. Terahertz spectroscopy for astronomy: From comets to cosmology. *IEEE Transactions on Terahertz Science and Technology*, 1(1):232–240, Sept 2011.

[52] Emma Pickwell-MacPherson and Vincent P. Wallace. Terahertz pulsed imaginga potential medical imaging modality? *Photodiagnosis and Photodynamic Therapy*, 6(2):128 – 134, 2009.

[53] B. B. Hu and M. C. Nuss. Imaging with terahertz waves. *Opt. Lett.*, 20(16):1716–1718, Aug 1995.

[54] Andrew C. Strikwerda, Kebin Fan, Hu Tao, Daniel V. Pilon, Xin Zhang, and Richard D. Averitt. Comparison of birefringent electric split-ring resonator and meanderline structures as quarter-wave plates at terahertz frequencies. *Opt. Express*, 17(1):136–149, Jan 2009.

[55] Hu Tao, Emil A. Kadlec, Andrew C. Strikwerda, Kebin Fan, Willie J. Padilla, Richard D. Averitt, Eric A. Shaner, and X. Zhang. Microwave and terahertz wave sensing with metamaterials. *Opt. Express*, 19(22):21620–21626, Oct 2011.

[56] T. J. Yen, W. J. Padilla, N. Fang, D. C. Vier, D. R. Smith, J. B. Pendry, D. N. Basov, and X. Zhang. Terahertz magnetic response from artificial materials. *Science*, 303(5663):1494–1496, 2004.

[57] Hou-Tong Chen, Willie J Padilla, Michael J. Cich, Abul Kalam Azad, Richard Douglas Averitt, and Antoinette J. Taylor. A metamaterial solid-state terahertz phase modulator. 2009.

[58] Teodor K Todorov, Kathy Reuter, and David B Mitzi. High-efficiency solar cell with earth-abundant liquid-processed absorber. 22:E156–9, 05 2010.

[59] Claire Watts, David Shrekenhamer, John Montoya, Guy Lipworth, John Hunt, Timothy Sleasman, Sanjay Krishna, D Smith, and Willie Padilla. Terahertz compressive imaging with metamaterial spatial light modulators. 8, 08 2014.

[60] Thomas Maier and Hubert Brueckl. Multispectral microbolometers for the midinfrared. *Opt. Lett.*, 35(22):3766–3768, Nov 2010.

[61] Na Liu, Martin Mesch, Thomas Weiss, Mario Hentschel, and Harald Giessen. Infrared perfect absorber and its application as plasmonic sensor. *Nano Letters*, 10(7):2342–2348, 2010. PMID: 20560590.

[62] X. Zhao, Y. Wang, J. Schalch, G. Duan, K. Cremin, J. Zhang, C. Chen, R. D. Averitt, and X. Zhang. Optically modulated ultra-broadband all-silicon metamaterial terahertz absorber. in preperation.

[63] Meng Wu, Xiaoguang Zhao, Jingdi Zhang, Jacob Schalch, Guangwu Duan, Kevin Cremin, Richard Averitt, and Xin Zhang. A three-dimensional all-metal terahertz metamaterial perfect absorber. 111:051101, 07 2017.

[64] Xiaoguang Zhao, Jacob Schalch, Jingdi Zhang, Huseyin R. Seren, Guangwu Duan, Richard D. Averitt, and Xin Zhang. Electromechanically tunable metasurface transmission waveplate at terahertz frequencies. *Optica*, 5(3):303–310, Mar 2018.

[65] M. Rini, Z. Hao, R. W. Schoenlein, C. Giannetti, F. Parmigiani, S. Fourmaux, J. C. Kieffer, A. Fujimori, M. Onoda, S. Wall, and A. Cavalleri. Optical switching in vo2 films by below-gap excitation. *Applied Physics Letters*, 92(18):181904, 2008.

[66] R. Marques, F. Mesa, J. Martel, and F. Medina. Comparative analysis of edge- and broadside- coupled split ring resonators for metamaterial design - theory and experiments. *IEEE Transactions on Antennas and Propagation*, 51(10):2572–2581, Oct 2003.

[67] Na Liu, Hui Liu, and Harald Giessen. Stereometamaterials. In *Frontiers in Optics 2008/Laser Science XXIV/Plasmonics and Metamaterials/Optical Fabrication and Testing*, page PDPA7. Optical Society of America, 2008.

[68] G. R. Keiser, H. R. Seren, A. C. Strikwerda, X. Zhang, and R. D. Averitt. Structural control of metamaterial oscillator strength and electric field enhancement at terahertz frequencies. *Applied Physics Letters*, 105(8):081112, 2014.

[69] H. A. Haus and W. Huang. Coupled-mode theory. *Proceedings of the IEEE*, 79(10):1505–1518, Oct 1991.

[70] Ranjan Singh, Carsten Rockstuhl, and Weili Zhang. Strong influence of packing density in terahertz metamaterials. *Applied Physics Letters*, 97(24):241108, 2010.

[71] G. Scalari, C. Maissen, D. Turčinková, D. Hagenmüller, S. De Liberato, C. Ciuti, C. Reichl, D. Schuh, W. Wegscheider, M. Beck, and J. Faist. Ultrastrong coupling of the cyclotron transition of a 2d electron gas to a thz metamaterial. *Science*, 335(6074):1323–1326, 2012.

[72] W. C. Tay and E. L. Tan. Mur absorbing boundary condition for efficient fundamental 3-d lod-fdtd. *IEEE Microwave and Wireless Components Letters*, 20(2):61–63, Feb 2010.

[73] G. Duan, J. Schalch, X. Zhao, J. Zhang, R. D. Averitt, and X. Zhang. An air-spacer terahertz metamaterial perfect absorber for sensing and detection applications. In *2017 19th International Conference on Solid-State Sensors, Actuators and Microsystems (TRANSDUCERS)*, pages 1999–2002, June 2017.

[74] G. A. Wolff and A. I. Mlavsky. Crystal growth, theory and techniques. *Ed. C.H. L. Goodman*, pages 193–232, 1974.

[75] H. H. Haus. A theory of forced mode locking. *IEEE Journal of Quantum Electronics*, 11:323–330, 1975.

[76] François Salin, Jeff Squier, and Michel Piché. Mode locking of ti:al2o3 lasers and self-focusing: a gaussian approximation. *Opt. Lett.*, 16(21):1674–1676, Nov 1991.

[77] H. Haus. Theory of mode locking with a slow saturable absorber. *IEEE Journal of Quantum Electronics*, 11(9):736–746, September 1975.

[78] D. Kuizenga and A. Siegman. Fm and am mode locking of the homogeneous laser - part i: Theory. *IEEE Journal of Quantum Electronics*, 6(11):694–708, November 1970.

[79] T. Brabec, Ch. Spielmann, P. F. Curley, and F. Krausz. Kerr lens mode locking. *Opt. Lett.*, 17(18):1292–1294, Sep 1992.

[80] P. Uhd Jepsen, R. H. Jacobsen, and S. R. Keiding. Generation and detection of terahertz pulses from biased semiconductor antennas. *J. Opt. Soc. Am. B*, 13(11):2424–2436, Nov 1996.

[81] Matthew C. Beard, Gordon M. Turner, and Charles A. Schmuttenmaer. Subpicosecond carrier dynamics in low-temperature grown gaas as measured by time-resolved terahertz spectroscopy. *Journal of Applied Physics*, 90(12):5915–5923, 2001.

[82] John F. OHara, J. M. O. Zide, A. C. Gossard, A. J. Taylor, and R. D. Averitt. Enhanced terahertz detection via eras:gaas nanoisland superlattices. *Applied Physics Letters*, 88(25):251119, 2006.

[83] S. Vidal, J. Degert, M. Tondusson, E. Freysz, and J. Oberlé. Optimized terahertz generation via optical rectification in znte crystals. *J. Opt. Soc. Am. B*, 31(1):149–153, Jan 2014.

[84] Jian Lu, Harold Y. Hwang, Xian Li, Seung-Heon Lee, O-Pil Kwon, and Keith A. Nelson. Tunable multi-cycle thz generation in organic crystal hmq-tms. *Opt. Express*, 23(17):22723–22729, Aug 2015.

[85] Ryo Shimano, Shinichi Watanabe, and Ryusuke Matsunaga. Intense terahertz pulse-induced nonlinear responses in carbon nanotubes. *Journal of Infrared, Millimeter, and Terahertz Waves*, 33(8):861–869, Aug 2012.

[86] J. Hebling, K. Yeh, M. C. Hoffmann, and K. A. Nelson. High-power thz generation, thz nonlinear optics, and thz nonlinear spectroscopy. *IEEE Journal of Selected Topics in Quantum Electronics*, 14(2):345–353, March 2008.

[87] K.-L. Yeh, M. C. Hoffmann, J. Hebling, and Keith A. Nelson. Generation of 10j ultrashort terahertz pulses by optical rectification. *Applied Physics Letters*, 90(17):171121, 2007.

[88] Nishant Kumar, Andrew C. Strikwerda, Kebin Fan, Xin Zhang, Richard D. Averitt, Paul C. M. Planken, and Aurèle J. L. Adam. Thz near-field faraday imaging in hybrid metamaterials. *Opt. Express*, 20(10):11277–11287, May 2012.

[89] Jing Chen, Hai Nie, Tangqun Zha, Peng Mao, Chaojun Tang, Xueyang Shen, and Gun-Sik Park. Optical magnetic field enhancement by strong coupling in metamaterials. *J. Lightwave Technol.*, 36(13):2791–2795, Jul 2018.

[90] C. Sun and J. Li. Bandpass filter based on metamaterials in terahertz wave region. In *2011 4th IEEE International Symposium on Microwave, Antenna, Propagation and EMC Technologies for Wireless Communications*, pages 252–254, Nov 2011.

[91] Oliver Paul, René Beigang, and Marco Rahm. Highly selective terahertz bandpass filters based on trapped mode excitation. *Opt. Express*, 17(21):18590–18595, Oct 2009.

[92] Wonjoo Suh, Zheng Wang, and Shanhui Fan. Temporal coupled-mode theory and the presence of non-orthogonal modes in lossless multimode cavities. *IEEE Journal of Quantum Electronics*, 40(10):1511–1518, Oct 2004.

[93] S. E. Miller. Coupled wave theory and waveguide applications. *The Bell System Technical Journal*, 33(3):661–719, May 1954.

[94] Andrey A. Sukhorukov, Alexander S. Solntsev, Sergey S. Kruk, Dragomir N. Neshev, and Yuri S. Kivshar. Nonlinear coupled-mode theory for periodic plasmonic waveguides and metamaterials with loss and gain. *Opt. Lett.*, 39(3):462–465, Feb 2014.

[95] Longqing Cong, Prakash Pitchappa, Yang Wu, Lin Ke, Chengkuo Lee, Navab Singh, Hyunsoo Yang, and Ranjan Singh. Active multifunctional microelectromechanical system metadevices: Applications in polarization control, wavefront deflection, and holograms. *Advanced Optical Materials*, 5(2):1600716.

[96] Qi-Ye Wen, Yun-Song Xie, Huai-Wu Zhang, Qing-Hui Yang, Yuan-Xun Li, and Ying-Li Liu. Transmission line model and fields analysis of metamaterial absorber in the terahertz band. *Opt. Express*, 17(22):20256–20265, Oct 2009.

[97] F. Costa, S. Genovesi, A. Monorchio, and G. Manara. A circuit-based model for the interpretation of perfect metamaterial absorbers. *IEEE Transactions on Antennas and Propagation*, 61(3):1201–1209, March 2013.

[98] G. Duan, J. Schalch, X. Zhao, J. Zhang, R. D. Averitt, and X. Zhang. Identifying the perfect absorption of metamaterial absorbers. *Phys. Rev. B*, 97:035128, Jan 2018.

[99] Hou-Tong Chen. Interference theory of metamaterial perfect absorbers. *Opt. Express*, 20(7):7165–7172, Mar 2012.

[100] Markus Walther, Geoffrey S. Chambers, Zhigang Liu, Mark R. Freeman, and Frank A. Hegmann. Emission and detection of terahertz pulses from a metal-tip antenna. *J. Opt. Soc. Am. B*, 22(11):2357–2365, Nov 2005.

[101] B. S. . Ung, J. Li, H. Lin, B. M. Fischer, W. Withayachumnankul, and D. Abbott. Dual-mode terahertz time-domain spectroscopy system. *IEEE Transactions on Terahertz Science and Technology*, 3(2):216–220, March 2013.

[102] Giuseppe Cataldo, James A. Beall, Hsiao-Mei Cho, Brendan McAndrew, Michael D. Niemack, and Edward J. Wollack. Infrared dielectric properties of low-stress silicon nitride. *Opt. Lett.*, 37(20):4200–4202, Oct 2012.

[103] Hu Tao, Andrew C. Strikwerda, Mengkun Liu, Jessica P. Mondia, Evren Ekmekci, Kebin Fan, David L. Kaplan, Willie J. Padilla, Xin Zhang, Richard D. Averitt, and Fiorenzo G. Omenetto. Performance enhancement of terahertz metamaterials on ultrathin substrates for sensing applications. *Applied Physics Letters*, 97(26):261909, 2010.

[104] Xin Hu, Gaiqi Xu, Long Wen, Huacun Wang, Yuncheng Zhao, Yaxin Zhang, David R. S. Cumming, and Qin Chen. Metamaterial absorber integrated microfluidic terahertz sensors. *Laser & Photonics Reviews*, 10(6):962–969.

[105] D. Grischkowsky, Søren Keiding, Martin van Exter, and Ch. Fattinger. Far-infrared time-domain spectroscopy with terahertz beams of dielectrics and semiconductors. *J. Opt. Soc. Am. B*, 7(10):2006–2015, Oct 1990.

[106] P. R. Smith, D. H. Auston, and M. C. Nuss. Subpicosecond photoconducting dipole antennas. *IEEE Journal of Quantum Electronics*, 24(2):255–260, Feb 1988.

[107] J. C. Wiltse. History of millimeter and submillimeter waves. *IEEE Transactions on Microwave Theory and Techniques*, 32(9):1118–1127, September 1984.

[108] Mukesh Jewariya, Masaya Nagai, and Koichiro Tanaka. Ladder climbing on the anharmonic intermolecular potential in an amino acid microcrystal via an intense monocycle terahertz pulse. *Phys. Rev. Lett.*, 105:203003, Nov 2010.

[109] S. Uchida and Tamasuku K. C-axis optical spectra and charge dynamics in la2-xsrxcuo4. *Phys. Rev. B.*, 53:14558–14574, 1996.

[110] Tadao Nagatsuma, Shogo Horiguchi, Yusuke Minamikata, Yasuyuki Yoshimizu, Shintaro Hisatake, Shigeru Kuwano, Naoto Yoshimoto, Jun Terada, and Hiroyuki Takahashi. Terahertz wireless communications based on photonics technologies. *Opt. Express*, 21(20):23736–23747, Oct 2013.

[111] H. Song and T. Nagatsuma. Present and future of terahertz communications. *IEEE Transactions on Terahertz Science and Technology*, 1(1):256–263, Sept 2011.

[112] Shuzhen Fan, Feng Qi, Takashi Notake, Kouji Nawata, Yuma Takida, Takeshi Matsukawa, and Hiroaki Minamide. Diffraction-limited real-time terahertz imaging by optical frequency up-conversion in a dast crystal. *Opt. Express*, 23(6):7611–7618, Mar 2015.

[113] J. B. Pendry, D. Schurig, and D. R. Smith. Controlling electromagnetic fields. *Science*, 312(5781):1780–1782, 2006.

[114] Mehmet Unlu and Mona Jarrahi. Miniature multi-contact mems switch for broadband terahertz modulation. *Opt. Express*, 22(26):32245–32260, Dec 2014.

[115] A Q Liu, W M Zhu, D P Tsai, and N I Zheludev. Micromachined tunable metamaterials: a review. *Journal of Optics*, 14(11):114009, 2012.

[116] Z. Han, K. Kohno, H. Fujita, K. Hirakawa, and H. Toshiyoshi. Tunable terahertz filter and modulator based on electrostatic mems reconfigurable srr array. *IEEE Journal of Selected Topics in Quantum Electronics*, 21(4):114–122, July 2015.

[117] Xinyu Liu and Willie J. Padilla. Reconfigurable room temperature metamaterial infrared emitter. *Optica*, 4(4):430–433, Apr 2017.

[118] K. Fan, X. Zhao, J. Zhang, K. Geng, G. R. Keiser, H. R. Seren, G. D. Metcalfe, M. Wraback, X. Zhang, and R. D. Averitt. Optically tunable terahertz metamaterials on highly flexible substrates. *IEEE Transactions on Terahertz Science and Technology*, 3(6):702–708, Nov 2013.

[119] Hou-Tong Chen, John F. OHara, Abul Kalam Azad, Antoinette J. Taylor, Richard Douglas Averitt, David B Shrekenhamer, and Willie J Padilla. Experimental demonstration of frequency-agile terahertz metamaterials. 2008.

[120] Xiaoguang Zhao, Kebin Fan, Jingdi Zhang, Huseyin R. Seren, Grace D. Metcalfe, Michael Wraback, Richard D. Averitt, and Xin Zhang. Optically tunable metamaterial perfect absorber on highly flexible substrate. *Sensors and Actuators A: Physical*, 231:74 – 80, 2015. Special Issue of the Micromechanics Section of Sensors and Actuators based upon contributions revised from the Technical Digest of the 27th IEEE International Conference on MICRO ELECTRO MECHANICAL SYSTEMS (MEMS-14; 2630 January 2014, San Francisco, CA, USA).

[121] Kebin Fan, Jonathan Suen, Xueyuan Wu, and Willie J. Padilla. Graphene metamaterial modulator for free-space thermal radiation. *Opt. Express*, 24(22):25189–25201, Oct 2016.

[122] Hou-Tong Chen, John F. O'Hara, Abul K. Azad, D. Shrekenhamer, Willie J. Padilla, Joshua M. O. Zide, Arthur C. Gossard, Richard D. Averitt, and Antoinette J. Taylor. Active terahertz metamaterial devices. In *Frontiers in Optics 2008/Laser Science XXIV/Plasmonics and Metamaterials/Optical Fabrication and Testing*, page MMD5. Optical Society of America, 2008.

[123] E. F. C. Driessen and M. J. A. de Dood. The perfect absorber. *Applied Physics Letters*, 94(17):171109, 2009.

[124] Claire M. Watts, Xianliang Liu, and Willie J. Padilla. Metamaterial electromagnetic wave absorbers. *Advanced Materials*, 24(23):OP98–OP120.

[125] Teodor K. Todorov, Kathleen B. Reuter, and David B. Mitzi. High-efficiency solar cell with earth-abundant liquid-processed absorber. *Advanced Materials*, 22(20):E156–E159.

[126] Yu Hui and Matteo Rinaldi. Fast and high resolution thermal detector based on an aluminum nitride piezoelectric microelectromechanical resonator with an integrated suspended heat absorbing element. *Applied Physics Letters*, 102(9):093501, 2013.

[127] Christopher L. Holloway, Andrew Dienstfrey, Edward F. Kuester, John F. OHara, Abul K. Azad, and Antoinette J. Taylor. A discussion on the interpretation and characterization of metafilms/metasurfaces: The two-dimensional equivalent of metamaterials. *Metamaterials*, 3(2):100 – 112, 2009.

[128] Quan Li, Z. T. Tian, Xueqian Zhang, Ranjan Singh, Liangliang Du, Jianqiang Gu, Jiaguang Han, and Weili Zhang. Active graphenesilicon hybrid diode for terahertz waves. In *Nature communications*, 2015.

[129] Jie Ji, Siyan Zhou, Jingcheng Zhang, Furi Ling, and J. G. Yao. Electrical terahertz modulator based on photo-excited ferroelectric superlattice. In *Scientific reports*, 2018.

[130] Yapeng Cao, Sheng Gan, Zhaoxin Geng, Jian Liu, Yu-Ping Ou Yang, Qiaoling Bao, and Hongda Chen. Optically tuned terahertz modulator based on annealed multilayer mos2. *Scientific reports*, 6:22899, 2016.

[131] Berardi Sensale-Rodriguez, Rusen Yan, Michelle M. Kelly, Tian Fang, Kristof Tahy, Wan Sik Hwang, Debdeep Jena, Lei Liu, and Huili Grace Xing. Broadband graphene terahertz modulators enabled by intraband transitions. *Nature communications*, 3:780, 2012.

[132] Lyubov V. Titova, Ayesheshim K. Ayesheshim, Andrey Golubov, Dawson Fogen, Rocio Rodriguez-Juarez, Frank A. Hegmann, and Olga Kovalchuk. Intense thz pulses cause h2ax phosphorylation and activate dna damage response in human skin tissue. *Biomed. Opt. Express*, 4(4):559–568, Apr 2013.

[133] M. B. Agranat, O. V. Chefonov, A. V. Ovchinnikov, S. I. Ashitkov, V. E. Fortov, and P. S. Kondratenko. Damage in a thin metal film by high-power terahertz radiation. *Phys. Rev. Lett.*, 120:085704, Feb 2018.

[134] Liang-Hui Du, Jiang Li, Zhao-Hui Zhai, Kun Meng, Qiao Liu, Sen-Cheng Zhong, Ping-Wei Zhou, Li-Guo Zhu, Ze-Ren Li, and Qi-Xian Peng. A high-performance broadband terahertz absorber based on sawtooth-shape doped-silicon. *AIP Advances*, 6(5):055112, 2016.

[135] Mingbo Pu, Min Wang, Chenggang Hu, Cheng Huang, Zeyu Zhao, Yanqin Wang, and Xiangang Luo. Engineering heavily doped silicon for broadband absorber in the terahertz regime. *Opt. Express*, 20(23):25513–25519, Nov 2012.

[136] R. Kakimi, M. Fujita, M. Nagai, M. Ashida, and T. Nagatsuma. Capture of a terahertz wave in a photonic-crystal slab. *Nat. Photon.*, 8:657–663, 2014.

[137] Ying Xiong, Qi-Ye Wen, Zhi Chen, Wei Tian, Tian-Long Wen, Yu-Lan Jing, Qing-Hui Yang, and Huai-Wu Zhang. Tuning the phase transitions of vo 2 thin films on silicon substrates using ultrathin al 2 o 3 as buffer layers. *Journal of Physics D: Applied Physics*, 47(45):455304, 2014.

[138] Computer Simulation Technologies. Microwave studio suite. *Phys. Rev. Lett.*, 2016, Nov 2016.

[139] Yan Peng, XiaoFei Zang, YiMing Zhu, Cheng Shi, Lin Chen, Bin Cai, and SongLin Zhuang. Ultra-broadband terahertz perfect absorber by exciting multi-order diffractions in a double-layered grating structure. *Opt. Express*, 23(3):2032–2039, Feb 2015.

[140] Xinyu Liu, Kebin Fan, Ilya V. Shadrivov, and Willie J. Padilla. Experimental realization of a terahertz all-dielectric metasurface absorber. *Opt. Express*, 25(1):191–201, Jan 2017.

[141] Xue-Yong Deng, Xin-Hua Deng, Fu-Hai Su, Nian-Hua Liu, and Jiang-Tao Liu. Broadband ultra-high transmission of terahertz radiation through monolayer mos2. *Journal of Applied Physics*, 118(22):224304, 2015.

[142] J. Wang, J. Tian, T. Li, J. Zhou, and S. Gong. Transmittance and sheet conductivity of monolayer mos2 measured by terahertz time-domain spectroscopy. In *2017 42nd International Conference on Infrared, Millimeter, and Terahertz Waves (IRMMW-THz)*, pages 1–2, Aug 2017.

[143] Dong-Hong Qiu, Qi-Ye Wen, Qing-Hui Yang, Zhi Chen, Yu-Lan Jing, and Huai-Wu Zhang. Electrically-driven metalinsulator transition of vanadium dioxide thin films in a metaloxide-insulatormetal device structure. *Materials Science in Semiconductor Processing*, 27:140 – 144, 2014.

[144] L. Y. Hao, X. J. Zhou, Z. B. Yang, H. L. Zhang, H. C. Sun, H. X. Cao, P. H. Dai, J. Li, T. Hatano, H. B. Wang, Q. Y. Wen, and P. H. Wu. A power-adjustable superconducting terahertz source utilizing electrical triggering phase transitions in vanadium dioxide. *Applied Physics Letters*, 109(23):233503, 2016.

[145] John G. Simmons. Poole-frenkel effect and schottky effect in metal-insulator-metal systems. *Phys. Rev.*, 155:657–660, Mar 1967.

[146] Giwan Seo, Bong-Jun Kim, Changhyun Ko, Yanjie Cui, Yong Lee, Jun-Hwan Shin, Shriram Ramanathan, and Hyun-Tak Kim. Voltage-pulse-induced switching dynamics in vo2 thin-film devices on silicon. *Electron Device Letters, IEEE*, 32:1582 – 1584, 12 2011.

[147] B. W. Shore and N. V. Vitanov. Overdamping of coherently driven quantum systems. *Contemporary Physics*, 47(6):341–362, 2006.

[148] Ashok Kodigala, Thomas Lepetit, and Boubacar Kanté. Exceptional points in three-dimensional plasmonic nanostructures. *Phys. Rev. B*, 94:201103, Nov 2016.

[149] David Pile. Nano-optics: Exceptional plasmonics. *Nature Photonics*, 11:24–24, 01 2017.

[150] Anonymous. Proceedings of the american physical society. *Phys. Rev.*, 69:674–674, Jun 1946.

[151] A. F. Kockum, A. Miranowicz, S. De Liberato, S. Savasta, and F. Nori. Ultrastrong coupling between light and matter. *arXiv*, 1807.11636, 2018.

[152] J. M. Raimond, M. Brune, and S. Haroche. Manipulating quantum entanglement with atoms and photons in a cavity. *Rev. Mod. Phys.*, 73:565–582, Aug 2001.

[153] Aji A. Anappara, Simone De Liberato, Alessandro Tredicucci, Cristiano Ciuti, Giorgio Biasiol, Lucia Sorba, and Fabio Beltram. Signatures of the ultrastrong light-matter coupling regime. *Phys. Rev. B*, 79:201303, May 2009.

[154] D. Meschede, H. Walther, and G. Müller. One-atom maser. *Phys. Rev. Lett.*, 54:551–554, Feb 1985.

[155] R. J. Thompson, G. Rempe, and H. J. Kimble. Observation of normal-mode splitting for an atom in an optical cavity. *Phys. Rev. Lett.*, 68:1132–1135, Feb 1992.

[156] C. Weisbuch, M. Nishioka, A. Ishikawa, and Y. Arakawa. Observation of the coupled exciton-photon mode splitting in a semiconductor quantum microcavity. *Phys. Rev. Lett.*, 69:3314–3317, Dec 1992.

[157] Xiu Gu, Anton Frisk Kockum, Adam Miranowicz, Yu xi Liu, and Franco Nori. Microwave photonics with superconducting quantum circuits. *Physics Reports*, 718-719:1 – 102, 2017. Microwave photonics with superconducting quantum circuits.

[158] R. H. Dicke. Coherence in spontaneous radiation processes. *Phys. Rev.*, 93:99–110, Jan 1954.

[159] P. Forn-Diaz, L. Lucas, E. R. Ortega, J. Kono, and E. Solano. Ultrastrong coupling regimes of light-matter interaction. *arXiv*, 1804.0927, 2018.

[160] D.J. Shelton, I. Brener, J. C. Ginn, M. B. Sinclair, D. W. Peters, K. R. Coffey, and G. D. Boreman. Strong coupling between nanoscale metamaterials and phonons. *Nano Letters*, 11(5):2104–2108, 2011. PMID: 21462937.

[161] Y. Todorov, A. M. Andrews, R. Colombelli, S. De Liberato, C. Ciuti, P. Klang, G. Strasser, and C. Sirtori. Ultrastrong light-matter coupling regime with polariton dots. *Phys. Rev. Lett.*, 105:196402, Nov 2010.

[162] Iacopo Carusotto and Cristiano Ciuti. Quantum fluids of light. *Rev. Mod. Phys.*, 85:299–366, Feb 2013.

[163] Cristiano Ciuti, Gérald Bastard, and Iacopo Carusotto. Quantum vacuum properties of the intersubband cavity polariton field. *Phys. Rev. B*, 72:115303, Sep 2005.

[164] Curdin Maissen, Giacomo Scalari, Federico Valmorra, Mattias Beck, Jérôme Faist, Sara Cibella, Roberto Leoni, Christian Reichl, Christophe Charpentier, and Werner Wegscheider. Ultrastrong coupling in the near field of complementary split-ring resonators. *Phys. Rev. B*, 90:205309, Nov 2014.

[165] Andreas Bayer, Marcel Pozimski, Simon Schambeck, Dieter Schuh, Rupert Huber, Dominique Bougeard, and Christoph Lange. Terahertz lightmatter interaction beyond unity coupling strength. *Nano Letters*, 17(10):6340–6344, 2017. PMID: 28937772.

[166] Maximilian P E Lock and Ivette Fuentes. Dynamical casimir effect in curved spacetime. *New Journal of Physics*, 19(7):073005, 2017.

[167] A. Ridolfo, S. Savasta, and M. J. Hartmann. Nonclassical radiation from thermal cavities in the ultrastrong coupling regime. *Phys. Rev. Lett.*, 110:163601, Apr 2013.

[168] Markus Aspelmeyer, Tobias J. Kippenberg, and Florian Marquardt. Cavity optomechanics. *Rev. Mod. Phys.*, 86:1391–1452, Dec 2014.

[169] L S. Bilbro, Rolando Valds Aguilar, G Logvenov, O Pelleg, and N P. Armitage. Temporal correlations of superconductivity above the transition temperature in la2xsrxcuo4 probed by terahertz spectroscopy. *Nature Physics*, 7:298–302, 04 2011.

[170] J. Bardeen, L. N. Cooper, and J. R. Schrieffer. Theory of superconductivity. *Phys. Rev.*, 108:1175–1204, Dec 1957.

[171] Vitaly L. Ginzburg. On superconductivity and superfluidity (what i have and have not managed to do), as well as on the physical minimum at the beginning of the 21st century. *ChemPhysChem*, 5(7):930–945.

[172] R. C. Jaklevic, John Lambe, A. H. Silver, and J. E. Mercereau. Quantum interference effects in josephson tunneling. *Phys. Rev. Lett.*, 12:159–160, Feb 1964.

[173] Hiroshi Shimada, Kenji Miyawaki, Ayano Hagiwara, Kouichi Takeda, and Yoshinao Mizugaki. Characterization of superconducting single-electron transistors with small al/alo img [http://ej.iop.org/images/0953-2048/27/11/115015/toc$_s ust$502162$ieqn$1$.gif]_x$ /v josephson junctions. *Superconductor Science and Technology*, 27(11):115015, 2014.

[174] Lilia Vitalyevna Yerosheva, Director Dr, and Peter M. Kogge. High-level prototyping for the htmt petaflop machine, 2001.

[175] E. Altshuler and R. Garca. Josephson junctions in a magnetic field: Insights from coupled pendula. *American Journal of Physics*, 71(4):405–408, 2003.

[176] J. G. Bednorz and K. A. Müller. Possible high T_c superconductivity in the Ba-La-Cu-O system. *Zeitschrift fur Physik B Condensed Matter*, 64:189–193, June 1986.

[177] A.M. Gerrits, A. Wittlin, V.H.M. Duijn, A.A. Menovsky, J.J.M. Franse, and P.J.M. van Bentum. Josephson plasma oscillations in la1.85sr0.15cuo4. *Physica C: Superconductivity*, 235-240:1117 – 1118, 1994.

[178] W. E. Lawrence and Doniach S. Lawrencedoniach model. *12th international Conference on Low Temperature Physics*, page 361, 1971.

[179] S Savelev, Alexander Rakhmanov, V A Yampol 'skii, and Franco Nori. Analogues of nonlinear optics using terahertz josephson plasma waves in layered superconductors. *Nature Physics*, 2, 08 2006.

[180] J. Hammer, M. Aprili, and I. Petković. Microwave cooling of josephson plasma oscillations. *Phys. Rev. Lett.*, 107:017001, Jun 2011.

[181] D. Nicoletti, E. Casandruc, Y. Laplace, V. Khanna, C. R. Hunt, S. Kaiser, S. S. Dhesi, G. D. Gu, J. P. Hill, and A. Cavalleri. Optically induced superconductivity in striped $la_{2-x}ba_xcuo_4$ by polarization-selective excitation in the near infrared. *Phys. Rev. B*, 90:100503, Sep 2014.

[182] S. Rajasekaran, E. Casandruc, Y. Laplace, D. Nicoletti, G. D. Gu, S. R. Clark, D. Jaksch, and A. Cavalleri. Parametric amplification of a superconducting plasma wave. *Nat. Phys.*, 12:1012–1016, Jul 2016.

[183] Y. Laplace, S. Fernandez-Pena, S. Gariglio, J. M. Triscone, and A. Cavalleri. Proposed cavity josephson plasmonics with complex-oxide heterostructures. *Phys. Rev. B*, 93:075152, Feb 2016.

[184] H. T. Stinson, J. S. Wu, B. Y. Jiang, Z. Fei, A. S. Rodin, B. C. Chapler, A. S. McLeod, A. Castro Neto, Y. S. Lee, M. M. Fogler, and D. N. Basov. Infrared nanospectroscopy and imaging of collective superfluid excitations in anisotropic superconductors. *Phys. Rev. B*, 90:014502, Jul 2014.

[185] Hu Tao, C. M. Bingham, A. C. Strikwerda, D. Pilon, D. Shrekenhamer, N. I. Landy, K. Fan, X. Zhang, W. J. Padilla, and R. D. Averitt. Highly flexible wide angle of incidence terahertz metamaterial absorber: Design, fabrication, and characterization. *Phys. Rev. B*, 78:241103, Dec 2008.

[186] Kunihiko Oka, M.J.V. Menken, Z. Tarnawski, A.A. Menovsky, A.M. Moe, T.S. Han, Hiromi Unoki, Toshimitsu Ito, and Yorio Ohashi. Crystal growth of la2xsrxcuo4 by the travelling-solvent floating-zone method. *Journal of Crystal Growth*, 137(3):479 – 486, 1994.

[187] S. V. Dordevic, Seiki Komiya, Yoichi Ando, and D. N. Basov. Josephson plasmon and inhomogeneous superconducting state in $la_{2-x}sr_xcuo_4$. *Phys. Rev. Lett.*, 91:167401, Oct 2003.

[188] S. Tajima, Y. Fudamoto, T. Kakeshita, B. Gorshunov, V. Železný, K. M. Kojima, M. Dressel, and S. Uchida. In-plane optical conductivity of $la_{2-x}sr_xCuo_4$: Reduced superconducting condensate and residual drude-like response. *Phys. Rev. B*, 71:094508, Mar 2005.

[189] B. B. Varga. Coupling of plasmons to polar phonons in degenerate semiconductors. *Phys. Rev.*, 137:A1896–A1902, Mar 1965.

[190] K. S. Singwi and M. P. Tosi. Interaction of plasmons and optical phonons in degenerate semiconductors. *Phys. Rev.*, 147:658–662, Jul 1966.

[191] Said Rahimzadeh-Kalaleh Rodriguez. Classical and quantum distinctions between weak and strong coupling. *European Journal of Physics*, 37(2):025802, 2016.

[192] Yifu Zhu, Daniel J. Gauthier, S. E. Morin, Qilin Wu, H. J. Carmichael, and T. W. Mossberg. Vacuum rabi splitting as a feature of linear-dispersion theory: Analysis and experimental observations. *Phys. Rev. Lett.*, 64:2499–2502, May 1990.

[193] Lukas Novotny. Strong coupling, energy splitting, and level crossings: A classical perspective. *American Journal of Physics*, 78(11):1199–1202, 2010.

[194] R. Houdr. Early stages of continuous wave experiments on cavity-polaritons. *Physica Status Solidi (b)*, 242:1002, 2005.

[195] V. M. Muravev, I. V. Andreev, I. V. Kukushkin, S. Schmult, and W. Dietsche. Observation of hybrid plasmon-photon modes in microwave transmission of coplanar microresonators. *Phys. Rev. B*, 83:075309, Feb 2011.

[196] A. E. Koshelev, L. N. Bulaevskii, and M. P. Maley. Josephson coupling, phase correlations, and josephson plasma resonance in vortex liquid phase. *Phys. Rev. B*, 62:14403–14418, Dec 2000.

[197] B.-Y. Jiang, L. M. Zhang, A. H. Castro Neto, D. N. Basov, and M. M. Fogler. Generalized spectral method for near-field optical microscopy. *Journal of Applied Physics*, 119(5):054305, 2016.

[198] L. M. Zhang, G. O. Andreev, Z. Fei, A. S. McLeod, G. Dominguez, M. Thiemens, A. H. Castro-Neto, D. N. Basov, and M. M. Fogler. Near-field spectroscopy of silicon dioxide thin films. *Phys. Rev. B*, 85:075419, Feb 2012.

[199] Andrey S. Potemkin, Alexander N. Poddubny, Pavel A. Belov, and Yuri S. Kivshar. Green function for hyperbolic media. *Phys. Rev. A*, 86:023848, Aug 2012.

[200] A. Poddubny, I. Iorsh, Belov. P, and Y. Kivshar. Hyperbolic metamaterials. *Nat. Photon.*, 7:948–957, 2013.

[201] Caner Guclu, Salvatore Campione, and Filippo Capolino. Array of dipoles near a hyperbolic metamaterial: Evanescent-to-propagating floquet wave transformation. *Phys. Rev. B*, 89:155128, Apr 2014.